

https://dspace.org/

U-Pb and Ar-Ar geochronology and geochemistry of the south-eastern Basement Complex of South Sudan

Tshwane, Itumeleng

2020

https://hdl.handle.net/10539/31029

Downloaded from a DSpace repository. https://dspace.org/

U-Pb and Ar-Ar geochronology and geochemistry of the south-eastern Basement Complex of South Sudan

By

Itumeleng Tshwane

A dissertation submitted to the Faculty of Science, University of the Witwatersrand, Johannesburg, in fulfilment of the requirements for the degree of Master of Science



School of Geosciences

University of the Witwatersrand

Private Bag 3

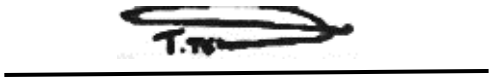
2050 Wits

South Africa

2019

Declaration

I, Itumeleng Tshwane, declare that this dissertation is my own, unaided work. It is being submitted for the Degree of Master of Science at the University of the Witwatersrand, Johannesburg. It has not been submitted before for any degree or examination at any other University.



(Itumeleng Tshwane)

On the 25th day of August 2020 at Braamfontein, Johannesburg

Abstract

A few studies have suggested that the poorly studied and undifferentiated Basement Complex of South Sudan was part of the Congo Craton. In this work, granitic gneisses and biotite schists are examined to enhance our knowledge of the nature and mode of tectonic and geological evolution of this geological unit. Zircon U-Pb, Lu-Hf and Ar-Ar isotope systematics, petrographical observations and whole rock geochemistry reveal a single major crust-forming magmatic or crustal reworking event at 981-924 Ma. The zircons show a mean crustal residence age of 2.3 Ga and εHf(t) values of -24 to -30 suggesting the existence of older Precambrian crust. This magmatic event gave rise to calc-alkaline, peraluminous I-type granites with high SiO_2 (74 -75wt. %) and K_2O (3.8-5.3 wt. %) and low CaO (1.0-1.3 wt. %) contents. The gneissic granites also show enrichment of LILE and LREE, depletion in HREE and negative P and Ti anomalies in normalized multi-element diagrams indicating a possible subduction-related origin.

Biotite schists were originally lithic arenites derived from mixed felsic and basic source rocks from NE Congo Craton in northern Uganda and deposited in an oceanic island tectonic setting sometime after 920 Ma as inferred from geochemical fingerprinting. The granitic gneisses and schists all show evidence of high-temperature peak metamorphism (M1) at 633 ± 17 Ma, attributed to continent-continent collision between the Congo Craton and the Saharan Metacraton. This tectono-metamorphic event was followed by retrograde metamorphism at 555 ± 3 Ma due to cooling (M2) and subsequent crystal-plastic deformation (D1) linked to the ductile-brittle deformation stage of the Aswa Shear Zone. The above data reveal a strong similarity in the geodynamic evolution between the Basement Complex in South Sudan and the Western Mozambique Belt in Tanzania, corroborating earlier speculations regarding the extension of the Mozambique Belt into South Sudan.

Acknowledgements

My most sincere gratitude and acknowledgement is directed to VM Investment Company (Pty) Ltd and Dr. Sharad Master for the financial support afforded to the project. I would also like to thank Prof. Roger Gibson for his assistance in obtaining additional financial support from the School of Geosciences.

A very special and big thank you is to my supervisors, Dr. Sharad Master and Prof. Robert Bolhar for having guided me from the inception stages of the project to its very end. The great insight you have both shared with me has contributed so much towards this project. I am thankful for all the sacrifices that were made to ensure the success of this project.

I would like to also thank Dr. Yashirvad Thakurdin and Mr. Tim Marais for their expertise and guidance throughout the duration of the project. Your time and willingness to help is highly appreciated. I am tremendously grateful to the late Mr. Joe Aphane for the amazing help and guidance pertinent to the mineral separation process. Mr. Marlin Patchappa and Prof. Jan Kramers are thanked for having performed the geochemical analyses and Ar-Ar geochronology, respectively. Gratitude is also directed to Prof. Alexander Ziegler for training me to operate the EPMA and ensuring that I obtain my CL images in time. Thanks to Henriette Ueckermann and Prof. Robert Bolhar for assisting me with the U-Pb and Hf isotopes analyses, as well as the process of data reduction done thereafter. This project wouldn't have been possible without the help of the staff at the rock crushing and preparation lab at the School of Geosciences, University of the Witwatersrand.

My acknowledgements would be incomplete without the mention of my family and friends who have contributed so much to the completeness of this project, your love and emotional support has kept me going. To my mom, Mamogolo Tshwane and my younger sister, Palesa Tshwane, I can never thank you both enough; I'm forever indebted to you. My final and very

important gesture of appreciation is directed to my father and brother, Patrick Aphane and Tshepiso Ledwaba for the timely words of encouragement, you have both been my greatest source of motivation.

Table of Contents

Declaration i
Abstract ii
Acknowledgements iii
List of Figures viii
List of Tables xviii

Chapter 1: Introduction 1

1.1 Background 1
1.2 Research problem 1
1.3 Aims and objectives 2
1.4 Description of the study area 3
1.5 Structure of the dissertation 4
1.6 Previous work 5
1.7 Tectonic setting and regional geology 8
1.7.1 Geology of the Congo Craton 12
1.7.1.1 Mboumou-Uganda block 13
1.8 Local geology 17
1.8.1 Geological structures and mineralisation in the study area 19

Chapter 2: Petrography and mineralogy 21

2.1 Introduction 21
2.2 Analytical methods 21
2.3 Results 21
2.4 Discussion 37
2.5 Summary and conclusions 45

Chapter 3: Geochemistry 47

3.1 Introduction 47
3.2 Analytical methods 47
3.3 Results 47

3.3.2.1 Whole rock major elements 50
3.3.2.1 Trace Elements 54
3.3.2.1 Rare Earth Elements 55
3.3.3 Biotite schists 59
3.3.3.1 Whole rock major elements 59
3.3.3.2 Trace elements 60
3.3.3.3 Rare earth elements 61
3.4 Discussion 67
3.4.1 Granitic gneisses 67
3.4.2 Biotite schists 73
3.5 Summary and conclusions 77

Chapter 4: Ar-Ar geochronology 79

4.1 Introduction 79
4.2 Analytical methods 79
4.3 Results 80
4.4 Discussion 82
4.5 Summary and conclusions 84

Chapter 5: Zircon U-Pb geochronology 86

5.1 Introduction 86
5.2 Analytical methods 86
5.3 Results 88
5.4 Discussion 97
5.5 Summary and conclusions 100

Chapter 6: Zircon Lu-Hf isotopes 102

6.1 Introduction 102
6.2 Analytical methods 102
6.3 Results 103
6.4 Discussion 108

6.5 Summary and Conclusions 111

Chapter 7: Integrated discussion and conclusions 113

7.1 Integrated discussion 113
7.2 Conclusions 118
7.3 Future work 120

References 121

Appendices 135

List of Figures

Figure 1.1: Google Earth map displaying the location of the study area in South Sudan. Yellow pin indicates the position of Jebel Kujur and Juba is indicated by the small red star (Google Earth, 2020). _____3

Figure 1.2: Photographs of the study area. A and B: Jebel Kujur mountain photographed from varying angles (Miettaux, 2013), C: Aerial view of the Bahr el Jebel river, about 6.5 km, East of Jebel Kujur (McKenna, 2011). _____4

Figure 1.3: Distribution of crustal domains in Central Africa. Small red triangle indicates the position of the study area on the regional geological map, ANS: Arabian-Nubian Shield (modified after Garzanti et al., 2018).____10

Figure 1.4: Location of the study area relative to the Obanguides Orogenic Belt, Saharan Metacran and the Congo Craton. Small red triangle indicates the position of the study area. CAR: Central African Republic (modified after Abdelsalam et al., 2002). _____12

Figure 1.5: Sketch map of the constituents of the Congo Craton, indicating the six Archaean cratonic terranes (purple), Eburnean (green) and Kibaran (orange and yellow). All the Pan-African fold and thrust belts are shown in brown (from De Wit and Linol, 2015). _____13

Figure 1.6: A simplified geological map of South Sudan with a focus on the Basement Complex. Red triangle indicates the position of the study area (Jebel Kujur) (modified after Civetta et al., 1979). _____17

Figure 2.1: Hand specimen of the biotite-hornblende gneiss (sample JK/1) from Jebel Kujur, with a specific illustration of the biotite bands crosscut by a possible quartz vein. _____23

Figure 2.2: Microphotograph of the biotite-hornblende gneiss (sample JK/1), image in XPL is shown on the left and PPL on the right. Hbl: interstitial hornblende, Bio: biotite, Pl: plagioclase, Kfs: alkali-feldspar, myrmekite fabric in plagioclase, showing intergrowth of vermicular quartz; also shown is deformation twinning in plagioclase. Subgrain rotation (SGR) of plagioclase is indicated. _____23

Figure 2.3: Biotite-hornblende gneiss (sample JK/1) showing deformation twinning in plagioclase and muscovite (Ms) replacing biotite (bio).____24

Figure 2.4: Hand specimen of muscovite-hornblende gneiss (sample JK/2).____25

Figure 2.5: Microphotograph of muscovite-hornblende gneiss (sample JK/2), image in XPL is shown on the left and PPL on the right. Qtz ribbons: Polycrystalline quartz ribbons in response to deformation, deformation twinning as a result of intracrystalline deformation. Grain boundary migration (GBM) of quartz. _____26

Figure 2.6: Muscovite-hornblende gneiss (sample JK/2) showing myrmekite fabric in plagioclase and alteration of plagioclase into sericite (Ser), GBM: Grain boundary migration in quartz. _____26

Figure 2.7: Hand specimen of the muscovite-biotite gneiss (sample JK/3). _____28

Figure 2.8: Microphotograph of the muscovite-biotite gneiss (sample JK/3) showing inequigranular texture with interlobate to amoeboid grain boundaries, spaced foliation is defined by layered biotite and alkali-feldpar-quarttz-muscovite. _____28

Figure 2.9: Muscovite-biotite gneiss (sample JK/3) showing recrystallized quartz with alternating long and short polycrystalline ribbons (RQ), RR: Reaction rims along the boundaries of feldspars producing myrmekitic fabric, Sil: sillimanite. _____29

Figure 2.10: Hand specimen of the biotite-muscovite gneiss (sample JK/4).____30

Figure 2.11: Microphotograph of the biotite-muscovite gneiss (sample JK/4), image in XPL is shown on the left and PPL on the right. Sil: Sillimanite, Ser: Sericite laths within plagioclase, Grt: Garnet porphyroblast, Crd: Cordierite and cordierite-bearing symplectites. Development of myrmekite deformation fabric in plagioclase is also shown. _____31

Figure 2.12: QAP diagram classifying the gneisses (samples JK/1, JK/2, JK/3 and JK/4). 1: Alkali Quartz Syenite, 2: Quartz Monzodiorite, 3: Quartz Diorite, 4: Alkali Syenite, 5: Syenite, 6: Monzonite, 7: Monzodiorite, 8: Diorite (after Streckeisen, 1976). _____31

Figure 2.13: Hand specimen of the biotite schist (sample JK/5). _____33

Figure 2.14: Microphotograph of biotite schist (sample JK/5). Image in XPL is shown on the left and PPL on the right. Penetrative secondary foliation with interlobate to amoeboid texture is shown. The spaced and anastomosing foliation is defined by biotite+garnet+opaques (cleavage domains) and quartz+plagioclase+alkali-feldspar (microlithons). _____33

Figure 2.15: Biotite schist (sample JK/5) showing polycrystalline quartz, Grt: garnet grain with corona texture separating it from the biotite, Bio: Biotite rich layers defining a penetrative secondary foliation, SGR: Subgrain rotation of alkali-feldspar and biotite, Kfs: Alkali-feldspar, Pl: Plagioclase CAT: Cataclasis with melt flow in the plagioclase grain. __34

Figure 2.16: Biotite schist (sample JK/5) showing deformation twinning in plagioclase and myrmekitic fabric in alkali-feldspar, GBM: Grain boundary migration, shown as lobate grain boundaries in alkali-feldspar. _____34

Figure 2.17: Hand specimen of the biotite-garnet schist (sample JK/6) from Jebel Kujur. __36

Figure 2.18: Microphotograph of the biotite-garnet schist (sample JK/6) image in XPL is shown on the left and PPL on the right. Anastomosing foliation is defined by biotite+garnet+hornblende (cleavage domains) and quartz+plagioclase+alkali-feldspar (microlithons). Overall texture is inequigranular- interlobate. _____36

Figure 2.19: Biotite-garnet schist (sample JK/6) showing biotite porphyroblasts (BIO) with undulose extinction, plagioclase (Pl) subgrain, Ser: Alteration of feldspars into sericite, Grt: Garnet porphyroblasts overprinting biotite and straight garnet boundaries._____37

Figure 2.20: PPL and XPL microphotographs of garnet porphyroblast enveloping feldspars from sample JK/4, also shown is the skeletal laths of sillimanite overprinting the garnet, Bio: Secondary biotite and Crd: Cordierite and cordierite bearing-symplectites produced from the retrograde reaction: Grt+Kspar+Liq= Crd+Bio. CAT: Melt-filled fractures indicating cataclasis, subgrain rotation (SGR) and grain boundary migration (GBM) on feldspars in the matrix. _____42

Figure 3.1: K_2O/Al_2O_3 vs Na_2O/Al_2O_3 discrimination diagram for the granitic gneisses (samples JK/1, JK/2, JK/3 and JK/4) and biotite schists (samples JK/5 and JK/6) (after Garrels and McKenzie, 1971). _____49

Figure 3.2: MgO vs Al_2O_3 discrimination diagram for the granitic gneisses (samples JK/1, JK/2, JK/3 and JK/4) and biotite schists (samples JK/5 and JK/6) (after Marc, 1992). _____49

Figure 3.3: SiO_2 vs K_2O+Na_2O (TAS) classification diagram for plutonic rocks, plots of the granitic gneisses is indicated (Middlemost, 1994).____51

Figure 3.4: SiO_2 vs FeO_{total}/ ($MgO+FeO_{total}$) diagram for the granitic gneisses (Frost et al., 2001). _____51

Figure 3.5: SiO_2 vs Na_2O+K_2O-CaO diagram for granitic gneisses (Frost et al., 2001).____52

Figure 3.6: Al_2O_3 /$CaO+Na_2O+K_20$ vs Al_2O_3/Na_2O+K_2O diagram for the granitic gneisses (after, Shand 1943).____52

Figure 3.7: The AFM (Na_2O+K_2O: FeO*: MgO) plot showing calc-alkaline trend of the granitic gneisses (after Irvine and Baragar, 1971) _____53

Figure 3.8: K_2O vs Na_2O discrimination diagram for the granitic gneisses (Chapell and White, 1974). _____53

Figure 3.9: Granitoid classification diagram of Zr+Nb+Ce+Y vs (K_2O+Na_2O)/CaO plotted for the granitic gneisses. FG= fractionated M-, I- and S-type felsic granites, OGT=unfractionated M-, I- and S-type granites (Whalen et al., 1987).____54

Figure 3.10: Primitive Mantle-normalized multi-element diagram of the granitic gneisses (after Sun and McDonough, 1989) _____55

Figure 3.11: REE plot normalized against chondrites after Sun and McDonough (1989) for the granitic gneisses. _____56

Figure 3.12: SiO_2 vs K_2O discrimination diagram for the granitic gneisses. IAG+CAG+CCG+RRG+CEUG+POG indicates a field for orogenic granites, OP= Oceanic plagiogranites (after Maniar and Piccioli, 1989). _____57

Figure 3.13: Y vs Nb discrimination diagram for the granitic gneisses (after Pearce et al., 1984). _____57

Figure 3.14: Y+Nb vs Rb discrimination diagram for granitic gneisses (after Pearce et al., 1984). _____58

Figure 3.15: SiO_2 vs Rb/Zr discrimination diagram for the granitic gneisses (Harris et al., 1986). _____58

Figure 3.16: Zr/TiO_2 vs Ce/P_2O_5 discrimination diagram for the granitic gneisses (Muller et al., 1997). _____59

Figure 3.17: Log Fe_2O_3/K_2O vs log SiO_2/Al_2O_3 classification diagram showing the location of the biotite schists (after Herron, 1988). _____60

Figure 3.18: Chondrite-normalized REE patterns for the biotite schists. Normalization constants are from Evensen et al. (1978). UCC=Upper Continental Crust, AAS=Archaean Australian Shale, PAAS- Post-Archaean Australian Shale. _____61

Figure 3.19: Provenance discrimination diagram for the biotite schists (after Roser and Korsch, 1988). Discriminant function 1 (F1) = (-1.773 TiO_2+0.607 Al_2O_3+0.76 Fe_2O3t-1.5 MgO+0.616 CaO+0.509 Na_2O-1.224 K_2O)-9.09; Discriminant function 2 (F2) = (0.445 TiO_2 + 0.07 Al_2O_3-0.25 Fe_2O_3t-1.142 MgO+0.438 CaO+1.475 Na_2O+1.426 K_2O)-6.81. _____63

Figure 3.20: Al_20_3 vs TiO_2 diagram for the biotite schists (after Hayashi et al., 1997).____63

Figure 3.21: La/Sc vs Co/Th diagram for the biotite schists (after Gu et al., 2002). _____64

Figure 3.22: Hf vs La/Th diagram for the biotite schists (after Floyd and Leveridge, 1987). 64

Figure 3.23: SiO_2 vs K_2O/Na_2O tectonic setting discrimination diagram for biotite schists (after Roser and Korsch, 1986). _____65

Figure 3.24: La/Sc vs Ti/Zr diagram for the biotite schists, OIA: Oceanic Island Arc, CIA: Continental Island Arc, ACM: Active Continental Margin, PM: Passive Margin (after Bhatia and Crook, 1986). _____65

Figure 3.25: Th vs La for the biotite schists (after Bhatia and Crook, 1986) _____66

Figure 3.26: Th vs La diagram for biotite schists (after Taylor and McLennan, 1985). ____67

Figure 4.1: $^{40}Ar/^{39}Ar$ age spectra of biotite extracted from muscovite-biotite gneiss (sample JK/3). Data is plotted as age vs accumulative percentage of ^{39}Ar released. A weighted average of the age, including 56 % of the ^{39}Ar, is indicated in the top right corner. Errors are 1 sigma. 81

Figure 4.2: $^{40}Ar/^{39}Ar$ age spectra of muscovite extracted from muscovite-biotite gneiss (JK/3). Data is plotted as age vs accumulative percentage of ^{39}Ar released. A weighted average of the age, including 99.3% of the ^{39}Ar is, indicated in the top right corner. Errors are 1 sigma. 81

Figure 4.3: $^{40}Ar/^{39}Ar$ age spectra of biotite extracted from biotite-garnet schist (JK/6). Data is plotted as age vs accumulative percentage of ^{39}Ar released. A weighted average of the age, including 99.5 % of the ^{39}Ar, is indicated in the top right corner. Errors are 1 sigma. 82

Figure 5.1: Representative CL images of zircons from sample JK/1, biotite-hornblende gneiss from Jebel Kujur. Zircon 207Pb/206Pb ages (Ma) are indicated. Brown, purple and yellow circles show the analysed spot. Colour coding used to highlight similar age groups. 89

Figure 5.2: Zircon data of biotite-hornblende gneiss (sample JK/1) presented in a Tera-Wasserburg diagram, data points define a discordia line with lower intercepts at 464 ± 49 Ma and upper intercept at 943 ± 47 Ma, MSWD= 5.7. 89

Figure 5.3: Zircon data of muscovite-hornblende gneiss (sample JK/2) from Jebel Kujur presented on a Concordia diagram, inset with a CL image of typical zircon grains. 91

Figure 5.4: Representative CL images of zircons from sample JK/4, biotite-muscovite gneiss from Jebel Kujur. Zircon $^{206}Pb/^{238}U$ ages (Ma) are indicated. Red, black and yellow circles show the analysed spots. Colour coding used to highlight similar age groups. _____92

Figure 5.5: Zircon data of biotite-muscovite gneiss (sample JK/4) from Jebel Kujur presented on a Concordia diagram indicating two recognizable phases (A), inset with weighted mean ages for the rim and core analysis. Relative probability plot indicating two distinct populations based on $^{206}Pb/^{238}U$ ages (Ma) (B). _____93

Figure 5.6: Representative CL images of zircons from sample JK/5, biotite schist. Zircon $^{207}Pb/^{206}Pb$ ages (Ma) are indicated by red and yellow circles. Colour coding highlights similar age groups. _____94

Figure 5.7: Zircon data of biotite schist (sample JK/5) presented on a Concordia diagram (wetherill), inset with weighted mean age of the two youngest concordant zircon grains (A), relative probability for $^{207}Pb/^{206}Pb$ (> 1000 Ma) and $^{206}Pb/^{238}U$ ages (< 1000 Ma) (B). Relative probability plot shows only concordant data (< 20% discordance)._____94

Figure 5.8: Representative CL images of zircons from sample JK/6, biotite-garnet schist. Zircon $^{207}Pb/^{206}Pb$ ages (>1000 Ma) and $^{206}Pb/^{238}U$ ages (<1000 Ma) are indicated. Red and yellow circles show the analysed spots. Colour coding is used to highlight similar age groups. _____96

Figure 5.9: Zircon data of biotite-garnet schist (sample JK/6) presented on a concordia diagram (wetherill), inset with weighted mean age of the two youngest concordant zircon

grains (A), relative probability for $^{207}Pb/^{206}Pb$ (> 1000 Ma) and $^{206}Pb/^{238}U$ ages (< 1000 Ma) (B). Relative probability plot shows only concordant data (< 20% discordance). _____96

Figure 5.10: Comparison of U-Pb age spectra of detrital zircons for analysis and results from Garzanti et al. 2018 (A) and present study (B). Comparison between the two indicates similarly dominant Aruan followed by significant peaks reflecting Pan-African detrital zircon ages (modified after Garzanti et al., 2018). _____100

Figure 6.1: $^{207}Pb/^{206}Pb$ (Ma) vs 176Hf/177Hf (initial) plot for the Jebel Kujur zircons. DM: Depleted Mantle, CHUR: Chondritic Uniform Reservoir. _____107

Figure 6.2: $^{207}Pb/^{206}Pb$ (Ma) vs εHf plot for the Jebel Kujur zircons. DM: Depleted Mantle, CHUR: Chondritic Uniform Reservoir. Diagonal blue dotted lines indicate a field for NE African Archaean basement (Fielding et al., 2017). _____107

Figure 6.3: Schematic diagram of CL-revealed internal features (A) and Cathoduluminescence (CL) image with corresponding $^{206}Pb/^{238}U$ ages (B) for zircon crystals from biotite-muscovite gneiss (sample JK/4). _____109

Figure 7.1 Location of geochronological sample sites for rocks from the Basement Complex in South Sudan. Red triangle shows the location of the present study area. The ages highlighted in pink are from Civetta et al. (1979) obtained through K-Ar dating method. Ages highlighted in blue and green are Ar-Ar and U-Pb zircon ages, respectively, all obtained from the present work._____117

List of Tables

Table 1.1: General geological column for the Sudan Republic (after Whiteman, 1971) _____7

Table 1.2: Descriptions of the different rocks found in the Gneiss Group (after, Hunting Geology and Geophysics Ltd, 1967) _____16

Table 3.1: Al_2O_3 against selected trace elements for samples JK/5 and JK/6 (biotite schists)60

Table 3.2: Selected trace elements and trace element ratios for samples JK/5 and JK/6 ____66

Table 3.3: Composition of sandstones formed in different tectonic settings (after Bhatia, 1983) _____77

Table 6.1: Zircon Hf isotope composition data for granitic gneisses and biotite schists.___104

Chapter 1
Introduction

1.1 Background

South Sudan is a north-central African country underlain largely by Precambrian basement. The geology of South Sudan comprises the north-eastern edge of the Congo Craton (De Wit and Linol, 2015). This region of the Congo Craton consists of extensive Archaean granitoid-greenstone terranes that continue into adjacent territories, including the Central African Republic and northern Uganda. These cratonic Archaean rocks abut against the Mozambique Belt in the East and are presented as old basement gneisses with an age of about 3500 Ma (Westerhof et al., 2014). The geological framework of South Sudan is made up of three main geological units: An extensive crystalline Basement Complex and associated granitic intrusions as well as basaltic rift volcanics and widespread Tertiary-Quaternary cover sequences.

1.2 Research problem

South Sudan is one of the world's last large remaining Precambrian terrains still to be mapped in detail, making it significant for studies not only for academic purposes but also for prospecting of valuable minerals, including gold. Very limited systematic geological studies were conducted in South Sudan, particularly the Basement Complex, which forms the basis of this study. Important aspects of the geochronology, petrogenesis and tectonic evolution of the Basement Complex are poorly understood. As a result, most of the geological units within the Basement Complex have remained to this day undifferrentiated. This work presents petrographical, geochemical, zircon U-Pb, Lu-Hf and Ar-Ar geochronological data from the south-eastern part of the Basement Complex. These will serve for the larger discussion on the

magmatic evolution and the timing of some of the tectono-magmatic events in the area and contribute to differentiating this ancient crustal domain.

1.3 Aims and objectives

This study investigates high-grade basement gneisses and biotite/muscovite-bearing schists from the "Undifferentiated Gneiss Group" of the Basement Complex in South Sudan. Rock specimens used in this study were initially analyzed as part of an honours project (Tshwane, 2016) and due to further research questions, the project was extended into a Masters project. The main objective of this study is to discern the petrological characteristics and ages pertinent to the crystallization, deposition and metamorphic reworking of the rock assemblage from this geological unit. Specific objectives can be outlined as follows:

- To conduct geochronological analysis in order to determine precise magmatic, depositional and metamorphic ages.
- To geochemically characterize the analyzed rock assemblage.
- To use petrological and geochemical data to identify the tectonic setting of the study area.
- To use the petrographical and geochronological analysis to establish the deformational history of the study area.
- To uncover aspects of the nature and mode of tectonic and geological evolution of the study area.
- To use the age and petrological characteristics of the studied lithologiess to correlate the Basement Complex with the surrounding geological terrains.

1.4 Description of the study area

The area under study is formally known as Jebel Kujur or "Jebel Kuruk" and is situtated in the westernmost areas of the capital city of South Sudan, Juba. Jebel Kujur is a mountain standing at an altitude of about 685 m in a state known as the Central Equatoria (Fig. 1.1) and is defined by the coordinates; 04° 51' 09.6'' N and 31° 33' 15.7'' E, (Datum: Cape).

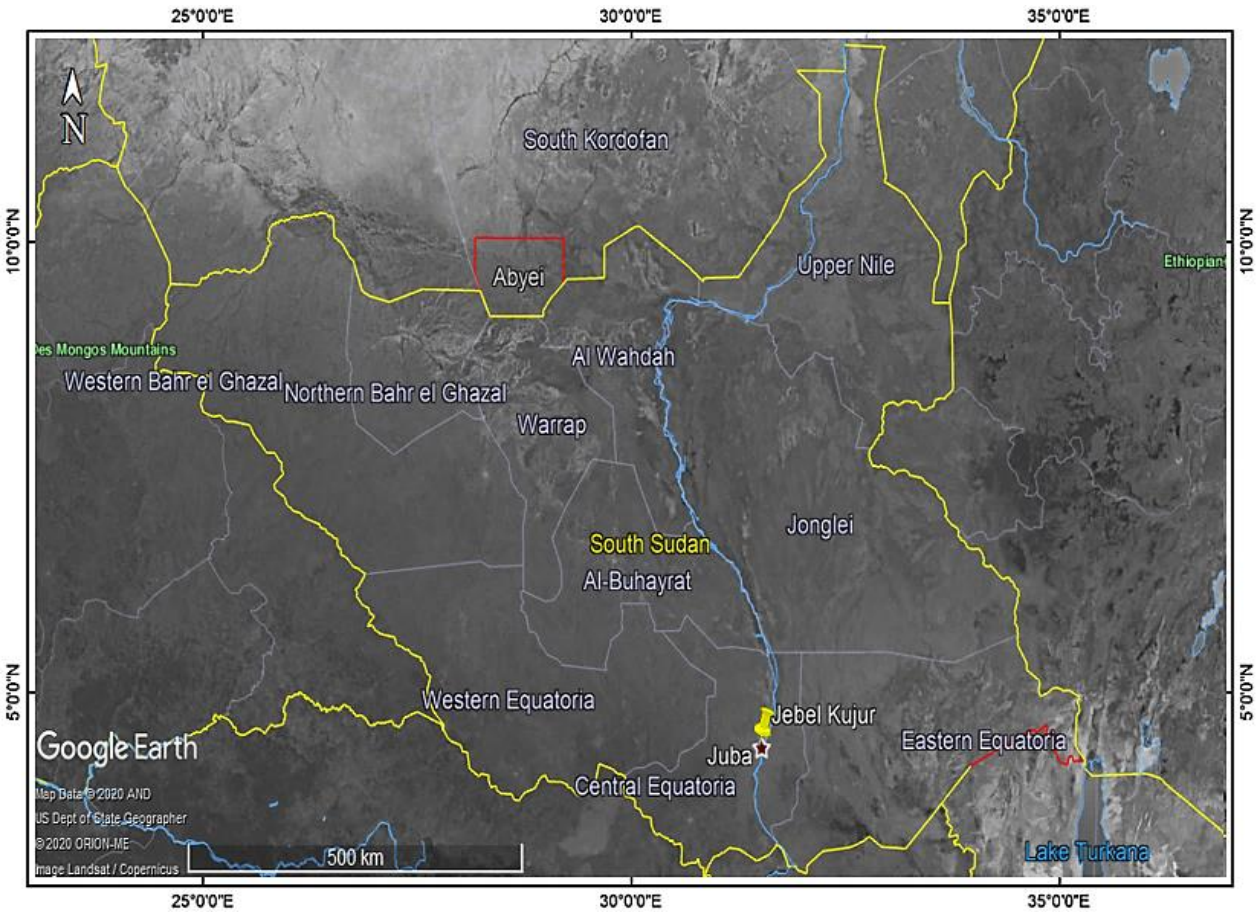


Figure 1.1: Google Earth map displaying the location of the study area in South Sudan. Yellow pin indicates the position of Jebel Kujur and Juba is indicated by the small red star (Google Earth, 2020).

Regarding the physiography, the study area is hilly, undulating and forms a sheer cliff (Fig. 1.2 A-B). Juba is intersected by several non-perennial rivers forming a dendritic drainage pattern. The Bahr el Jebel (White Nile) is one of the large rivers in and around the study area. Bahr el Jebel occurs about 6.5 km, East of Jebel Kujur, producing a luxuriant greenway in the area (Fig. 1.2 C) and forms a local ecological zone for various flora and fauna. Juba generally

has a biologically diverse vegetation with tropical and grassland dominating. Jebel Kujur has attracted geoscientific interest because of the Precambrian rocks, believed to contain metallic mineralization.



Figure 1.2: Photographs of the study area. A and B: Jebel Kujur mountain photographed from varying angles (Miettaux, 2013), C: Aerial view of the Bahr el Jebel river, about 6.5 km, East of Jebel Kujur (McKenna, 2011).

1.5 Structure of the dissertation

This dissertation is divided into a total of seven chapters. Chapter 1 gives a brief overview of the project; outlines aims and objectives and finally places the study area into a regional context. Chapter 2 presents the petrography and mineralogy of the samples used in the study. Chapter 3 provides the geochemical data, descriptions and interpretations of the geochemical characteristics. Chapter 4 provides muscovite and biotite Ar-Ar ages from selected samples.

Chapter 5 presents new zircon U-Pb age data for all samples. Chapter 6 builds on chapter 5 and presents Lu-Hf isotopes. Chapter 7 provides a consolidated discussion of all the results and finally presents a set of conclusions.

1.6 Previous work

The first overall review of the regional geology of Sudan and surrounding areas was supplied by Whiteman (1971), who provided brief descriptions of the igneous and metamorphic rocks from selected localities. Whiteman (1971) also produced a general geological column of the former Sudan Republic (Table 1.1). This geological column indicates the percentage of the total surface area occupied by each geological unit. Vail (1975) published a geological map (1: 2 000 000), compiled through extrapolation of accessible data from adjacent countries (Appendix A). This map includes an additional structural scheme map indicating the tectonic structures of Sudan. Furthermore, the map verifies that South Sudan is underlain mainly by basement lithologies.

According to Whiteman (1971), the geology of the study area comprises foliated basic to siliceous gneisses containing hypersthene and feldspar; these are intruded into foliated paragneisses and paraschist. As a result of the scattered and discontinuous distribution of outcrops and the similarity of the lithologies, dating techniques remain the only way to subdivide the basement rocks into separate age-defined terrains. Preliminary work on the structure and chronology of the Sudanese Basement Complex was provided by Vail (1978). A structural map and sparse radiometric data were used to propose that much of southern and north-central Sudan is underlain by a “Sudan shield” of ancient rocks that are continuous with the basement rocks of Northern Uganda. More workers have similarly correlated the basement rocks of northern Uganda with those found in South Sudan (Almond, 1969; Goodwin, 1996; Whiteman, 1971). The notes to the published maps highlight that the Madi sequence, Karasuk

and Gneiss groups make up the stratigraphy of the Basement Complex (Vail, 1978; Yassin et al., 1984).

The Basement Complex was reworked during the late Precambrian Pan-African orogenic event and was intruded by post-tectonic granitoids during the Palaeozoic era (Yassin et al., 1984). Furthermore, the area appears to have been subjected to extensional tectonics that consequently opened east-west fractures. These fractures were later filled by doleritic dykes cutting across the basement as well as granitic intrusions. Hunting (1980) suggested that the basement rocks in the area underwent four tectonothermal events, recognized in the neighbouring northern Uganda. These events include the 2.88 Ga Watian, considered the oldest event within the Imatong mountains area. The Aruan is a younger Archaean tectonothermal event recorded in the Imatong mountain area and in the east of Juba-Nimule road.

The Mirian and Chuan events are identified between the regions of Yei and Lainya and along the line of the Nile from Nimule towards Juba. Reliable evidence of the Chuan tectonothermal event is the Aswa Shear Zone (ASZ) (Adak, 2015). The ASZ is a striking feature in South Sudan and is regarded as a fundamental NW-SE trending Precambrian structure in the central part of Gondwana (Katumwehe et al., 2015). Saalmann et al. (2016) interpreted the ASZ as an intra-cratonic crustal feature close to north- eastern margin of the Congo Craton. The Aswa mylonite zone enters South Sudan near Nimule and dissipates as it approaches the unconsolidated sediments towards the north west of South Sudan.

Civetta et al. (1979) investigated the geological and structural outlines of South Sudan through mapping and K-Ar age determination. This work produced an age of 443 ± 12 Ma for the mylonite and 511 ± 14 Ma for the granite in the Central Equatoria state. These ages were proposed to reflect the Chuan metamorphic event and the Aswa zone mylonitization, both associated with the Pan-African/ Mozambiquan event (Vail, 1990). Based on mapping by Adak

(2015), the following rock types in and around the Central Equatoria state were identified: gneisses: Banded gneisses, augen gneisses and biotite gneisses. The gneisses are cut by either dolerite or gabbroic dykes with an E-W trend.

Table 1.1: General geological column for the Sudan Republic (after Whiteman, 1971)

Name of unit (Sudan Geological Survey 1:4 000 000 maps, 2nd and 3rd editions)	**Name of unit (Whiteman (1971))**	**Age (Whiteman (1971))**	**Surface area (%)**
Superficial deposits	Superficial deposits	Quaternary-Tertiary	Not differentiated
Coastal deposits (Red Sea margin)	Continental marine formations Red sea Littoral	Quaternary-Tertiary-Mesozic	<1
Umm Ruwaba Series	Gezira Umm Ruwaba and El Asthan Formations	Quaternary-Tertiary	19
Lavas, Tertiary	Volcanic and intrusive rocks, mainly lavas (undifferentiated)	Quaternary-Tertiary	2
Hudi Chert, Middle Tertiary	Hudi Chert Formation	Tertiary? (Oligocene)	<1
Nubian Series, Mesozoic	Nubian Sandstone Formation	Late Cretaceous	28
Yirol beds	Yirol Formation (equivalent to Nubian formation)	Late Cretaceous	<0.1
Not differentiated	Gedaref Sandstone Formation	Jurassic (pre-Oxfordian)	Included in Nubian estimate
Nawa Series	Nawa Formation	Palaeozoic?	<1
Palaeozoic sandstones	Palaeozoic Formations	Palaeozoic?	<0.5
Basement Complex	Basement Complex Group	Precambrian mainly	49

Vail (1990) compiled four hundred and twenty-nine isotopic analyses of geological materials from Sudan. These results were collected from all accessible literature as well as unpublished sources. Most isotopic data were produced by K-Ar, Rb-Sr, Pb-Pb, U-Pb and Sm-Nd methods, and only twelve ages relate to rock samples from South Sudan (previously Southern Sudan).

Most of the twelve ages yielded Pan-African ages of ~550 Ma, whilst a few samples analysed by Civetta et al. (1979) produced ages around ~1200 Ma. A map by Anon (1981) shows K-Ar ages of ~549 - 546 Ma obtained from biotites of younger granite intrusions and interpreted as Pan-African. Snelling (1962, 1964) conducted radiometric age determinations on younger granites associated with the basement rocks and obtained an apparent age of 550 ± 100 Ma, also reflecting a Pan-African tectonothermal event.

Gold production has been known in Sudan since Phardonic times. The type of gold found in Sudan is mainly in the form of auriferous quartz veins (Yassin et al., 1984), most of which strike in the NE-SW and E-W directions. Although some published work exists on the mineral deposits of Sudan (Dunn, 1911), limited geological information does not allow classification of the mineral deposits by age or origin and, therefore deposits are classified based on their economic value (Yassin et al., 1984). The gold around Nimule (White Nile), Juba and Kapoeta in the southeastern areas of South Sudan occurs in the crystalline amphibolite-facies basement rocks, which are fractured and folded to serve as dilation zones for mineral accumulation (Mishra et al., 2014).

The local people collect gold grains using artisanal digging and panning. There is not any scientific evidence that the gold deposits in South Sudan are worthy of being mined industrially. Nevertheless, exploration companies have been attracted to the country for various reasons, including widespread artisanal mining and an existing mineral development/mining license (Kibali mine) across the border in the Republic of Congo (Martin and Martin 2017).

1.7 Tectonic setting and regional geology

North-central Africa is composed of two distinct crustal domains, the Saharan Metacraton also referred to as the “East Sahara ghost craton” (Abdelsalam et al., 2002) and the northern part of the East African orogenic belt (Johnson and Woldehaimanot, 2003). The Saharan Metacraton

continues from the Tuareg shield in the west and joins the East African orogenic belt in the east. In the South, the Saharan Metacraton is separated from the Congo Craton by the Obanguides orogenic belt also known as the Central African Fold Belt (Fig. 1.3). All these geological terranes surround South Sudan, and some are believed to extend into the country. Immediately surrounding the south-eastern Basement Complex of South Sudan is the Congo Craton, Mozambique Belt of the East African orogeny and the Obanguides belt. These geological terranes are therefore of relevance to the geology and geodynamic development of the south-eastern Basement Complex of South Sudan.

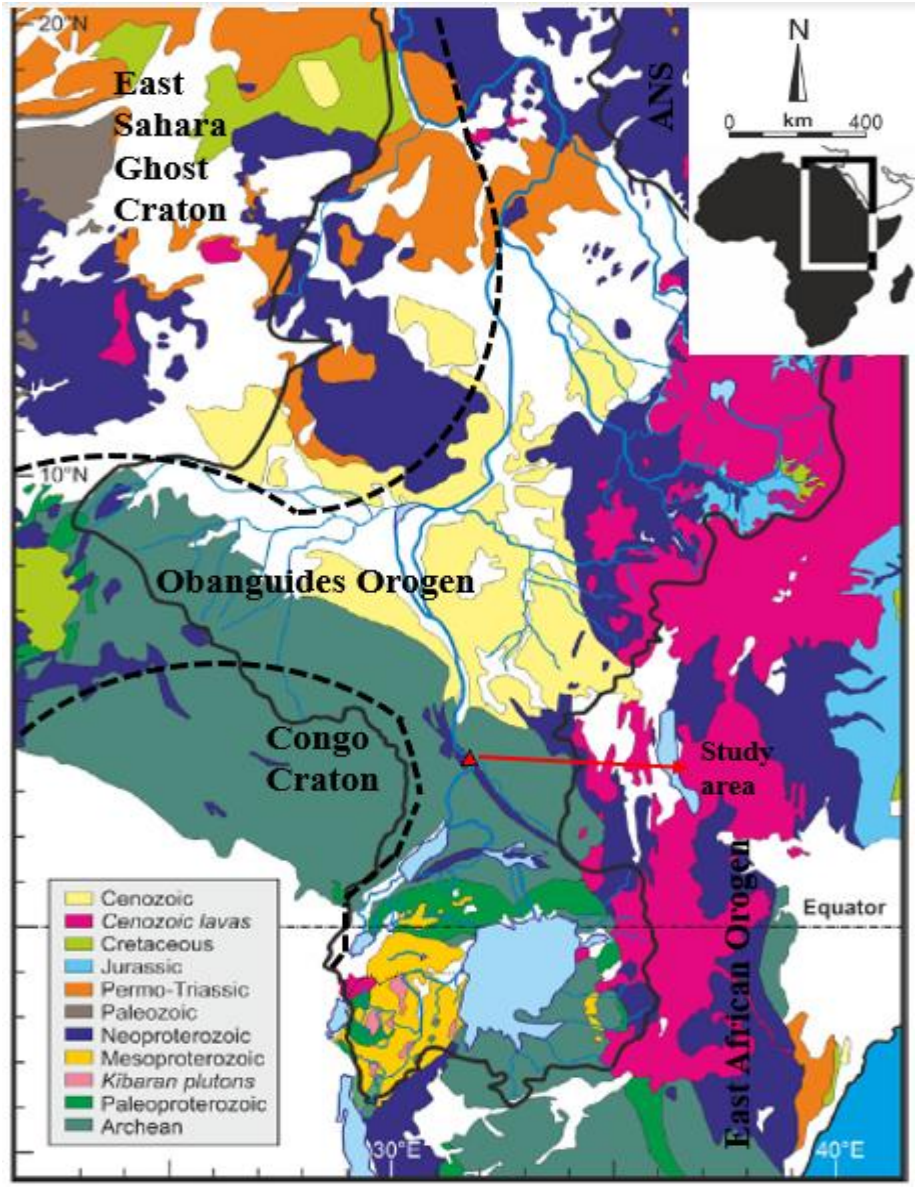


Figure 1.3: Distribution of crustal domains in Central Africa. Small red triangle indicates the position of the study area on the regional geological map, ANS: Arabian-Nubian Shield (modified after Garzanti et al., 2018).

Abdelsalam et al. (2002) deduced that the Saharan Metacraton formed part of the western Gondwana supercontinent and was remobilized during the Neoproterozoic collision, which resulted in its assembling from exotic terranes. The Metacraton comprises predominantly medium- to high-grade old Precambrian gneisses, meta-sedimentary rocks, migmatites and rare granulites that are intruded by granitoids.

The Arabian-Nubian Shield (ANS) makes up the northern half of the East African Orogen and stretches from Southern Israel and Jordan south as far as Ethiopia and Yemen, where it transitions into the Mozambique Belt. This young basement terrain comprises the Arabian and the Nubian segments currently separated by the Red Sea; originally both segments formed one unit. The ANS is dominated by Neoproterozoic arc terranes. These terranes are suggested to be intra-oceanic island arc/back arc-basin complexes formed by the Pan-African orogeny during the period of 900-500 Ma (Stern, 1994). Geochemical and isotopic studies of the magmatic rocks in the Arabian-Nubian shield indicate derivation from a Depleted Mantle source (Stern, 1994). What distinguishes the ANS from the Mozambique Belt is its dominating juvenile nature, relatively low-grade of metamorphism and abundance of island-arc rocks (Kennedy, 1964). The Mozambique Belt defines the southern part of the East African Orogeny and essentially consists of medium to high-grade gneisses and voluminous granitoids. It extends south from the ANS into southern Ethiopia, Kenya and Somalia, through Tanzania to Malawi, Mozambique and Madagascar. The Mozambique Belt consists of highly deformed para- and orthogneisses, generally in amphibolite to granulite facies of regional metamorphism (Cahen et al., 1984).

The Obanguides Orogenic Belt extends eastwards from Cameroon through the Central African Republic to Southern Sudan (Fig. 1.4). In width the belt has been described to extend for 500-700 km from the Congo foreland on the south to the East African Saharan Metacraton. The belt occupies a critical intracratonic position and is composed of complex granulite- to amphibolite-facies gneisses, migmatites and metasediment associated with numerous syn- to late-tectonic granitoids. This Pan-African belt was in many previous studies referred to as “Central African shear zone” and is believed to have resulted from the collision between the Congo Craton and the East Saharan Craton (Castaing et al., 1994).

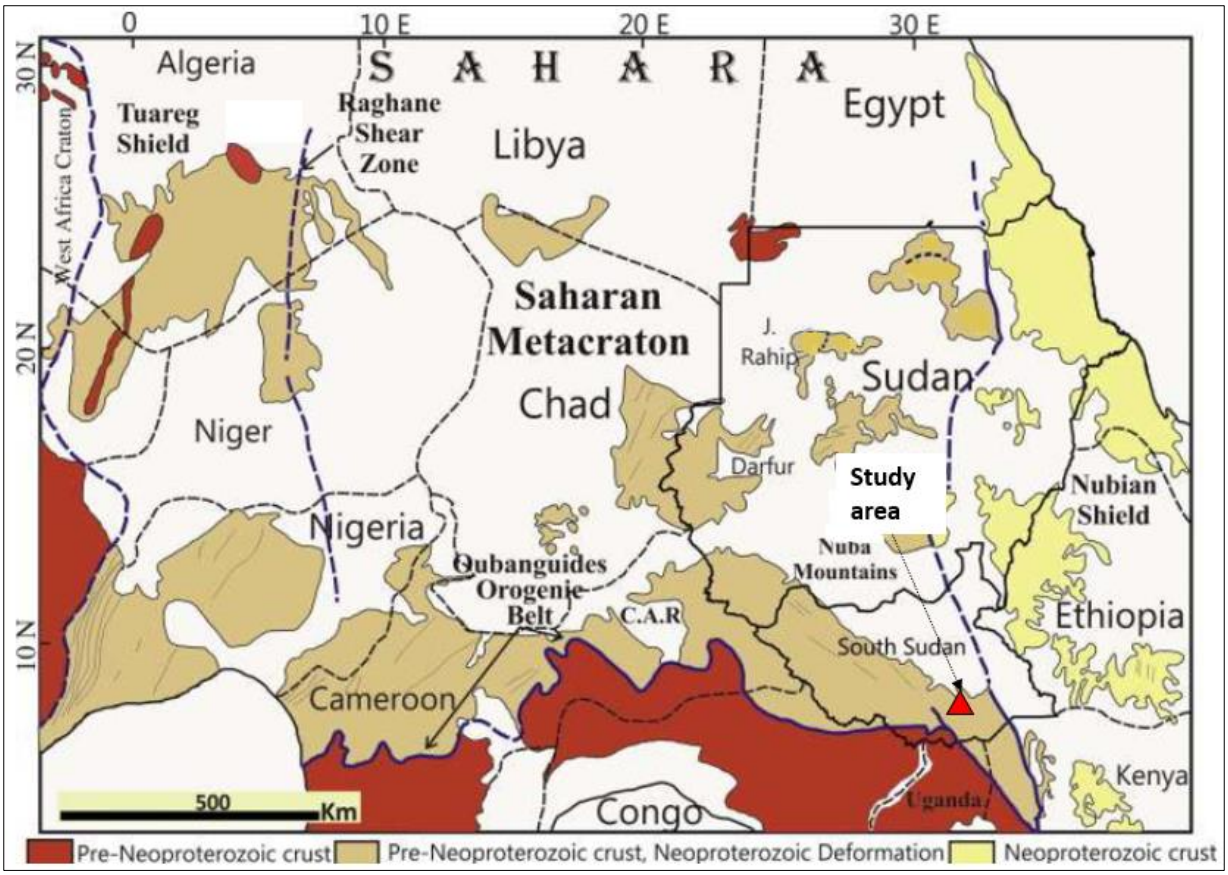


Figure 1.4: Location of the study area relative to the Obanguides Orogenic Belt, Saharan Metacran and the Congo Craton. Small red triangle indicates the position of the study area. CAR: Central African Republic (modified after Abdelsalam et al., 2002).

1.7.1 Geology of the Congo Craton

The Congo Craton, also termed Proto-Congo Craton by de Waele et al., (2008), is briefly described as a central African land mass that amalgamated at the time of Gondwana assembly (de Waele et al., 2008). This Archaean landmass was welded together by Palaeoproterozoic mobile belts. The Proto-Congo Craton has remained relatively stable and welded since the Palaeoproterozoic (Tack, 2009) with only intra-cratonic tectonic inversion events affecting it. Nonetheless, all the major/dominant tectonothermal events related to the 0.55 Ga Pan-African orogenic cycles are traced along the margins of the Craton. Presently, the Proto-Congo Craton is bordered by high-grade belts that formed during the Pan-African collisional events. The belts include the East African Orogeny (EAO) in the East and the Oubanguides orogeny in the North (Schenk et al., 2004).

According to Fernandez-Alonso et al. (2011), the Proto-Congo Craton is an assemblage of six Archaean terranes nucleated around 2.1 Ga, and subsequently exposed during the Eburnean at around 1.8 Ga and eventually culminating in amalgamation of the Columbia supercontinent (Westerhoff et al., 2014). The six terranes include the Tanzania Craton, the Ntem Block, the Kasai Shield, Cuango Block, Bouca and Mboumou-Uganda blocks (de Wit and Linol, 2015) (Fig. 1.5). These shields vary in terms of their geological history and have therefore been postulated to have formed separately (Westerhoff et al., 2014). For the scope of this study, the Mboumou-Uganda block will be described in detail.

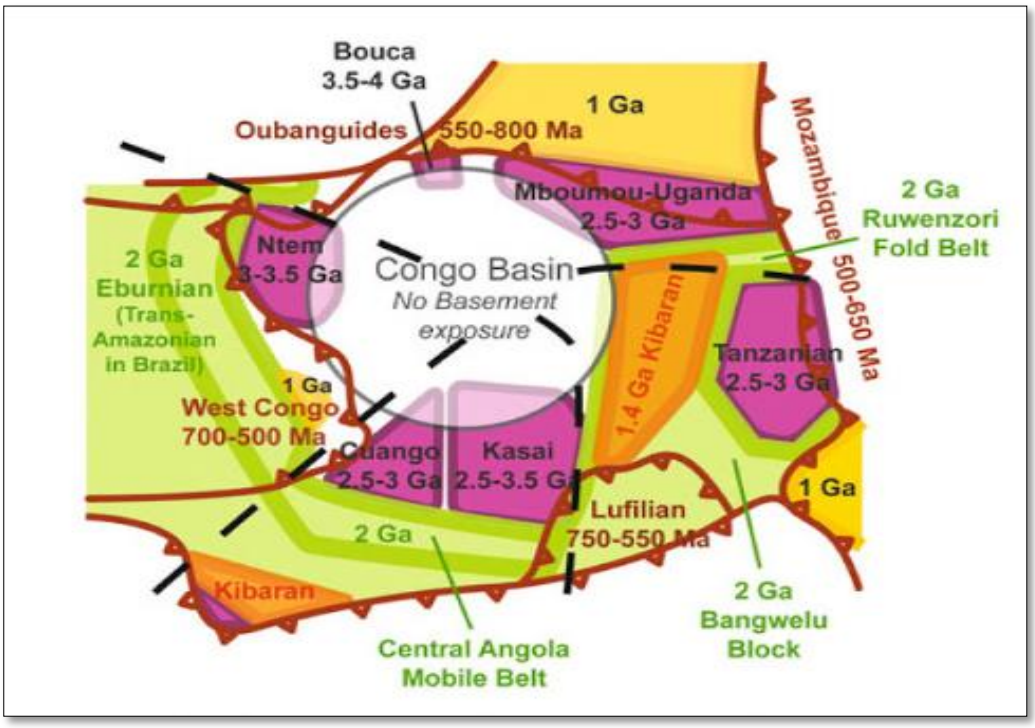


Figure 1.5: Sketch map of the constituents of the Congo Craton, indicating the six Archaean cratonic terranes (purple), Eburnean (green) and Kibaran (orange and yellow). All the Pan-African fold and thrust belts are shown in brown (from De Wit and Linol, 2015).

1.7.1.1 Mboumou-Uganda block

The Mboumou-Uganda Block, also known as the 'Bomu-Kibalian Shield' (Schenk et al., 2004) or the NE Congo-Uganda Block (Leggo, 1974) is a major tectonothermal domain in the north-eastern corner of the Congo Craton (Fig. 1.5). The Archaean gneisses and granulite-greenstone terranes of this part of the Congo Craton are widely distributed and extend into adjacent

countries, including the Central African Republic, western Uganda and South Sudan (Schlüter, 2006). These Archaean rocks contain three major assemblages, namely old basement gneisses, greenstone belts and two main generations of granitoids. The old basement gneisses have an age of ~3500 Ma and are known as the Bomu and the West Nile gneissic complexes (Schlüter, 2006). The greenstone belts assemblage is divided into the Ganguan Greenstone Belt in the west and the Kibalian Greenstone Belt in the east, both of which represent two periods of greenstone emplacement between ~3200 and ~2600 Ma (Schlüter, 2006). The Kibalian Greenstone Belt is host to a giant orogenic gold deposit and is composed of metasedimentary rocks, banded iron formations and basalts intruded by ca. 2600 Ma igneous plutons (Bird, 2016).

The Bomu gneisses are well exposed around the Bomu and Ude rivers at the border of the Democratic Republic of Congo and the Central African Republic. These gneisses are schistose and garnetiferous and have undergone retrograde metamorphism. The geological history of the gneisses began with the deposition of oceanic crustal precursors at ~3500 Ma. This process was then followed by a high-grade tectonothermal activity and later the intrusion of tonalites at about 3410 Ma (Schlüter, 2006).

The West Nile Complex comprises several basement gneisses that are poorly exposed in the West Nile province in north-western Uganda and in the north-eastern part of the Democratic Republic of Congo, through southern Sudan and into the Central African Republic (Westerhoff et al., 2014). Previously, the crystalline basement of northern Uganda and the West Nile Gneiss were grouped as one unit, namely the gneissic granulite complex or more commonly ‘the Basement Complex’. Field observations, Rb-Sr whole rock dating and petrographic studies were applied to study the evolution of the Basement Complex of the West Nile province (Hepworth, 1964). The 985 Ma West Nile Gneiss is suggested to have collided with, and

overthrust the Kibalian Greenstone Belt between 600 and 400 Ma (Bird, 2016). This event is associated with the collision between the Congo Craton and the Saharan Metacraton.

Basement Complex

Four main units belonging to the Basement Complex have been identified in and around the southernmost regions of South Sudan. These units include: Madi Sequence, Karasuk Group, also known as the Miriam Group, Gneiss Group and the Strongly Banded Group.

The Madi Sequence

The Madi Sequence of northern Uganda was observed to continue into southern Sudan (Hepworth and Macdonald, 1966). In southern Sudan, the sequence is exposed along the Yei road, just west of Juba. This sequence contains quartzite interbanded with muscovite schists, quartz-feldspar-biotite-hornblende gneisses and amphibolites. The Madi Sequence was initially a succession of arenaceous and argillaceous clastic sediments with some calcareous beds and a few volcanic rocks (Yassin et al., 1984). Hunting Geology and Geophysics Ltd (1967) suggests that the deposition of this sequence predates the Miriam and Chuan deformations and postdates the Aruan event.

The Karasuk Group

The Karasuk Group (Miriam Group) (Hepworth, 1967) covers a large area of the eastern extremity of South Sudan and extends northwards into areas such as Daga Post (Yassin et al., 1984). This group contains an assemblage of meta-sedimentary and meta-igneous rocks, including, amphibolites, biotite- and hornblende-bearing gneisses, anorthosites, marbles, schists, granites and metagabbros. Amphibolite and greenschist-facies metamorphism have been identified in the Karasuk Group rocks (Almond, 1969).

The Gneiss Group

The gneissic rocks cover a large area of the South Sudanese Basement Complex. Hunting Geology and Geophysics Ltd (1967) observed the following rock types in the Boya Hills area of Yambio, the Lafit Mountains and areas south-east and south-west of Juba (Table 1.2).

Table 1.2: Descriptions of the different rocks found in the Gneiss Group (after, Hunting Geology and Geophysics Ltd, 1967)

Rock Types	Description
Massive weathered and foliated granites and poorly banded gneisses	Rich in medium-grained quartz
Biotite-hornblende gneisses with minor amphibolite and quartz-feldspathic	Show minor lenticles and isolated narrow beds of muscovite quartzites
Muscovite-biotite gneisses	Contains quartz, potash feldspar plagioclase, muscovite and biotite

Vail (1978) observed an additional rock unit in the Gneissic Group consisting of charnockites. The charnockites are an older unit in the Basement Complex and are referred to in Uganda as the Watian (Hepworth and Macdonald, 1966). The Gneissic Group contains granitic gneisses, rare quartzites, quartzofeldspathic rocks and banded meta-gabbros, referred to in Uganda as Kitgum Group (Almond, 1969) and Aruan (Hepworth and McDonald, 1966).

Strongly banded rocks, gneisses, migmatites and local meta-sedimentary rocks

This unit occurs in the east, north and west of the Imatong mountains (Fig. 1.6). Lithologies include quartz-feldspar-biotite-garnet gneisses, graphite-sillimanite gneisses and migmatites as well as quartzites, schists and marbles belonging to the metasedimentary sequences (Yassin et al., 1984).

The Nile gneisses of the Precambrian basement are found occupying the east bank of the Nile River and extending westward closer to Jebel Kujur. The Madi meta-sedimentary rocks mostly occur around Jebel Kujur and are traced west beyond Jebel Kunufi. The Madi meta-sedimentary rocks in Jebel Kujur are found to have undergone high to medium-grade metamorphism (Adak, 2015). Umm Rwaba Formation occurs north of Juba and is widely

distributed in South Sudan. This formation is believed to be of Quaternary to Tertiary age, and is composed of clay, sand and gravels. The Umm Rwaba Formation covers most of the Precambrian basement and is divided into the Lower, Middle and Upper units (Vail, 1978).

1.8 Local geology

The local geology is summarized according to Adak (2015). The study area contains meta-sedimentary rocks (schists), amphibolite, deformed nepheline-syenites and banded gneisses intruded by numerous granites and doleritic dykes. These rocks make up the basement, which is in turn covered unconformably by lateritic alluvial and surficial deposits (Fig. 1.6).

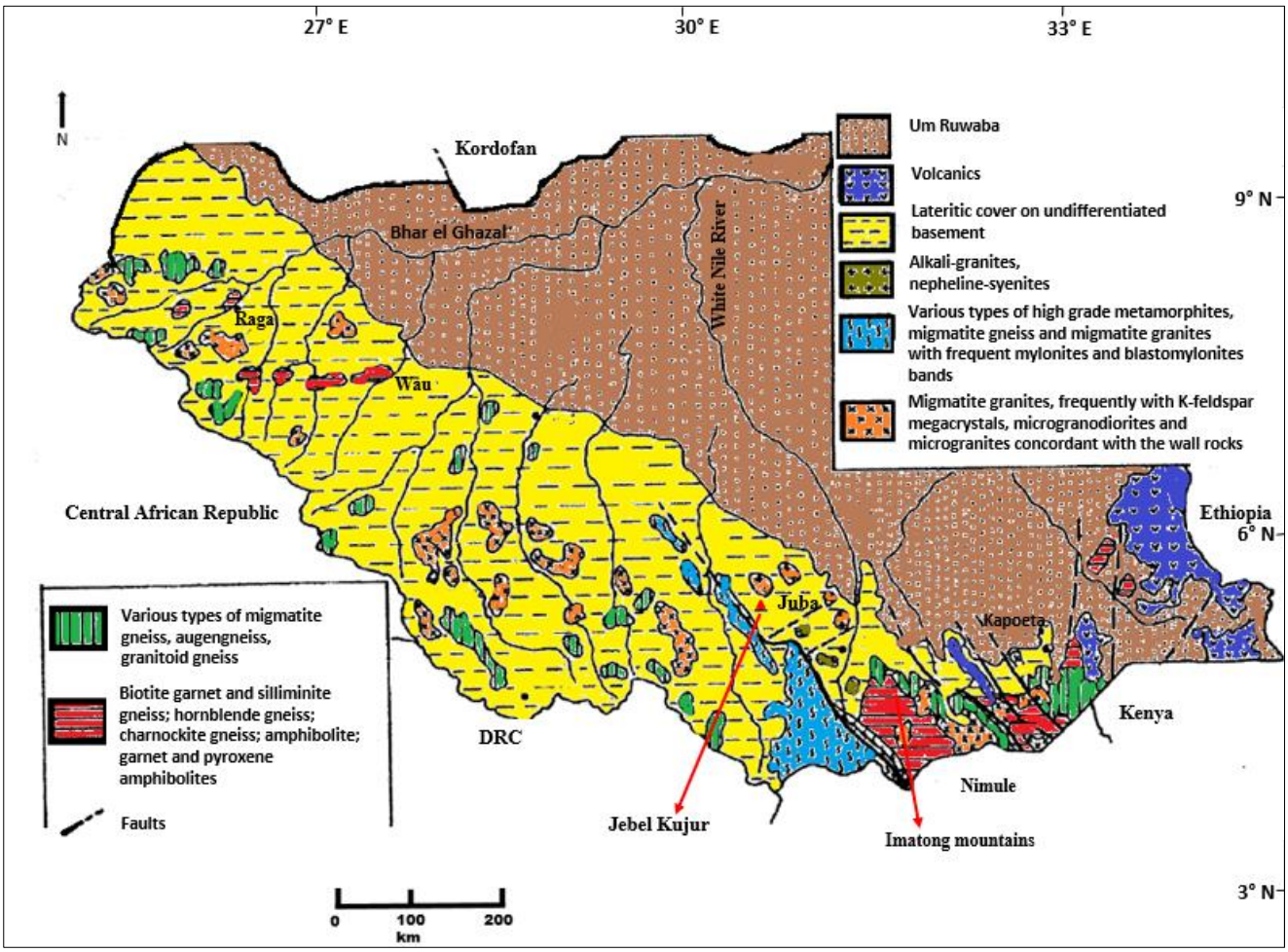


Figure 1.6: A simplified geological map of South Sudan with a focus on the Basement Complex. Red triangle indicates the position of the study area (Jebel Kujur) (modified after Civetta et al., 1979).

Migmatites

Migmatites in Jebel Kujur have a granitic composition and occur in association with the granitic plutons. The migmatites are characterized by large feldspar, microcline and mica crystals. They form nebulitic structures which merge into one another.

Banded gneisses

Gneisses are generally abundant in and around the study area, specifically in Jebel Kujur. The gneisses are well exposed and dominate the country rock. These rocks occur mostly as large angular masses forming sheer cliffs. These rocks are intruded frequently by granitic plutons and dykes. Clear bands of dark and light-coloured minerals are often observed in gneisses in the Jebel Kujur area. The rocks specifically display quartz-feldspar bands and biotite-rich selvages. The area has extensive quartz veins that crosscut the gneisses. The gneisses contain feldspars, quartz, biotite, muscovite and some accessory hornblende. They show a general medium to coarse grain texture, a dark brown weathered surface and a light grey fresh surface and are foliated.

Schists

Various schists occur in the area, distinguished by the most dominant mineral, either biotite or muscovite. All the schists are characterized by a typical schistose and a well-developed lepidoblastic texture. The mineral size distribution is variable. The biotite-rich bands are much more equigranular, whereas, the biotite poor bands are more serate. Mineral contacts are typically interlobate and amoeboid in the quartz-rich zones. The muscovite and biotite schists along the Yei road are interbedded with the quartzite of the Madi Sequence.

Amphibolite

The amphibolite occurs as lenses of about 1 m wide and 3 - 4 m long within the Jebel Kujur banded gneisses and as small pods in the garnetiferous granite. The amphibolites contain hornblende and plagioclase with subordinate quartz. The amphibolite is generally medium grained with a marked foliation and crude gneissosity. Locally, the amphibolitic body shows the effects of mild to intense deformation, indicated by size reduction as it changes from large lenses to small pods in the granites.

Granite

A specific type of granite has been observed in the study area, namely garnetiferous granite. This rock occurs as large linear intrusions. The garnetiferous granite contains visible garnet minerals. The rocks are medium-grained and display a weak foliation.

Dolerite

Dolerite occurs in the form of dykes with medium to fine-grained texture, and an east-west orientation. The dolerite cross-cuts the banded gneisses and some of the granitic intrusions.

1.8.1 Geological structures and mineralisation in the study area

The study area has been subjected to polyphase deformation, which is marked by the existence of different structural elements, including folds, foliations, faults, joints, dykes and quartz veins (Yassin et al., 1984).

The region to the south-east of the study area is marked by the prominent ASZ. The ASZ is associated with E-W splay faults and joints as it propagated into the area. The joints in Jebel Kujur are either vertically or horizontally orientated in both the country rock and the intrusions (Adak, 2015). Another major shear zone referred to as the “Chukudum” shear zone occurs farther east of the study area. The Chukudum shear zone acts as a major lithological boundary

and has been suggested to represent a possible craton edge (Marais, 2016). Jebel Kujur is also a host to many folds, which appear to be tilted. The base of the mountain contains numerous micro-folds, whereas very distinct macro-folds are evident towards the peak of the mountain.

Extensive small-scale artisanal alluvial gold mining is practised by local people in the Luri River, located about 17 km north east of the study area. No gold has been found yet in Jebel Kujur. Economically, Jebel Kujur is important for crushed gravels used specifically in construction (Adak, 2015).

Chapter 2
Petrography and mineralogy

2.1 Introduction

Petrography is used, along with whole rock geochemical data, to classify rocks and to determine the nature of the protolith. This technique therefore provides textural details, which can contribute to knowledge of the sequence of crystallization of the mineral constituents of the rock (Drake, et al., 1985). This chapter illustrates and discusses microscopic properties of hand samples and petrographic features for each rock sample.

2.2 Analytical methods

The samples used in this project were all originally collected by the late Dr. Elisa Longa-Tongu. Six hand specimens were labelled and photographed. Thereafter, the samples were sent to the rock cutting and thin section laboratory at the University of the Witwatersrand, School of Geosciences. At the rock crushing and thin section laboratory, thin slices of each sample were cut to produce polished thin sections. Cutting was done perpendicular to foliation.

2.3 Results

The results are presented as thorough descriptions, including modal estimates of the hand samples and thin sections of each rock. Images and photomicrographs of all samples are also included (Figs. 2.1-2.18).

Sample JK/1: Biotite-hornblende gneiss

The biotite-hornblende gneiss (sample JK/1) is a medium to coarse (4-7 mm) grained gneiss with a well-defined foliation, resulting from alternating bands of biotite-rich and leucocratic bands made up of quartz and feldspars. A grey-creamy-greenish colour and granitic texture is

obvious on the fresh surface, whereas yellow stains and brownish colour occur on the weathered surface of the rock (Fig. 2.1). Quartz is the most abundant mineral, followed by plagioclase and alkali-feldspar. The quartz occurs with the plagioclase, forming the white bands that are intercalated with flaky biotite bands. Feldspars are generally elongated and anhedral. Accessory minerals include zircon, apatite and opaques. A large extensive band of inter-granular quartz cross cuts biotite and felsic mineral-rich bands (Fig. 2.1). This large band is most likely part of a continuous quartz vein.

Orthoclase is inequigranular with striations and interlobate grain boundaries. A few large and intensely strained quartz grains occur. Smaller quartz and flaky biotite grains form the interstitial material in this sample. Biotite contains a few inclusions and is replaced in most instances by muscovite. Myrmekitic fabric is shown in alkali-feldspar with intergrowth of vermicular quartz (Fig. 2.2). The microcline is characteristically featureless in plane polarised light (PPL), wherein in crossed polarised light (XPL), the common tartan twinning pattern is visible. The twinning in this sample is, however, distinct in that it exudes a spindly, wispy feature. The plagioclase shows alterations and fine grains along the edges and striations, which were originally lamellae and were altered by deformation (deformation twinning) (Fig. 2.3). Further, plagioclase shows evidence of subgrain rotation.

There are prominent and large fluid inclusions occurring in the plagioclase grains, whereas in other minerals, including biotite and muscovite, the fluid inclusions are fewer and much smaller in size. Garnet occurs as fractured porphyroblasts with small alkali-feldspar inclusions. Hornblende occurs in the matrix. Overall intermediate to felsic composition with evidence of recrystallization and alteration to varying degrees is shown in this sample. The modal estimates are: 35% quartz, 20% plagioclase, 18% alkali-feldspar, 12% biotite, 8% muscovite, 3% hornblende, 2% garnet and less than 2% opaques (zircon, apatite, etc.).

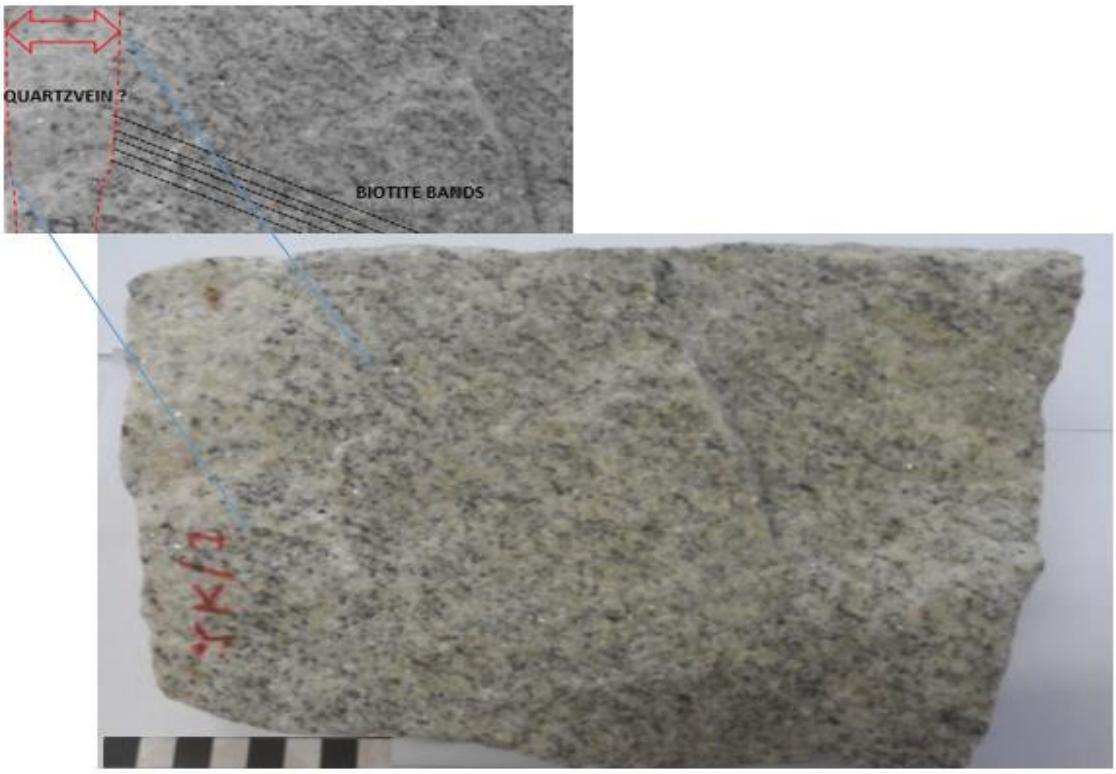


Figure 2.1: Hand specimen of the biotite-hornblende gneiss (sample JK/1) from Jebel Kujur, with a specific illustration of the biotite bands crosscut by a possible quartz vein.

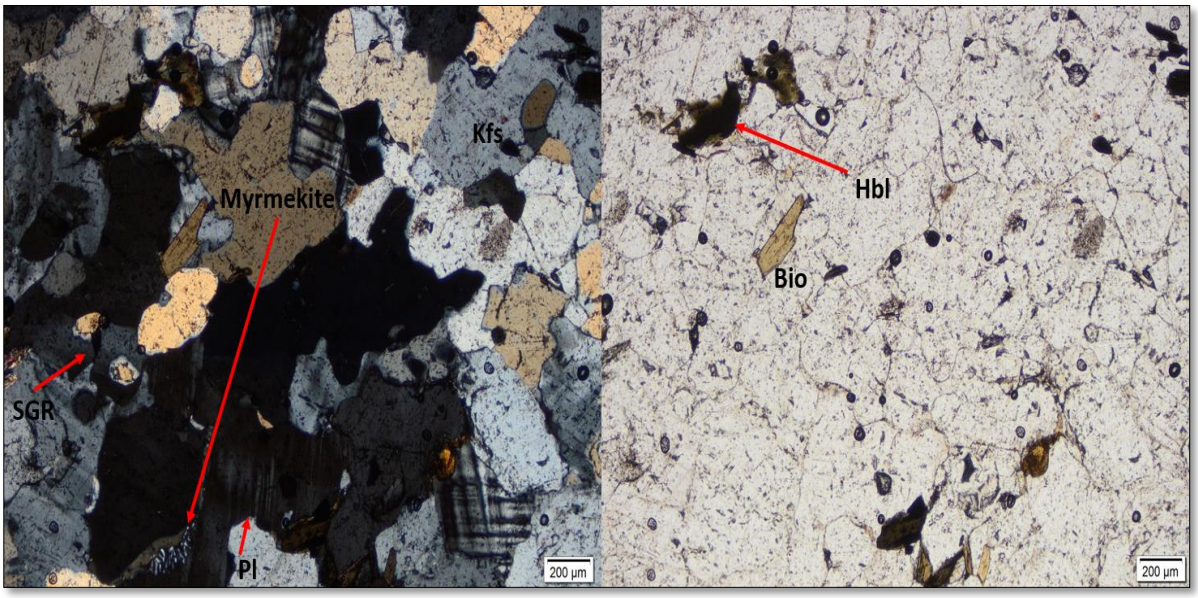


Figure 2.2: Microphotograph of the biotite-hornblende gneiss (sample JK/1), image in XPL is shown on the left and PPL on the right. Hbl: interstitial hornblende, Bio: biotite, Pl: plagioclase, Kfs: alkali-feldspar, myrmekite fabric in plagioclase, showing intergrowth of vermicular quartz; also shown is deformation twinning in plagioclase. Subgrain rotation (SGR) of plagioclase is indicated.

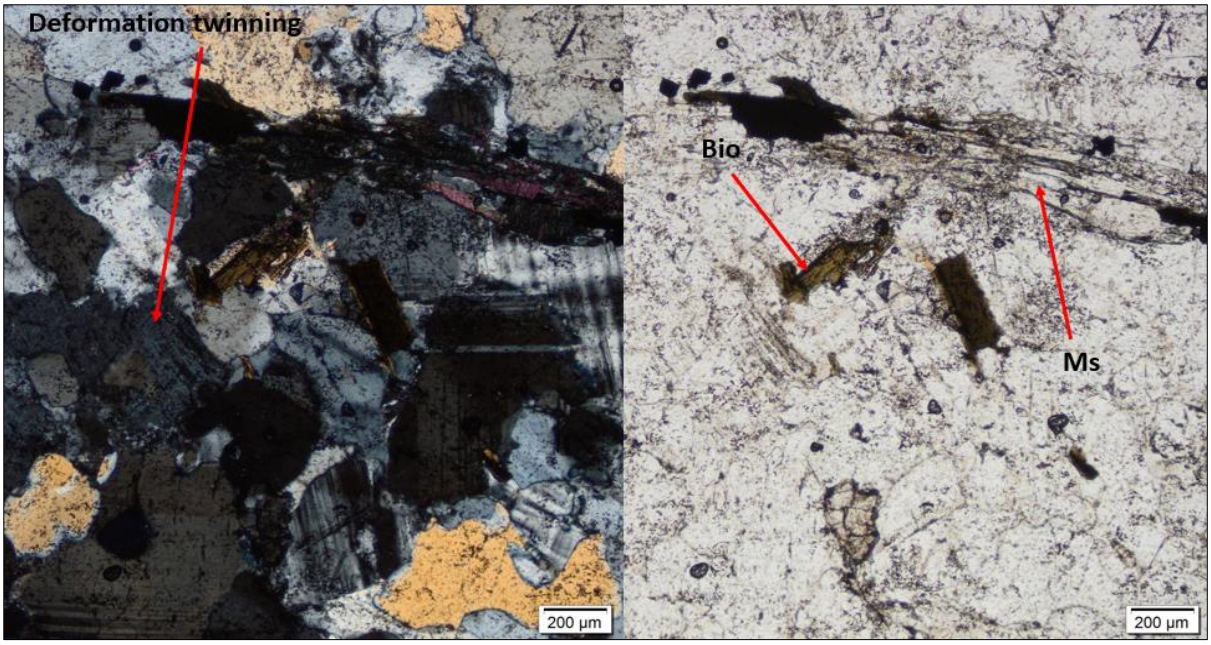


Figure 2.3: Biotite-hornblende gneiss (sample JK/1) showing deformation twinning in plagioclase and muscovite (Ms) replacing biotite (bio).

Sample JK/2: Muscovite-hornblende gneiss

Muscovite-hornblende gneiss (sample JK/2) is heterogranular and displays a predominantly porphyroblastic texture with grain size 6-10 mm and large euhedral (idioblastic) orthoclase and smaller, much rounded plagioclase (Fig. 2.4). It has an overall greenish-cream colour with faint pink patches on the fresh surface. The weathered surface has a greenish-yellow colour, with blackish-green 3-7 mm patches; these patches are restricted to areas with abundant biotite. The rock has a generally weak foliation with the mineral assemblage; quartz ± muscovite + orthoclase + plagioclase making up the light-coloured bands and biotite + hornblende + garnet making up the dark bands. Garnets appear as deep red spots. The orthoclase grains are enlarged and anhedral (xenoblastic) and give the rock its pinkish colour. Overall, the sample contains 31% alkali-feldspar, 28% plagioclase, 15% quartz, 12% muscovite, 5% hornblende, 4% biotite, 3% garnet and less than 2% accessory minerals (zircon, apatite, etc.).

Under the microscope, the muscovite-hornblende gneiss presents an inequigranular to seriate texture, with very large feldspar crystals surrounded by biotite and elongated polycrystalline

quartz ribbons (Fig. 2.5). Larger quartz crystals show grain boundary migration presented by their amoeboid grain boundaries. The megacrysts of alkali-feldspar show myrmekitic intergrowths and alteration into sericite (Fig. 2.6). The majority of plagioclase shows undulose extinction and deformation twinning. There seems to be only one generation of biotite, which is replaced by muscovite with only small patches indicating its presence.



Figure 2.4: Hand specimen of muscovite-hornblende gneiss (sample JK/2).

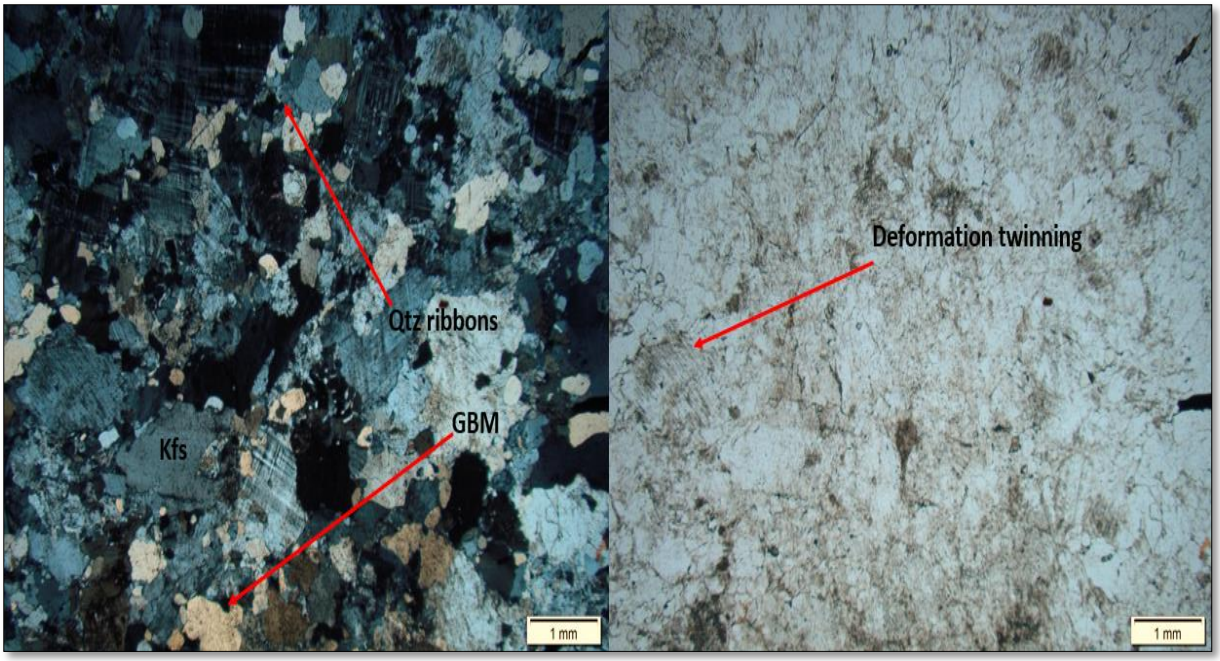


Figure 2.5: Microphotograph of muscovite-hornblende gneiss (sample JK/2), image in XPL is shown on the left and PPL on the right. Qtz ribbons: Polycrystalline quartz ribbons in response to deformation, deformation twinning as a result of intracrystalline deformation. Grain boundary migration (GBM) of quartz.

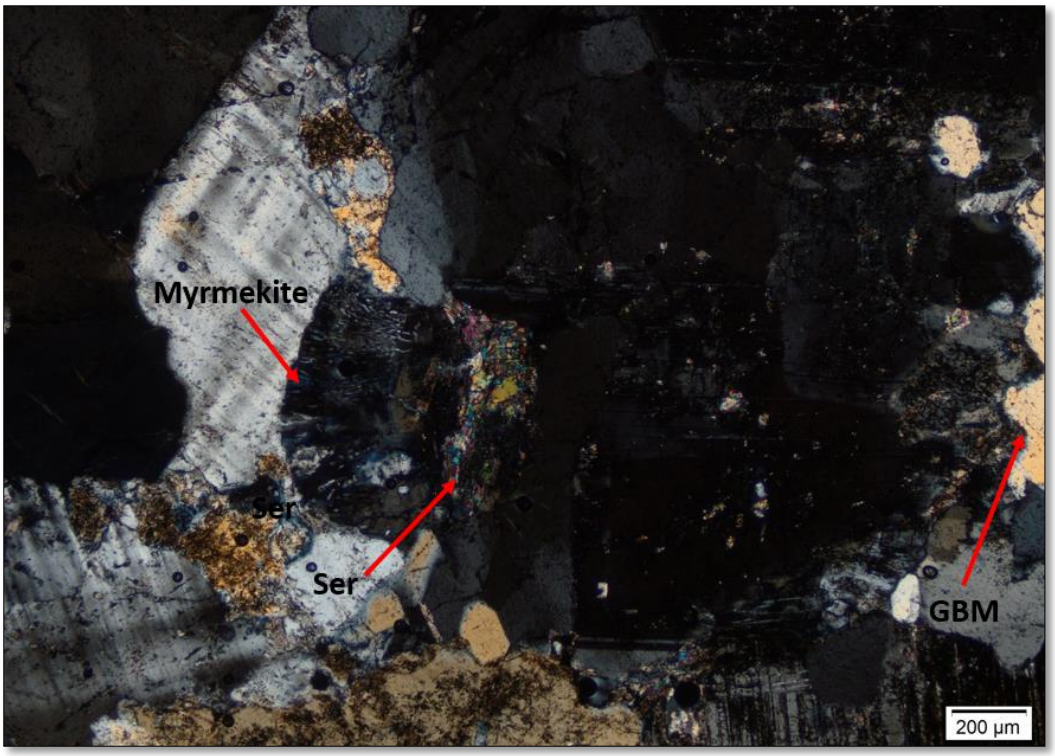


Figure 2.6: Muscovite-hornblende gneiss (sample JK/2) showing myrmekite fabric in plagioclase and alteration of plagioclase into sericite (Ser), GBM: Grain boundary migration in quartz.

Sample JK/3: Muscovite-biotite gneiss

Muscovite-biotite gneiss (sample JK/3) displays a fine- to medium-grained (1-4 mm) texture and creamy-grey colour on the fresh surface. Foliation is defined by an alignment of dark mica-rich layers and layers of light-coloured minerals (Fig. 2.7). The light-coloured minerals encompass clusters of rounded feldspar phenocrysts (3-4 mm) embedded in a groundmass composed mainly of quartz. The darker layers are very fine-grained muscovite and biotite (1-2 mm) and have a specific orientation. Overall, the sample contains 29% plagioclase, 24% alkali-feldspar, 18% quartz, 11% muscovite, 9% biotite, 4% siliminite, 3% garnet and less than 2% accessory minerals (zircon, chalcopyrite, etc.). The chalcopyrite occurs as shiny blebs.

Under the microscope, the sample shows an inequigranular texture with interlobate to amoeboid grain boundaries (Fig. 2. 8). There are elongate quartz and alkali-feldspars that show shape preferred orientation. Recrystallized quartz occurs as long and short polycrystalline ribbons with curved grain boundaries (Fig. 2.9). A myrmekitic fabric indicates intergrowth of vermicular quartz along the boundaries of alkali-feldspar. The alkali-feldspars also show fractures visible in both plane polarised light and crossed polarized light. Biotite is being outgrown by muscovite. Quartz subgrains are observed with different orientation relative to their larger counterparts. Plagioclase shows deformation twins.



Figure 2.7: Hand specimen of the muscovite-biotite gneiss (sample JK/3).

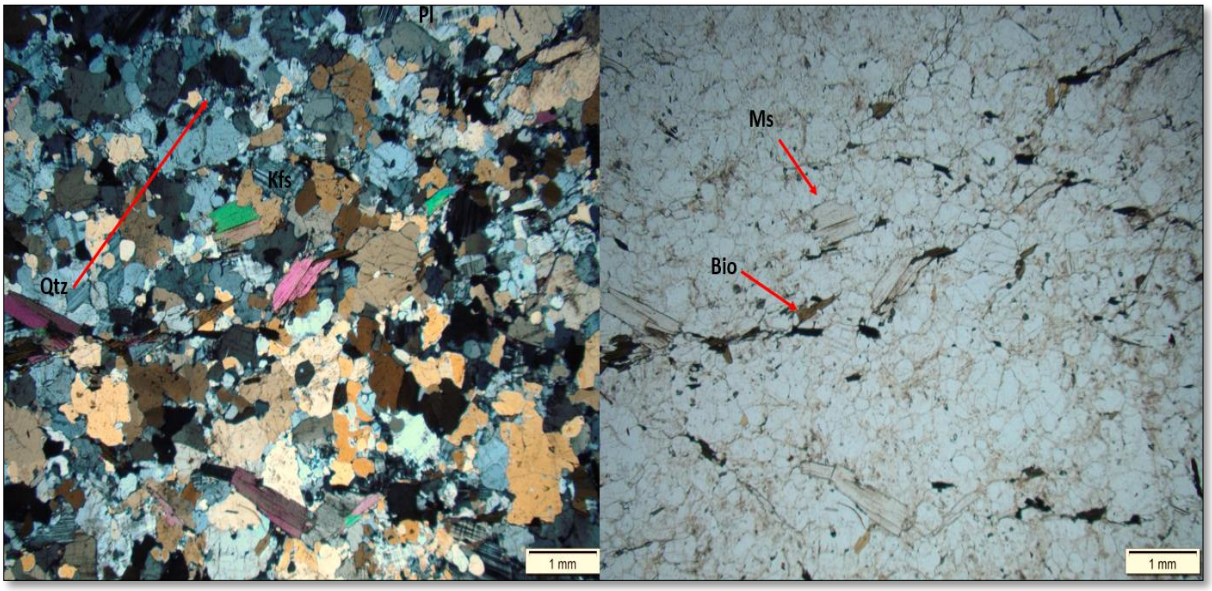


Figure 2.8: Microphotograph of the muscovite-biotite gneiss (sample JK/3) showing inequigranular texture with interlobate to amoeboid grain boundaries, spaced foliation is defined by layered biotite and alkali-feldpar-quarttz-muscovite.

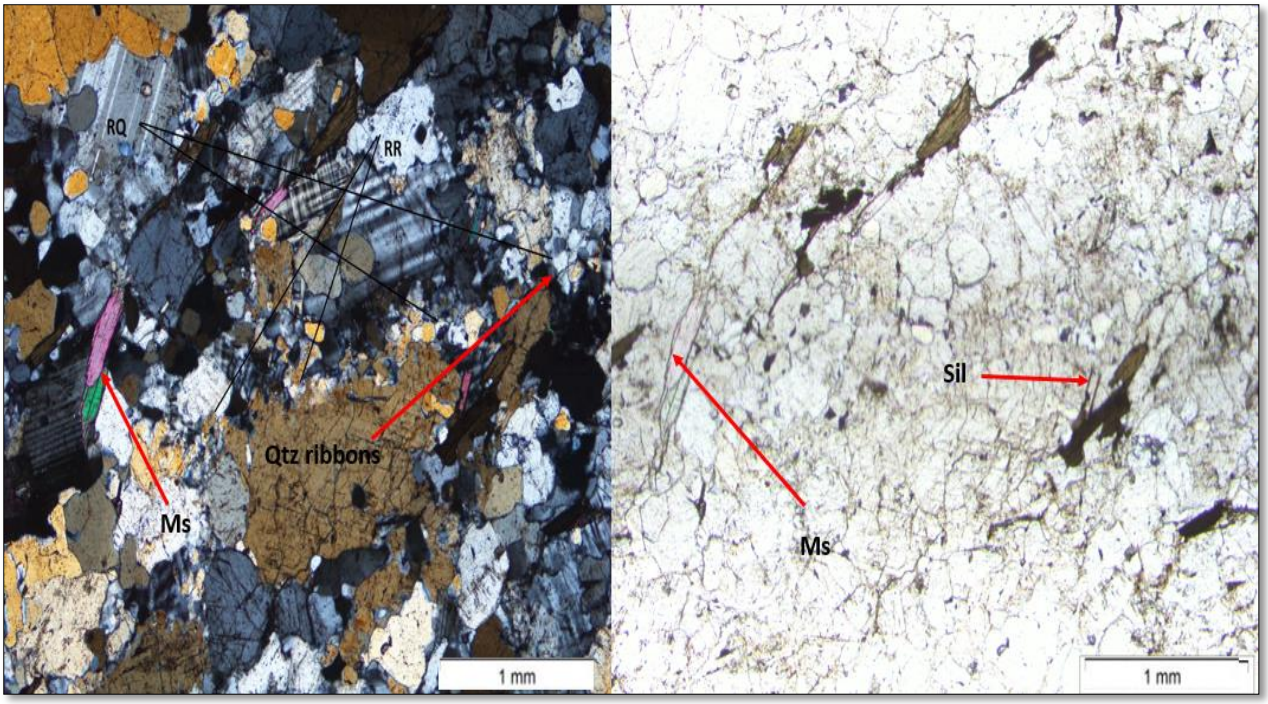


Figure 2.9: Muscovite-biotite gneiss (sample JK/3) showing recrystallized quartz with alternating long and short polycrystalline ribbons (RQ), RR: Reaction rims along the boundaries of feldspars producing myrmekitic fabric, Sil: sillimanite.

Sample JK/4: Biotite-muscovite gneiss

The biotite-muscovite gneiss (sample JK/4) can be described as a heterogranular rock with a medium- to fine-grained texture, grain sizes of 1 - 5mm (Fig. 2.10). The sample is characterized by a creamy-grey colour on the fresh surface and a yellow-pinkish colour on the weathered surface. The mica in this sample is spread across the rock in a decussate manner. The plagioclase occurs as creamy-white large crystals that are interlocking, forming phenocrysts embedded within a fine-grained groundmass made up of alkali-feldspar, quartz, hornblende, muscovite and biotite. Spots of reddish and lustrous garnet crystals occur in some areas of the rock sample. Shiny blebs of pyrite are also evident.

Sample JK/4 under the microscope shows plagioclase and alkali-feldspar phenocrysts surrounded by fine-grained groundmass of quartz, plagioclase, alkali-feldspar, hornblende and muscovite. Biotite occurs as an interstitial phase (fine material) around the large feldspar crystals (Fig. 2.11). Quartz shows abundant recrystallization with weak undulatory extinction

and elongate polycrystalline ribbons. Sericitization is observed through the presence of skeletal white mica inclusions within the alkali-feldspar. Some of the plagioclase phenocrysts have been scoured along their edges. Garnet porphyroblasts contain a few inclusions of alkali-feldspars and opaques as well as intergrowths of biotite. A few skeletal sillimanite crystals occur overprinting the garnet porphyroblasts. Cordierite-bearing symplectites separate cordierite from the garnet porphyrioblasts. Globular assemblages of zircon crystals occur dispersed within the groundmass. Overall, the sample contains 31% plagioclase, 21% alkali-feldspar, 15% quartz, 12% biotite, 6% muscovite, 4% garnet, 3% hornblende, 3% cordierite, 3% siliminite and less than 2% accessory minerals (zircon, apatite, etc.).

Sample JK/4, together with the other three granitic gneisses (samples JK/1, JK/2, JK/3) plots within the granite field of the QAP diagram by Streckeisen (1975) (Fig. 2.12).

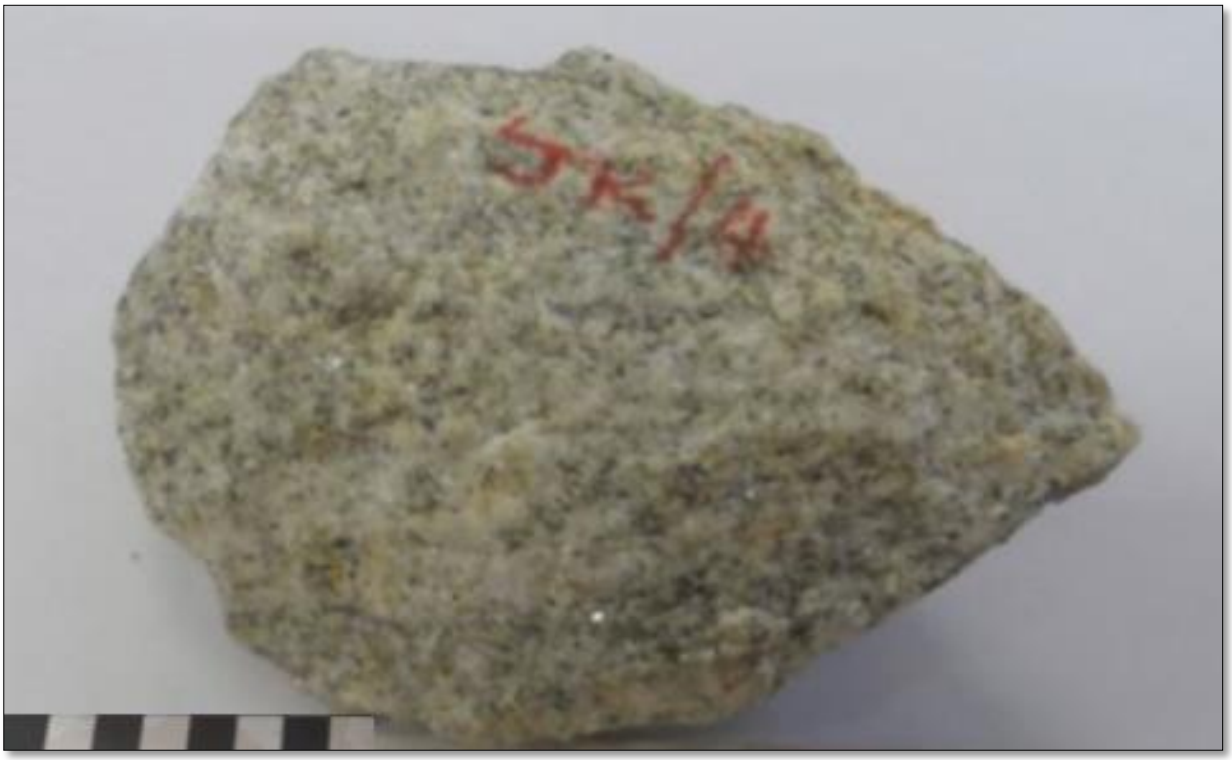


Figure 2.10: Hand specimen of the biotite-muscovite gneiss (sample JK/4).

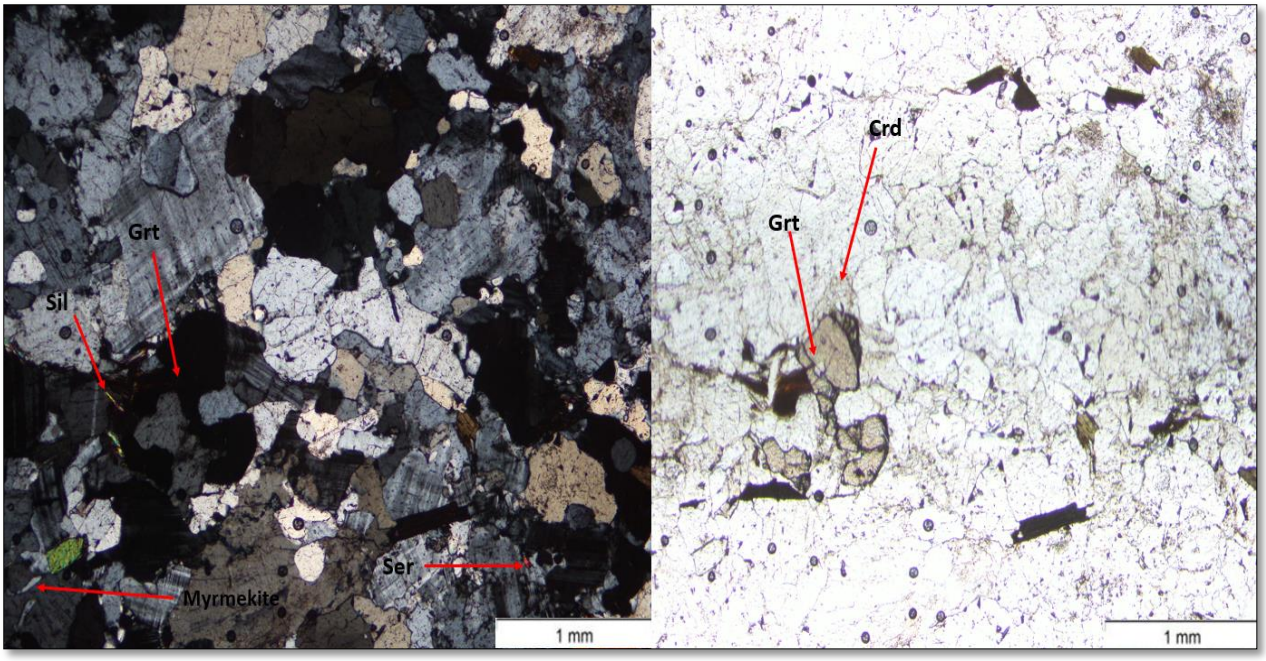


Figure 2.11: Microphotograph of the biotite-muscovite gneiss (sample JK/4), image in XPL is shown on the left and PPL on the right. Sil: Sillimanite, Ser: Sericite laths within plagioclase, Grt: Garnet porphyroblast, Crd: Cordierite and cordierite-bearing symplectites. Development of myrmekite deformation fabric in plagioclase is also shown.

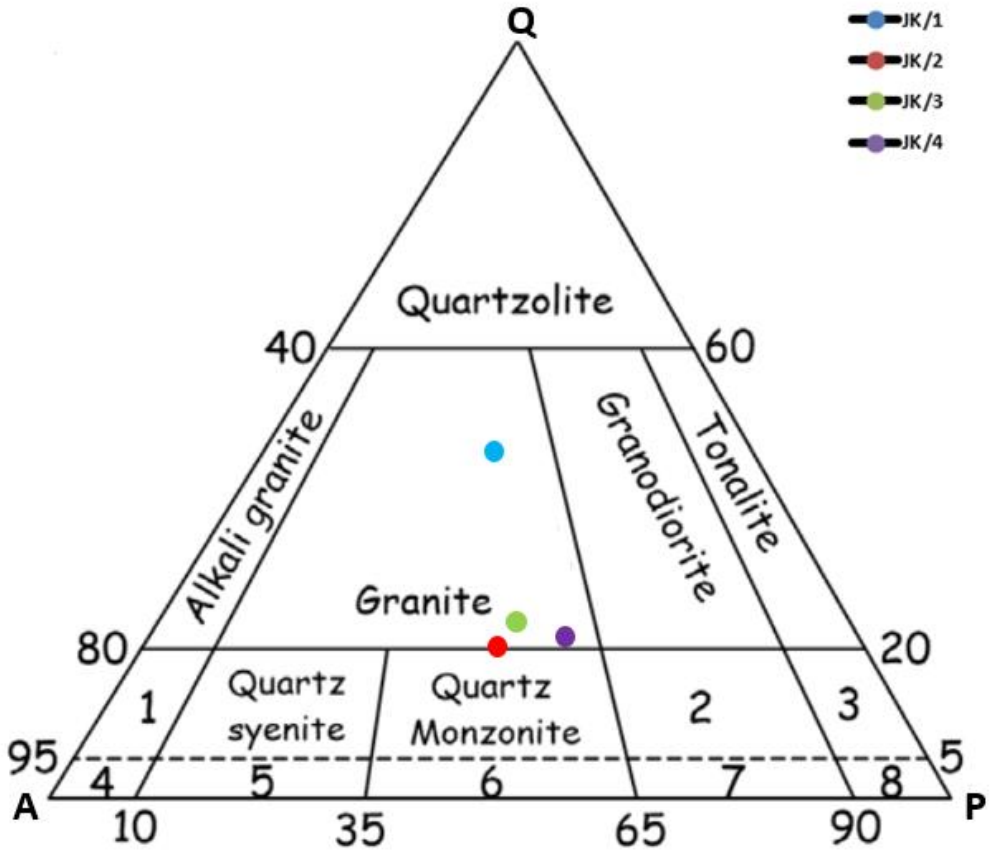


Figure 2.12: QAP diagram classifying the gneisses (samples JK/1, JK/2, JK/3 and JK/4). 1: Alkali Quartz Syenite, 2: Quartz Monzodiorite, 3: Quartz Diorite, 4: Alkali Syenite, 5: Syenite, 6: Monzonite, 7: Monzodiorite, 8: Diorite (after Streckeisen, 1976).

Sample JK/5: Biotite schist

The biotite schist (sample JK/5) is a grey-black coloured fine to medium (2-5 mm) grained rock with a weakly developed schistose cleavage (Fig. 2.13). Biotite is the most dominant mineral in the rock, followed by alkali-feldspars with minor occurrences of plagioclase and muscovite. Blebs of pyrite and chalcopyrite are disseminated within the rock. The matrix of this rock is rich in quartz with a few occurences of garnet. Garnet crystals in the matrix are very coarse and anhedral forming a porphyroblastic texture.

Under the microscope, the biotite schist (sample JK/5) shows interlobate to amoeboid texture. The spaced and anastomosing foliation observed in the sample is defined by biotite + garnet + opaques rich layers (cleavage domains) and quartz + plagioclase + alkali-feldspars layers (microlithons) (Fig. 2.14). There are two sets of biotite, the first set consists of fine grains and occurs as an interstitial phase, whereas in the second set, the biotite occurs as euhedral porphyroblasts. The euhedral porphyroblasts produced subgrains with different orientations (subgrain rotation). Quartz show a reduced grain size and lobate grain boundaries, wheras garnet shows resorption textures (coronas) that separate it from the flaky-skeletal biotite (Fig. 2.15). Alkali-feldspars occur as large grains and shows subgrain rotation, with serrated boundaries. Cataclasis with melt-flow is indicated in the fractured plagioclase (Fig. 2.15). Deformation twinning in plagioclase and myrmekitic fabric in alkali-feldspar is common. Also, most of the alkali-feldspars show grain boundary migration as lobate grain boundaries (Fig. 2.16). The modal estimates in this sample are: 30% biotite, 18% plagioclase, 16% alkali-feldspar, 14% muscovite, 9% quartz, 6% garnet, 3% hornblende and approximately 3% accessory minerals (chalcopyrite, apatite, etc.).



Figure 2.13: Hand specimen of the biotite schist (sample JK/5).

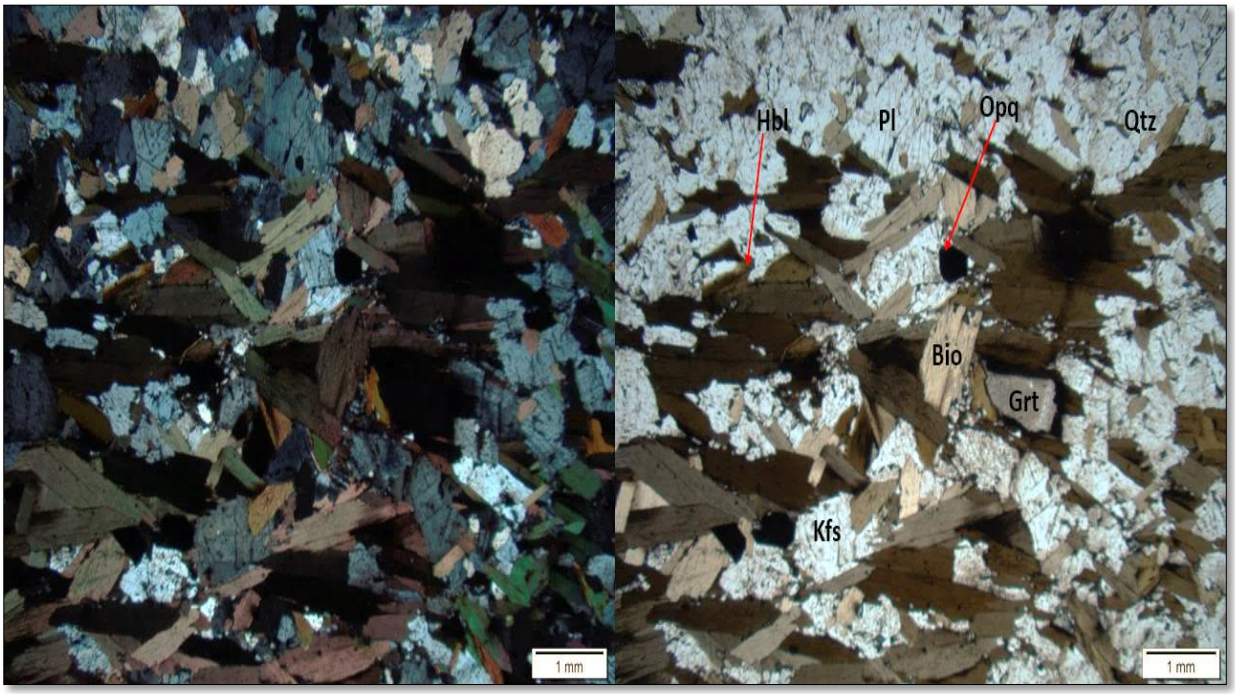


Figure 2.14: Microphotograph of biotite schist (sample JK/5). Image in XPL is shown on the left and PPL on the right. Penetrative secondary foliation with interlobate to amoeboid texture is shown. The spaced and anastomosing foliation is defined by biotite+garnet+opaques (cleavage domains) and quartz+plagioclase+alkali-feldspar (microlithons).

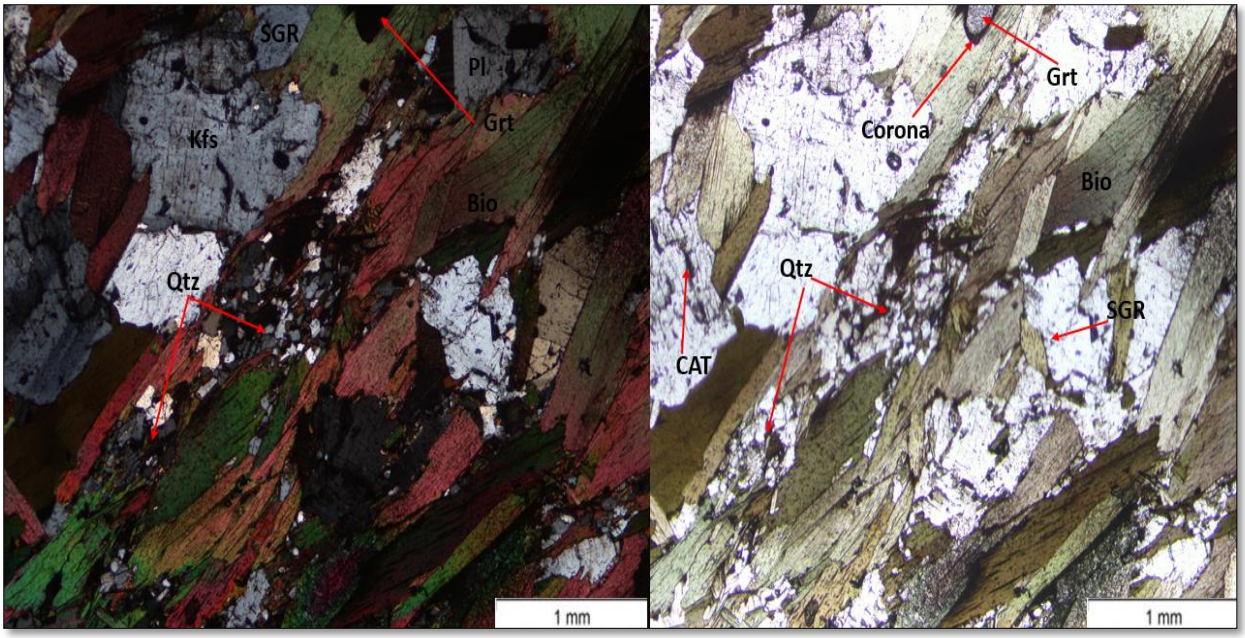


Figure 2.15: Biotite schist (sample JK/5) showing polycrystalline quartz, Grt: garnet grain with corona texture separating it from the biotite, Bio: Biotite rich layers defining a penetrative secondary foliation, SGR: Subgrain rotation of alkali-feldspar and biotite, Kfs: Alkali-feldspar, Pl: Plagioclase CAT: Cataclasis with melt flow in the plagioclase grain.

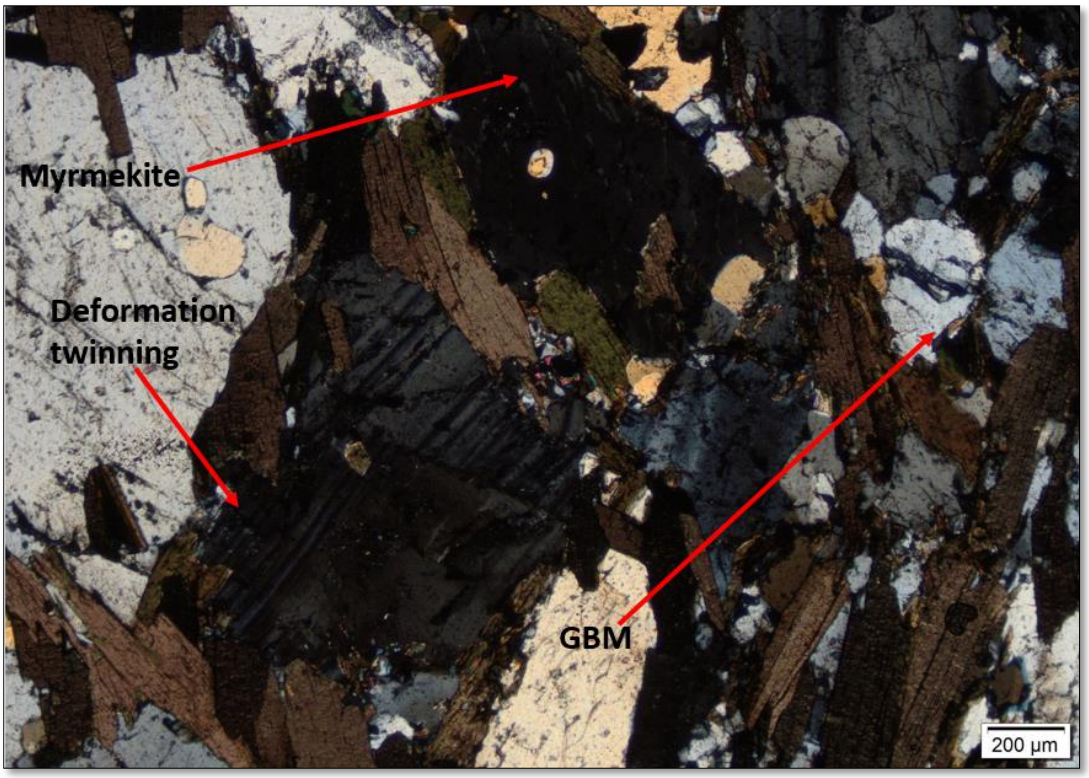


Figure 2.16: Biotite schist (sample JK/5) showing deformation twinning in plagioclase and myrmekitic fabric in alkali-feldspar, GBM: Grain boundary migration, shown as lobate grain boundaries in alkali-feldspar.

Sample JK/6: Biotite-garnet schist

Sample JK/6, biotite-garnet schist, is characterized by a granular texture and specific planar fabric that is defined by thick streaks of biotite and polycrystalline domains of strained quartz. Biotite occurs mostly as large euhedral flakes but also forms part of the matrix in some parts of the rock (Fig. 2.17). The biotite rich bands are much thicker (~1 cm) than the leucocratic minerals-dominated by quartz (10-25 mm). This rock sample has a general black-grey colour with some creamy-yellow patches indicating a weathered surface. Minor occurrences of reddish-brown garnet and brassy yellow sulphide minerals are present.

The sample is characterized by inequigranular-interlobate texture and anastomosing foliation. The foliation is defined by biotite+garnet+hornblende making up the cleavage domains and microlithons consist of alkali-feldspar+plagioclase+quartz (Fig. 2.18). Large alkali-feldspar contains tiny inclusions of quartz. Deformation in plagioclase is shown by formation of subgrains. Some garnet porphyroblast show amoeboid boundaries (Fig. 2.19). The feldspars and quartz mineral phases in this sample are highly strained, wherein most feldspars have fractures. Biotite occurrs as individual grains and as aggregates, individual biotite porphyroblasts show undulose extinction. This sample shows low to moderate sericitization. Tartan twinning is common whereas myrmekite formations are present but scarce. The modal estimate in this sample is: 39% biotite, 15% plagioclase, 11% alkali-feldspar, 10% muscovite, 9% quartz, 7% garnet, 7% hornblende and approximately 2% accessory minerals (apatite, chalcopyrite, etc.).

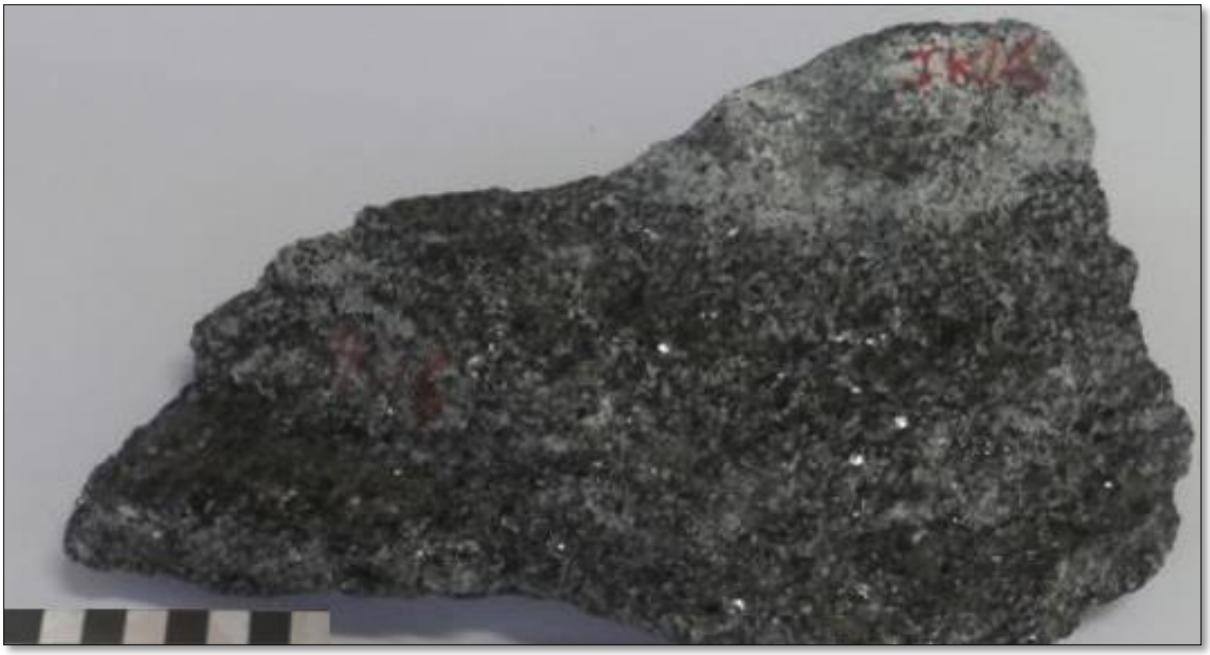


Figure 2.17: Hand specimen of the biotite-garnet schist (sample JK/6) from Jebel Kujur.

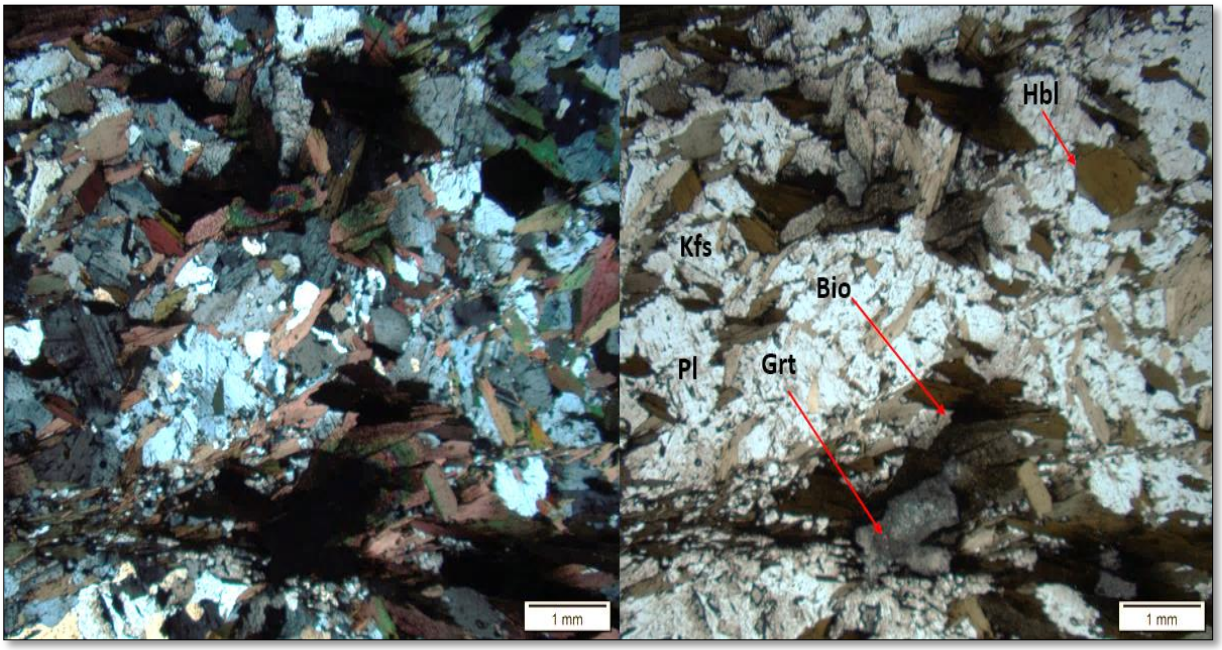


Figure 2.18: Microphotograph of the biotite-garnet schist (sample JK/6) image in XPL is shown on the left and PPL on the right. Anastomosing foliation is defined by biotite+garnet+hornblende (cleavage domains) and quartz+plagioclase+alkali-feldspar (microlithons). Overall texture is inequigranular- interlobate.

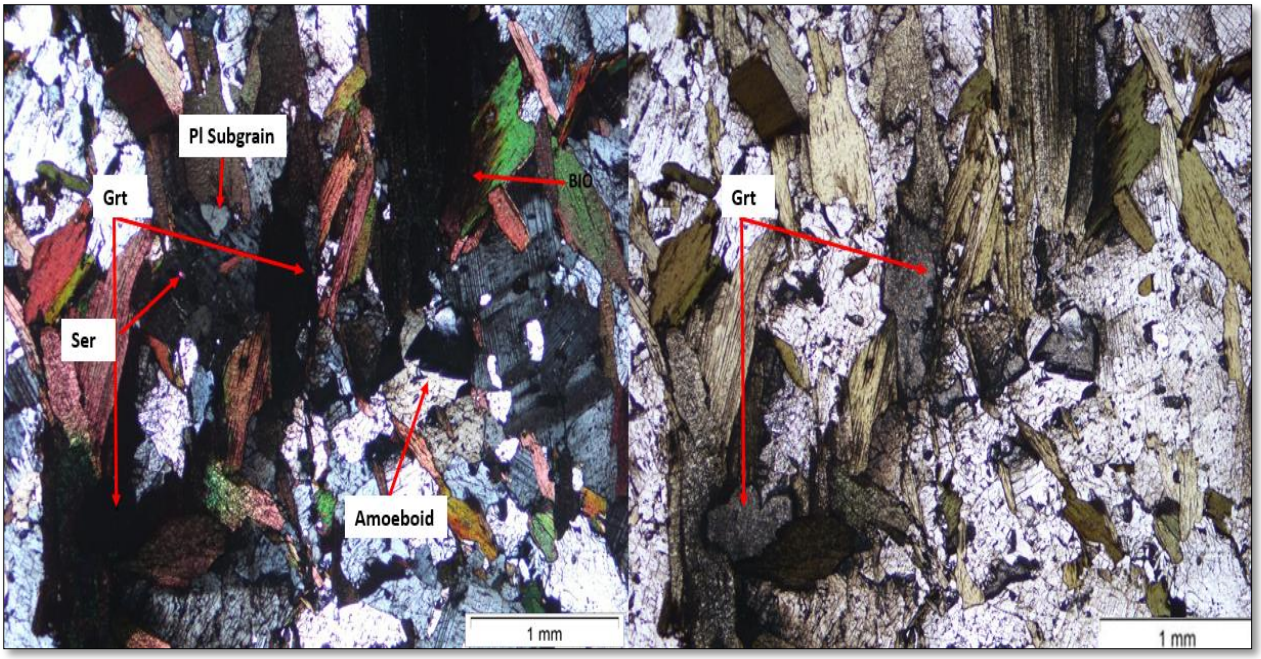


Figure 2.19: Biotite-garnet schist (sample JK/6) showing biotite porphyroblasts (BIO) with undulose extinction, plagioclase (Pl) subgrain, Ser: Alteration of feldspars into sericite, Grt: Garnet porphyroblasts overprinting biotite and straight garnet boundaries.

2.4 Discussion

The mineral assemblage (Pl + Qtz + Kfs + Bt + Grt + Hbl) observed in the biotite-hornblende gneiss (sample JK/1) signifies a rock that stabilized under amphibolite-metamorphic grade conditions (Eskola, 1920). Lobate grain boundaries seen within the quartz and feldspar assemblages are important microstructure, used to indicate high-temperature deformation (Fig. 2.2). According to Passchier and Trouw (2005), lobate boundaries are attributed to a recrystallization mechanism known as grain boundary migration, which commonly occurs at high temperatures. The exposure to high temperatures has also given rise to the deformation twinning observed in plagioclase, indicating crystal-plastic deformation (Fig. 2.3) (Pryer, 1993).

Furthermore, the biotite-hornblende gneiss shows a penetrative secondary foliation defined by subhorizontal biotite-rich and quartz-feldspars layers. The foliation is classified as a spaced foliation with interlobate grain boundaries and anastomosing spatial relationship between the different cleavage domains. This type of foliation is suggested to show an effect of new

compositional layering of tectonic origin (Vernon, 2004; Rustad, 2010). The foliation suggests high-grade metamorphism and deformation. Quartz inclusions that occur within the plagioclase, biotite and alkali-feldspar as well as lobate grain boundaries in these mineral aggregates show that they were present before the foliation.

The garnet grains are porphyroblasts with a subhedral shape and likely emerged from metamorphic overgrowth. Their internal fractures indicate that they were also subjected to yet another but later deformation event. Concerning the geochemical implications of the minerals, the red-brown colour of biotite reflects on the Fe-rich and low $Fe^{3+}/(Fe^{2+}+Fe^{3+})$ content of the rock (Lalonde and Bernard, 1993). Microcline suggests high K, and garnet indicates high Fe, Mg and Mn or Ca. The high antiperthitic content in the sample may be attributed to the excess K and Na ions (Carlsson, 2014).

Muscovite-hornblende gneiss (sample JK/2) shows inequiganular to seriate texture with interlobate grain boundaries (Fig. 2.5). These microstructures are commonly associated with high temperature deformation (Passchier and Trouw, 2005). The undulose extinction and deformation twinning shown by the plagioclase suggest crystal plastic deformation (Fig. 2.5). Furthermore, the presence of myrmekite and sericitization of the feldspars record a partial adjustment to falling temperatures (Fig. 2.6) (Shelley, 1993).

There are micro-fractures in this sample that indicate deformation due to high strain, including: The formation of subgrains and recrystallization into smaller grains, as shown by the presence of feldspars, sericite and quartz in the matrix. This sample reveals three deformation events in the area, the sequence of these events could be established by analysing a porphyroblast with a good inclusion pattern. Unfortunately, the biotite porphyroblasts in this sample do not have a well-developed inclusion pattern.

The mineral assemblage (Pl + Qtz + Kfs + Bt + Grt + Hbl) shown by the muscovite-biotite gneiss (sample JK/3) implies amphibolite-grade metamorphic conditions (Eskola, 1920). Muscovite-biotite gneiss also shows an inequigranular texture with interlobate to amoeboid grain boundaries (Fig. 2.9). These microstructures, together with deformation twins in the feldspars and subgrain rotation of quartz, suggest deformation under high temperature conditions (Passchier and Trouw, 2005). Tartan twinning and sparse myrmekite formations in the feldspars as well as alteration of feldspars to sericite indicate retrograde metamorphism and the presence or involvement of water (Fig. 2.9). The large content of muscovite in this rock corroborates hydrous conditions (Carlsson, 2014). The fractured oligoclase, recrystallized polycrystalline quartz and alkali-feldspars suggest deformation caused by high strain conditions. Moreover, the secondary spaced disjunctive foliation with wriggly cleavage domains most likely indicates a new compositional layering of tectonic origin (Vernon, 2004). Deformation events due to high temperature, cooling and high strain conditions are shown in this sample.

Biotite schist (sample JK/5) shows a penetrative secondary foliation represented by horizontal biotite-rich layers and quartz-feldspars layers. This feature, together with recrystallized polycrystalline quartz grains shows deformation due to induced high strain. The interlobate to amoeboid grain boundaries and undulose extinction in the feldspars serve as indicators of crystal-plastic deformation at high-grade conditions (Fig. 2.15) (Passchier, 1982). Cataclasis is shown by fractured plagioclase with isotropic shock produced melt flow that fills the cracks (Fig. 2.15). There are also biotite subgrains with different orientations relative to larger euhedral biotite grains (Fig. 2.15). This can be explained by a process known as subgrain rotation recrystallization, whereby a progressive misorientation of the subgrain results in two differently orientated grains that cannot be classified as part of the same grain (Passchier and Trouw, 2005). This process is associated with high temperatures. High temperatures are

corroborated by a mineral assemblage (Pl + Qtz + Kfs + Bt + Grt + Hbl) that stabilizes under high-grade metamorphic conditions (amphibolite-facies) (Eskola, 1920).

Biotite-garnet schist (sample JK/6) signifies a rock that was subjected to high temperature metamorphism up to uppper amphibolite-facies (Fyfe et al., 1958). This is shown through the mineral assemblage Pl + Qtz + Kfs + Bt + Grt + Hbl, the replacement and outgrowth of biotite by garnet as well as the high temperature lobate grain boundaries around feldspars and quartz grains. The garnet prophyroblast suggested to have grown from this high temperature metamorphism, shows serrated grain boundaries (Fig. 2.19). This feature indicates that the garnets were subjected to a deformation event that occurred subsequent to its formation. High strain deformation is shown as subgrains and recrystallization into smaller grains of quartz, feldspars and biotite.

Sericitization of feldspars occurring as small skeletal inclusions of sericite along the boundaries and within some of the feldspar grains as well as the presence of myrmekite suggest a cooling event in the rock (Fig. 2.19). Three tectono-metamorphic events can be deduced from this sample, namely metamorphism at high temperatures followed by retrogression as a result of cooling and subsequent high-strain deformation.

Reconstruction of the tectono-metamorphic evolution

The sequence of deformation events as stated earlier can be reconstructed using porphyroblasts with well-developed inclusion patterns. Biotite-muscovite gneiss (sample JK/4) contains suitable garnet porphyroblasts with a slightly developed inclusion pattern that could be used, together with information reflected in the other samples, to unravel the tectono-metamorphic evolution of the study area. Porphyroblasts often trap inclusions that reflect the structure of the matrix during their growth. After crystallization, the solid and rigid porphyroblasts will protect these patterns from further deformation, whereas the matrix remains prone to later modification

(Passchier and Trouw, 2005). Porphyoblast-matrix relationship and possible reaction rims can therefore be used to establish a relative sequence of metamorphic events and deformation phases.

A garnet porphyroblast in the biotite gneiss envelopes subhedral feldspar grains (Fig. 2.20). In the matrix, the feldspar grains show abundant deformation structures, including serrated-amoeboid grain boundaries indicating grain boundary migration, subgrain rotation and cataclasis presented as melt-filled fractures (Fig. 2.20). This porphyroblast-matrix relationship would suggest that the feldspar grains preserved within the garnet were present before the growth of the garnet (Vernon, 1975; Shelley, 1993). Nonetheless, the metamorphic event that resulted in the growth of garnet most likely caused deformation to pre-existing mineral crystals, such as plagioclase, alkali-feldspars and quartz as seen through their undulose extinction and lobate grain boundaries. These microstructures are attributed to high-temperature metamorphism as explained earlier, and therefore indicate that the early deformation event (M1) occurred as a result of an increase in temperature, consistent with early stabilization of the mineral assemblage: Pl + Qtz + Kfs + Grt + Crd + Sil, indicating granulite-facies conditions (Barker, 2013).

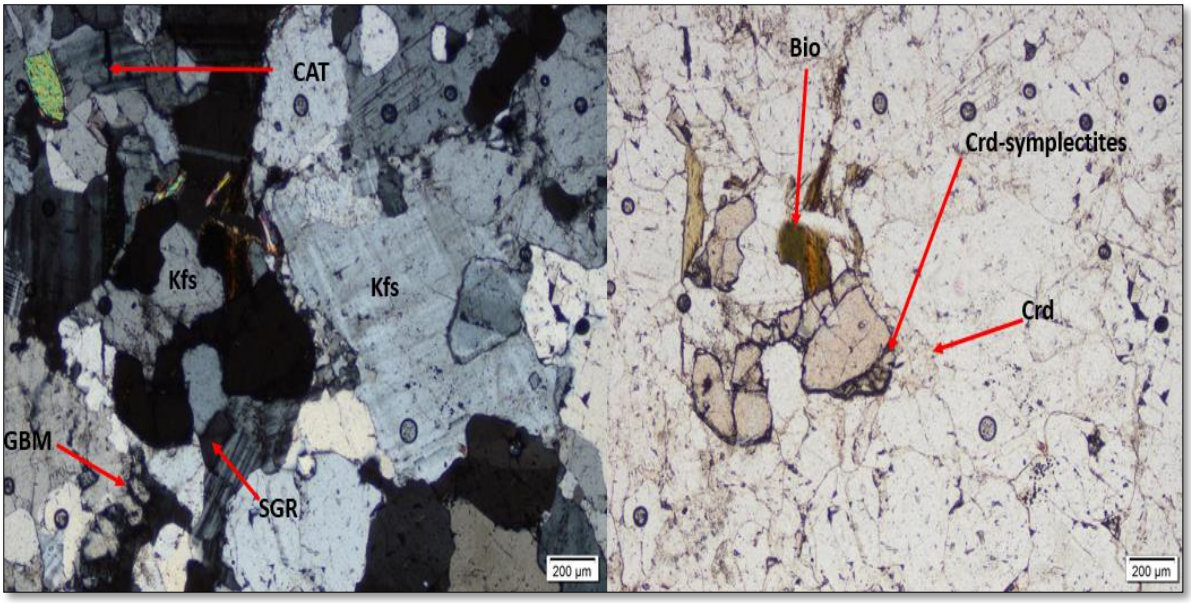


Figure 2.20: PPL and XPL microphotographs of garnet porphyroblast enveloping feldspars from sample JK/4, also shown is the skeletal laths of sillimanite overprinting the garnet, Bio: Secondary biotite and Crd: Cordierite and cordierite bearing-symplectites produced from the retrograde reaction: Grt+Kspar+Liq= Crd+Bio. CAT: Melt-filled fractures indicating cataclasis, subgrain rotation (SGR) and grain boundary migration (GBM) on feldspars in the matrix.

Three phases of alkali-feldspar occur in the sample; one is in the form of large subhedral crystals with perthitic microstructures and appears to be overprinting older plagioclase with undulose extinction. Another set occurs as smaller crystals with lobate grain boundaries and appears to be overprinted by the former phase. The perthitic exsolution observed in the youngest alkali-feldspar phase and biotite that appears as an alteration product within the cracks of a garnet porphyroblast indicate slow cooling of high-grade metamorphic rocks (Deer et al., 1992). Furthermore, alteration of alkali-feldspar into sericite occurs in the form skeletal inclusions. This reaction indicates the involvement of water and serves as evidence of retrograde metamorphism (Shelley, 1993). This is also supported by the presence of myrmekites in the alkali-feldspar.

Butcher and Frey (1994) deduced that cooling from high temperatures will regress ganulite-facies rocks to amphibolite facies and give rise to hydrous minerals. The cordierite-bearing symplectites around garnet indicate that the cooling path is probably part of clockwise P-T path and suggests near isothermal decompression (Yoshimura et al., 2008). This metamorphic event

may have occurred as a result of initial cooling from peak temperatures that caused the first metamorphism (M1); hence granulite-facies metamorphism that gave rise to garnet preceded the cooling stage. Cooling of high-grade metamorphic rocks commonly gives rise to sillimanite through the reaction: Grt + Kfs + Crd + H_2O = Bt + Qtz + Sil (Butcher and Frey, 1994). Sillimanite in the sample appears to be overprinting garnet porphyroblasts, which indicates that cooling occurred after the metamorphic garnet had formed. Metamorphism due to cooling can therefore be classified as M2. Paragenesis of minerals in response to cooling can be defined by: Grt - Crd - Kfs - Qtz - Pl - Bt - Ms - Hbl – Sil.

A similar sequence of metamorphism was reported for granulites in the central part of the Mozambique Belt in Tanzania where granulite-facies metamorphism peaked at 14 kbar and 800 ºC and later retrogressed to upper amphibolite facies at 8 kbar and 680-720 ºC (Sommer et al., 2003). An age of 640 Ma obtained from metamorphic rims of zircons from these granulites was interpreted to reflect the age of the peak metamorphism (Sommer et al., 2003). Kröner et al. (2003) reported high-grade rocks in the Mozambique Belt of Tanzania that were defomed and metamorphosed during an intense Neoproterozoic event, constrained at 620 Ma. In the same sense, the ductile sinistral shearing stage of the Aswa shear zone is linked to the advanced stages of high-grade metamorphism and intense deformation as a result of ultra-high temperatures. The timing of this event in the Aswa Shear Zone is, however, constrained at 685-655 Ma (Saalmann et al., 2016).

In northeastern Sudan, granulite-facies rocks are found in Sabaloka inlier and are correlated with Archaean granulites of northern Uganda (Dawoud and Dobrik, 2017). Granulite- and amphibolite-facies rocks are very common in the Central African Republic, with the largest occurrence in the Bouca Massif, although these rocks indicate granulite-facies metamorphism, and they are found within basement of a lower metamorphic grade (Clifford, 1974). Mestraud (1964) proposed that the disparity of these suites represent basement and cover, whereby the

amphibolite-facies metamorphism of the cover gave rise to retrograde metamorphism of the older granulite-facies rocks. In the the Aswa shear zone, the event of cooling is signified by fracturing of feldspar, elongate quartz ribbons and overprinting of mylonitic fabric by brittle fractures (Saalmann et al., 2016).

The transformation of newly formed large subhedral quartz, feldspars and biotite crystals into smaller crystals (subgrains) in the matrix around the garnet porphyroblast indicateS another phase of deformation (D1) after formation of garnet porphyroblasts. This event caused the fracturing of the garnet, size reduction of the quartz, plagioclase and biotite. These serve as evidence for brittle deformation (Passchier and Trouw, 2005). Further, D1 gave rise to subgrain rotation in the alkali-feldspars and deformed the grain boundaries of the pre-existing mineral phases to lobate-amoeboid shape, forming an inequigranular rock fabric, which shows new grains that formed from dynamic recrystallization. These imply crystal-plastic/ ductile deformation. The alkali-feldspars also show melt-filled cracks, which implies cataclasis was followed by melt flow. The intergration of all these microstructures indicates that during D1, crystal-plastic deformation was accompanied by fracturing. This deformation event can be defined by the following, recrystallized paragenesis: Grt - Qtz - Pl - Bt – Kfs (amphibolite-facies, Barker: 2013), also defining the faint foliation.

This deformation (D1) event could be linked to the ductile-brittle evolution stage of the Aswa shear zone that occurred during progressive convergence. Deformation during this stage resulted in dynamic recrystallization of quartz predominantly seen through subgrain rotation, fractures of large feldspar grains with inclusions of smaller feldspar grains as well as solid state foliation (Saalmann et al., 2016). Saalmann et al. (2016) deduced that the shear strain is notably low towards the north of the shear zone and has therefore caused deformation associated with general shear strain rather than sinistral shear. In contrast to general shear straining, sinistral shearing generates more intensive solid-state ductile shear overprint. Samples from the

Basement Complex in South Sudan do not show a mylonitic shear overprint but rather a faint foliation, which suggests mild solid-state deformation. This effect therefore corroborates the weakening of the shear strain (Aswa shear zone) from south to north. In the Aswa shear zone, the ductile-brittle (D1) deformation event is assigned to an age bracketed between 645 and 620 Ma (Saalmann et al., 2016).

2.5 Summary and conclusions

Samples from the Basement Complex in South Sudan predominantly exhibit high-temperature granulite-facies asssemblages, with subsequent amphibolite-facies retrograde overprint accompanied by a later brittle and crystal-plastic deformation. A similar sequence and nature of metamorphism has been reported from granulites in the Central African Republic, northern Uganda and the Mozambique Belt of eastern and central Tanzania. In all these regions, the high-grade metamorphic event is attributed to the Pan-African tectonothermal event, dated at 685-630 Ma. The first metamorphic event (M1) is characterized by undulose extinction in feldspars, lobate grain boundaries of the mineral phases, deformation twinning in plagioclase, subgrain rotation and grain boundary migration observed in various minerals. The mineral assemblage that stabilized under these metamorphic conditions is Pl + Qtz + Kfs + Bt + Grt ± Hbl ± Crd.

Cooling from peak temperatures (M2) is signified in the samples by perthite exsolution observed in plagioclase, alteration of feldspars into sericite, mymerkitic texture in feldspars, penetrative secondary foliation in some samples and coronas mostly in the form of symplectites between various reactive minerals. This deformation event implies retrogression from granulite-facies to amphibolite-facies metamorphism, with mineral paragenesis of Grt - Crd - Kfs - Qtz - Pl - Bt - Ms - Hbl – Sil. The final deformation event (D1) caused crystal-plastic deformation accompanied by brittle shearing. This event is linked to the ductile-brittle

deformation stage of the Aswa shear zone. Fracturing of garnet and feldspars, reduced grain size of earlier phases, subgrain rotation and lobate grain boundaries characterize this event.

Chapter 3
Geochemistry

3.1 Introduction

The Basement Complex contains a lot of unsampled lithologies, which include, but are not limited to, quartzofeldspathic para- and orthogneisses, garnetiferous schists and migmatites. Moreover, geochemical studies of these lithologies are necessary for contextualizing the geological history of the Basement Complex in South Sudan.

This chapter will describe the geochemical characteristics of the medium-grained granitic gneisses and biotite schists from the south-eastern segment of the Basement Complex in South Sudan (Jebel Kujur) and classify them accordingly. In this chapter, the nature of the protoliths of the metamorphosed samples and possible petrogenesis and provenance will be determined. Thereafter possible correlates in surrounding areas will be identified.

3.2 Analytical methods

Six samples from the Basement Complex of South Sudan were cut, crushed and milled in preparation for geochemical analysis. Major elements were determined by X-Ray Fluorescence (XRF), whereas trace element, including Rare Earth Element (REE) analysis was carried out by ICP-MS, both were done at the Earthlab (School of Geosciences, University of the Witwatersrand). Fused glass beads were used for major elements and pressed powder pellets for trace elements and REEs.

3.3 Results

3.3.1 Major elements

The geochemical data for major, trace and REEs is provided in Tables 1B and 2B (Appendix B). The granitic gneisses are characterized by moderate to high silica contents (74.08-75.48 wt %), whereas the biotite schists show a 49.84-55.63 wt %. The alumina content is similarly high

for both the granitic gneisses and the biotite schists in the range of 13.5-19.56 wt%. The Fe_2O_3 content is very low for the granitic gneisses (0.012-0.04 wt %) and a bit higher for the biotite schists at 0.14-0.18 wt%. The two groups of rocks have similarly low to moderate Na_2O ranging between 3.26 and 4.57 wt %. Furthermore, Al_2O_3 is consistently high in both the granitic gneisses and biotite schists, ranging between 13.76 and 19.5 wt%. The Al saturation index (Al_2O_3/ ($CaO+Na_2O+K_2O$)) is 1.4-1.7, indicating a peraluminous character. The abundance of CaO and MgO shows a great variation between the two groups of rocks, with a range of 1.04-1.27 wt% and 0.06-0.16 wt% in the granitic gneisses and 2.92-3.14 wt% and 4.94-6.4 wt% for the biotite schists, respectively.

The K_2O/Al_2O_3 vs Na_2O/Al_2O_3 discrimination diagram is used to identify the origin of the rocks as either sedimentary or magmatic. In the diagram, the granitic gneisses fall within the igneous field, whereas the schists plot in the sedimentary field (Fig. 3.1). As illustrated in the MgO vs Al_2O_3 discrimination diagram, the granitic gneisses display low MgO values with varying amounts of Al_2O_3, plotting within the field of orthogneiss. In addition, the biotite schists show very high MgO values coupled with high Al_2O_3 plot within the paragneiss field (Fig. 3.2). Having distinguished the origin of the rock samples, the results and discussion from hereon will be separated for the granitic gneisses and biotite schists.

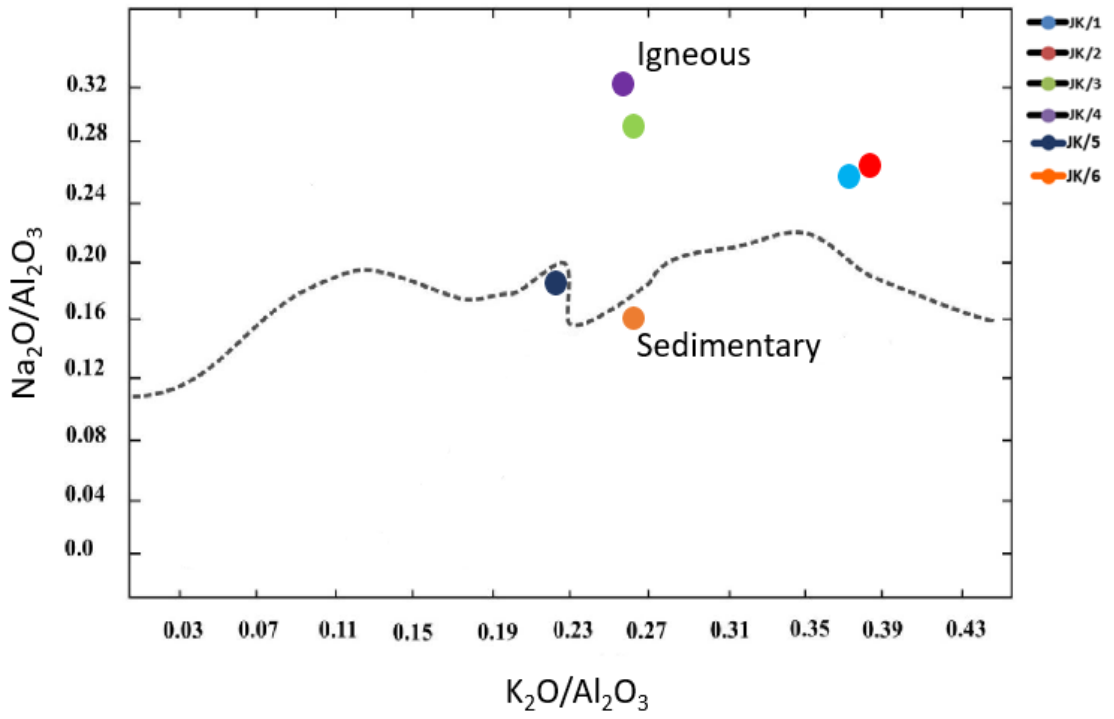


Figure 3.1: K_2O/Al_2O_3 vs Na_2O/Al_2O_3 discrimination diagram for the granitic gneisses (samples JK/1, JK/2, JK/3 and JK/4) and biotite schists (samples JK/5 and JK/6) (after Garrels and McKenzie, 1971).

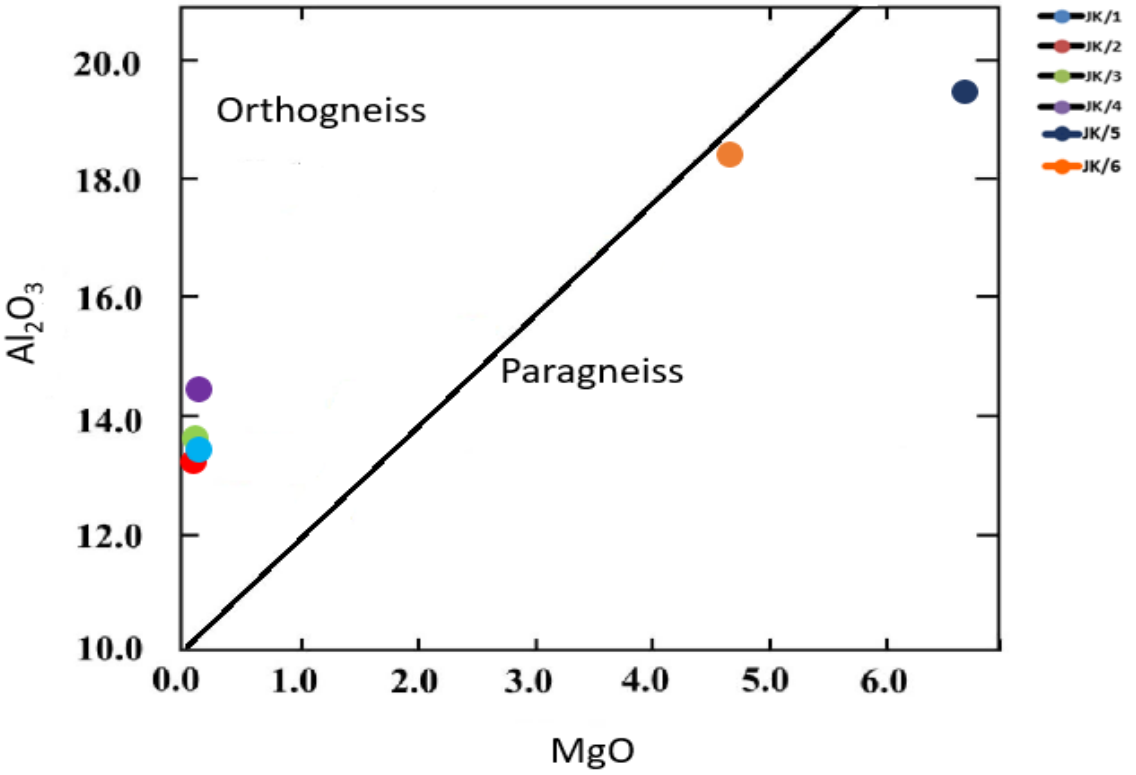


Figure 3.2: MgO vs Al_2O_3 discrimination diagram for the granitic gneisses (samples JK/1, JK/2, JK/3 and JK/4) and biotite schists (samples JK/5 and JK/6) (after Marc, 1992).

3.3.2 Granitic gneisses

3.3.2.1 Whole rock major elements

Samples JK/1, JK/2, JK/3 and JK/4 all plot in the granite field of the SiO_2 vs K_2O+Na_2O (TAS) diagram by Middlemost (1994) (Fig. 3.3). Furthermore, samples JK/1, JK/3, and JK/4 plot in the ferroan field, whereas sample JK/2 plots within the magnesian field of the SiO_2 vs FeO_{total}/ ($MgO+FeO_{total}$) diagram by Frost et al. (2001) (Fig. 3.4). All the granitic gneisses fall within the alkali-calcic field of the SiO_2 vs Na_2O+K_2O-CaO diagram by Frost et al. (2001) (Fig. 3.5). In the Shand (1943) $Al_2O_3/CaO+Na_2O+K_2O$ vs Al_2O_3/Na_2O+K_2O diagram, all the granitic gneiss samples indicate a peraluminous character (Fig. 3.6). Moreover, all the granitic gneisses indicate a calk-alkaline trend (Fig. 3.7). In the K_2O vs Na_2O discrimination diagram, the granitic gneisses plot in the I-type field (Chapell and White, 1974) (Fig. 3.8). The granitic gneisses were further classified in the granite classification diagram of Zr+ Nb+ Ce+ Y vs FeOtotal /MgO, in which all samples plotted within the field for fractionated M, S or I-type granites (Whalen et al., 1987) (Fig. 3.9).

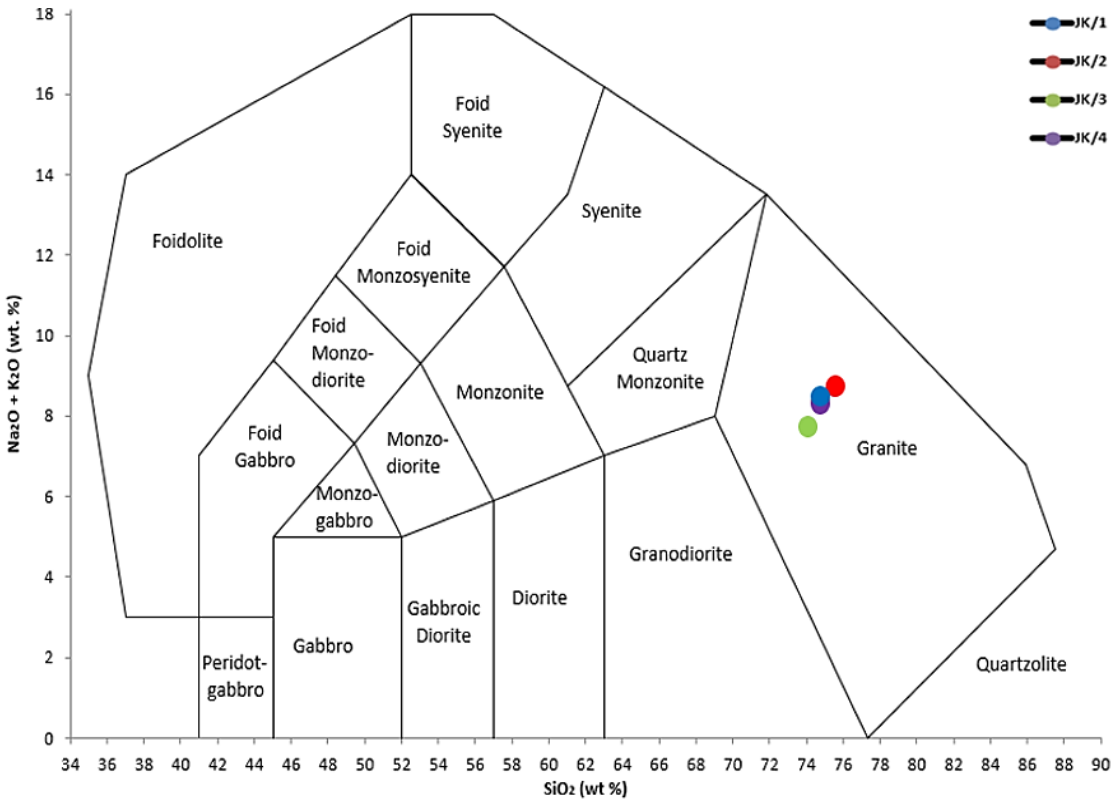


Figure 3.3: SiO_2 vs K_2O+Na_2O (TAS) classification diagram for plutonic rocks, plots of the granitic gneisses is indicated (Middlemost, 1994).

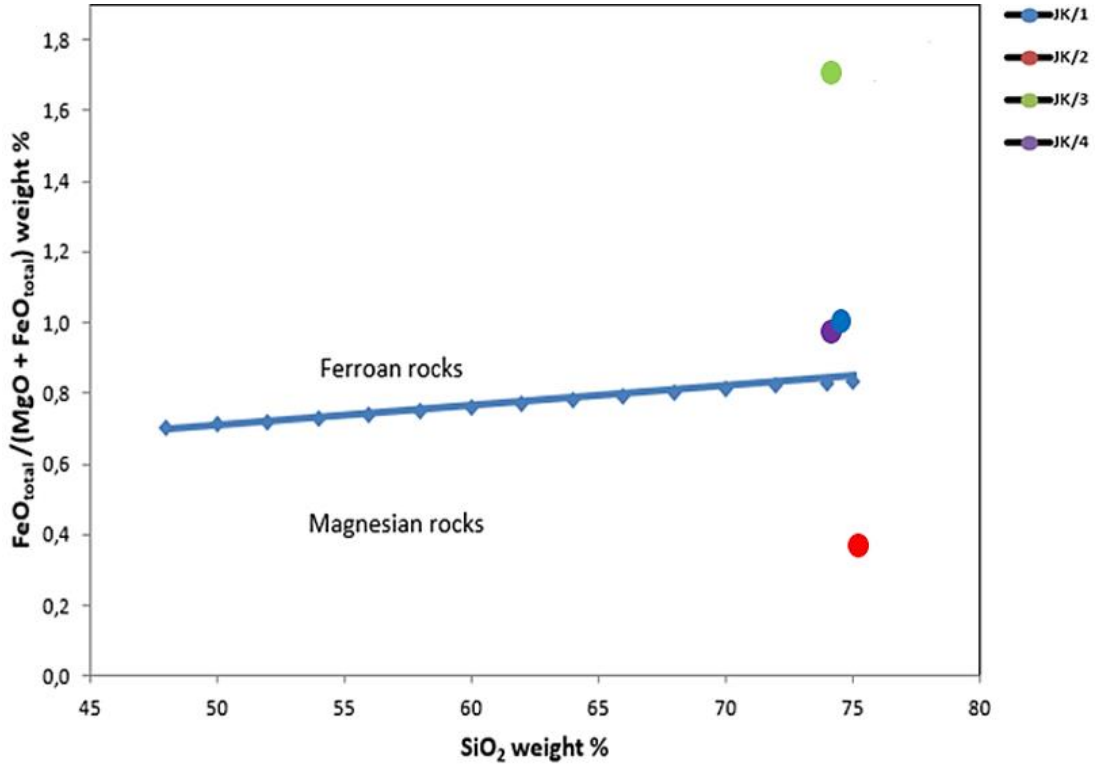


Figure 3.4: SiO_2 vs FeO_{total}/ ($MgO+FeO_{total}$) diagram for the granitic gneisses (Frost et al., 2001).

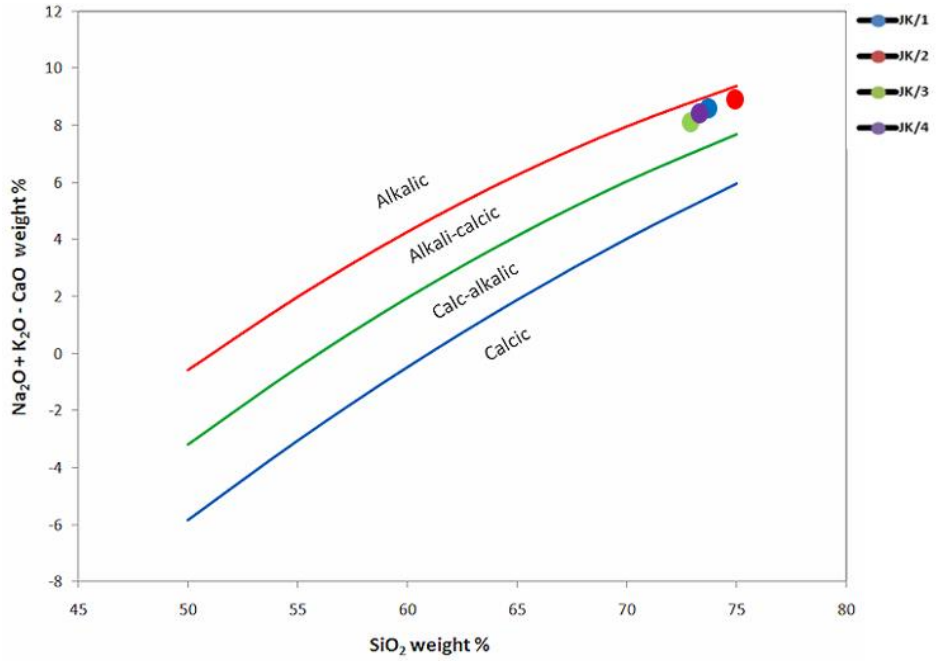


Figure 3.5: SiO_2 vs Na_2O+K_2O-CaO diagram for granitic gneisses (Frost et al., 2001).

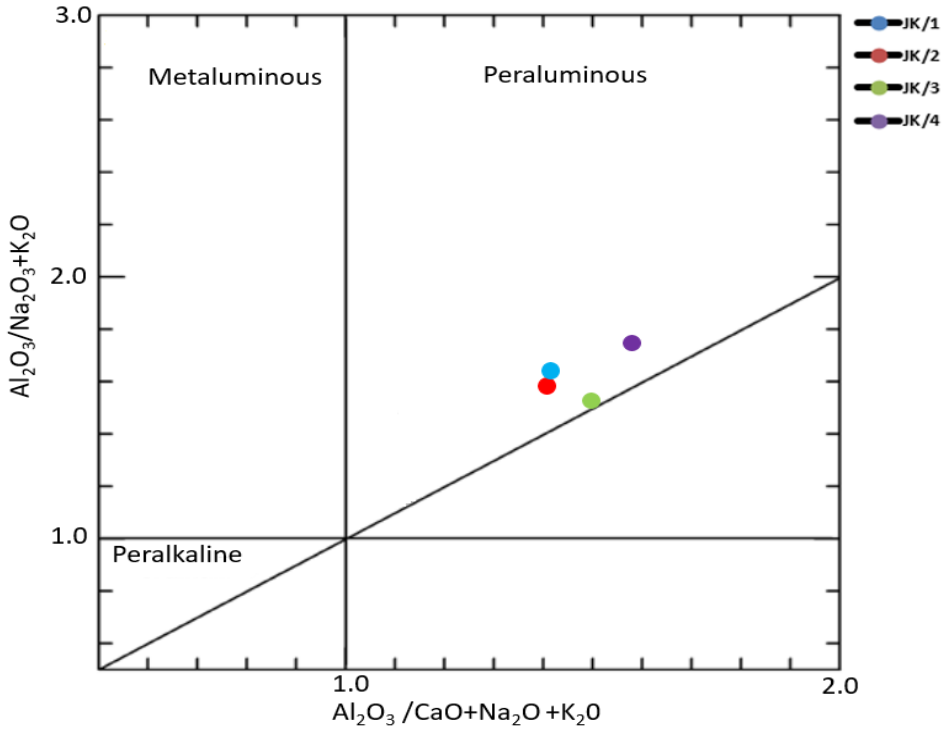


Figure 3.6: Al_2O_3 /CaO+Na_2O +K_20 vs Al_2O_3/Na_2O+K_2O diagram for the granitic gneisses (after, Shand 1943).

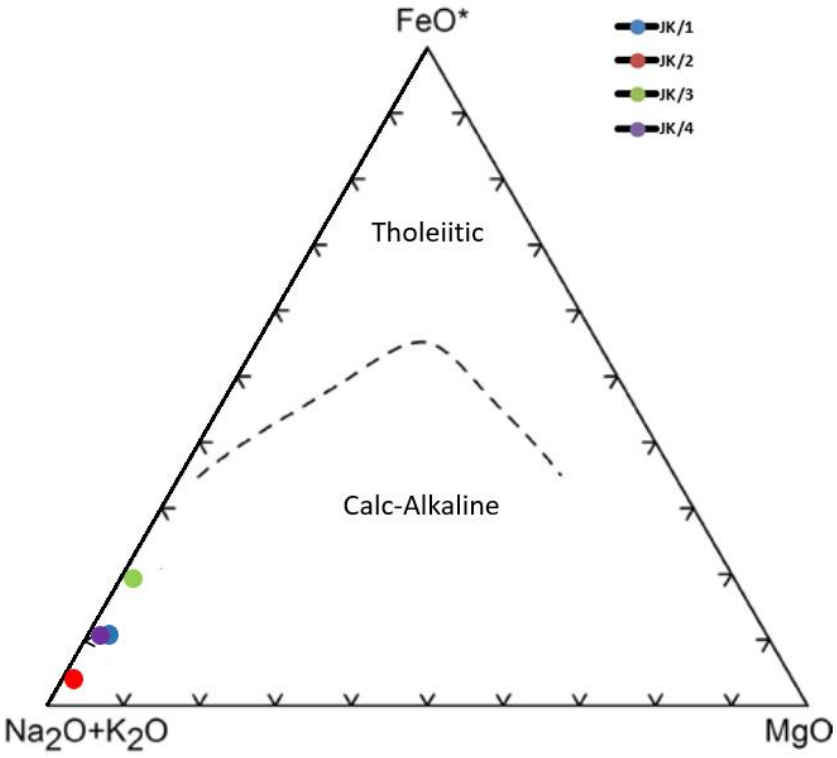


Figure 3.7: The AFM (Na_2O+K_2O: FeO*: MgO) plot showing calc-alkaline trend of the granitic gneisses (after Irvine and Baragar, 1971)

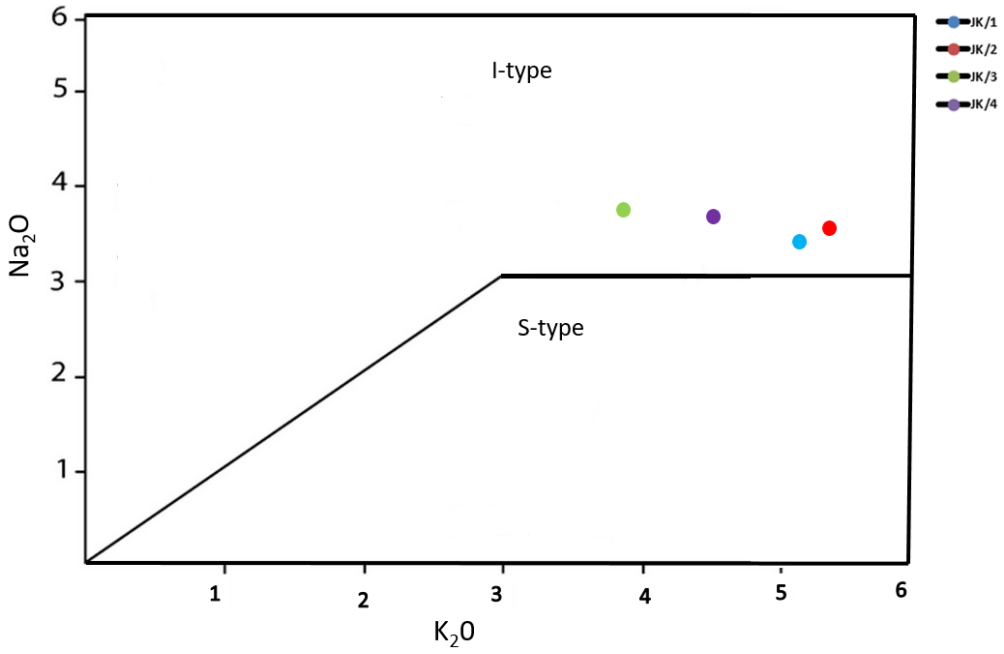


Figure 3.8: K_2O vs Na_2O discrimination diagram for the granitic gneisses (Chapell and White, 1974).

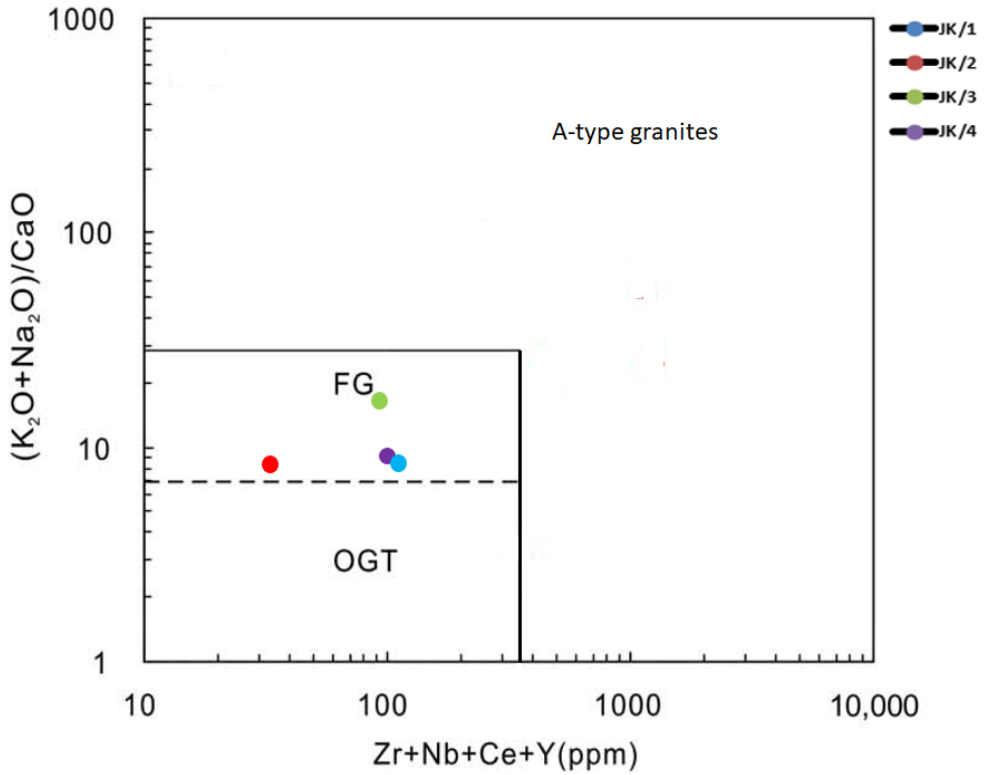


Figure 3.9: Granitoid classification diagram of Zr+Nb+Ce+Y vs (K_2O+Na_2O)/CaO plotted for the granitic gneisses. FG= fractionated M-, I- and S-type felsic granites, OGT=unfractionated M-, I- and S-type granites (Whalen et al., 1987).

3.3.2.1 Trace Elements

The granitic gneisses show very high Ti, Rb, Sr, Ba and Zr values and relatively low Sc, Co, Y, Nb, Sn, Cs, and Hf (Table 2B, Appendix B). Concentrations of Ta, W and U are much lower. The Primitive Mantle-normalized trace element plots (normalization values after, Sun and McDonough, 1989) show that the granitic gneisses are characterized by a negative slope produced by enrichment in the incompatible elements and low High field strength elements (HFSE) (Fig. 3.10). All samples display pronounced negative Ba, Sr, P and Ti anomalies and positive Th, K and Nd anomalies. Generally, the trace element distributions are quite similar with some notable exceptions.

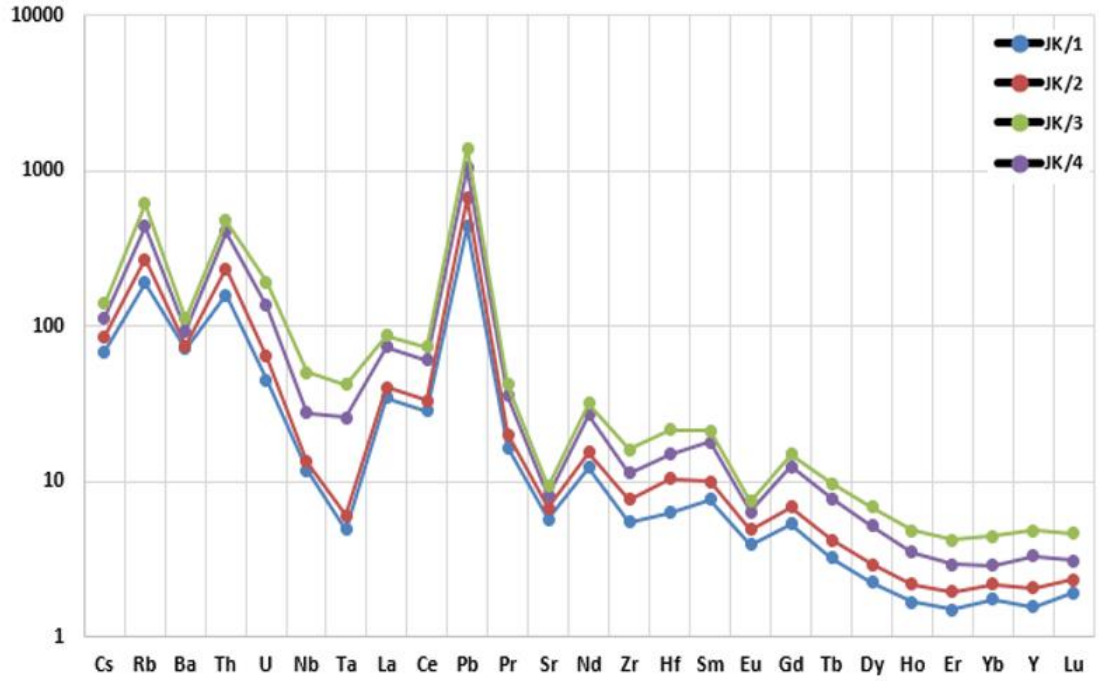


Figure 3.10: Primitive Mantle-normalized multi-element diagram of the granitic gneisses (after Sun and McDonough, 1989)

3.3.2.1 Rare Earth Elements

The REE contents of the granitic gneisses from the Basement Complex are reported in Table 2B (Appendix B). The gneisses present a profile characterized by moderate LREE enrichment relative to the HREE, with $(La/Yb)_N$ ratios ranging from 8.43 to 45.31 (Fig. 3.11). Furthermore, the profile for the granitic gneisses is distinguished by the almost flat HREES and a pronounced Eu negative anomaly. A positive Gd anomaly is also notable on the REE pattern, although not as pronounced as the latter.

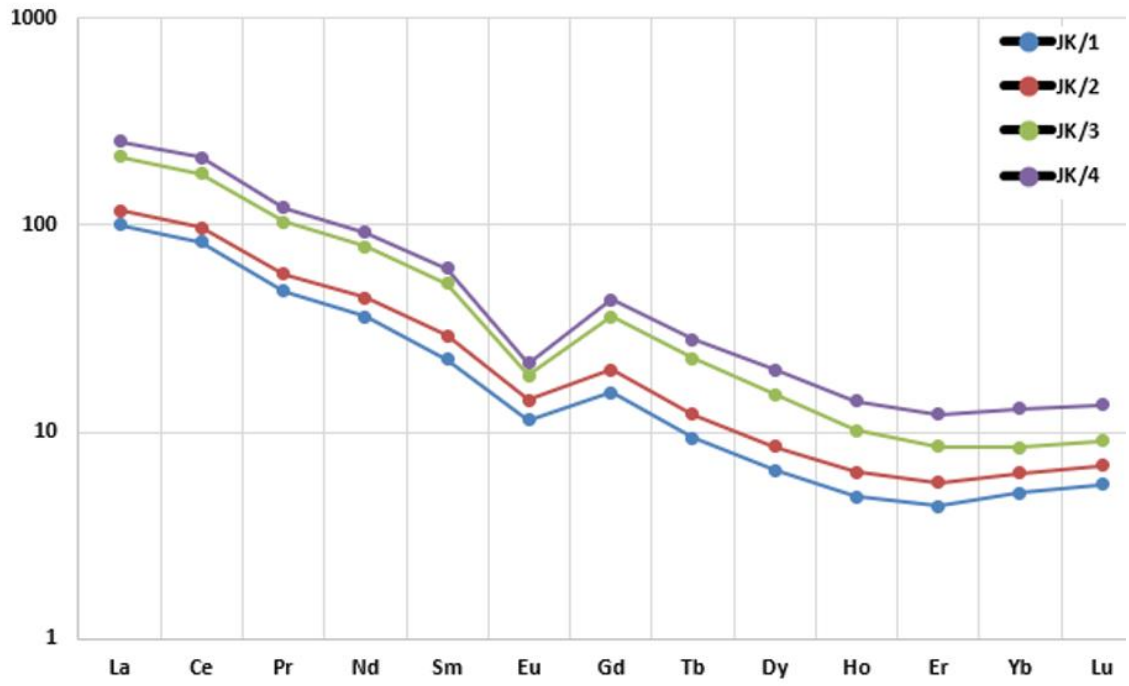


Figure 3.11: REE plot normalized against chondrites after Sun and McDonough (1989) for the granitic gneisses.

Tectonic environment

Concerning the tectonic environment, granitic rocks can be classified as either orogenic or anorogenic. The SiO_2 vs K_2O discrimination diagram by Maniar and Piccioli (1989) indicates that the Basement Complex gneisses are orogenic granitic rocks and plot in the field specified for orogenic granites (Fig. 3.12). Based on the Y vs Nb granite discrimination diagram by Pearce et al. (1989), the Basement Complex gneisses plot in the volcanic arc granite (VAG) and syn-collisional granite (syn-COLG) field (Fig. 3.13). Further discrimination in the Y+Nb vs Rb diagram indicates that the protoliths are volcanic arc granites (VAG) (Fig. 3.14). In the SiO_2 vs Rb/Zr discrimination diagram by Harris et al. (1986), the gneisses plot in the syn-collision granites field (Fig. 3.15). In addition, the gneisses are classified as continental arc potassic rocks in the Zr/TiO_2 vs Ce/P_2O_5 tectonic setting discrimination diagram by Muller et al. (1997) (Fig. 3.16).

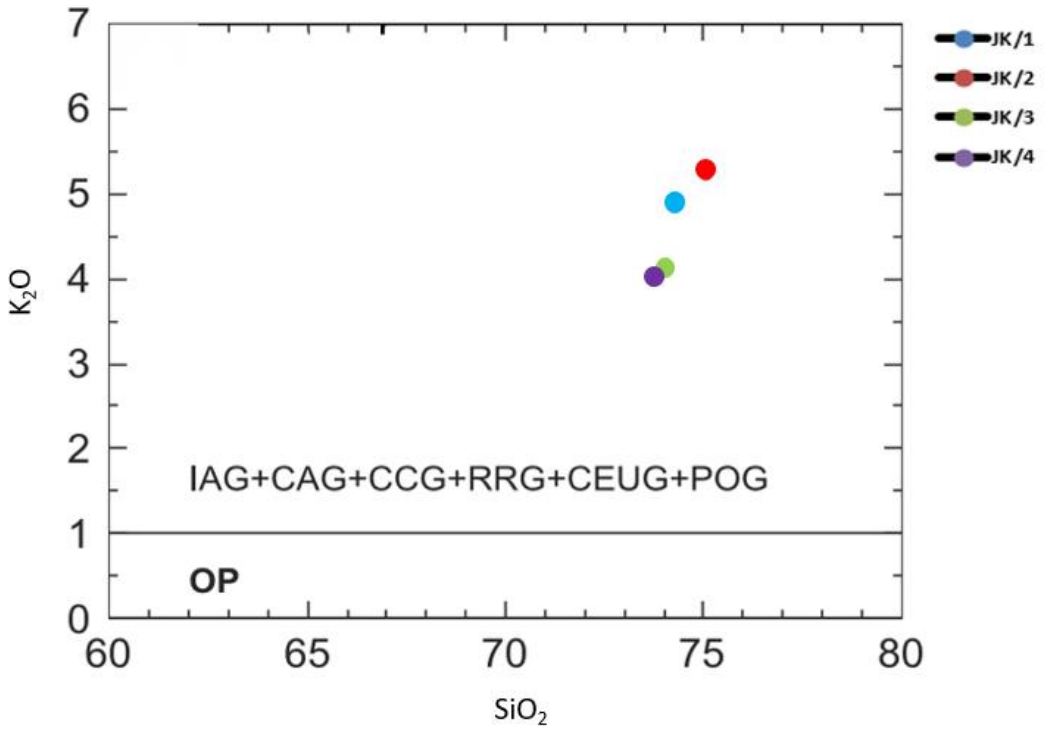


Figure 3.12: SiO_2 vs K_2O discrimination diagram for the granitic gneisses. IAG+CAG+CCG+RRG+CEUG+POG indicates a field for orogenic granites, OP= Oceanic plagiogranites (after Maniar and Piccioli, 1989).

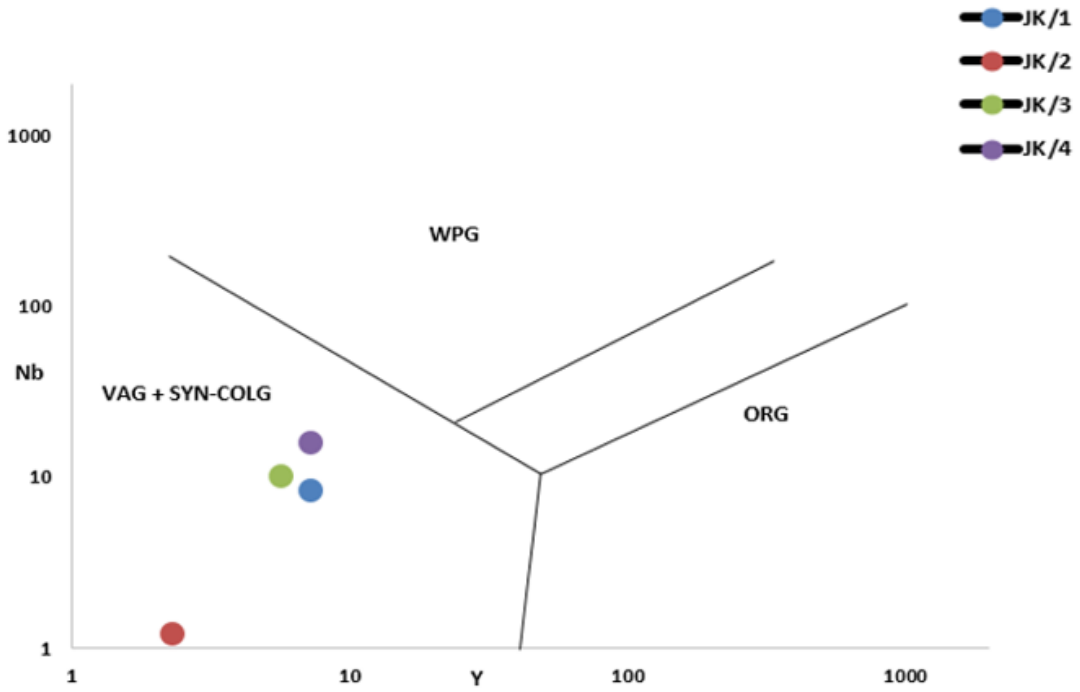


Figure 3.13: Y vs Nb discrimination diagram for the granitic gneisses (after Pearce et al., 1984).

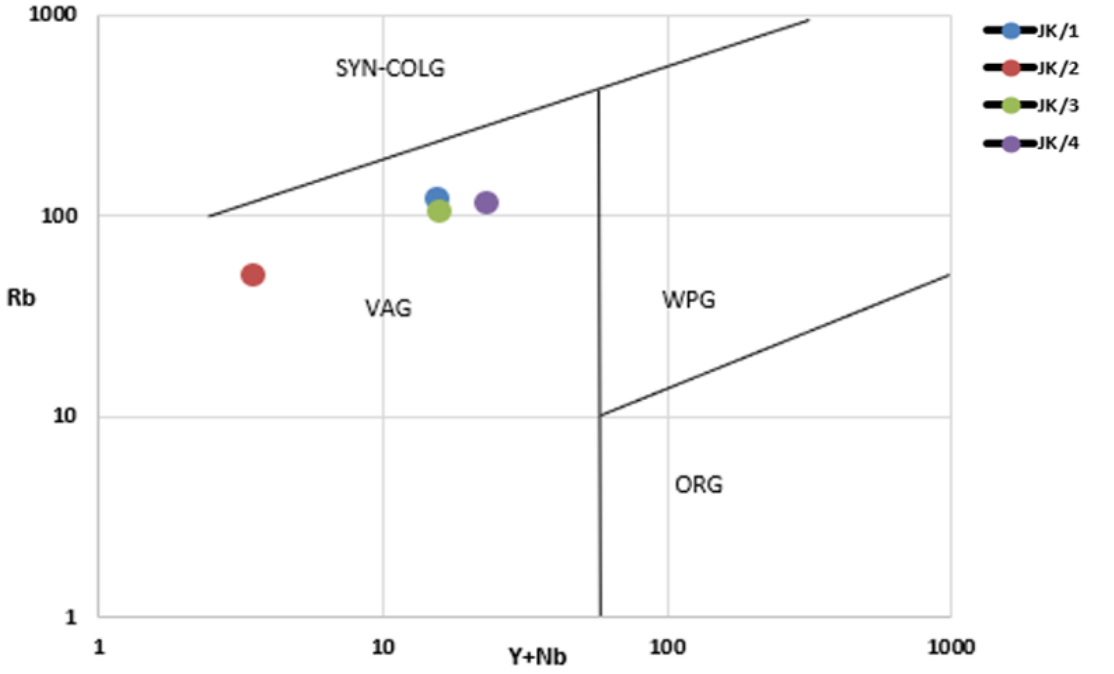


Figure 3.14: Y+Nb vs Rb discrimination diagram for granitic gneisses (after Pearce et al., 1984).

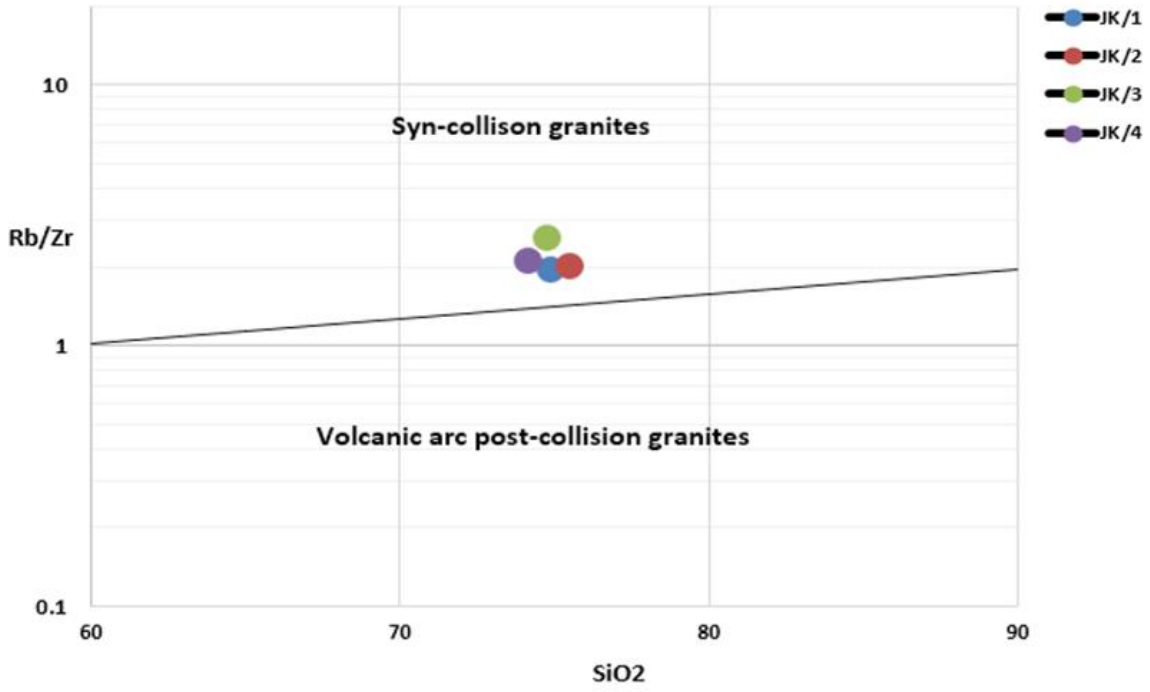


Figure 3.15: SiO_2 vs Rb/Zr discrimination diagram for the granitic gneisses (Harris et al., 1986).

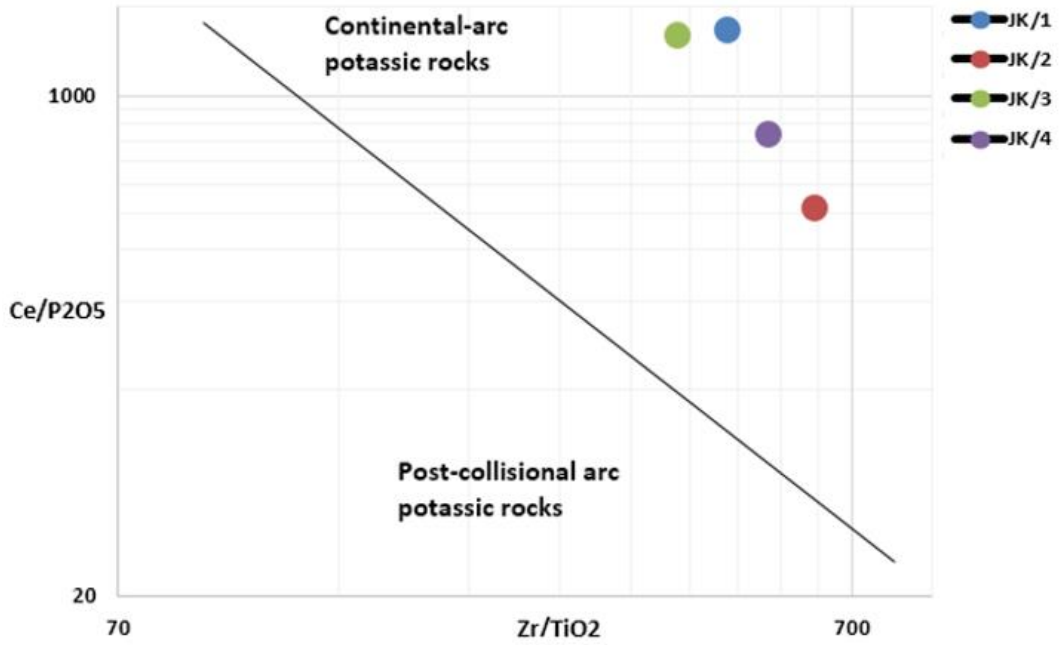


Figure 3.16: Zr/TiO_2 vs Ce/P_2O_5 discrimination diagram for the granitic gneisses (Muller et al., 1997).

3.3.3 Biotite schists

3.3.3.1 Whole rock major elements

The two metasedimentary rocks classified as biotite schist and biotite-garnet schist from the Basement Complex were plotted in the log Fe_2O_3/K_2O vs log SiO_2/ Al_2O_3 classification diagram of Herron (1988). Sample JK/5 plots within the litharenite field, whereas sample JK/6 is classified as sublitharenite (Fig. 3.17). The empirical discrimination $100TiO_2/Zr$ (Wt %/ppm) values (Abu El-Enen, 2011) for JK/5 and JK/6 are 1.21 and 0.94, respectively.

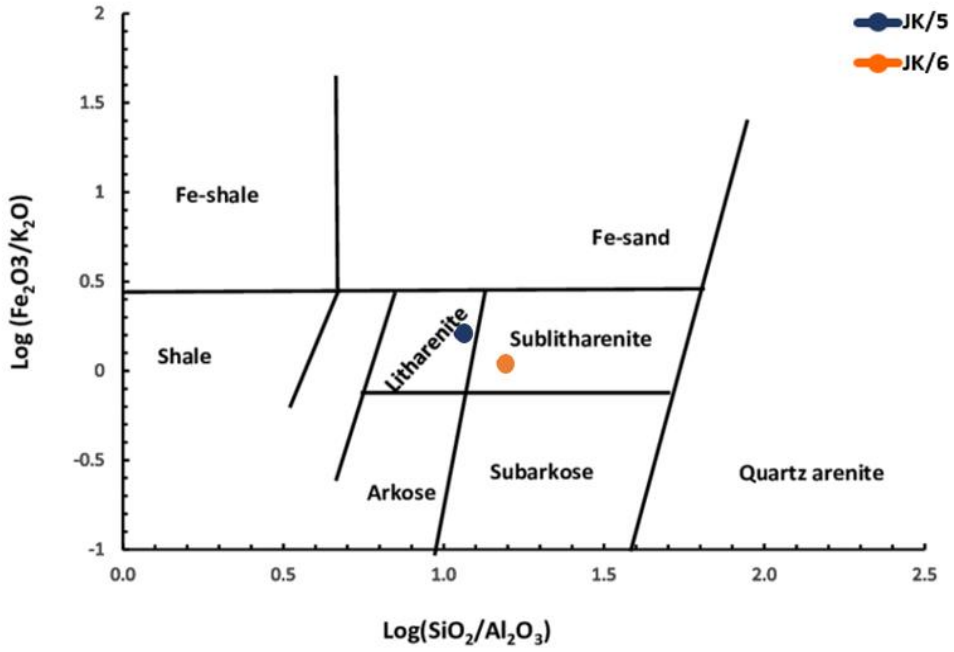


Figure 3.17: Log Fe_2O_3/K_2O vs log SiO_2/Al_2O_3 classification diagram showing the location of the biotite schists (after Herron, 1988).

3.3.3.2 Trace elements

Regarding trace elements, biotite schists from the Basement Complex show high Ti, Cr, Ni, Rb, Zr and Ba concentrations and a depletion of Ta, W and U (Table 2B, Appendix B). Correlation diagrams are commonly used when indicating the relationship between various elements. However, correlation diagrams are not so efficient in this case where there are only two samples. Table 3.1 is used to present observable trends between Al_2O_3 and selected trace elements. The table indicates a negative correlation between Zr, Hf, Nb, Ba, and Al_2O_3, whereas the relationship between Cs and Al_2O_3 is positive.

Table 3.1: Al_2O_3 against selected trace elements for samples JK/5 and JK/6 (biotite schists)

Elements	**JK/5**	**JK/6**
Al_2O_3 (wt %)	19.56	18.48
Zr (ppm)	112. 59	119.41
Hf (ppm)	2.93	3.13
Cs (ppm)	3.45	2.99

Nb (ppm)	8.41	8.95
Ba (ppm)	357.57	378.55

3.3.3.3 Rare Earth Elements

The REE patterns (normalized to chondrite from Evensen et al. (1978)) of the biotite schists are similar to those of the PAAS, AAS, and UCC (Fig. 3.18). The pattern shows light rare earth element enrichment, negative slope, and high Ce values. The biotite schists show lower REE content relative to the PAAS, AAS, and UCC, there is also a much lower abundance of immobile elements such as Zr, Hf, and Nb. In addition, the light rare earth elements for the biotite schists are much lower than those of the upper average continental crust. The REEs including Eu, Tb, Ho, Tm, and Lu for sample JK/6 overlap with those of AAS, PAAS and UCC.

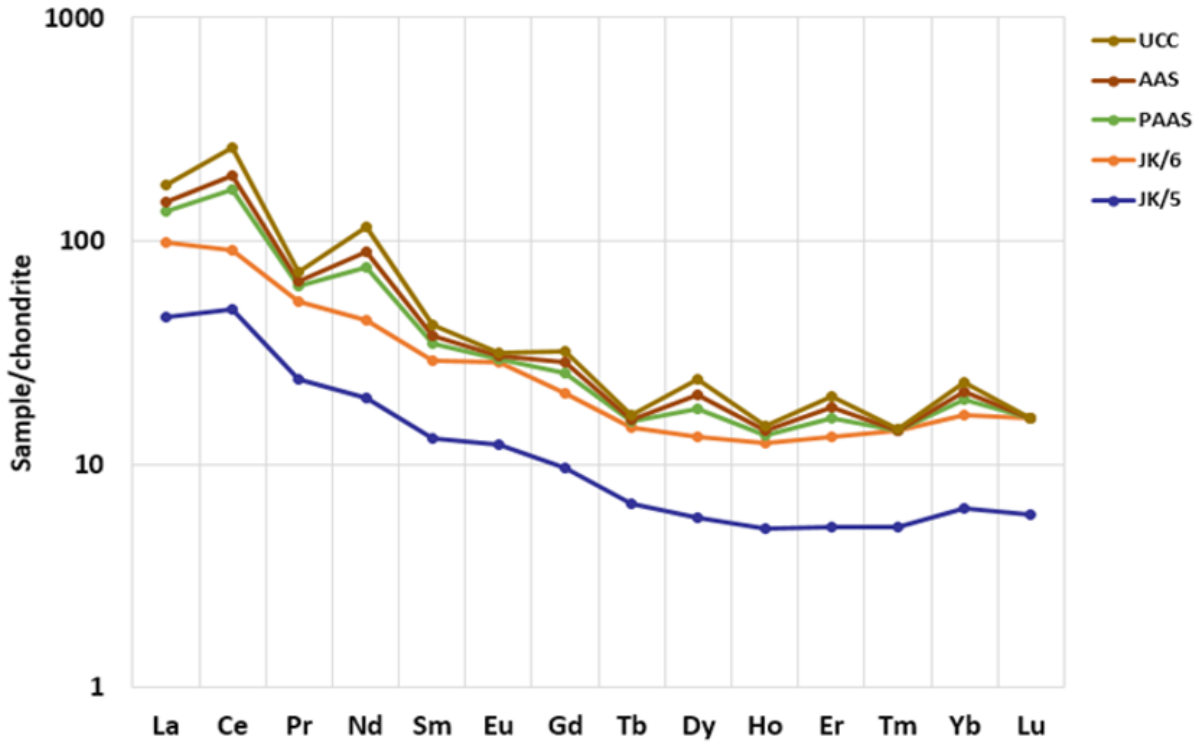


Figure 3.18: Chondrite-normalized REE patterns for the biotite schists. Normalization constants are from Evensen et al. (1978). UCC=Upper Continental Crust, AAS=Archaean Australian Shale, PAAS- Post-Archaean Australian Shale.

Provenance and tectonic setting

A few attempts have been made to use major and trace elements to decipher the provenance of the Basement Complex biotite schists. In the discriminant function 1 (F1) vs discriminant function 2 (F2) diagram of Roser and Korsch (1988), sample JK/6 plots within the felsic igneous provenance field, whereas sample JK/5 falls in the field for quartzose sedimentary provenance (Fig.3.19). The Al_2O_3 vs TiO_2 diagram by Hayashi et al. (1997) shows that the biotite schists have intermediate igneous rocks for their provenance (Fig. 3.20). In addition, the trace element plot of La/Sc vs Co/Th indicates that the biotite schists under study have andesitic source rocks (Fig. 3.21). Similarly, the biotite schists indicate a mixed felsic-basic source as per the Hf vs La/Th diagram by Floyd and Leveridge (1987) (Fig. 3.22).

In the SiO_2 vs K_2O/Na_2O discrimination diagram by Roser and Korsch (1986), the samples plot in the field for oceanic island arc margin setting (Fig. 3.23). Table 3.2 shows the low abundances of La, Th, Zr and Nb, low ratios of Th/U and La/Sc and high La/Th and Zr/Th ratios for the Basement Complex biotite schists. In the La/Sc vs Ti/Zr and Th vs La diagrams by Bhatia and Crook (1986), the Jebel Kujur biotite schists plot in the oceanic Island arc fields (Fig. 3.24 and 3.25). In La vs Th diagram by Taylor and Mclennan (1985), the biotite schists under study fall in the Archaean field (Fig. 3.26).

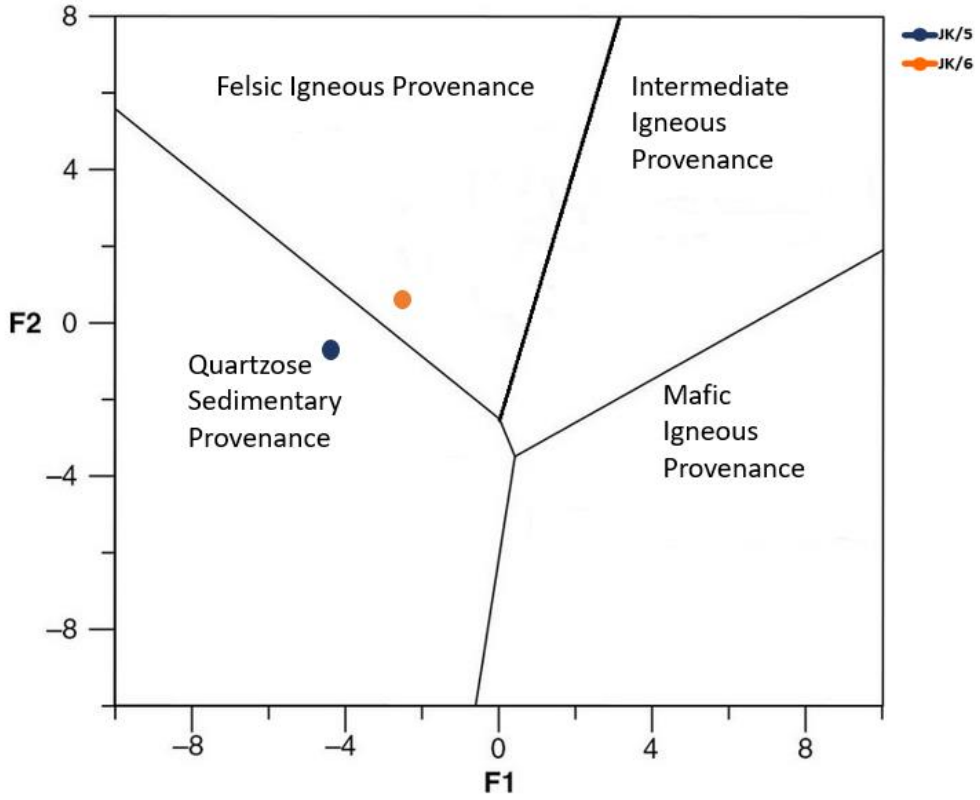


Figure 3.19: Provenance discrimination diagram for the biotite schists (after Roser and Korsch, 1988). Discriminant function 1 (F1) = (-1.773 TiO_2+0.607 Al_2O_3+0.76 Fe_2O3t-1.5 MgO+0.616 CaO+0.509 Na_2O-1.224 K_2O)-9.09; Discriminant function 2 (F2) = (0.445 TiO_2 + 0.07 Al_2O_3-0.25 Fe_2O_3t-1.142 MgO+0.438 CaO+1.475 Na_2O+1.426 K_2O)-6.81.

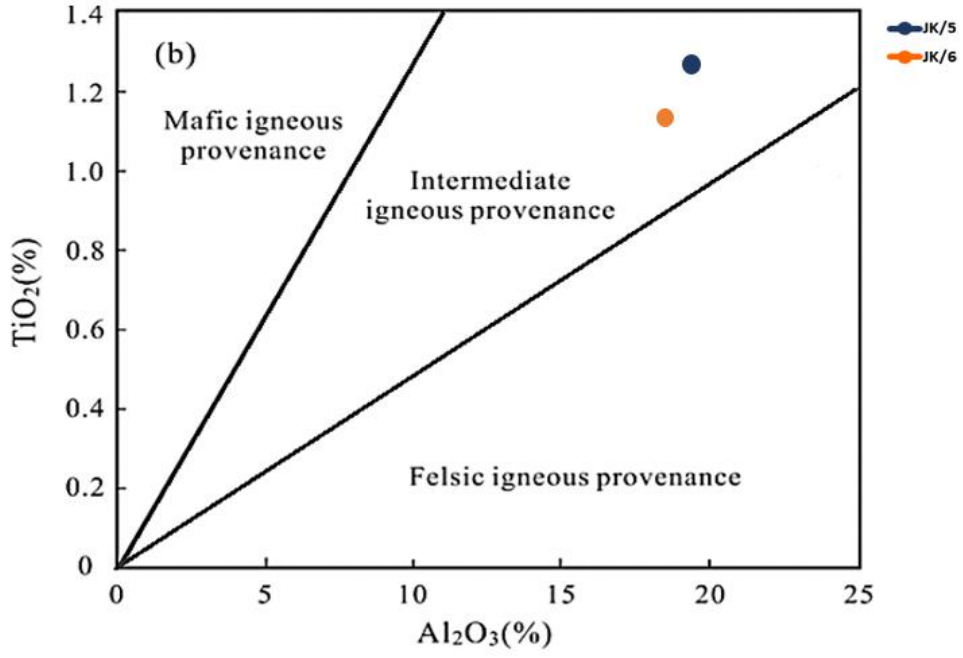


Figure 3.20: Al_20_3 vs TiO_2 diagram for the biotite schists (after Hayashi et al., 1997).

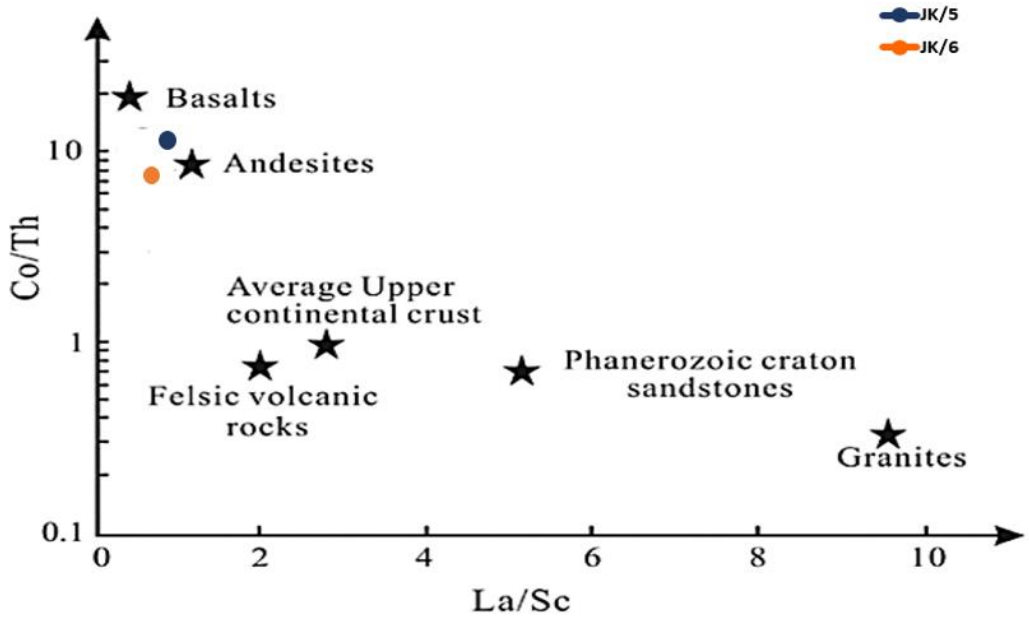


Figure 3.21: La/Sc vs Co/Th diagram for the biotite schists (after Gu et al., 2002).

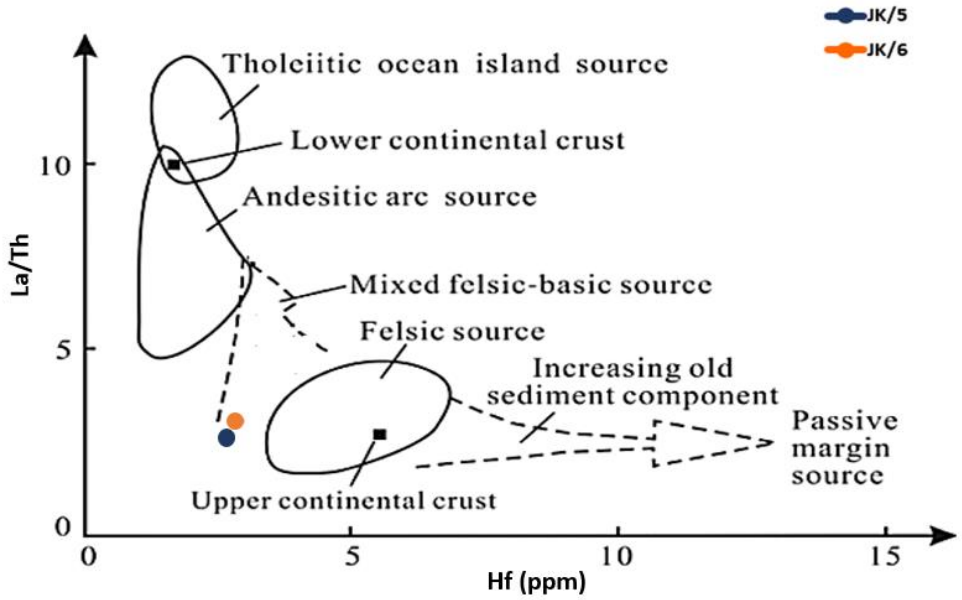


Figure 3.22: Hf vs La/Th diagram for the biotite schists (after Floyd and Leveridge, 1987).

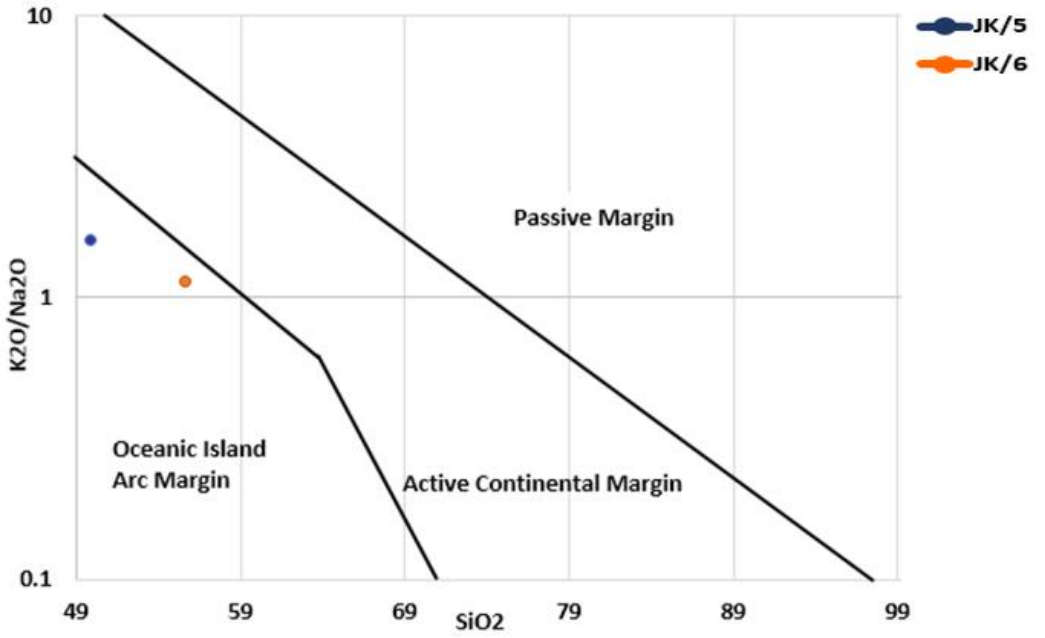


Figure 3.23: SiO_2 vs K_2O/Na_2O tectonic setting discrimination diagram for biotite schists (after Roser and Korsch, 1986).

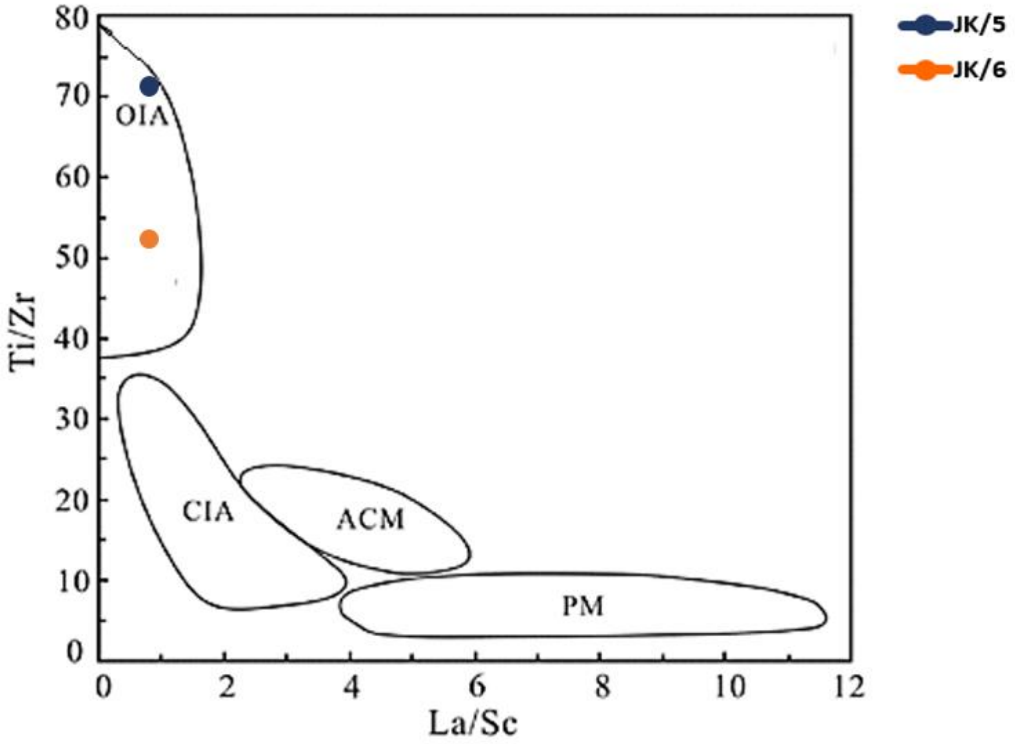


Figure 3.24: La/Sc vs Ti/Zr diagram for the biotite schists, OIA: Oceanic Island Arc, CIA: Continental Island Arc, ACM: Active Continental Margin, PM: Passive Margin (after Bhatia and Crook, 1986).

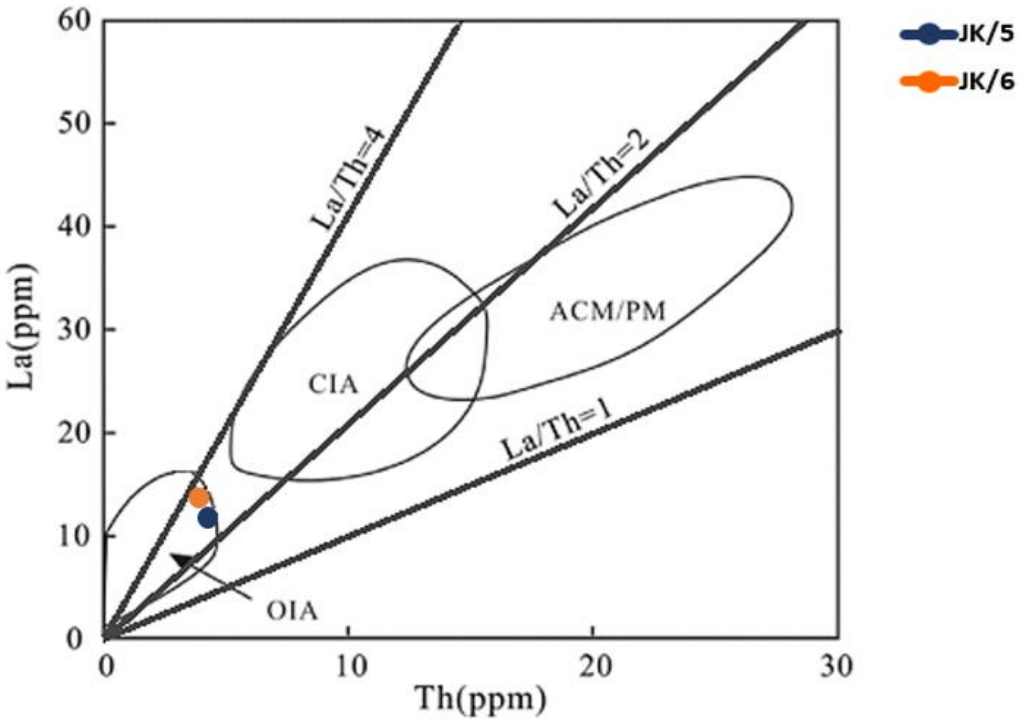


Figure 3.25: Th vs La for the biotite schists (after Bhatia and Crook, 1986)

Table 3.2: Selected trace elements and trace element ratios for samples JK/5 and JK/6

Element (ppm)	JK/5	JK/6
La	11.139	13.04
Th	4.442	4.069
Zr	112.585	119.409
Nb	8.405	8.956
Th/U	4.210427	3.2709
La/Sc	1.335612	1.057841
La/Th	2.507654	3.204719
Zr/Th	25.34557	29.34603

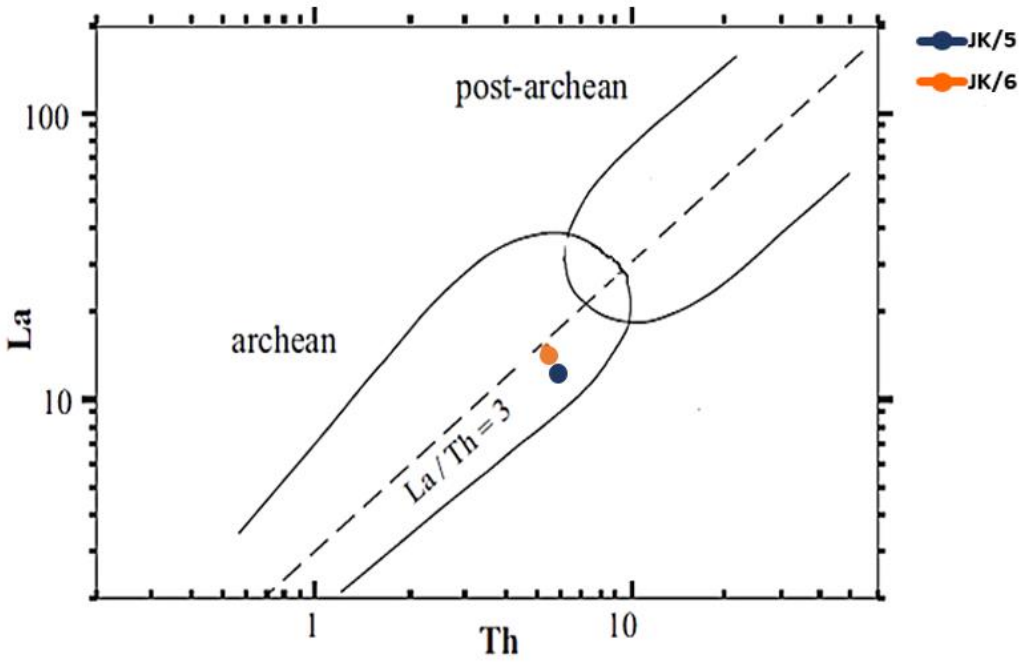


Figure 3.26: Th vs La diagram for biotite schists (after Taylor and McLennan, 1985).

3.4 Discussion

3.4.1 Granitic gneisses

Major elements are very sensitive to weathering, hydrothermal alteration, as well as metamorphic processes and thereof, have very limited application to the understanding of rock petrogenesis. The major element data is therefore used mainly for rock classification and very seldom to determine rock origin. In the same sense, the geochemical classification of granitic rocks is based upon three variables, ie., FeO/(FeO+MgO), which is equivalent to the Fe-number, the alkali-lime index (Na_2O+K_2O-CaO) and the aluminium saturation index (Al/ (Ca-1.67P+Na+K)) (Frost, et al., 2001). The Fe-number is used to distinguish between magnesian and ferroan granitoids, based on the notion that ferroan granitoids will always manifest strong iron enrichment. Magnesian granitoids are further classified into alkalic, alkali-calcic on the basis of the Modified Alkali-Lime Index (MALI) and subdivided based on the Aluinium Saturation Index (ASI) into peralkaline, metaluminous and peraluminous (Shand, 1943).

Granitoids are the most abundant rock types in the continental crust and can stem from differentiation of any hypersthene-normative melt and from partial melting of any other rock type. Granitic melts can also be derived from crustal material, forming from evolved mantle-derived melts or sometimes even a mixture of both crustal and mantle-derived melts. Notably, granitoids are the most challenging rock types to classify and have encouraged a holistic range of classification schemes, based on either tectonic and/or genetic association (Frost et al., 2001).

The granitic gneisses from the Basement Complex in South Sudan show high SiO_2 and very low Fe_2O_3 and MgO contents, implying a felsic source. This implication is further supported by the petrogenetic plot of SiO_2 vs K_2O+Na_2O by Middlemost (1994), wherein all samples plot in the granite field (Fig. 3.3). The gneisses show a consistency in the contents of Na to K, which reflects the abundance of potassium-bearing silicate minerals such as microcline and biotite. Further classification of the rocks indicates that three of the samples belong to the ferroan group, with only one showing magnesian affinity and all are characterised by alkali-calcic composition (Figs. 3.4, 3.5).

Most of the granitic gneisses are ferroan, alkali-calcic and peraluminous (Figs. 3.4-3.6). The excess alumina is probably accommodated in Al-rich biotite and muscovite present in all the samples. As per Frost et al. (1991), ferroan, metaluminous to peraluminous granites with alkali-calcic composition commonly form in intracratonic settings and most likely under anhydrous conditions. The gneisses also show calc-alkaline affinity and may be attributed to their low Fe-Mg bearing silicates (Fig. 3.7) (Elatikpo et al., 2013).

Granites are classified into three main types, namely: I-, S- and A-type granites (Chappel and White, 1992). The A-type granites are markedly different from the I- and S-type groups. The distinction is as a result of the high enrichment of high field strength elements (Zr, Nb, and Y),

high-temperature phases (fayalite and pyroxenes) as well as the occurrence of late crystallizing biotite and hornblende (Whalen, et al., 1987). The granitic gneisses under study are depleted in high field strength elements and lack minerals commonly associated with A-type granites. Additionally, the discrimination diagram based on the calcium content by Chappell and White (1974) indicates that the composition of the sampled granitic gneisses coincides with that assigned for I-type granites (Fig. 3.8). Further discrimination of the granites in this classification scheme, places them in the highly fractionated I- S- and M- type granites field (Fig. 3.9).

There have been three models to date that have been suggested for the generation of highly fractionated I-type granites with metaluminous to peraluminous compositions. The first one proposes partial melting of crustal components (Roberts and Clemens, 1993). The second model suggests mixing of melts from mantle-derived magmas and partial melting of crustal materials (Koteas et al., 2010) and thirdly, advanced fractional crystallization from primary mantle-derived magmas (Li et al., 2009).

The SiO_2 contents of the Basement Complex granitic gneisses are notably greater than 74% and together with the low (negative) εHf (t) values observed in the Hf isotope chapter are antagonistic towards the generation of granites from primarily mantle-derived magmas. These two factors rule out the second and third models. The high potassium, I-type, calc-alkaline nature of the granitic gneisses from the Basement Complex support the first model by Roberts and Clemens (1993), which suggests that granitoids of this nature are generated from the partial melting of hydrous calc-alkaline mafic to intermediate metamorphic rocks in the crust.

An interesting feature observed from the Basement Complex granitic gneisses is that they show a slight difference relative to granitoids that coincide with the first model (Chappel and Stephens, 1988; Roberts and Clemens, 1993; Griffin et al., 2002). The Basement Complex

gneisses show a much stronger peraluminous nature (A/CNK > 1.3), whereas granitoids in the latter references are metaluminous to slightly peraluminous (A/CNK<1.1). This strongly peraluminous nature of granitoids in the Basement Complex gneisses may indicate the presence of sedimentary material in the parental magma, whereby the shift from S to I-type granites classification may be attributed to lesser amounts of the proposed sedimentary material involved in crustal re-melting (Collins and Richards, 2008).

Another model by Ibrahim et al. (2005) proposes that syn-collisional peraluminous granites, common in metamorphosed terrains are most likely generated from partial melting of metapelites. In this model, water that is required for magma generation is obtained by the breaking down of hydrous silicates in the metapelites, including biotite and muscovite. This model can, therefore, contribute to the understanding of the uncommon strongly peraluminous I-type granites. Nonetheless, the best way to explain the petrogenesis of the Basement Complex granitic gneisses is by looking concurrently at the two models by Roberts and Clemens (1993) and Ibrahim et al. (2005).

A combination of the two models along with implications made by the trace and REEs would help discern the petrogenesis of the Basement Complex gneisses. Nonetheless, concerning trace elements patterns, the Basement Complex granitic gneisses generally show enrichment of Rb, Pb, Th and other large lithophile elements when compared to the Primitive Mantle. This is better illustrated in a spider diagram normalized against Primitive Mantle (Fig. 3.10). The spider diagram also shows a depletion of high field strength elements, including; Nb, P, Ta, Ti, etc. The depletion in Nb, P, and Ti is associated with subduction-related granites (Condie, 1998).

The Ba, K, and Pb occur in high concentrations in felsic melts that are derived from the partial melt of alkali-feldspars (Thompson et al., 1983), which coincides with the generation of magma

through partial melting of metapelites or any quartzo-feldspathic rock. The high concentration of Ba in the studied granitic gneisses is also suggested to indicate partial melting, but particularly above subduction zones of volcanic arc tectonics (Welay, 2014). The depletion of transition elements such as V and Cr may indicate a moderate degree of partial melting at a depth of about 80Km (Elatikpo, 2013). The three samples with low Sr contents can be said to have been formed at a shallow depth and by a small degree of partial melting. In addition, the elements, Rb and Sr in a magmatic melt are known to be influenced by the degree of fractionation of phases including biotite, muscovite, alkali and potassic feldspars (Ibrahim et al., 2005). The Rb/Sr ratios for the Basement Complex granitic gneisses ranges between 1 and 4.49. Such low Rb/Sr ratios indicate a very low degree of fractionation and vapour-present melting conditions (Harris et al., 1993).

The REE contents are moderate with patterns characterized by an enrichment of the light REEs, evident in the REE plot (Fig. 3.11). Enrichment in both the LILE and LREEs is associated with volcanic rocks from island arc or active central margin setting (Grove et al., 2003). The granitic gneisses indicate a very distinct negative Eu and slight positive Gd anomalies. The Eu negative anomalies presented by samples JK/3 and JK/4 are, however, much deeper than those observed in the other two samples, which has been suggested a characterizing feature of highly fractionated granites (Pál-Molnár et al., 2005). A further interpretation is that the negative Eu anomalies suggest plagioclase fractionation during magma evolution of the granitic protoliths of the sampled rocks.

Previous workers including Clarke (1992) highlighted limitations and shortcomings that accompany the use of geochemical discrimination methods to decipher petrogenetic and/or tectonic environment. Förster et al. (1997) argue that the connection between different rock types and tectonic environments is not a mere association but more, the possibility of the geochemical characterization of tectonic environments. This may, therefore, be related to the

rock source or evolution process that is specific to a certain environment. Pearce et al. (1984) suggested that the discrimination diagrams used for granites almost only reflect source regions as opposed to tectonic regimes.

Maniar and Picciolli (1989) used the SiO_2 vs K_2O discrimination diagram (Fig. 3.12) as the first step for discrimination of granites. This diagram uses major elements to discriminate oceanic plagiogranite (OP) from other granites and is based on the idea that oceanic plagiogranites have low K_2O content as a result of minor K-feldspar occurrences (Pál-Molnár et al., 2005). The granitic gneisses from the Basement Complex all plot in the orogenic granite field and undoubtedly excludes the oceanic plagiogranites (OP). In the trace element discrimination diagrams by Pearce et al. (1984) and Harris et al. (1986), the results classify the protoliths of the sampled granitic gneisses as volcanic arc and syn-collisional granites (figs 3.13, 3.14 and 3.15). Further discrimination of the samples in the diagram by Muller et al. (1997) suggests continental arc potassic rocks (Fig. 3.16). It would, therefore, be sensible to suggest a syn-collisional (continent-continent collision zone) tectonic environment for the studied rocks, which support the sediment involved magmatism model, as volatiles that are obtained from sediments are required to generate magmatism in this setting.

The geochemical characteristics displayed by the Basement Complex gneisses are summarised as SiO_2 rich, strongly peraluminous, high potassium, calc-alkaline granites with depletion in HFSE, particularly Nb, Ta and Ti. The Ti and Eu negative anomaly, together with the enrichment in LILE and LREE also characterize the studied gneisses. These characteristics together with the combination of the suitable models discussed above can be utilized to suggest a possible mechanism by which the rocks under study formed. It can, therefore, be proposed that the parental magma of the Basement Complex granitic gneisses was generated by the reworking and partial melting of crustal rocks, with a particular but slight involvement of

metapelites in crustal remelting and subsequent fractional crystalization. Moreover, the protoliths of the Basement Complex were emplaced in a syn-collisional setting.

3.4.2 Biotite schists

Samples JK/5 and JK/6 experienced amphibolite facies metamorphism. Their compositions are therefore expected to have been strongly altered by metamorphic overprint and anatexis. Nonetheless, the bulk-rock major geochemistry as indicated above, as well as trace element composition, can still be used to constrain both the nature and provenance of the supposed protoliths (Abu El-Enen, 2011). On the geochemical classification diagram by Herron (1988) (Fig. 3.17), the protoliths of the biotite schists classified in the petrography section as biotite schist and biotite-garnet schist are discriminated as litharenite and sublitharenite respectively. The high alumina content (average of 19.02%) of the meta-arenites is indicative of high clay content. The samples are furthermore enriched in K_2O, Fe_2O_3, and TiO_2, also suggestive of high clay content.

The rock maturity is evaluated using the SiO_2/Al_2O_3 and K_2O/Na_2O ratios. As per Roser and Korsch (1999), these ratios increase with rock maturation, this is due to the concentration of quartz at the expense of less resistant minerals and conversion of feldspar to K-rich clays. The biotite schists under study show SiO_2/Al_2O_3 ratios between 2.5 and 3.0, whereas K_2O/Na_2O ratios are 1.6 and 1.1. The slight increase in the two ratios suggests some variability in the parent rock composition or even the recycling processes (Ghabrial et al., 2013). Furthermore, the moderate to high K_2O/Na_2O ratios suggest a relatively high proportion of secondary post-depositional metamorphic changes and protolith control indicating semi-maturity of samples.

In Table 3.1, Al_2O_3 is shown to increase with decreasing Zr, Hf, and Cs; this can be attributed to the fractionation of heavy minerals such as zircon and sphene, in the early phases of crystallization of the source rocks (McLennan and Taylor, 1985).

During chemical weathering larger cations including Cs, Rb, Ba, etc. remain fixed, whereas smaller cations such as Na, Ca and K are leached out. These smaller cations are therefore used to measure the degree of chemical weathering (Rollinson, 1993). Nesbitt and Young (1982, 1984) and various other workers proposed weathering indices, ie. CIA, CIW and PIA. These indices are used to determine the abundance of mobile elements relative to immobile elements during chemical weathering. According to Nesbitt and Young (1982), the high values of CIA indicate the removal of mobile elements, whereas low values suggest absent to very little chemical weathering (50-60%; low, 60-80%; intermediate, 80-100%; extremely high chemical weathering). The chemical index of alteration (CIA) can be calculated as follows: CIA= $((Al_2O_3/ (Al_2O_3+CaO+Na_2O+K_2O))*100$. The studied biotite schists gave CIA values of 63.34 and 62.01%, an average of 62.68%. These values support the idea that the analyzed samples underwent an intermediate degree of chemical weathering in the source area.

Harnois (1988) proposed a chemical index of weathering (CIW), which can be used to determine the extent of conversion of feldspars to clay minerals. The index is defined as CIW= $((Al_2O_3/ (Al_2O_3+CaO+Na_2O))*100$. The CIW values for Jebel Kujur samples are 75.99 and 73.22, an average of 74.60. This indicates a moderate degree of chemical weathering in the source area. The given CIW values also support a provenance from igneous intermediate crustal sources. In addition, Mclennan and Taylor (1991) proposed that Th/U ratios greater than 4 serve as indicators of chemical weathering of the source rock. The Basement Complex biotite schists under study present Th/U ratios of 4.21 and 3.27 with an average of 3.74, suggesting little to an intermediate degree of chemical weathering in the source rocks.

When compared with the average Upper Continental Crust (UCC), Post-Archaean Australian Average Shale (PAAS) and the Archaean Australian Average Shale (AAS) representative of continentally derived sediments with values from Taylor and McLennan (1985), the biotite schists under study are depleted in SiO_2 and other elements. The observed depletion in Na_2O,

MnO and CaO may either be as a result of quartz dilution or may rather suggest that the sediments underwent extreme weathering and recycling (Jin et al, 2006). Ca and Na are strongly controlled by feldspars, the great depletion in CaO and Na_2O indicates destruction of plagioclase during elemental weathering in the source or during the transportation process of the sediments.

Conformable results are indicated by the empirical discrimination ratio $100TiO_2/Zr$ (wt%/ppm), which is based on the immobile behavior of the transition metal (Ti) and HFSE (Zr) during metamorphism. The ratio of both samples is greater than 0.4 and indicate their derivation is from psammitic material (Abu El-Enen, 2011).

Provenance and tectonic setting

Immobile elements (Ti, Al, and Zr) play a major role in estimating the composition of the source rock. This is explained by the resistance of these elements making them the least mobile and least fractionated during sedimentary and metamorphic processes (Nesbitt and Young, 1982). The studied biotite schists from the Basement Complex present an average Al_2O_3/TiO_2 ratio of 15.37 and SiO_2 content ranging between 49.84 and 55.63 wt%, suggesting derivation from intermediate source rock. The biotite schists, when plotted in the F1-F2 diagram by Roser and Korsch (1986), show both felsic igneous and quartzose sedimentary provenance (Fig. 3.19). Further provenance investigation for the samples, suggest intermediate igneous origin, as indicated in the Al_2O_3 Vs TiO_2 discrimination diagram by Hayashi et al., (1997), wherein, the Jebel Kujur biotite schists plot in the intermediate igneous provenance field (Fig. 3.20). Furthermore, the analyzed samples indicate basaltic and andesitic source rocks, as per the trace element diagram of La/Sc vs Co/Th by Gu et al. (2002) (Fig.3.21). The analyzed samples further display mixed felsic and basic source in the Hf vs La/Th plot after Floyd and Liveridge (1987) (Fig. 3.22).

Bhatia and Crook (1986) proposed that the tectonic settings in which sandstones can be formed include: Oceanic island arcs, continental island arcs, active continental margins, as well as passive margins. Bhatia (1983) noted that the TiO_2, Fe_2O_3*+MgO and Al_2O_3/SiO_2 increase as the tectonic setting changes from passive margin to an active continental margin to a continental island arc to an oceanic island arc. From the study of Bhatia (1983), percentages and ratios of compositions for the different tectonic settings were determined (Table 3.3). The Jebel Kujur biotite schists show a high abundance of TiO_2 and Fe_2O_3*+ MgO and Al_2O_3/SiO_2 ratios. The contents are conformable with sandstones formed in an oceanic island arc setting. Additionally, the SiO_2 vs K_2O/Na_2O tectonic setting discrimination diagram of Roser and Korsch (1986) indicate that the sediment deposition of the protoliths of the rocks under study would have occurred in an oceanic island setting (Fig. 3.23).

The chondrite normalized REE patterns show light REE enrichment compared with heavy REE and generally smooth patterns (Fig. 3.18). These patterns are consistent with those of an oceanic island arc setting. Griffin et al. (2004) and Xiao et al. (2016) and many earlier workers have successfully used immobile trace elements to identify the tectonic settings of clastic sediments. The low abundances of La, Th, Zr, and Nb, low ratios of Th/U and La/Sc as well as high ratios of La/Th and Zr/Th, as indicated in table 4 are characteristic of sedimentary rocks that formed in an oceanic island arc setting (Lang et al., 2019). The Basement Complex biotite schists under study plot in the oceanic island arc field of the La/Sc vs Ti/Zr and Th vs La tectonic discrimination diagrams by Bhatia and Crook (1986) (Figs.3.24, 3.25). In the Th vs La diagram of Taylor and McLennan (1985) (Fig. 3.26), the analysed biotite schists plot in the Archaean field, implying that the protoliths for the biotite schists were derived from a source consisting particularly of typical Archaean material.

Table 3.3: Composition of sandstones formed in different tectonic settings (after Bhatia, 1983)

Tectonic setting	TiO_2 (wt. %)	Fe_2O_3+MgO (wt. %)	Al_2O_3/SiO_2 (ratio)
Passive Margin	0.49	2.89	0.10
Active continental margin	0.46	4.63	0.18
Continental island arc	0.64	6.79	0.20
Oceanic island arc	1.06	11.73	0.29

3.5 Summary and conclusions

The geochemical characteristics of the medium grained granitic gneisses from the Basement Complex are characterized by high SiO_2 and alkali contents, with low CaO, MgO, Fe_2O_3, MnO_2, TiO_2 and P_2O_5. The granitic gneisses also present a high potassium calc-alkaline and peraluminous affinity. There is an enrichment of LILE and depletion of HFSE indicating partial melting in a volcanic arc and syn-collisional setting. The granitic gneisses are categorized as I-type granites with fractionated REE patterns and high concentration of LREEs relative to HREEs. The strongly peraluminous nature of these gniesses is uncommon in I-type granites and is suggested to indicate involvement of sediments in crustal remelting. Discrimination diagrams suggest a volcanic arc tectonic setting and subduction-related origin indicated by negative Nb, Ti and P troughs.

The geochemical data indicate that the precursor of the biotite schists from the Basement Complex had lithic arenite compositions which underwent an intermediate degree of chemical weathering. These lithic arenites were most possibly derived from erosion of intermediate igneous rocks. Sediment deposition would have most likely occurred in an oceanic island arc

setting. These samples further show geochemical behaviour characteristic of Archaean source material.

Chapter 4
Argon-Argon geochronology

4.1 Introduction

Argon-Argon geochronology has been employed in the Basement Complex of South Sudan with the objective of obtaining age constraints on metamorphism in this high-grade terrain. Biotite and muscovite in the studied samples are metamorphic, sufficiently abundant and will serve as good chronometers for understanding the metamorphism in the area. $^{40}Ar/^{39}Ar$ ages obtained from biotite separates reflect the time since cooling below about 300°C, wherein $^{40}Ar/^{39}Ar$ ages from muscovite represent the time at which the rock sample cooled through 350 - 430° C (Huntington et al., 2006). The incorporation of surplus argon gas in muscovite is better than that in biotite and for this reason ages obtained from biotite grains may be inconsistently young (Dodson, 1973). Hence, analysing both mineral phases is imperative for a better interpretation of the ages. The $^{40}Ar/^{39}Ar$ age dating method relies on the assumption that the concentrations of Ar outside of the mineral separate remain close to zero (Konstanze et al, 2017).

4.2 Analytical methods

Two samples, namely JK/3 and JK/6, were defragmented with the Selfrag machine at the Geology Department, University of Pretoria. After sieving the crushed material, <500 µm was taken and washed in water and dried overnight in an oven at about 65 °C. Frantz magnetic separator was then used to separate the minerals. These minerals were then observed under the FZ6-ILST high-resolution stereo zoom microscope to pick biotite and muscovite grains with a desirable size. Eight biotite and muscovite grains from each sample were picked, packaged and sent to the Ar geochronology laboratory at the University of Johannesburg.

Concisely, the biotite and muscovite separates were wrapped in single aluminium foils and vacuum-sealed in a silica glass tube, with standards placed at the top and bottom of the package in the sealed tube. Thereafter, the tube was irradiated at NTP Radioisotopes' SAFARI1 nuclear reactor at Phelindaba, South Africa. The micas were irradiated for 20 hours at Nuclear Energy Corporation of South Africa (NECSA). The Argon isotopes were nonetheless measured in seven cycles. All blank measurements were obtained at four step intervals. The ^{40}Ar decay parameters of Renne et al. (2010) were used.

4.3 Results

The results of $^{40}Ar/^{39}Ar$ step-heating experiments and inverse isochron calculations are presented in Tables 1C-3C (Appendix C) and plotted as ^{39}Ar released vs apparent age (Ma) spectrum (Figs. 4.1, 4.2 and 4.3). The biotite grains extracted from muscovite-biotite gneiss (sample JK/3) yielded a disturbed age spectrum ("staircase" shape) with a plateau age of 445 ± 2 Ma (Fig. 4.1). Data from one muscovite grain also from sample JK/3 produced a uniform and undisturbed release spectrum and a weighted age of 555 ± 3 Ma (Fig. 4.2). Furthermore, biotite grains from the biotite-garnet schist (sample JK/6) yielded a moderately disturbed and a weighted age of 548 ± 3Ma (Fig. 4.3).

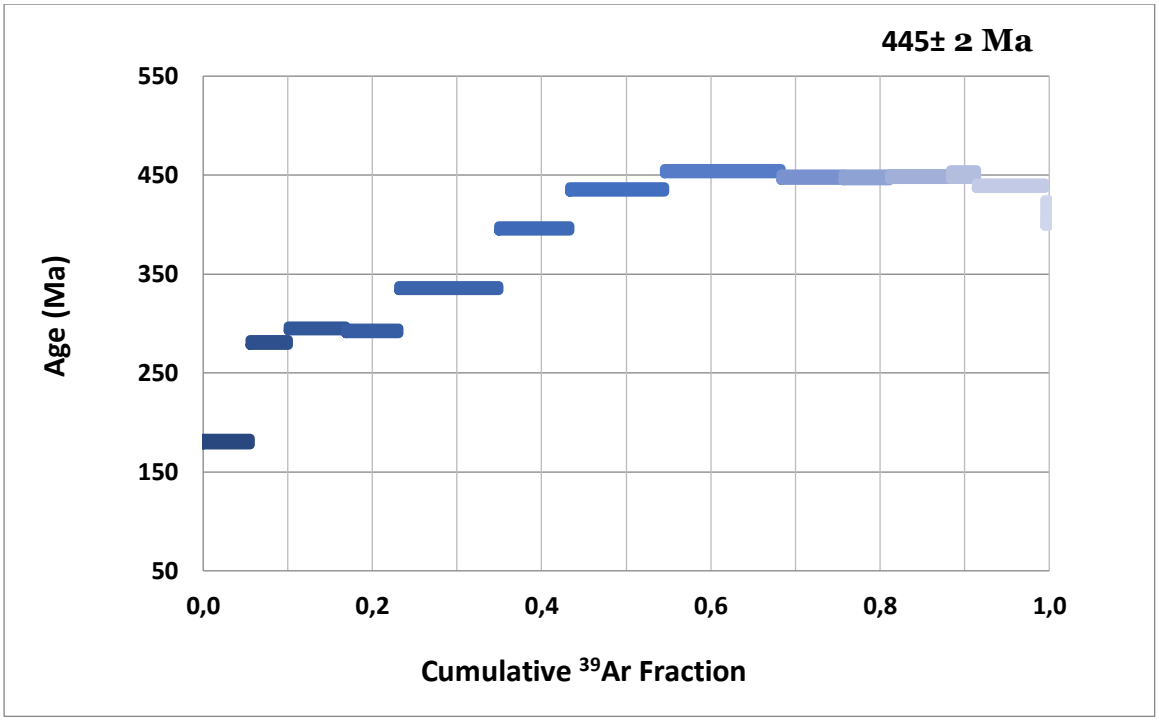


Figure 4.1: $^{40}Ar/^{39}Ar$ age spectra of biotite extracted from muscovite-biotite gneiss (sample JK/3). Data is plotted as age vs accumulative percentage of ^{39}Ar released. A weighted average of the age, including 56 % of the ^{39}Ar, is indicated in the top right corner. Errors are 1 sigma.

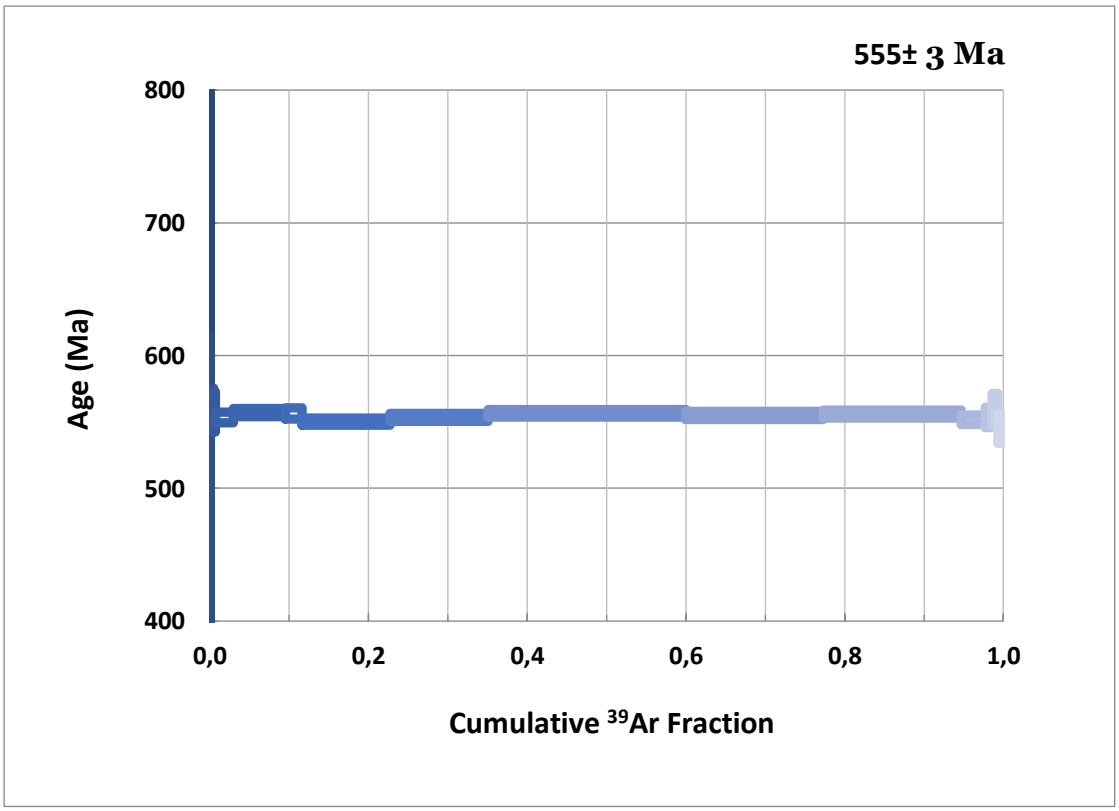


Figure 4.2: $^{40}Ar/^{39}Ar$ age spectra of muscovite extracted from muscovite-biotite gneiss (JK/3). Data is plotted as age vs accumulative percentage of ^{39}Ar released. A weighted average of the age, including 99.3% of the ^{39}Ar is, indicated in the top right corner. Errors are 1 sigma.

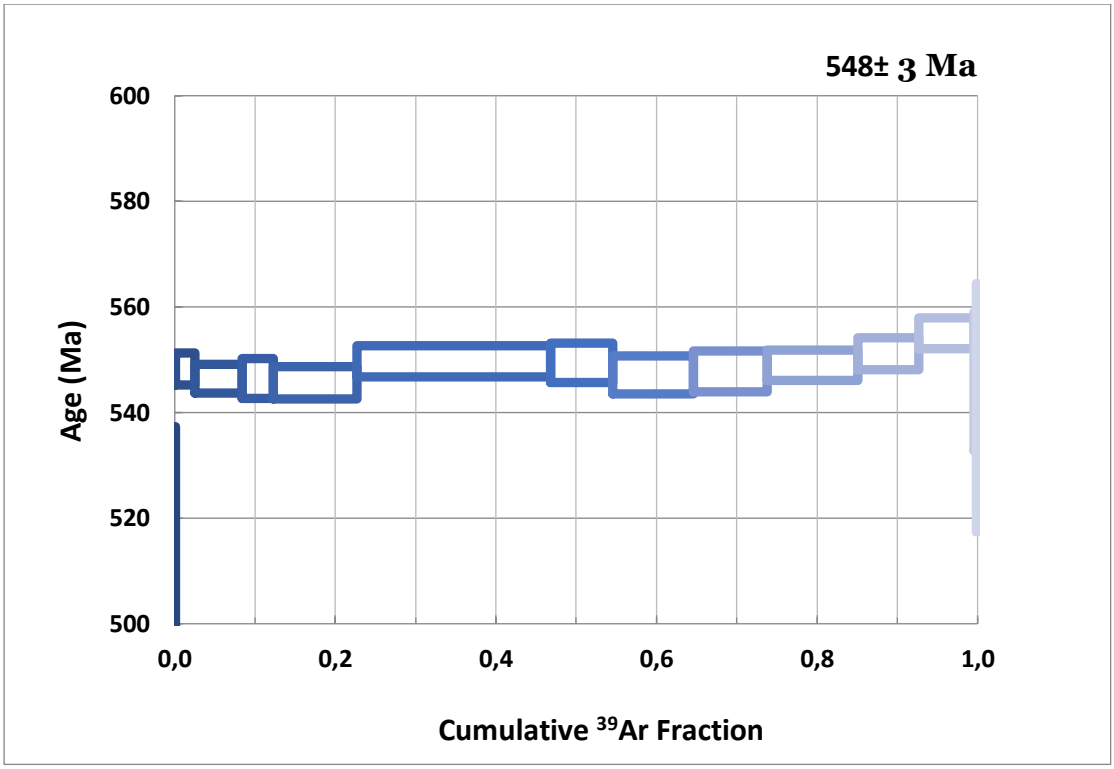


Figure 4.3: $^{40}Ar/^{39}Ar$ age spectra of biotite extracted from biotite-garnet schist (JK/6). Data is plotted as age vs accumulative percentage of ^{39}Ar released. A weighted average of the age, including 99.5 % of the ^{39}Ar, is indicated in the top right corner. Errors are 1 sigma.

4.4 Discussion

Biotite and muscovite grains from the same sample (sample JK/3) have yielded varying $^{40}Ar/^{39}Ar$ age spectra and weighted mean ages (Figs. 4.1 and 4.2). This may be attributed to the fact that muscovite retains argon at higher temperatures than biotite, resulting in biotite with younger ages than those obtained from muscovite of the same sample (Hart, 1964; Huntington et al., 2006). Dallmeyer (1978) explains that minerals that require excessively high temperatures for the process of argon retention will tend to close first relative to the interrupted diffusive loss of radiogenic argon during metamorphic cooling resulting in older ages.

The disturbed or "staircase" shaped age spectra produced by biotite from sample JK/3 can be attributed to either (1) excess ^{40}Ar in the biotite mineral or fluid inclusions (Bachmann et al., 2010), (2) ^{39}Ar recoil effects during irradiation process (Smith et al., 2008), (3) Argon inherited from older pre-existing biotites (Vavassis et al., 2000). As per Dahl (1996), biotite crystals

readily incorporate excess ^{40}Ar and its effectiveness to cause a disturbed age spectrum has been recognized in many studies (Dahl, 1996; Bachmann et al., 2010). Baksi (2003) suggested that $^{40}Ar/^{36}Ar$ values obtained from inverse isochron intercepts can be used to detect the effect of excess ^{40}Ar in a sampled mineral grain. $^{40}Ar/^{36}Ar$ values greater than the atmospheric argon (295.5) can be said to have excess ^{40}Ar, whereas $^{40}Ar/^{36}Ar$ values less than 295 indicate disturbed samples and the resultant age cannot hold any geological significance. Biotite from sample JK/3 shows $^{40}Ar/^{36}Ar$ intercept of -2887.59 ± 997 (Table 1C, Appendix C). This value is far less than that of the atmospheric argon and disputes the presence of excess argon. As per Baksi (2003), the 445 ± 2 Ma obtained from such a disturbed mineral cannot hold any geological significance.

Recoil effect during irradiation is common in $^{40}Ar/^{39}Ar$ dating. This problem mainly arises in small biotite crystals (Paine et al., 2006). Large biotite grains (≥220 μm) from sample JK/3 were analysed and for this reason, the disturbed Ar age spectra may not so much be attributed to the recoil effect. However, the effect of inherited Ar from older crystals is shown through a staircase pattern indicating ages that get older during later heating steps (Fig. 4.1). Inherited Ar is often incorporated in the most retentive areas of the crystal, which during analysis will result in Ar release spectra with ages that get older with later heaing steps (Bachmann et al., 2007).

Samples without excess ^{40}Ar will yield $^{40}Ar/^{36}Ar$ intercept values that overlap with the atmospheric argon i.e. $^{40}Ar/^{36}Ar$ = 295.5 (Kuiper, 2002). Inverse isochron calculations for muscovite from Sample JK/3 shows $^{40}Ar/^{36}Ar$ intercept of 296.6 ± 10 (Table 3C, Appendix C). This value overlaps with the atmospheric argon and suggests that there is no excess Ar in the analysed muscovite mineral. The 555 ± 3 Ma age from muscovite (sample JK/3) should therefore be considered reliable. Petrographical features show that the analysed muscovite is a product of retrograde metamorphism; hence, the 555 ± 3 Ma age is interpreted as the cooling age following the amphibolite-facies retrogradation (refer to the petrography and mineralogy

chapter). Inverse isochron calculations for biotite separates (sample JK/6) present a $^{40}Ar/^{36}Ar$ intercept of 1452.4 ± 9883, which is far greater than the atmospheric argon and therefore implies the presence of excess argon (Table 3C, Appendix C). This suggests that the 548 ± 3 Ma age obtained from the biotite (sample JK/3) may be flawed.

The only reliable $^{40}Ar/^{39}Ar$ age from this data is the 555 ± 3 Ma yielded by muscovite (sample JK/3), whereas all the analysed biotites produced flawed ages. The inability of biotite to produce usable and meaningful age spectra is common (Vavassis et al., 2000; McDougall and Harrison, 1999) and is atttributed the instability of biotite during heating in vacuo (McDougall and Harrison, 1999). This instability occurs as the radiogenic-Ar diffusion gradients are destroyed by the in-vacuo heating process at all steps with a temperature lower than 600°C (Hua Lo et al., 2000).

Civetta et al. (1980) used the K-Ar method to decipher ages of different material from Southern Sudan. In this study an age of 559 ± 18 Ma is reported for a gneiss sample from an area south-east of the study area of this current work. Civetta et al. (1980) suggested that this age (559 ± 18 Ma) reflects the Pan-African tectonothermal event. Similar ages have been obtained for material collected from in and around the present study area. Snelling (1964) used the K-Ar dating method to determine ages of younger rocks from the Basement Complex of northern Uganda and attained apparent ages that clustered around 555 ± 100 Ma. Almond (1980) accepted and associated these ages with the the Pan-African orogenic event.

4.5 Summary and conclusions

Biotite from sample JK/3, muscovite-biotite gneiss yielded a disturbed age spectrum ("staircase" shape) with a plateau age of 445 ± 2 Ma. The inverse isochron calculations of the sample shows $^{36}Ar/^{40}Ar$ intercept value far less than the value of the atmospheric argon, albeit with large errors and as a result, the age yielded by this sample is regarded errounous. The

disturbed age spectra and high $^{40}Ar/^{36}Ar$ value obtained from biotite (sample JK/6) suggests that the biotite contains excess Ar and its plateau age (548 ± 3 Ma) is considered flawed. The only $^{40}Ar/^{39}Ar$ age regarded reliable from this study, is the 555 ± 3 Ma obtained from muscovite (sample JK/3), which yielded a flat and undisturbed age spectrum and $^{40}Ar/^{36}Ar$ value that overlaps with that of the atmospheric argon. The 555 ± 3 Ma age is interpretted as the cooling age following the amphibolite-facies retrogradation and is coeval to an age of metamorphism reflected in gneisses from an area south-east of the current study area.

Chapter 5
Zircon U-Pb geochronology

5.1 Introduction

The U-Pb dating of zircon using the laser ablation-inductively coupled plasma mass spectrometry (LA-ICPMS) technique has undergone substantial improvements making it the most preferred, particularly for detrital work. LA-ICPMS offers rapid data acquisition at a much lower cost. This method is ideal for deciphering the distribution of crustal age provinces, specifically the tectonothermal history of the high-grade basement rocks of South Sudan. The South Sudanese Basement Complex has been assigned Archaean and Palaeoproterozoic ages, even though no Pre-Neoproterozoic crust has ever been reported. This chapter provides the first U-Pb zircon data from Jebel Kujur, an area within the Basement Complex. Cathodoluminescence (CL) images are used along with the U-Pb ages to make informed interpretations regarding crystallization, metamorphic and maximum depositional ages for the selected samples.

5.2 Analytical methods

All six samples collected from the study area were processed for U-Pb dating. Zircon grains were handpicked from heavy mineral separates of crushed, milled and panned biotite schists and granitic gneisses. Thereafter, the grains were set in circular epoxy mounts and polished to expose their cores. Subsequently, the zircon grains were scanned and imaged using a CAMECA SX5-FE electron probe micro-analyser (EPMA) equipped with both cathodoluminescence (CL) and backscattered electron (BSE) detectors at the Microscopy and microanalysis unit (MMU) at the Biological Sciences Department of the University of the Witwatersrand (Wits). The CL and BSE images provided information on the internal structures

of the magmatic, metamorphic and detrital grains. The CL images were further used to locate potential target sites for U-Pb dating.

Zircon U-Pb isotopic analysis was done using the laser ablation multi-collector inductively coupled plasma source mass spectrometer (LA-MC-ICPMS) housed in the Geology Department at the University of Johannesburg. More zircons were later analysed by LA-single collector ICPMS at the Earthlab, University of the Witwatersrand. The laser-ablation system used at the University of Johannesburg is an ASI Resolution SE155, equipped with a 193 nm ArF excimer laser. All analyses were performed on the Nu Plasma II MC-ICPMS (Nu Instruments, Wrexham) with 16 Faraday detectors and 5 ion counting detectors. The spot size of laser ablation was 30 µm, with a repetition rate of 2 Hz and 4 mJ beam energy. Primary standards (zircons OGC1 and A382) were used to correct for instrumental mass bias and depth-dependent elemental fractionation. Secondary standard (zircon CDQGNG) was used to evaluate accuracy.

The laser-ablation system used at the Earthlab, University of the Witwatersrand, is also an ASI Resolution SE155, equipped with 193 nm ArF excimer laser. The laser was fired at 2-2.5 J/cm^2, frequency of 10 Hz and beam diameter of 30 µm. An acquisition measures a blank for 25 seconds, followed by U-Pb signal from ablated zircon spots for 20 seconds. Zircon GJ1 was used as primary standard, whereas Temora-2, Plesovice and 91500 were used as secondary standard zircons. NuAge2 program (Andersen, 2002) was used to calculate corrected ratios and ages. More details regarding instrumentation, conditions and settings, see Appendix D (Table 1D).

5.3 Results

The results of the U-Pb analyses of detrital, magmatic and inherited zircon grains extracted from the granitic gneisses and the schists are listed in Tables 2D-6D (Appendix D) and graphically displayed in various geochronological diagrams (Figs. 5.2, 5.3, 5.5, 5.7 and 5.9). Cathodoluminescence (CL) imaging presents information on the internal features of the zircon grains (Figs. 5.1, 5.4, 5.6 and 5.8).

Biotite-hornblende gneiss, sample JK/1

Zircons extracted from biotite-hornblende gneiss (sample JK/1) are generally large and display a yellow to amber colour. The grains are mostly ovoid in shape, a few others with stubby shapes were also observed. CL images reveal complex internal textures. Ghost zoning is shown in most grains and this feature makes it challenging to differentiate between the rims and the cores (Fig. 5.1). The grains show a general trend of four domains made up of a core and three growth rims (R1, R2 and R3). R1 is observed in most grains as a thick band with a high CL response. R2 is homogneous with a low CL response and shows variable thickness. R3 is also homogneous with a medium CL response and posseses a discontinuous nature. The core is heterogeneous with tiny inclusions and material from R1 that is cross cutting the core. In most grains, the R1 material in the core is widely spread; such cores are classified as C1, whereas cores with none or little R1 material are classified as C2. R2 and R3 were too thin to be analysed, therefore the data contains analysis of R1 and C2. R1 and C2 contain Th/U ratios in the ranges: 0.28 ± 0.014 to 7.80 ± 0.35 and 0.06 ± 0.043 to 0.11 ± 0.64, respectively. Seventy-eight analyses were carried out on sixty-two grains targeting distinct domains within the grains, particularly R1 and C2. Plotted in a Tera-Wasserburg diagram, the data defines a discordia line with an upper intercept at 943 ± 47 Ma and a lower intercept at 464 ± 49 Ma, MSWD= 5.7 (Fig. 5.2).

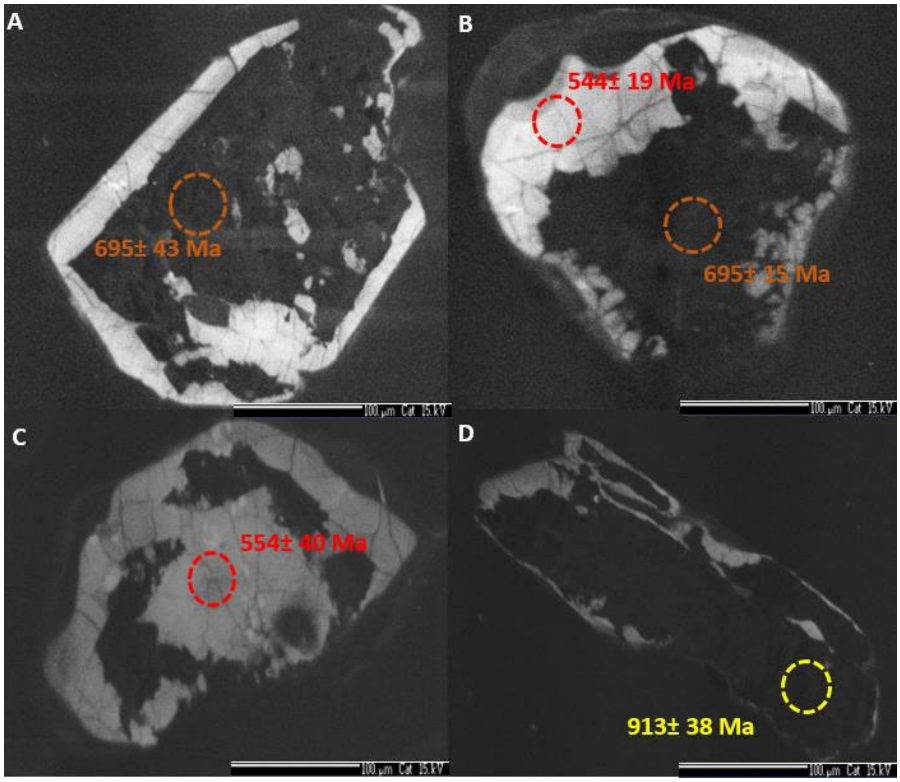


Figure 5.1: Representative CL images of zircons from sample JK/1, biotite-hornblende gneiss from Jebel Kujur. Zircon 207Pb/206Pb ages (Ma) are indicated. Brown, purple and yellow circles show the analysed spot. Colour coding used to highlight similar age groups.

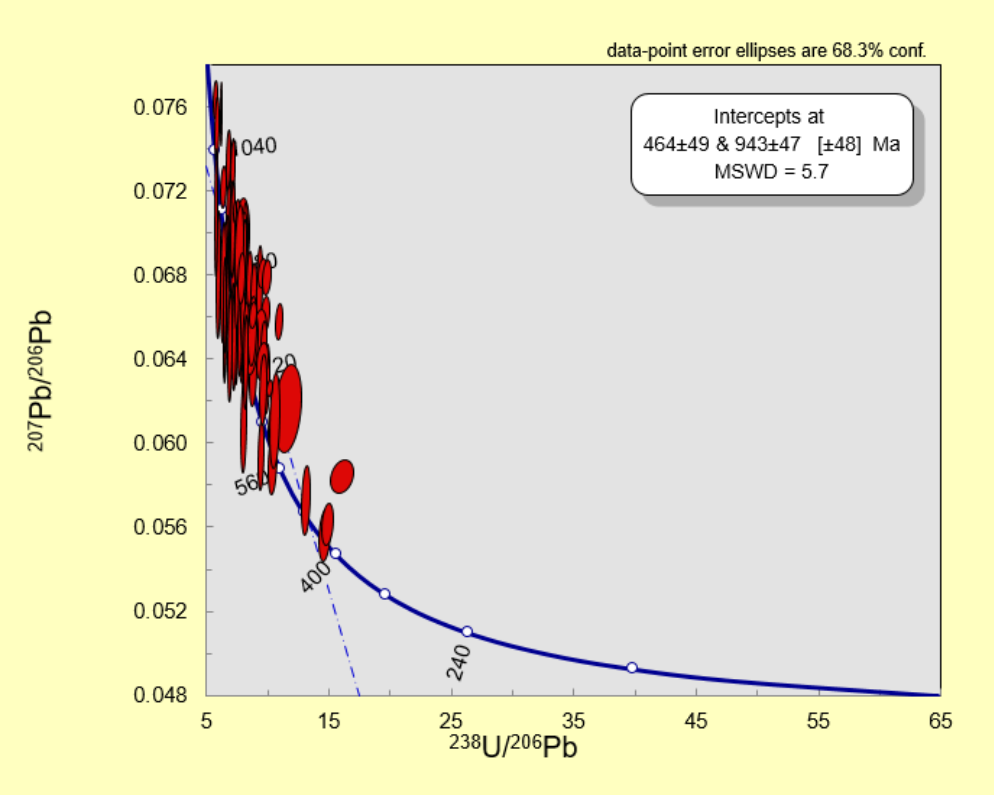


Figure 5.2: Zircon data of biotite-hornblende gneiss (sample JK/1) presented in a Tera-Wasserburg diagram, data points define a discordia line with lower intercepts at 464 ± 49 Ma and upper intercept at 943 ± 47 Ma, MSWD= 5.7.

Muscovite-hornblende gneiss, sample JK/2

Zircons from muscovite-hornblende gneiss (sample JK/2) are very small with an elongated and prismatic shape. There are also grains with slightly rounded edges. The grains are further characterised by their yellow to bronze colour. CL images revealed simple internal structures for these grains. The internal structure is made up of a homogenous core (C1) (low CL response) with faint oscillatory zoning and two homogneous rims (R1 and R2). R1 is characterized by a high CL response and thick nature. R1 is cross-cutting and in some cases overprinting C1. R2 is very thin with a very low CL response. Analyses were done on C1 and R1; R2 was too thin for analyses. The results are shown on a Wetherill Concordia diagram together with a CL image of a typical zircon grain and position of the analysed spot (Fig. 5.3). One concordant data point (core) yielded a concordia age of 981 ± 12 Ma (MSWD=1.9). A weighted mean age of 487 ± 27 Ma was obtained for the rims.

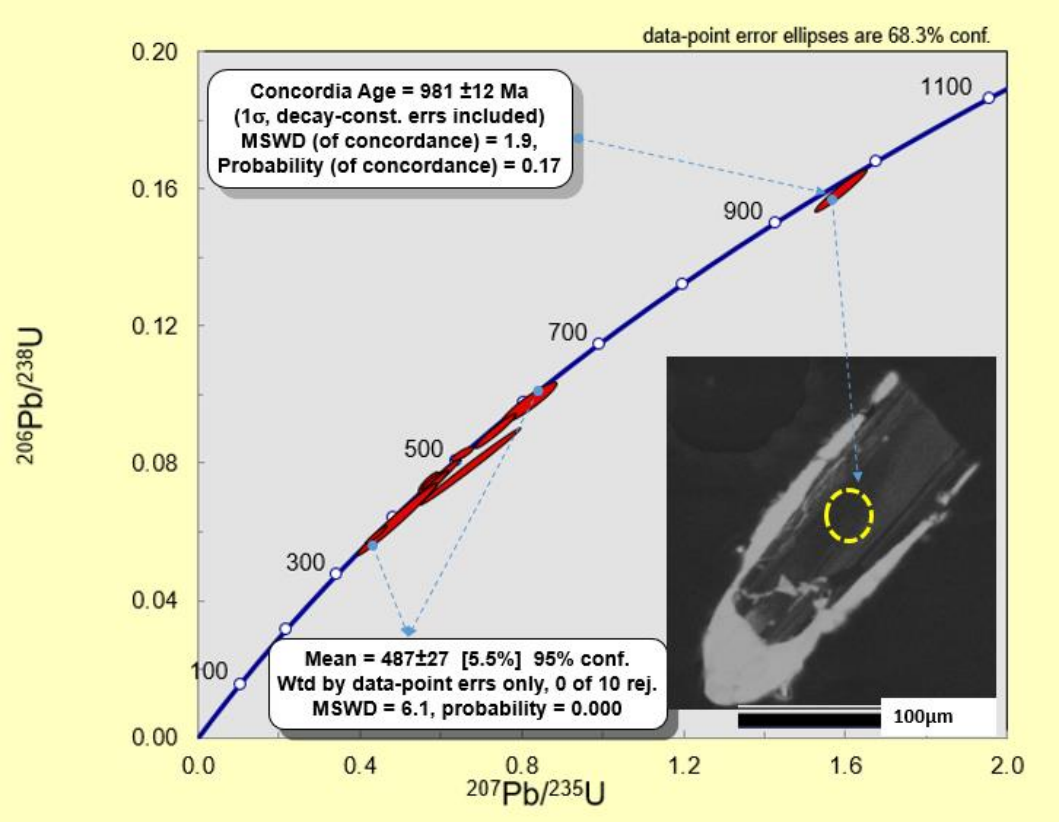


Figure 5.3: Zircon data of muscovite-hornblende gneiss (sample JK/2) from Jebel Kujur presented on a Concordia diagram, inset with a CL image of typical zircon grains.

Muscovite-biotite gneiss, sample JK/3

Muscovite-biotite gneiss (sample JK/3) has proven to be poor in zircon phases and as a result only one zircon grain was obtained from this sample. The analysed zircon is small and rounded with a complex internal structure made up of a large featureless CL bright making up the "core" and in turn surrounded by a very thin CL dark ("rim"). This concordant zircon yielded $^{206}Pb/^{238}U$ age of 924 ± 26 Ma, measured from the core. The rim was too thin to be analysed.

Biotite-muscovite gneiss, sample JK/4

Biotite-muscovite gneiss (sample JK/4) yielded very few zircon grains. Approximately twelve zircon grains were extracted of which seven could be analysed. The remaining grains were discarded due to very poor CL response. Zircons are characterised by a very large size (120-220 µm), elongated and irregular shapes and are yellow to bronze in colour. CL imaging

indicate simple zoning signified by a grey core (C) with faint oscillatory zoning and a dark and thick rim (R), a few grains show a bright middle rim (R1) (Fig. 5.4). Analyses were done on C and R and due to its small size, the middle rim (R1) was not analysed. Th/U ratios for the cores (C) range between 0.71-0.85, whereas Th/U ratios of 0.010-0.014 characterize the rims (R). Six data points indicate two age populations (Fig. 5.5B). A weighted mean age of 933 ± 20 Ma was obtained for the cores and 633 ± 17 Ma weighted mean age for the rims (Fig. 5.5A).

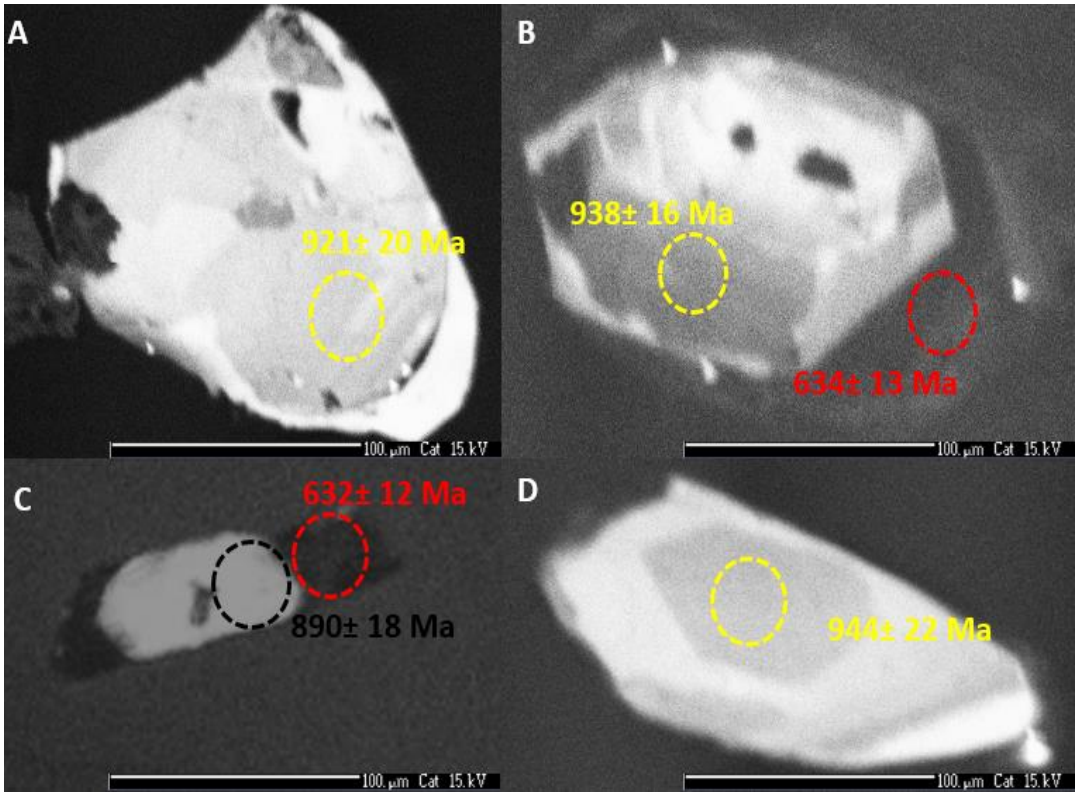


Figure 5.4: Representative CL images of zircons from sample JK/4, biotite-muscovite gneiss from Jebel Kujur. Zircon $^{206}Pb/^{238}U$ ages (Ma) are indicated. Red, black and yellow circles show the analysed spots. Colour coding used to highlight similar age groups.

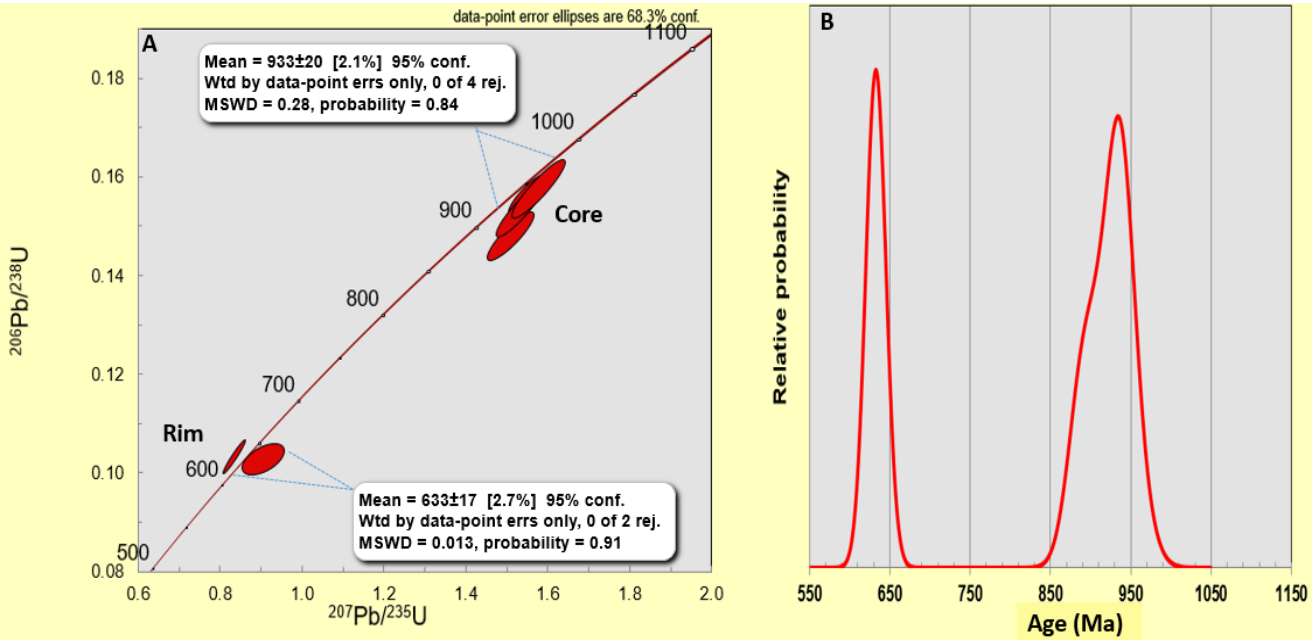


Figure 5.5: Zircon data of biotite-muscovite gneiss (sample JK/4) from Jebel Kujur presented on a Concordia diagram indicating two recognizable phases (A), inset with weighted mean ages for the rim and core analysis. Relative probability plot indicating two distinct populations based on $^{206}Pb/^{238}U$ ages (Ma) (B).

Biotite Schist, sample JK/5

Zircons separated from biotite schist (sample JK/5) vary in size from 55 to 250µm. Most of the zircons are colourless; some display a faint yellow colour. The CL images reveal oscillatory-zoned core and overgrowth rims of variable dimensions (Fig.5.6A-D). Seventy analyses were performed on fifty-six zircon grains. Most of the spots are discordant, with fifty-three spots showing <20% discordance (Fig. 5.7A). The ages with <20% discordance vary from 2837 ± 5 Ma ($^{207}Pb/^{206}Pb$ age) to 910 ± 10 Ma ($^{206}Pb/^{238}U$ age). Their Th/ U ratios are in the range of 0.01-9.4. The density probability and concordia diagrams indicate two youngest zircons with a weighted mean age of 920 ± 17 Ma, MSWD= 3.6 and two age clusters (Fig. 5.7A-B). Concordant (< 20% discordance) ages obtained from the cores are distributed from early Archaean to late Palaeoproterozoic (2876 ± 22 Ma to 2414 ± 7 Ma) with a few mid-Palaeoproterozoic grains (2346 ± 50 Ma to 2187 ± 55 Ma). Ages of rims and mantles with <20 % discordance vary from 1070 ± 18 Ma ($^{207}Pb/^{206}Pb$ age) to 910 ± 10 Ma ($^{206}Pb/^{238}U$ age). Th/U ratios of the older Archaean grains (> 2601 ± 6 Ma) display a range of 0.513-0.993. The

Th/U ratios of the mid-Palaeoproterozoic and late Neoproterozoic spots fall within the ranges of 0.21-9.4 and 0.29-0.64, respectively.

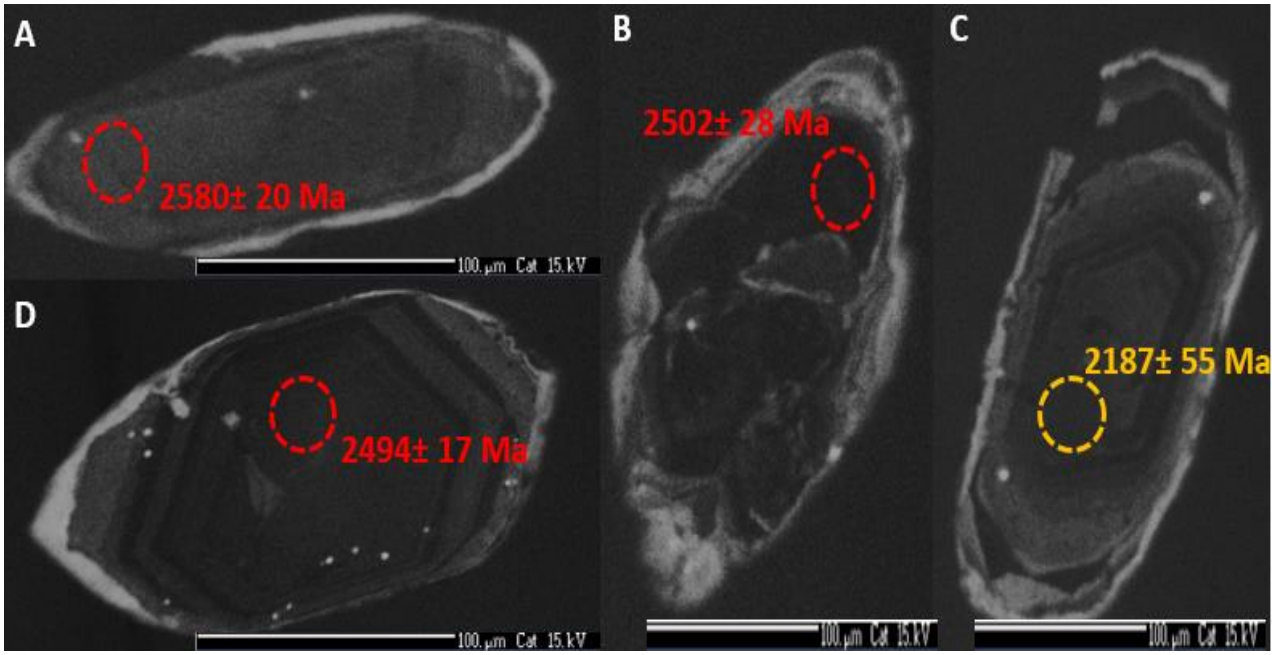


Figure 5.6: Representative CL images of zircons from sample JK/5, biotite schist. Zircon $^{207}Pb/^{206}Pb$ ages (Ma) are indicated by red and yellow circles. Colour coding highlights similar age groups.

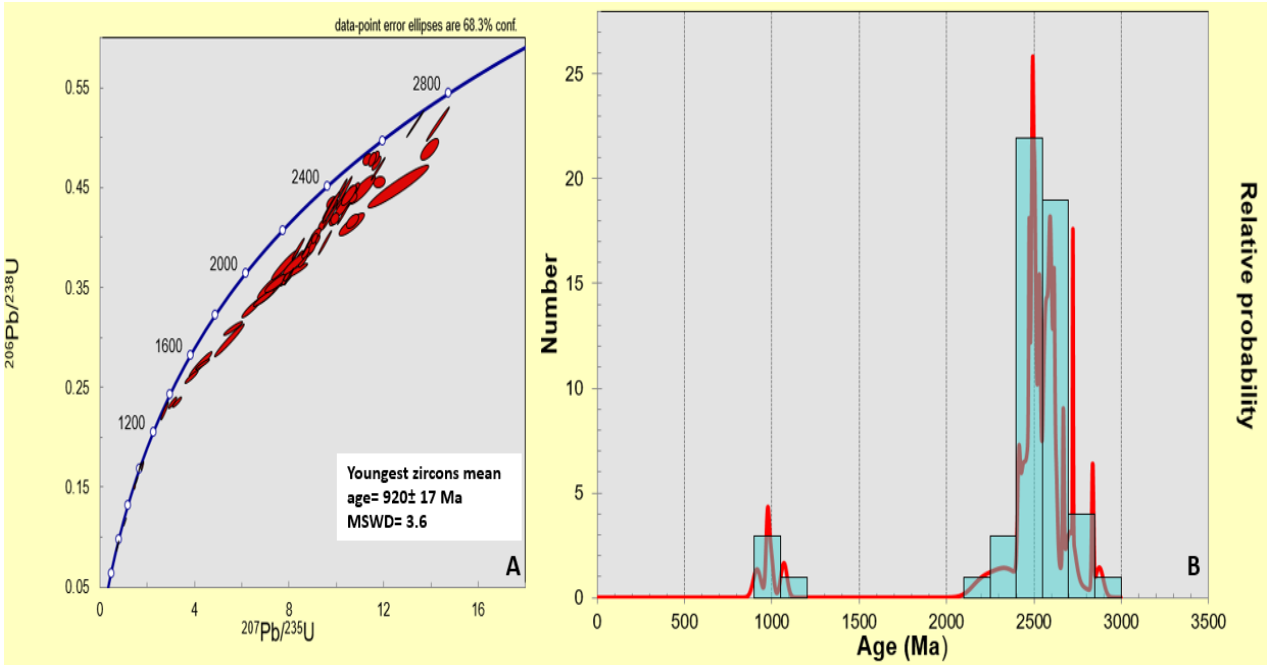


Figure 5.7: Zircon data of biotite schist (sample JK/5) presented on a Concordia diagram (wetherill), inset with weighted mean age of the two youngest concordant zircon grains (A), relative probability for $^{207}Pb/^{206}Pb$ (> 1000 Ma) and $^{206}Pb/^{238}U$ ages (< 1000 Ma) (B). Relative probability plot shows only concordant data (< 20% discordance).

Biotite-garnet schist, JK/6

Sample JK/6 yields zircons with varying sizes (50-210 μm) and prismatic shapes. A few grains appear to be rounded and almost all are translucent. CL images indicate that most of the grains are euhedral and contain oscillatory zoned cores surrounded by overgrowth rims of variable widths (Fig.5.8). In a few cases, the cores are xenocrystic, characterized by high luminescence and corroded core boundary. Fifty-seven analyses were performed on fifty zircon grains. Most of the spots are discordant, with forty spots showing <20% discordance (Fig. 5.12A). Ages with <20% discordance vary from 2755 ± 8 Ma ($^{207}Pb/^{206}Pb$ age) to 947 ± 19 Ma ($^{206}Pb/^{238}U$ age) (Fig. 5.9A). Th/U ratios of the spots display a range of 0.01-3.4. The relative density probability diagram ($^{207}Pb/^{206}Pb$ ages for ages > 1000 Ma and $^{206}Pb/^{238}U$ ages for ages < 1000 Ma) indicate that the zircons fall into two age clusters (Fig.5.9B). The cores show Neoarchaean to late Palaeoproterozoic ages (2755 ± 8 Ma to 2353 ± 7 Ma) and Th/U ratios ranging between 0.01 and 3.4, whereas rims show early Neoproterozoic ages (947 ± 19 Ma to 967 ± 15 Ma) and Th/U ratios of 0.05-0.29. The three youngest zircon ages yield a weighted mean age of 959 ± 11 Ma, MSWD=2.3.

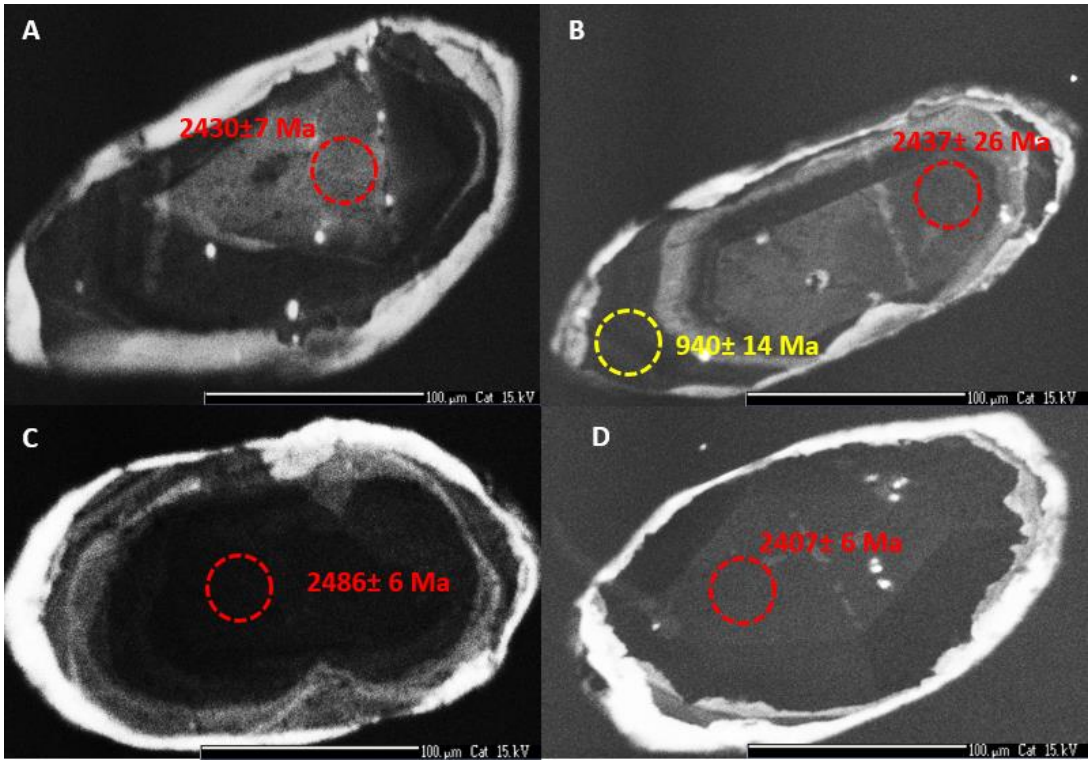


Figure 5.8: Representative CL images of zircons from sample JK/6, biotite-garnet schist. Zircon $^{207}Pb/^{206}Pb$ ages (>1000 Ma) and $^{206}Pb/^{238}U$ ages (<1000 Ma) are indicated. Red and yellow circles show the analysed spots. Colour coding is used to highlight similar age groups.

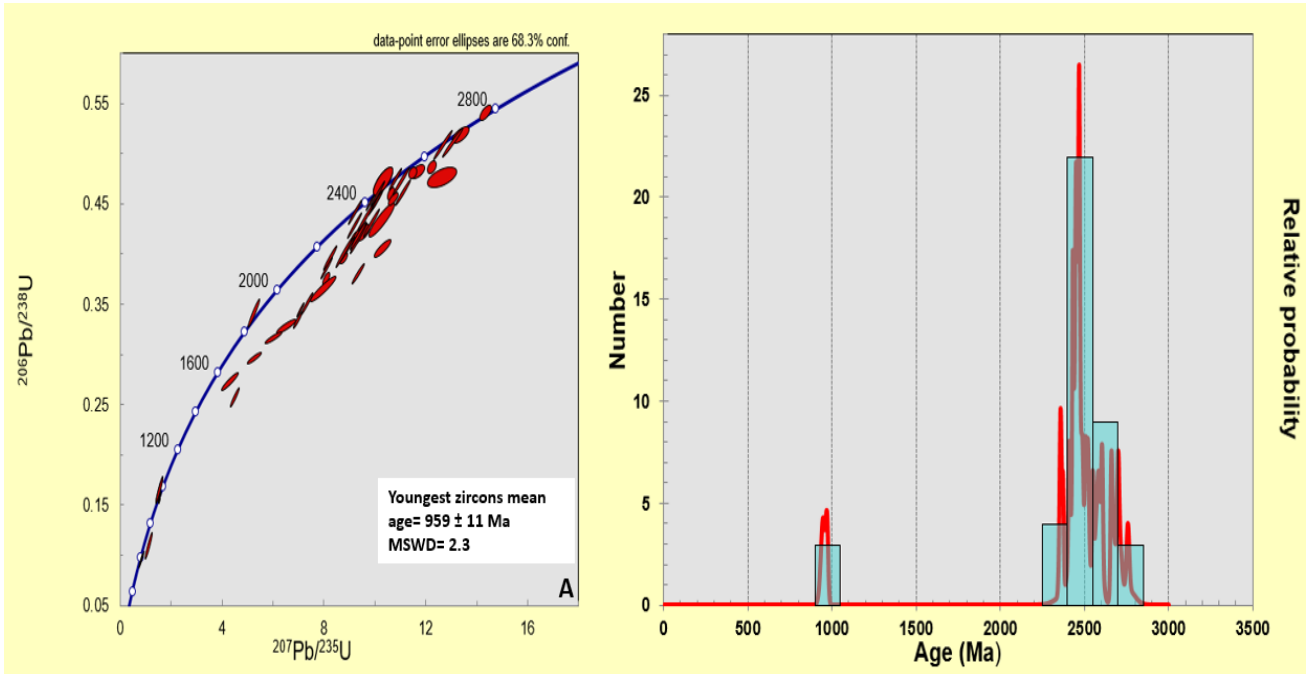


Figure 5.9: Zircon data of biotite-garnet schist (sample JK/6) presented on a concordia diagram (wetherill), inset with weighted mean age of the two youngest concordant zircon grains (A), relative probability for $^{207}Pb/^{206}Pb$ (> 1000 Ma) and $^{206}Pb/^{238}U$ ages (< 1000 Ma) (B). Relative probability plot shows only concordant data (< 20% discordance).

5.4 Discussion

The complex CL patterns and discordant age results shown by zircons in the biotite-hornblende gneiss (sample JK/1) can be attributed to either Pb-loss or recrystallization during a pervasive high-grade metamorphic event (Corfu, 2013) (Figs. 5.3-5.4.). The Th/U ratios of greater than 0.1 obtained from zircon rims (typical of magmatic zircons) negate the effect of recrystallization due to metamorphism. The lower intercept age of 464 ± 49 Ma is therefore interpreted as an indicator of Pb-loss rather than an age of metamorphic zircon growth. The upper intercept age (943 ± 47 Ma) is interpreted as the crystallization age of the protoliths of the biotite-hornblende gneiss (Fig 5.2).

In the muscovite-hornblende gneiss (sample JK/2), the concordia age of 981 ± 12 Ma obtained from the one concordant data point, measured from the magmatic core (Th/U ratio > 0.1) is interpreted as the closest approximation of the crystallization age of the igneous protolith (Fig.5.5). The weighted mean age of 487 ± 27 Ma obtained from the rims is suggested to reflect Pb-loss rather than the timing of a metamorphic zircon overgrowth. This is supported by the magmatic nature (Th/U ratios > 0.1) of all the analysed rims. Furthermore, the convoluted zonation pattern is commonly caused by Pb-loss and/or migration of trace elements during late to post magmatic recrystallization (Corfu, 2013). In addition, Kröner et al. (2014) suggest that complex internal textures in zircons are associated with the occurrence of magmatic zircon in high-grade metamorphic rocks.

The $^{206}Pb/^{238}U$ age of 924 ± 26 Ma obtained from the core of the concordant single zircon grain (muscovite-biotite gneiss, sample JK/3) is interpreted as the time of crystallization for the igneous protolith (is interpreted as the emplacement age of the protolith. Th/U ratios (> 0.1) indicate that the core is indeed magmatic. Furthermore, Th/U ratios obtained from zircons belonging to the biotite-muscovite gneiss (sample JK/4) imply that the cores are magmatic

(>0.1) and as a result, the weighted mean age of 933 ± 20 Ma is interpreted as the crystallization age of the protolith of the biotite gneiss (Fig. 5.8). The 933 ± 20 Ma age overlaps within error with the accepted age for the granitic emplacement of the Mirian gneisses. Furthermore, the rims show Th/U ratios less than 0.1, typical of metamorphic zircons (Rubatto, 2017).

The 633 ± 17 Ma weighted mean age obtained from the rims is therefore suggested to indicate the time of metamorphic zircon overgrowth in relation to the the Pan-African tectono-metamorphic event. Civetta, et al. (1979) having conducted a geochronological study of the South Sudanese Basement Complex, obtained radiometric ages in the range 654 to 443 Ma, associated with the formation of the Aswa shear zone in northern Uganda and South Sudan. In addition, Mänttari (2010) obtained U-Pb zircon age of 656 ± 16 Ma for emplacement of granitoids, also attributed to the development of the sinistral Aswa shear zone event associated with the Pan-African event (Saalmann et al., 2016).

The four gneisses from this study provide Neoproterozoic crystallization ages for their protoliths (943 ± 47 Ma for sample JK/1, 981 ± 12 Ma for sample JK/2, 924 ± 26 Ma for sample JK/3 and 933 ± 20 Ma for sample JK/4). These Neoproterozoic ages are a close match to the 950 ± 20 Ma age (Holmes, 1951; Cahen and Snelling, 1966) used to characterize rocks that formed during the Mirian tectono-magmatic event of the West Nile in Uganda. The Mirian Group/event in Uganda is characterised by recumbent isoclinal folds overturned towards the NW or NNW with development of flaggy axial plane cleavage and retrograde amphibolite facies metamorphism (Hepworth and Macdonald, 1966)

The Mirian event is suggested to be an equivalent of the Kibaran orogeny (1000 ± 200 Ma). Cahen and Snelling (1966) define the Kibaran Orogeny as a series of orogenic events that have been recognized in southern and central Africa, with one set of major metamorphism and igneous activity dated at 1000 ± 200 Ma. In western Sudan and the Central African Republic,

a linear belt belonging to this cycle with NE-SW fold trends yielded ages between 800 and 1200 Ma (Vail, 1978). Vail (1978) suggested that the "Sudan shield" also known as the Basement Complex in Sudan formed during the Kibaran orogeny and is not Pre-Kibalian (Archaean) as suggested by most workers including Tanner (1973).

The two youngest zircon grains from the biotite schist (sample JK/5) yield a weighted mean age of 920 ± 17 Ma suggested to indicate the maximum depositional age. The early Archaean to late Palaeoproterozoic (2876 ± 22 to 2414 ± 7 Ma) grains, defined by the largest peak on the density probability plot, may reflect the Neoarchaean Aruan tectono-magmatic event (Link et al., 2010) (Fig. 5.10B). The Th/U ratios of greater than 0.1 for these ages corroborate a magmatic origin for the zircon ages. These zircons may have been derived from the Aruan gneisses of the West Nile Belt further south of the current study area. The minor mid-Palaeoproterozoic grains (2346 ± 50 to 2187 ± 55 Ma) are associated with the mid-Palaeoproterozoic Buganda-Toro assemblage rocks (Ubendian) (1950 ± 150 Ma) in the Ruwenzori fold belt of Uganda (Tanner, 1973). The late Neoproterozoic (1070 ± 18 to 910 ± 10 Ma) is suggested to reflect the Mirian tectono-magmatic event and possible provenance is the ~ 950 Ma Mirian flaggy grey gneisses of the West Nile Belt in northern Uganda (Leggo, 1974).

The three youngest zircons from the biotite-garnet schist (sample JK/6) yield a weighted mean age of 959 ± 11 Ma interpreted as the maximum depositional age. The two peaks seen on the density probability diagram (Fig. 5.12B) correspond to ages for different magmatic events within the North Eastern Congo Craton. The 2755 ± 8 Ma to 2353 ± 7 Ma age peak reflects the Neoarchaean Aruan thermal event and suggests an Aruan unit in the West Nile Belt as possible provenance. The 947 ± 19 to 967 ± 15 Ma ages correspond to the age of the Mirian tectono-magmatic event.

A study by Garzanti et al. (2018) shows that Albert Nile, a headstream of the Nile River and a tributary of Lake Albert, brings sediments through Bahr el Jebel into and past the current study area. Sediments brought into the study area are sourced from the high-grade Archaean gneisses of the Congo Craton in Uganda (Link et al., 2010). Hence the presence of the Mirian/Kibaran, Ubendian and Aruan detrital zircon ages in Jebel Kujur. Comparison of detrital zircon ages and age distributions presented by Garzanti et al. (2018) for South Sudan indicate similarly dominant Aruan ages and a significant number of Pan-African ages. This similarity in zircon ages suggests similar provenance (Fig. 5.10A-B).

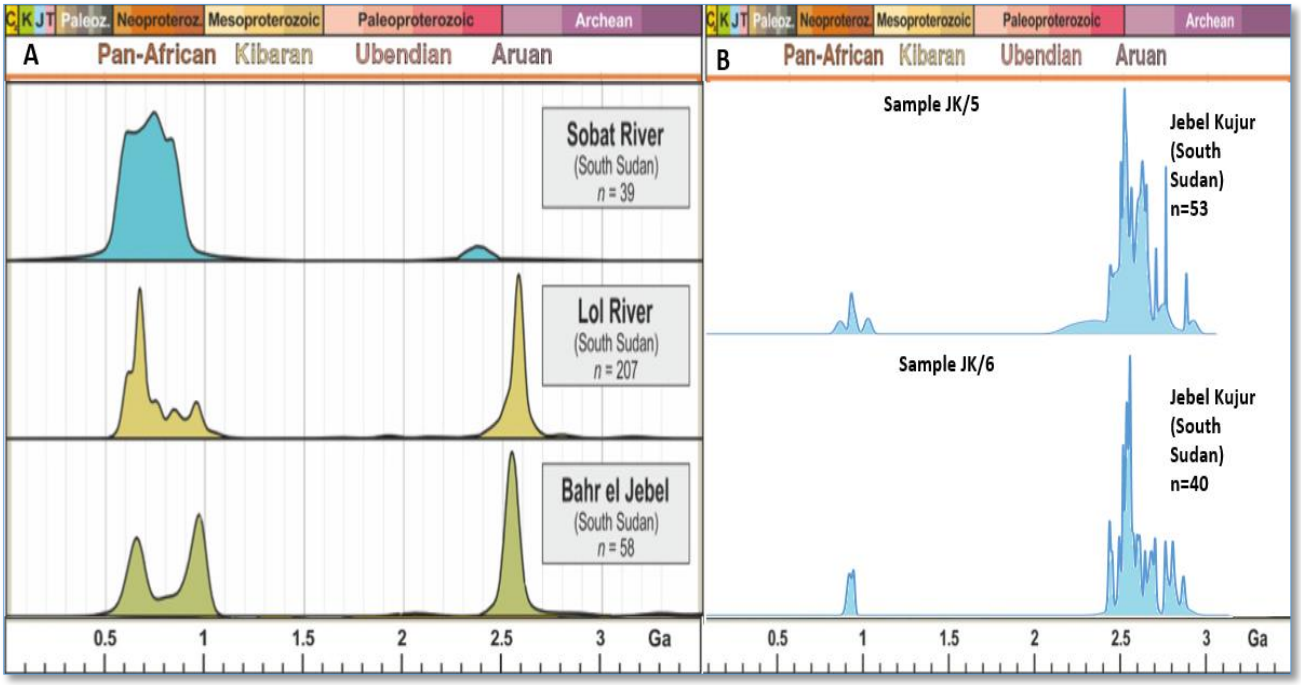


Figure 5.10: Comparison of U-Pb age spectra of detrital zircons for analysis and results from Garzanti et al. 2018 (A) and present study (B). Comparison between the two indicates similarly dominant Aruan followed by significant peaks reflecting Pan-African detrital zircon ages (modified after Garzanti et al., 2018).

5.5 Summary and conclusions

The U-Pb zircon geochronology documents emplacement between 981 and 924 Ma for the granitic gneisses, attributed to the 950 Ma Mirian event. One sample (sample JK/4) gives a lower intercept age of 633 ± 17 Ma interpreted as the time of metamorphic zircon overgrowth related to the Pan-African tectono-metamorphic event. The lower intercept ages yielded by the

rest of the granitic gneisses is attributed to Pb-loss. These ages indicate that Jebel Kujur, a part of the Basement Complex in South Sudan is actually Neoproterozoic in age rather than Archaean as proposed by previous workers and most likely formed during the Mirian event.

Detrital zircon ages recorded in the schists suggest that units from the Congo Craton served as sources for the protoliths of the meta-sedimentary rocks found in the study area. The identified source rocks include; the Aruan gneisses, Buganda-Toro Group (Ubendian) and Mirian flaggy grey gneisses. The 920 ± 17 Ma and 959 ± 11 Ma ages obtained from the youngest zircons from samples JK/5 and JK/6, respectively, probably reflect the maximum depositional ages for the protoliths of the biotite schists from Jebel Kujur.

Chapter 6
Zircon Lu-Hf isotopes

6.1 Introduction

This study utilizes the ability of lutetium-hafnium (Lu-Hf) isotopes to provide information on the timing of addition of new mantle material into the crust as well as the processes under which the crust differentiates. In this chapter, the cathodoluminescence (CL) images are used in combination with U-Pb zircon ages and Hf isotope composition to decipher the crustal evolution of the Basement Complex.

6.2 Analytical methods

Individual zircon grains previously dated by LA-ICPMS were selected by the degree of concordance criteria for Lu-Hf analyses. Zircons with concordance of greater than 90% were selected for analyses. The Nu Plasma II ICP-MS coupled to a 193 nm excimer laser system at the Department of Geology (University of Johannesburg) was used to analyse the *in-situ* zircon Lu-Hf isotopic compositions, with helium used as a carrier gas. The spot size was varied between 40 and 60 µm, depending on the size of the preferred locus selected for analysis. Fifty percent beam attenuation and 40 mJ beam energy was applied during the analyses at a repetition rate of 7 Hz.

^{171}Yb and ^{173}Yb were used to calculate Yb mass fractionation and correct Yb and Lu mass fractionation. ^{179}Hf and ^{177}Hf was used to calculate Hf mass fractionation. The ^{171}Yb was used to calculate and correct ^{174}Yb interference on ^{174}Hf and the ^{176}Yb interference on ^{176}Hf, ^{175}Lu used to correct the ^{176}Lu interference on ^{176}Hf. Mud Tank, Temora 2 and LV11 were used as secondary standards and measured as unknowns to evaluate and monitor accuracy of internally corrected Hf isotope ratios and instrumental drift as per the Lu-Hf ratio. Background correction

was done by measuring background signal on mass prior to ablation and subtracting from signal.

For the $^{176}Hf/^{177}Hf$ ratios, 0.282684 ± 0.000019 and 0.282489 ± 0.000018 were obtained for Temora and Mud Tank, respectively. The values are within two standard error in agreement with values recommended for $^{176}Hf/^{177}Hf$ ratios (Wu et al., 2006). Furthermore, εHf values were calculated using decay constant (λ) of 1.867 *10-11yr-1 for ^{176}Lu by Scherer et al. (2001) and the $^{176}Hf/^{177}Hf$ and $^{176}Lu/^{177}Hf$ CHUR values of 0.282785 and 0.0336, (Bouvier et al., 2008). For the calculations, the measured $^{176}Hf/^{177}Hf$ ratio firstly needed to be corrected for the interpreted crystallization age of each sample, the value obtained from such a calculation is referred to as $^{176}Hf/^{177}Hf$ initial ratio.

U-Pb ages and the corresponding $^{176}Hf/^{177}Hf$ obtained from the same spot were used to obtain the corrected $^{176}Hf/^{177}Hf$ initial. Moreover, having normalized the $^{176}Hf/^{177}Hf$ initial ratios to the $^{176}Hf/^{177}Hf$ value of the present-day bulk earth, the εHf values could then be calculated. Two-stage model ages were determined by projection of the initial $^{176}Hf/^{177}Hf$ values of zircon back to the Depleted Mantle growth curve using $^{176}Lu/^{177}Hf$ =0.012 for average continental crust (Vervoort et al., 1999), $^{176}Lu/^{177}Hf$ =0.03976 and $^{176}Hf/^{177}Hf$ =0.283238 for the Depleted Mantle (Vervoort, 2015).

6.3 Results

The Lu-Hf ablation spots were in most cases centred on top of the pre-existing U-Pb ablation spot. In cases where this was impossible mostly as a result of very thin zircon growth zones, then ablation spot was then positioned just next to the U-Pb ablation spot, in what seemed to be a coeval growth zone of the zircon. Initial Hf composition for the selected zircon grains was calculated using the U-Pb age of the corresponding spot. The $^{206}Pb/^{207}Pb$ ages were used for

old zircons (>1000 Ma) and for the younger zircons (<1000 Ma), the $^{206}Pb/^{238}U$ ages were considered.

The Lu-Hf data is shown in Table 6.1. Figures 6.1 and 6.2 show the graphical representation of the data, in these figures, the relationship between the U-Pb ages and initial Hf-isotope composition/ εHf (t) is indicated. In these diagrams, zircons that plot between the Depleted Mantle (DM) and Chondritic Uniform Reservoir (CHUR) curves indicate derivation from juvenile magmas, whereas points below the CHUR curve can be considered as material derived from pre-existing crustal material.

Table 6.1: Zircon Hf isotope composition data for granitic gneisses and biotite schists.

Sample	$^{176}Hf/^{177}Hf$	2SE	$^{176}Lu/^{177}Hf$	2SE	Age (Ma)	(176Hf/177Hf)t	εHf(t)	TDM (Ma)
Muscovite-hornblende gneiss (JK/2)								
TRA_Data_33533-JK2-1.csv	0,281505	0,000032	0,0016	0,000007	955	0,281476	-24,97	2347
TRA_Data_33535-JK2-3.csv	0,281510	0,000023	0,0004	0,000010	878	0,281503	-25,74	2310
Muscovite-biotite gneiss (JK/3)								
TRA_Data_33531-JK3-1.csv	0,281465	0,000021	0,0006	0,000001	924	0,281455	-26,41	2374
Biotite gneiss (JK/4)								
TRA_Data_33522-JK4-1.csv	0,281503	0,000019	0,0005	0,000001	938	0,281494	-24,73	2324
TRA_Data_33523JK4-2.csv	0,281545	0,000011	0,0003	0,000001	634	0,281541	-29,88	2257
TRA_Data_33524-JK4-3.csv	0,281613	0,000011	0,0002	0,000001	632	0,281611	-27,47	2167
TRA_Data_33527-JK4-6.csv	0,281453	0,00002	0,0006	0,000001	921	0,281442	-26,95	2391
TRA_Data_33529-JK4-7.csv	0,281522	0,00002	0,0007	0,000001	944	0,281510	-24,02	2303
Biotite schist (JK/5)								
TRA_Data_33505-JK5-1.csv	0,281013	0,000019	0,0005	0,000002	2474	0,280989	-7,40	2970
TRA_Data_33507-JK5-2.csv	0,281095	0,000019	0,0006	0,000004	2616	0,281067	-1,29	2859
TRA_Data_33508-JK5-3.csv	0,280952	0,000019	0,0002	0,000002	2459	0,280941	-9,43	3034
TRA_Data_33509-JK5-4.csv	0,281075	0,000021	0,0009	0,000003	2669	0,281029	-1,39	2908
TRA_Data_33510-JK5-6.csv	0,280960	0,000016	0,0004	0,000002	2490	0,280941	-8,73	3033
TRA_Data_33511-JK5-7.csv	0,280948	0,000021	0,0008	0,000004	2724	0,280906	-4,49	3070
TRA_Data_33512-JK5-8.csv	0,282006	0,000019	0,0009	0,000006	944	0,281990	-7,02	1668
TRA_Data_33513-JK5-9.csv	0,281035	0,000018	0,0008	0,000003	2532	0,280996	-5,76	2957
TRA_Data_33514-JK5-10.csv	0,281069	0,000016	0,0005	0,000002	2494	0,281046	-4,88	2892
TRA_Data_33515-JK5-11.csv	0,280987	0,00004	0,0004	0,000007	2534	0,280970	-6,66	2993
TRA_Data_33516-JK5-12.csv	0,281726	0,000052	0,0007	0,000011	994	0,281713	-15,68	2035
TRA_Data_33518-JK5-14.csv	0,281102	0,000047	0,0009	0,000011	2601	0,281056	-2,03	2875
TRA_Data_33519-JK5-15.csv	0,280966	0,000024	0,0005	0,000006	2501	0,280940	-8,49	3034
TRA_Data_33520-JK5-16.csv	0,280976	0,000023	0,0005	0,000005	2837	0,280947	-0,36	3009
TRA_Data_33521-JK5-17.csv	0,281107	0,000016	0,0006	0,000005	2414	0,281080	-5,56	2851
Biotite-garnet schist (JK/6)								
TRA_Data_33541-JK6-1.csv	0,281539	0,000016	0,0002	0,000002	940	0,281535	-23,23	2270
TRA_Data_33543-JK6-2.csv	0,281040	0,000018	0,0010	0,000004	991	0,281021	-40,27	2941
TRA_Data_33545-JK6-4.csv	0,281143	0,000017	0,0005	0,000002	2464	0,281118	-3,03	2797
TRA_Data_33547-JK6-5.csv	0,281635	0,000019	0,0006	0,000005	947	0,281625	-19,87	2151
TRA_Data_33549-JK6-6.csv	0,281042	0,000036	0,0002	0,000003	2428	0,281031	-6,97	2915
TRA_Data_33551-JK6-7.csv	0,280978	0,000031	0,0002	0,000005	2465	0,280968	-8,34	2998
TRA_Data_33553-JK6-8.csv	0,280985	0,000019	0,0010	0,000004	2467	0,280939	-9,34	3037
TRA_Data_33555-JK6-9.csv	0,281340	0,000052	0,0010	0,000004	2331	0,281295	0,17	2565
TRA_Data_33557-JK6-12.csv	0,281037	0,000023	0,0008	0,000005	2446	0,281000	-7,65	2956
TRA_Data_33560-JK6-14.csv	0,281082	0,000019	0,0010	0,000013	2504	0,281034	-5,07	2908
TRA_Data_33562-JK6-26.csv	0,281068	0,00002	0,0008	0,000003	2657	0,281027	-1,76	2911

Muscovite-hornblende gneiss, sample JK/2

Two zircons from sample JK/2 presented concordant ages, hence only two Lu-Hf analyses were conducted. The analyses show very homogenous Hf composition with $^{176}Hf/^{177}Hf$ ratios of 0.281505 and 0.281510, and εHf (t) of -24.97 and -25.74. The Depleted Mantle model ages (T_{DM}) for the two Neoproterozoic zircons are also similar, yielding 2347 and 2310 Ma (Table 6.1). The Hf isotope data for this sample plots below the CHUR curve on the Hf isotope composition evolution diagrams (Figs. 6.1 and 6.2).

Muscovite-biotite gneiss, sample JK/3

For the one zircon grain obtained from sample JK/3, $^{176}Hf/^{177}Hf$ ratio of 0.281465 and εHf(t) of -26.41 was presented from the single Lu-Hf analysis. The T_{DM} is 2374 Ma, whereas the Hf isotope composition evolution plots show that the Hf isotope composition of this zircon plots below the CHUR curve (Figs. 6.1 and 6.2).

Biotite-muscovite gneiss, sample JK/4

Five Lu-Hf analyses were performed on five concordant zircons from sample JK/4. The $^{176}Hf/^{177}Hf$ ratio ranging between 0.281442 and 0.281611, εHf(t) shows similar values for three core-spot analysis with $^{206}Pb/^{238}Pb$ ages in the range of 921-944 Ma. Nonetheless, εHf(t) values between -24.02 and -26.95 are obtained. The grains with younger rim $^{206}Pb/^{238}Pb$ ages (632 and 634 Ma) yield εHf(t) values of -27.47 and -29.88, respectively. The T_{DM} range from 2303 to 2391 Ma for the core and 2167 and 2257 Ma for the younger rims. Furthermore, evolution plots indicate that Hf composition for both the core and the rim plot below the CHUR Hf composition line (Figs. 6.1 and 6.2).

Biotite schist, sample JK/5

Fifteen concordant zircon spots from sample JK/5 were analysed for Lu-Hf isotopes and $^{176}Hf/^{177}Hf$ ratios ranging between 0.280948 and 0.282006 were obtained. Zircons representing the Archaean/ Palaeoproterozoic and Neoproterozoic populations were analysed. Thirteen Archaean/ Palaeoproterozoic cores have εHf(t) values from -0.36 to -9.43 and the younger rims indicate εHf(t) values of -15.68 and -7.02. The T_{DM} range between 2970 and 3034 Ma for the Archaean/Palaeoproterozoic group and 1668 and 2035 Ma for the younger Neoproterozoic group. On the evolution diagrams in figure 6.1, the Hf isotope data of this sample indicates that most points plot below the CHUR curve, whereas about 3 points lie between the DM and CHUR curves. In Figure 6.2, a single point plots on the CHUR curve, and the rest of the points are below it.

Biotite-garnet gneiss, sample JK/6

For sample JK/6, eleven concordant zircon spots with ages belonging to two population zircon age groups were analysed for Lu-Hf isotope composition. The $^{176}Hf/^{177}Hf$ ratios obtained for this sample range between 0.28078 and 0.281635. The εHf (t) values for $^{206}Pb/^{207}Pb$ ages in the 2331-2755 Ma population are between -1.76 and 0.17 and are in the range of -19.87 to -40.27 for rims with younger $^{206}Pb/^{238}Pb$ ages (940-991 Ma). The T_{DM} range between 2565-3037 Ma for the older analyses and 2151-2941 Ma for the younger rims.

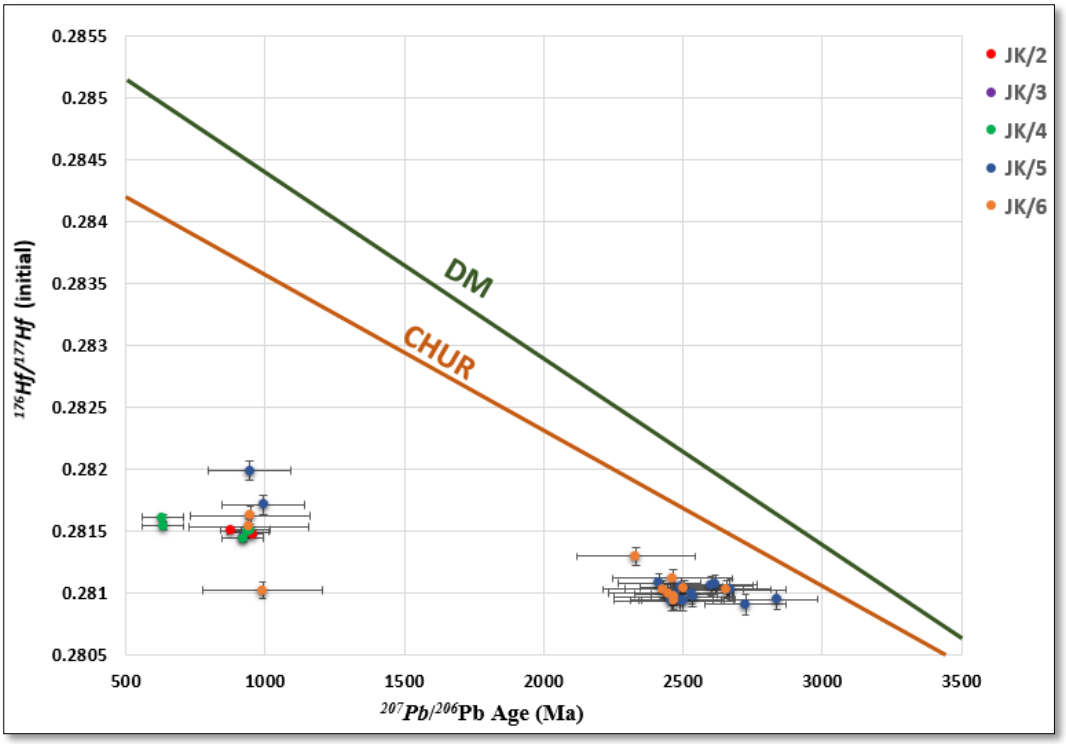


Figure 6.1: $^{207}Pb/^{206}Pb$ (Ma) vs 176Hf/177Hf (initial) plot for the Jebel Kujur zircons. DM: Depleted Mantle, CHUR: Chondritic Uniform Reservoir.

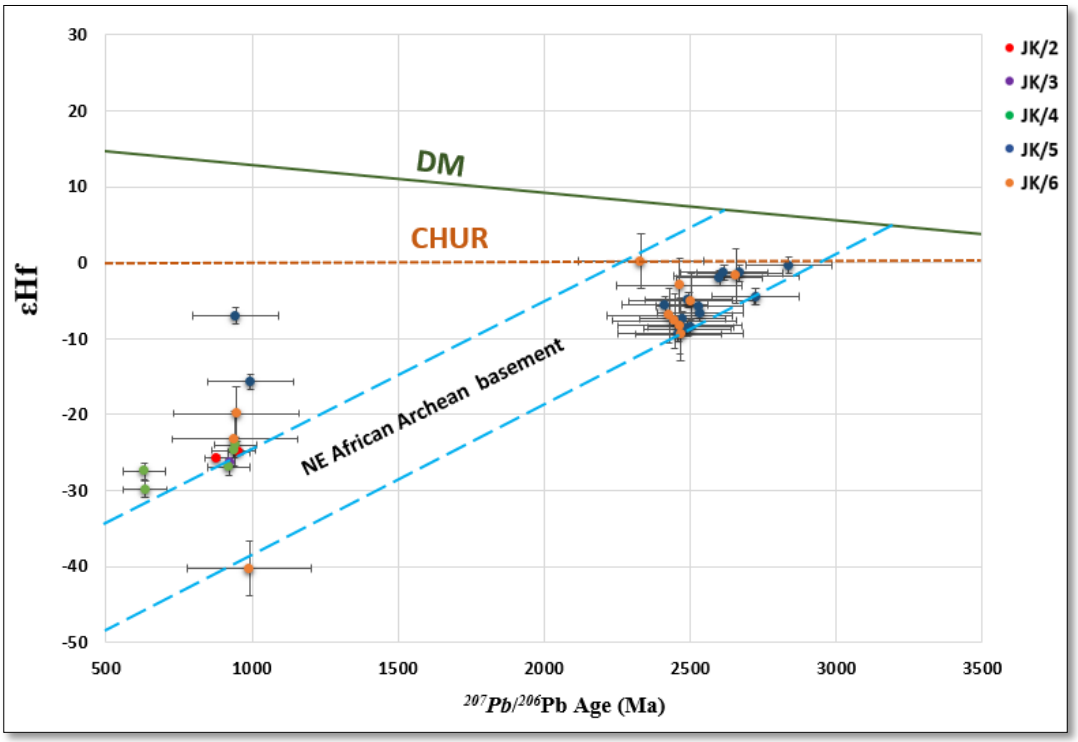


Figure 6.2: $^{207}Pb/^{206}Pb$ (Ma) vs εHf plot for the Jebel Kujur zircons. DM: Depleted Mantle, CHUR: Chondritic Uniform Reservoir. Diagonal blue dotted lines indicate a field for NE African Archaean basement (Fielding et al., 2017).

6.4 Discussion

U-Pb and Lu-Hf isotope data provide information on the magma source from which the zircon crystallized (Kinny and Maas, 2003; Scherer et al., 2007). The strongly negative εHf(t) values shown by the muscovite-hornblende gneiss (sample JK/2) imply that this sample was sourced from an older material (Fig. 6.2). The Hf model ages (2347 and 2310 Ma) indicate the time of segregation of its source from Depleted Mantle reservoirs. The zircons were formed at 981 ± 12 Ma, suggesting a crustal residence time of ca 1.4 Ga. The muscovite-biotite gneiss (Sample JK/3) crystallized at 926 ± 24 Ma. The Hf model age exceeds the crystallization age, implying that the protolith of this sample was sourced from an older crust.

The rims and cores from zircon grains in biotite-muscovite gneiss (sample JK/4) give similar $^{176}Hf/^{177}Hf$ ratios. The rims show much lower Lu/Hf ratios, typical of metamorphic overgrowths (Schmitz et al., 2004). The low Lu/Hf ratios in metamorphic zircon (zircon grown during metamorphism) imply that the $^{176}Hf/^{177}Hf$ ratio was preserved during metamorphic zircon growth (Kinny and Maas, 2003). Therefore, the similarity between the Hf isotope composition of the zircon cores and that of the rims, measured from the same zircon grains suggest that the younger rims are most likely recrystallization of the outer part of the zircon grain during the 633 ± 17 Ma metamorphic event (Matteini et al., 2010). This is supported by the transgressive, overprinting relations between the rims and the cores shown by CL images (Hoskin and Black, 2000) (Fig. 6.3). These features together with isolated patches within the cores, are consistent with recrystallization.

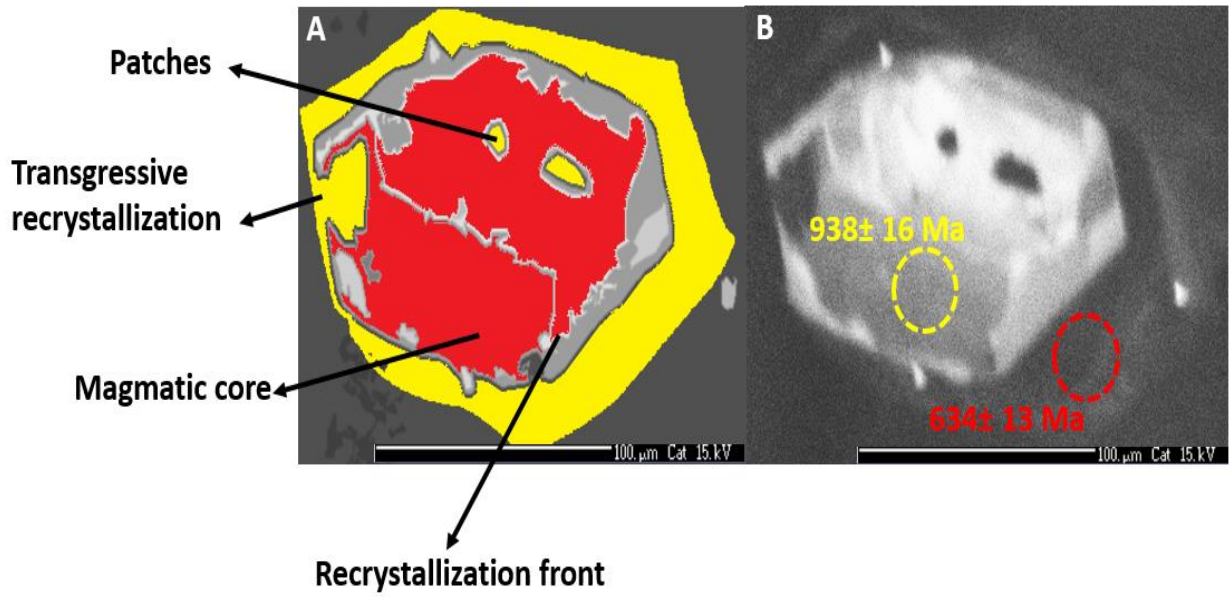


Figure 6.3: Schematic diagram of CL-revealed internal features (A) and Cathodulumines cence (CL) image with corresponding $^{206}Pb/^{238}U$ ages (B) for zircon crystals from biotite-muscovite gneiss (sample JK/4).

The process of recrystallization would reset the U-Pb isotopic system and leave the Hf composition unchanged. The idea of decoupling between Lu-Hf and U-Pb isotope systematics during metamorphism has been evidenced by several studies including Jiang et al. (2010) and Xiong et al. (2012). This interpretation agrees with Fielding et al. (2017), who suggested recrystallization in a closed system under metamorphic conditions for a single 630 Ma zircon rim that formed on a zircon grain from northern Uganda with a crystallization age of 800 Ma.

U-Pb zircon cores from samples JK/2, JK/3 and JK/4 show overlapping Neoproterozoic crystallization ages. The three samples also show similar εHf(t) values, measured from the magmatic zircon cores, this is consistent with a common or similar source. Nonetheless, the Hf isotope dataset is consistent with remelting of Palaeoproterozoic crust which agrees with previous studies that assigned a Precambrian age to the Basement Complex in the south-eastern region of South Sudan (Whiteman, 1979; Vail, 1978)). The basement was reworked during a single event two events; the earliest one took place at 981-924 Ma, followed by a later one at 633 ± 17 Ma. The two ages are similar to those seen in the detrital zircon grains (ca. 960 and

600 Ma) from northern Uganda and provide evidence for crustal reworking and new zircon growth (Fielding et al., 2017). While the U-Pb ages of the gneisses support the notion that the current study area forms part of the Mozambique Belt (Almond, 1980), the εHf (t) values suggest an older crustal source for the magma, whereas rocks belonging to the Mozambique Belt and the rest of the East African Orogeny are generally compatible with juvenile sources (Bailo et al., 2003; Küster et al., 2008; Maboko and Nakamura, 2002,).

DM model ages of >2000 Ma indicate extensive reworking of Palaeoproterozoic and Archaean crust during the Neoproterozoic (Kröner, 2001; Stern, 2002). Hepworth (1972) also supports the idea that the western part of the Mozambique Belt is underlain by the Archaean Tanzania Craton and was reworked during the Proterozoic eon. This therefore corroborates the idea that the current study area may form part of the Mozambique Belt. This notion will need to be evaluated with a broader comparison of the geochemical and geological evolution of the study area and that of the Mozambique Belt.

The detrital zircons in sample JK/5 all show negative εHf(t) values, indicating evolved crustal domains in their provenance. DM Hf model ages of the Palaeoproterozoic/Archaean indicate a crustal residence time of 3.0-2.8 Ga. The Neoproterozoic detrital zircons suggest a crustal residence time of 1.6-2.0 Ga.

The negative εHf(t) values of the Archaean zircon population group from sample JK/6 suggest an older Archaean crustal source for magma formation and is further supported by much older Archaean TDM2 Hf model ages. The Hf signatures observed in the Palaeoproterozoic group suggest recycling of predominantly Archaean crust. One zircon grain with a $^{207}Pb/^{206}Pb$ age of 2331 Ma age presents the only positive εHf(t) value (0.17), possibly due to ablation spot of two different zones. The Neoproterozoic detrital zircons in sample JK/6 suggest a crustal residence time of 2.1-2.9 Ga.

Samples JK/5 and JK/6 representing a metasedimentary sequence of Jebel Kujur, present interesting Lu-Hf isotope data. Archaean, Palaeoproterozoic and Neoproterozoic detrital zircons all possess Hf signatures that point to older Archaean or Palaeoproterozoic crustal domains in their provenance, with no hint of juvenile material. In order to discern the provenance of these rocks, the White Nile, the main river source of the sediments from which the protoliths formed, needs to be inspected. The White Nile, as one of the major tributaries of the longest river in the world (Nile River), drains Archaean and Proterozoic rocks of the Congo Craton as well as Precambrian rocks of the Saharan Meta-Craton (Abdelsalam et al., 2002). Fielding et al. (2017) conducted a detrital record study of the Nile River with some samples collected from the White Nile of the Murchison Falls and Sudd Marshes in northern Uganda.

The U-Pb and Lu-Hf data obtained from zircons sampled in northern Uganda areas (Murchison Falls) are indistinguishable from data in the current study. Zircons obtained from both Jebel Kujur and northern Uganda, have ages of 2620 to 2570 Ma, and show low negative εHf(t) values and Archaean DM Hf model ages. In the same sense, zircon populations with U-Pb ages of ca. 630 Ma and 900-1000 Ma show higher εHf(t) values of about -25. Similarity of the data from Jebel Kujur and Murchison Falls in northern Uganda (Fielding et al., 2017) suggest a similar source. For the northern Uganda sediments, the suggested source is terranes belonging to the north-eastern corner of the Congo Craton (Fielding et al., 2017; Garzanti et al., 2018).

6.5 Summary and Conclusions

The Lu-Hf data for the granitic gneisses confirm the existence of Precambrian crust, from which later crustal magmas were generated. This observation is indicated by the negative εHf(t) values and Palaeoproterozoic DM Hf model ages, and is in agreement with previous studies (Worrall, 1957; Vail, 1978; Vail, 1985; Adak; 2015), which supported the notion that the geology of the south-eastern end of South Sudan is underlain by a Precambrian basement.

Furthermore, reworking of this basement occurred during a single magmatic event at 981-924 Ma. The similarity in U-Pb zircon ages and Nd and Hf isotope ratios suggest that Jebel Kujur may be considered a part of the western terrain of the Mozambique Belt.

The Hf isotopic signatures suggest that the source rocks of the biotite schists were derived from old continental rocks, with Archaean and Palaeoproterozoic DM Hf model ages. Similarity in the U-Pb ages and Hf isotopic signatures of detrital zircons from Jebel Kujur and northern Uganda (Murchison Falls) imply a common provenance, suggested to be the north-eastern corner of the Congo Craton. The use of detrital age spectra in combination with Hf isotope data allows a special perspective on crustal growth and evolution of the Basement Complex of South Sudan and to a lesser extent, the NE Congo Craton.

Chapter 7
Integrated discussion and conclusions

7.1 Integrated discussion

Data from this study indicate that the magmatic history of the Basement Complex of South Sudan began in the Neoproterozoic (981-924 Ma) with the intrusion of highly evolved, peraluminous I-type granites, presently occurring as gneisses. The geochemical fingerprint suggests that the granites were generated by partial melting of much older crustal materials. This is particularly shown in their high potassic nature, calc-alkaline affinity and enrichment of LILE along with the depletion of HFSE. Similar I-type granites with strong peraluminosity are found in the neighbouring country, Ethiopia, Western Shire and were suggested to have formed from partial melting of the lower crust (Welay, 2014). Partial melting of an older crust as a model for the generation of the parental magma that formed the Basement Complex gneisses is further supported by their Hf isotopic composition (Augustsson et al., 2006). The granitic gneisses exhibit unradiogenic and homogenous zircon εHf(t) values ((-24) – (-27)) which are attributed to melts derived from the mature continental crust. Vapour-present melting conditions are supported by low Rb/Sr ratios. The Hf Depleted Mantle (DM) model ages further indicate that the parental magma that formed the 981-924 Ma granites separated from the Depleted Mantle at about 2.3 Ga.

The SiO_2-rich nature of these gneisses, coupled with relative depletion in Ba, Nb, Ta, Sr, P, Ti and Eu suggest petrogenesis above a subduction zone (Welay, 2014) and indicate fractional crystallisation subsequent to partial melting of the involved crustal material. Ibrahim et al. (2001) observed that peraluminous syn-collision granites often occur in regionally folded belts containing pelitic and quartzofeldspathic sediments. A good example of these granites is found

in the Tasman mobile belt, in Eastern Australia (Scheibner, 1985). Several studies have considered the present study area as a part of the Mozambique orogenic belt (Almond, 1978).

The Western Mozambique Belt (WMB), as opposed to the Eastern Granulite (Eastern Mozambique Belt), was subjected to Neoproterozoic reworking of older crustal material (Grantham et al., 2003). Reworking of the crust in the regions of the WMB occurred between ca. 899 Ma and 500-600 Ma (Thomas et al., 2014). Furthermore, the NNW and NNE trends observed in gneisses from South Sudan, through the current study area and into northern Uganda (Andrew, 1972) may indicate the western continuation of the Mozambique Belt (Dearnley, 1966). Also notable is the similarity of the geological sequence obtained in the Western Mozambique Belt in southern Tanzania (Thomas et al., 2014) and that observed in the Basement Complex of South Sudan.

This study confirms the presence of a Neoproterozoic group of rocks collectively known as the Karasuk Group in South Sudan. These rocks are proposed to have been emplaced during the Mirian event (northern Uganda), coeval with the Kibaran Orogeny (Hepworth, 1984). In South Sudan, the Karasuk rocks, which occur in the form of biotite granitic gneisses, were emplaced between 924 and 981 Ma. The Karasuk Group belonging to the Mozambique Belt in Kenya is also assigned a Neoproterozoic age and consists of gneisses, amphibolites and metasedimentary sequence of rocks, like those found in the Basement Complex of South Sudan (Schlüter, 2006). Similarly, a migmatitic granitic gneiss which forms the oldest unit to have evolved from the basement in the Ruangwa region of southern Tanzania yielded an emplacement age of 899 ± 9/16 Ma (Thomas et al., 2014). This unit forms part of the western Mozambique Belt and has yielded an age that is coeval to the age of the first magmatic event in Basement Complex of South Sudan, also considered as the oldest magmatic event in the area.

Subsequent to the 981-924 Ma magmatic event, the present data indicate that the South Sudanese Basement Complex was subjected to regional metamorphism at around 633 ± 17 Ma. During this time, the 981-924 Ma granites were subjected to metamorphism in the upper amphibolite to granulite facies. The WMB granites in the Masai area of southern Tanzania yielded an age of ca. 630 Ma, regarded to reflect the time of deformation and metamorphism of granitoid gneisses emplaced between 1100 and 950 Ma (Kröner et al., 2003).

Similarly, to the Basement Complex granitic gneisses, the WMB rocks are characterized by ancient model ages averaging 2.3 Ga (Stern, 2002), which further corroborate the parallelism of the geodynamic evolution between the two crustal domains. In Uganda (Appel et al., 2004) and in the Oubanguides belt of the Central African Republic (Pin and Poidevin, 1987), peak Neoproterozoic metamorphism is reported to have occurred at ca. 630 Ma. This metamorphism and the associated deformation are attributed to the collision between the Congo Craton and the poorly known Saharan Metacraton. An age of ca. 660 Ma was obtained on magmatic zircons from undeformed intrusive granites at Hofras en Nahas region in South Sudan, farther West of the current study area (Master et al., 2016). This age is interpreted as the minimum age for the mylonitic shear zone of the Central African Shear Zone, associated with the collision between Congo Craton and the Saharan Metacraton.

Similar $^{176}Hf/^{177}Hf$ initial ratios of the 921 Ma core and the 634 Ma growth rim in the biotite-muscovite gneiss (sample JK/4) suggest that the rims are a product of the recrystallization of the outer part of the zircon grain, suggested to have occurred during a high-grade metamorphic event (M1). Metamorphism and recrystallization due to a high-grade metamorphic event are supported by the presence of migmatites and mineralogy associated with granulite-facies metamorphism from rocks in the study area. Cooling from peak temperatures (M2) occurred subsequently with mineral paragenesis of Grt - Crd - Kfs - Qtz - Pl - Bt - Ms - Hbl – Sil. This event implies retrogradation from granulite-facies to amphibolite-facies metamorphism. Most

of the rocks show the effects of this overprint. Furthermore, the Ar-Ar geochronology results and interpretation indicate that cooling following the amphibolite-facies retrogradation occurred at 555 ± 3 Ma.

Many workers, including Cutten et al. (2006) and Kabete et al. (2012) have recognized metamorphic events of this age (ca. 550 Ma) in the WMB. This metamorphic age reflects cooling ages in the WMB (Thomas et al., 2014). Subsequent to cooling, microstructures and cross-cutting relations indicate that the rocks were subjected to another event (D1), which caused crystal-plastic deformation accompanied by brittle shearing. This event is associated with the ductile-brittle deformation stage of the Aswa shear zone (Saalmann et al., 2016). Available K-Ar, Ar-Ar and U-Pb (zircon) ages from the Basement Complex in South Sudan are summarised in Table 1E (Appendix E). The geochronological sample sites of these ages are indicated on a map (Fig. 7.1).

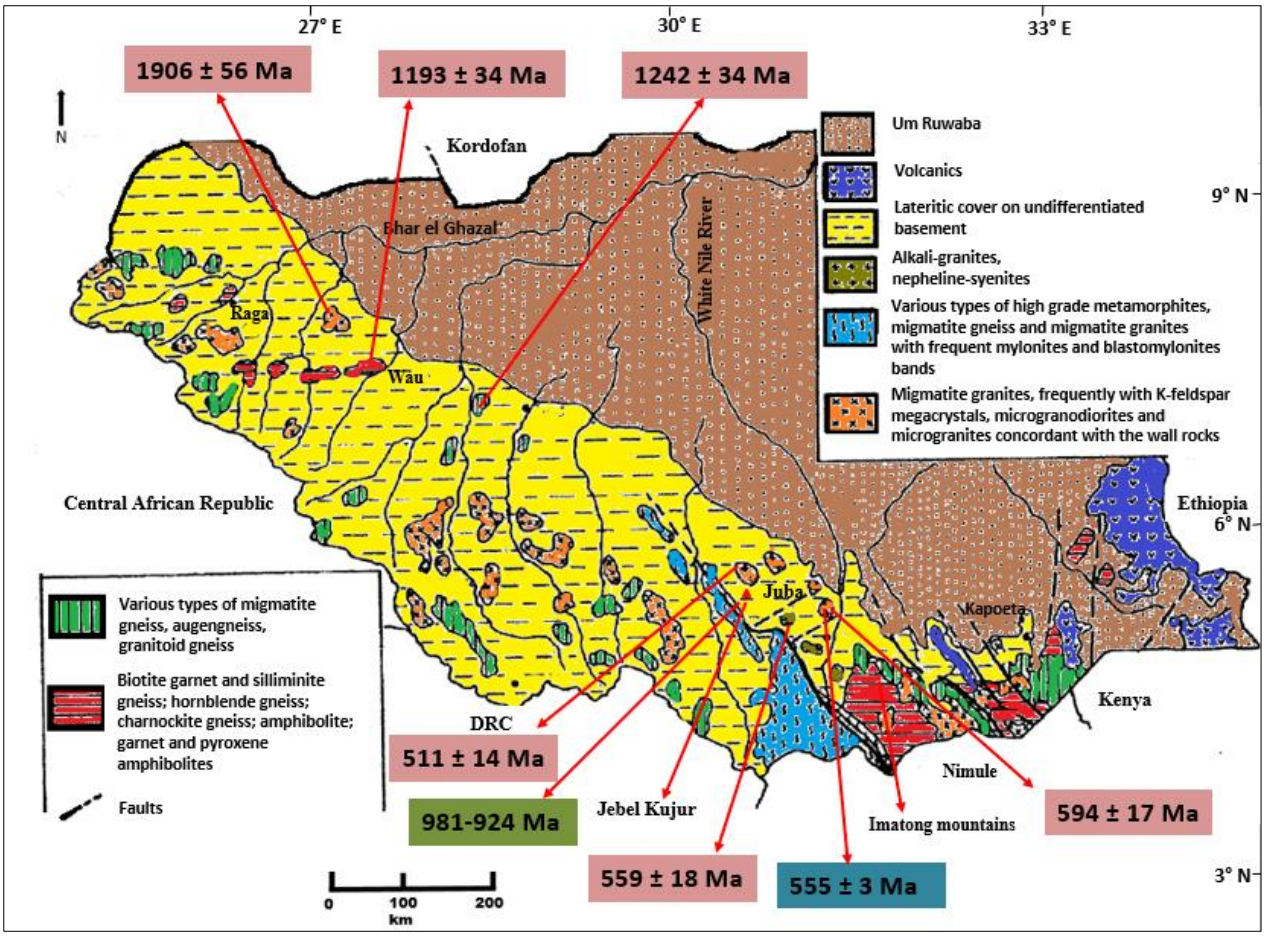


Figure 7.1 Location of geochronological sample sites for rocks from the Basement Complex in South Sudan. Red triangle shows the location of the present study area. The ages highlighted in pink are from Civetta et al. (1979) obtained through K-Ar dating method. Ages highlighted in blue and green are Ar-Ar and U-Pb zircon ages, respectively, all obtained from the present work.

Petrographical analysis, geochemical fingerprint, zircon U-Pb geochronology and Hf isotopic compositions of the biotite schists from the Basement Complex as discussed in their respective chapters provide important constraints on their source. The geochemical data suggest that the schists were initially lithic arenites derived from mixed felsic and basic source rocks with geochemical behaviour characteristic of Archaean material. These lithic arenites were deposited in an oceanic island tectonic setting sometime after 920 Ma. Moreover, geochemical indices indicate that the arenites underwent an intermediate degree of weathering.

Detrital zircon U-Pb results of the Basement Complex biotite schists indicate that the sediments from which the arenites formed were derived from the Aruan gneisses, Buganda Group (Ubendian) and Mirian flaggy gneisses in northern Uganda. The detrital zircons further exhibit

U-Pb ages and Hf isotope composition that correlate very well with those obtained in Murchison Hills in northern Uganda, suggesting the same provenance for Jebel Kujur (South Sudan) and Murchison Hills (northern Uganda). The suggested source rocks for the Basement Complex biotite schists are all part of the Archaean NE Congo Craton. This corroborates the idea that the Basement Complex schists were derived from an Archaean source as signalled by the geochemical data.

7.2 Conclusions

This work presents petrographical, geochemical, zircon U-Pb, Lu-Hf and Ar-Ar geochronological data from the south-eastern part of the poorly studied Basement Complex in South Sudan. The collected data gives an increased understanding of the magmatic evolution and the timing of some of the tectono-magmatic events in the area. A single major crust-forming or crustal reworking event at 981-924 Ma (Mirian event) with mean crustal residence age of 2342 Ma is recognised. This event gave rise to high calc-alkaline and peraluminous I-type granites characterised by high SiO_2 (74.08-75.48 wt. %), K_2O (3.78-5.32 wt. %) and low CaO (1.04-1.27 wt. %) contents. Enrichment in LILE and LREE, depletion in HREE and negative Ti and P troughs mark their subduction-related origin.

Values of εHf(t) confirm the existence of an older crust in the area and indicate that the parental magma from which the granitic gneisses formed was derived through partial melting of mature crustal materials. This corroborates the notion that South Sudan is underlain by a Pre-cambrian basement and is also a characteristic of granites particularly found in the western Mozambique Belt of southern Tanzania.

The Basement Complex biotite schists were initially lithic arenites derived from erosion of mixed felsic and basic source rocks and deposited in an oceanic island tectonic setting. U-Pb detrital zircon data suggests that these lithic arenites were deposited sometime after 920 Ma.

Geochemical data indicate that the biotite schists were derived from Archaean source rocks. U-Pb and Hf isotope systematics suggest that the NE Congo Craton with Aruan, Ubendian and Mirian ages reflected in the detrital zircons serve as the source rocks of the biotite schists of the Basement Complex. Correlatable detrital zircon ages are found in Murchison Hills of northern Uganda.

The 981-924 Ma granitic gneisses and 920 Ma schists are proposed to have all experienced peak metamorphism up to granulite-facies (M1) at 633 ± 17 Ma marked by: Pl + Qtz + Kfs + Bt + Grt ± Hbl ± Crd. This metamorphic event is attributed to the~630 Ma continent-continent collision between the Congo Craton and the Saharan Metacraton. Following this event, the Basement Complex gneisses and schists underwent retrograde metamorphism (cooling) to amphibolite-facies (M2) marked by perthite exsolution observed in plagioclase, alteration of feldspars into sericite, mymerkitic texture in feldspars, penetrative secondary foliation in some samples and coronas mostly in the form of symplectites between various reactive minerals. This cooling is proposed to have occurred at 555 ± 3 Ma. The last event recorded in these rocks is crystal-plastic deformation accompanied by brittle shearing (D1) and is linked to the ductile-brittle deformation stage of the Aswa shear zone.

One interesting deduction made from this study is that the lithology, metamorphic grade and magmatic evolution of the Basement Complex in South Sudan and that of the western Mozambique Belt in southern Tanzania are similar. This advocates for earlier speculations regarding the extension of the Mozambique Belt into South Sudan. It is tentatively suggested that the analysed granitic gneisses are a part of the Neoproterozoic Karasuk Group of the Western Mozambique Belt

7.3 Future work

On the existing maps, the Basement Complex is shown as undifferentiated, hence structural mapping and more age determinations need to be conducted in the area. I would recommend a combination of different isotope systems to allow a division of the Basement Complex into distinct Groups and Formations or igneous and metamorphic complexes based on varying geochemical and geologic characteristics. The SHRIMP dating method is suggested for further zircon age determinations, considering that the Basement Complex is a high-grade metamorphic terrane and most zircons from rocks in the area reveal complex internal structures from multi-phases of zircon growth and recrystallization. As a result, methods such as LA-ICPMS and/or SIMS may be quite tricky for such samples. Geophysical studies are also recommended for locating the extension of the basement complex. More structural, geochemical and geochronological studies should be done in other parts of NE Africa to bring forth a more robust reconstruction of terrane boundaries to allow a better understanding of the evolution and geodynamic setting of this ancient crustal domain.

References

Abdelsalam, M.G., Liégeois, J.P., and Stern, R.J., 2002. The Saharan Metacraton. Journal of African Earth Sciences 34, 119-136.

Abu El-Enen. M.M., 2011. Geochemistry. Provenance and metamorphic evolution of Gabal Samra Neoproterozoic metapelites. Sinai. Egypt. Journal of African Earth Sciences 59, 269-289.

Adak, S.M., 2015. Geology of Juba and the surrounding area, Central Equatoria. Available at: https://www.academia.edu/22921696/The_Geology_of_Juba_and_the_Surrounding_Area_Central_Equatoria_Field_Report (Accessed: 15 June 2017).

Almond, D.C., 1969. Structure and metamorphism of the Basement Complex of North-East Uganda. Overseas Geological Mineral Resources 10, 146-163.

Almond, D.C., 1978. New ideas on the geological history of the Basement Complex of North-East Sudan. Sudan Notes and Records 59, 107-136.

Almond, D.C., 1980. Precambrian events at Sabaloka, near Khartoum, and their significance in the chronology of the Basement Complex of North-East Africa. Precambrian Research 13, 4351-4762.

Andrew, G., 1972. New Light on the Geology of the Sudan: Review. The Geographical Journal, 138(1), 70-72.

Anon., 1981. Geological Map of the Sudan. Scale 1:10 000 000 Geological and Mineral Resources Department, Ministry of Energy and Mines, Khartoum, Sudan.

Augustsson, C., Muenker, C., Bahlburg, H., and Fanning, C.M., 2006. Provenance of late Palaeozoic metasediments of the SW South American Gondwana margin: a combined U–Pb and Hf-isotope study of single detrital zircons. Journal of the Geological Society 163(6), 983-995.

Bachmann, O., Oberli, F., Dungan, M.A., Meier, M., Mundil, R., and Fischer, H., 2007. $^{40}Ar/^{39}Ar$ and U–Pb dating of the Fish Canyon magmatic system, San Juan Volcanic field, Colorado: evidence for an extended crystallization history. Chemical Geology 236(1-2), 134-166.

Bachmann, O., Schoene, B., Schnyder, C., and Spikings, R., 2010. The $^{40}Ar/^{39}Ar$ and U/Pb dating of young rhyolites in the Kos-Nisyros volcanic complex, Eastern Aegean Arc, Greece: age discordance due to excess ^{40}Ar in biotite. Geochemistry, Geophysics, Geosystems, 11(8). Available at: https://doi.org/10.1029/2010GC003073 (Accessed: 29 November 2018).

Bailo, T., Schandelmeier, H., Franz, G., Sun, C.H., and Stern, R.J., 2003. Plutonic and metamorphic rocks from the Keraf Suture (NE Sudan): a glimpse of Neoproterozoic tectonic evolution on the NE margin of W. Gondwana. Precambrian Research 123(1), 67-80.

Baksi, A.K., 2003. Critical evaluation of $^{40}Ar/^{39}Ar$ ages for the Central Atlantic Magmatic Province: timing, duration and possible migration of magmatic centers. Washington DC American Geophysical Union Geophysical Monograph Series 136, 77-90.

Barker, A.J., 2013. Introduction to metamorphic textures and microstructures. Second edition. New York, Routledge, 162p.

Bhatia, M. R., 1983. Plate tectonics and geochemical composition of sandstones. Journal of Geology 91(6), 611-627.

Bhatia, M. R., and Crook, K. A., 1986. Trace element characteristics of greywackes and tectonic setting discrimination of sedimentary basins. Contributions to Mineralogy and Petrology 92(2), 181–93.

Bird, P. J., 2016. Evolution of the Kibali Granite-Greenstone Belt, North East Democratic Republic of the Congo, and controls on gold mineralisation at the Kibali Gold Deposit. Ph.D thesis, Kingston University, London, 325p.

Bouvier, A., Vervoort, J.D., and Patchett, P.J., 2008. The Lu–Hf and Sm–Nd isotopic composition of CHUR: constraints from unequilibrated chondrites and implications for the bulk composition of terrestrial planets. Earth and Planetary Science Letters 273(1-2), 48-57.

Brandt, S., Klemd, R., and Okrusch, M., 2003. Ultrahigh-temperature metamorphism and multistage evolution of garnet–orthopyroxene granulites from the Proterozoic Epupa Complex, NW Namibia. Journal of Petrology 44(6), 1121-1144.

Cahen, L and Snelling, N.J., 1966. The geochronology of equatorial Africa. North-Holland Publishing Company, Amsterdam, 195p.

Cahen, L., Snelling, N.J., Delhal, J., Vail, J.R., Bonhomme, M. and Ledent, D., 1984. The geochronology and evolution of Africa. Clarendon Press, Oxford, 512p.

Carlsson, D., 2014. Petrographic study of high-grade gneisses, Halland area. Available at: https://www.diva-portal.org/smash/get/diva2:802158/FULLTEXT01.pdf (Accessed: 24 May 2019).

Castaing, C., Feybesse, J.A., Thiéblemont, D., Triboulet, C., and Chevremont, P., 1994. Palaeogeographical reconstructions of the Pan-African/Brasiliano orogen: closure of an oceanic domain or intracontinental convergence between major blocks? Precambrian Research 69(1-4), 327-344.

Cawthorn, R.G., and Brown, P.A., 1976. A model for the formation and crystallization of corundum-normative calc-alkaline magmas through amphibole fractionation. The Journal of Geology 84(4), 467-476.

Chapell, B.W., and White, A.J.R., 1974. Two contrasting granite types. Pacific Geology 8, 173-180.

Chappell, B.W., Bryant, C.J., and Wyborn, D., 2012. Peraluminous I-type granites. Lithos 153, 142–153.

Civetta, L., De Vivo, B., Giunta, G., Ippolito, F., Lima, A., Orsi, G., and Perrone, V., 1979. Geological and structural outlines of the Southern Sudan. Atti dei Convegni Lincei 47, 175-183.

Clarke, D.B., 1992. Granitoid Rocks. Chapman Hall, London, 283p.

Clifford, T.N., 1974. Review of African granulites and related rocks. Geological Society of America 156, 49p.

Chappell, B.W., and Stephens, W.E., 1988. Origin of infracrustal (I-type) granite magmas. Earth and Environmental Science Transactions of the Royal Society of Edinburgh 79(2-3), 71-86.

Collins, W.J., and Richards, S.W., 2008. Geodynamic significance of S-type granites in circum-Pacific orogens. Geology 36, 559-562.

Condie, K.C., 1998. Plate Tectonics and Crustal Evolution. Butterworth-Heinemann, London, 69p.

Corfu, F., 2013. A century of U-Pb geochronology: The long quest towards concordance. Bulletin, 125(1-2), 33-47.

Cutten, H., Johnson, S.P., and De Waele, B., 2006. Protolith ages and timing of metasomatism related to the formation of whiteschists at Mautia Hill, Tanzania: implications for the assembly of Gondwana. The Journal of geology 114(6), 683-698.

Dahl, P.S., 1996. The crystal-chemical basis for Ar retention in micas: inferences from interlayer partitioning and implications for geochronology. Contributions to Mineralogy and Petrology 123(1), 22-39.

Dallmeyer, R.D., 1978. $^{40}Ar/^{39}Ar$ incremental-release ages of hornblende and biotite across the Georgia Inner Piedmont; their bearing on late Paleozoic-early Mesozoic tectonothermal history. American Journal of Science 278(2), 124-149.

Dawoud, A.S., and Schulz-Dobrik, B., 2017. PT conditions of Pan-African granulite facies metamorphism in Sabaloka inlier, north of Khartoum, Sudan. Geoscientific Research in Northeast Africa, CRC Press, 151-154.

Dearnley, R., 1966. Orogenic fold-belts and a hypothesis of earth evolution. Physics and Chemistry of the Earth 7, 1-114.

Deer, W.A., Howie, R.A., and Zussman, J., 1992. An Introduction to the Rock-Forming Minerals. Longman, Essex, UK, 696p.

De Waele, B., Johnson, S.P., and Pisarevsky, S.A., 2008. Palaeoproterozoic to Neoproterozoic growth and evolution of the eastern Congo Craton: Its role in the Rodinia puzzle. Precambrian Research 160, 130-139.

De Wit, M.J., and Linol, B., 2015. Precambrian basement of the Congo Basin and its flanking terrains. In: De Wit, M.J., Guillocheau, F. and De Wit, M.C. (Eds.), Geology and resource potential of the Congo Basin. Springer, Berlin, pp. 19-37.

Dodson, M.H., 1973. Closure temperature in cooling geochronological and petrological systems. Contributions to Mineralogy and Petrology 40(3), 259-274.

Dunn, S.C., 1911. Notes on the mineral deposits of the Anglo-Egyptian Sudan: Bull. Geol. Surv. Sudan 1, 70p.

Elatikpo, S.M., Danbatta, U.A., and Najime, T., 2013. Geochemistry and Petrogenesis of Gneisses around Kafur-Yari Bori-Tsiga area within the Malumfashi Schist Belt, Northwestern Nigeria. Journal of Environment and Earth Science 3(7), 171-181.

Eskola, P.E., 1920. The mineral facies of rocks. Norsk Geologisk Tidsskrift 6, 143-194.

Evensen, N.M., Hamilton, P.J and O'nions, R.K., 1978. Rare-earth abundances in chondritic meteorites. Geochimica et Cosmochimica Acta, 42(8), 1199-1212.

Fernandez-Alonso. M., Tack, L., Tahon, A., and De Waele, B., 2011. The Proterozoic history of the proto-Congo Craton of Central Africa. Abstract volume, 23rd Colloquium of African Geology (CAG23), University of Johannesburg, 142p.

Fielding, L., Najman, Y., Millar, I., Butterworth, P., Ando, S., Padoan, M., Barfod, D., and Kneller, B., 2017. A detrital record of the Nile River and its catchment. Journal of the Geological Society 174(2), 301-317.

Floyd, P. A., and Leveridge, B. E., 1987. Tectonic environment of the Devonian Gramscatho basin, south Cornwall: framework mode and geochemical evidence from turbiditic sandstones. Journal of the Geological Society 144(4), 531–42.

Foland, K. A. 1983. $^{40}Ar/^{39}Ar$ incremental heating plateaux for biotites with excess argon. Chemical Geology 41, 3-21.

Förster, H.J., Tischendorf, G., and Trumbull, R.B., 1997. An evaluation of the Rb vs.(Y+ Nb) discrimination diagram to infer tectonic setting of silicic igneous rocks. Lithos 40(2-4), 261-293.

Fritz, H., Abdelsalam, M., Ali, K.A., Bingen, B., Collins, A.S., Fowler, A.R., Ghebreab, W., Hauzenberger, C.A., Johnson, P.R., Kusky, T.M., and Macey, P., 2013. Orogen styles in the East African Orogen: a review of the Neoproterozoic to Cambrian tectonic evolution. Journal of African Earth Sciences 86, 65-106.

Frost, B. R., Barnes, C. G., Collins, W. J., Arculus R. J., Ellis, D. J., and Frost, C. D., 2001. A geochemical classification for granitic rocks. Journal of Petrology 42, 2033-2048.

Fyfe, W. S., Turner, F. J., and Verhoogen, J., 1958. Metamorphic reactions and metamorphic facies. Geological Society of America, Memoir 73, 259p.

Garzanti, E., Vermeesch, P., Rittner, M., and Simmons, M., 2018. The story of the Nile: Time-structure maps of source rocks and discontinuous propagation of detrital signals. Basin Research 30 (6), 1098-1117.

Ghabrial, D.S., Samuel, M.D., and Moussa, H.E., 2013. Geochemistry and tectonic setting of early Pan-African metamorphosed volcano–sedimentary sequence in southern Solaf zone, SW Sinai, Egypt. Arabian Journal of Geosciences 6(10), 3635-3649.

Goodwin, A.M., 1996. Principles of Precambrian geology. Academic Press, London, 327p.

Grantham, G.H., Maboko, M., and Eglington, B.M., 2003. A review of the evolution of the Mozambique Belt and implications for the amalgamation and dispersal of Rodinia and Gondwana. Geological Society, London, Special Publications 206(1), 401-425.

Griffin, W.L., Wang, X., Jackson, S.E., Pearson, N.J., O'Reilly, S.Y., Xu, X., and Zhou, X., 2002. Zircon chemistry and magma mixing, SE China: in-situ analysis of Hf isotopes, Tonglu and Pingtan igneous complexes. Lithos 61(3-4), 237-269.

Griffin, W.L., Belousova, E.A., Shee, S.R., Pearson, N.J., and O'Reilly, S.Y., 2004. Archaean crustal evolution in the northern Yilgarn Craton: U–Pb and Hf-isotope evidence from detrital zircons. Precambrian Research 131(3-4), 231-282.

Gu, X. X., Liu, J. M., Zheng, M. H., Tang, J. X., and Qi, L., 2002. Provenance and tectonic setting of the Proterozoic turbidites in Hunan, South China: geochemical evidence. Journal of Sedimentary Research 72(3), 393-407.

Harnois, L., 1988. The CIW index: a new chemical index of weathering. Sedimentary Geology 55, 319–22.

Harris, N.B.W., Pearce, J.A., and Tindle, A.G., 1986. Geochemical characteristics of collision-zone magmatism. In: Coward, M.P., Allison, A.C. (Eds.), Collision Tectonics, Geological Society, London, Special Publication, 67-81.

Harris, N., Massey, J., and Inger, S., 1993. The role of fluids in the formation of High Himalayan leucogranites. Geological Society, London, Special Publications 74(1), 391-400.

Hart, S.R., 1964. The petrology and isotopic-mineral age relations of a contact zone in the Front Range, Colorado. The Journal of Geology 72(5), 493-525.

Hayashi, K.I., Fujisawa, H., Holland, H. D., and Ohmoto, H., 1997. Geochemistry of 1.9 Ga sedimentary rocks from northeastern Labrador, Canada. Geochimica et Cosmochimica Acta 61(19), 4115–37.

Hepworth, J.V., 1964. Explanation of the geology of sheets 19, 20, 28 and 29 (Southern West Nile). Geology survey of Uganda Report 10, 128p.

Hepworth, J.V., and Macdonald, R., 1966. Orogenic belts of the northern Uganda basement. Nature 210(5037), 726p.

Hepworth, J.V., 1972. The Mozambique orogenic belt and its foreland in northeast Tanzania: a photogeologically-based study. Journal of the Geological Society 128(5), 461-494.

Herron. M. M., 1988. Geochemical classification of terrigenous sands and shales from core or log data. Journal of Sedimentary Petrology 58 (5), 820-829.

Hoskin, P.W.O., and Black, L.P., 2000. Metamorphic zircon formation by solid-state recrystallization of protolith igneous zircon. Journal of Metamorphic Geology, 18(4), 423-439.

Hua Lo, C., Lee. J.K.W., and Onstott. T.C., 2000. Argon release mechanism of biotite in vacuo and the role of short-circuit diffusion and recoil. Chemical Geology 165, 135-166.

Huntington, K.W., Blythe, A.E., and Hodges, K.V., 2006. Climate change and Late Pliocene acceleration of erosion in the Himalaya. Earth and Planetary Science Letters 252(1-2), 107-118.

Hunting Geology and Geophysics Ltd.., 1967. Assessment of the mineral potential of the Aswan region. United Arab Republic photo-geological survey: United Nations Development Programme, United Arab Republic Regional planning of Aswan, 138p.

Ibrahim, M.E., Saleh, G.M., and El-Naby, H.A., 2001. Uranium mineralization in the two-mica granite of Gabal Ribdab area, South Eastern Desert, Egypt. Applied Radiation and Isotopes 55(6), 861-872.

Ibrahim, M.E., Saleh, G.M., Ibrahim, I.H., Oraby, F., El Hassan, E.A., and Azab, M.S., 2005. Comparative study between pegmatitic and equigranular peraluminous granites, south eastern desert, Egypt. In: The 9th International Mining, Petroleum, and Metallurgical Engineering Conference, Cairo, University, Egypt, 21-24 February.

Irvine, T.N.J., and Baragar, W.R.A., 1971. A guide to the chemical classification of the common volcanic rocks. Canadian Journal of Earth Sciences 8(5), 523-548.

Jiang, N., Guo, J., Zhai, M., and Zhang, S., 2010. ~ 2.7 Ga crust growth in the North China craton. Precambrian Research 179(1-4), 37-49.

Jin, Z., Li, F., Cao, J., Wang, S., and Yu, J., 2006. Geochemistry of Daihai Lake sediments, Inner Mongolia, north China: implications for provenance, sedimentary sorting, and catchment weathering. Geomorphology 80(3-4), 147-163.

Johnson, P.R., and Woldehaimanot, B., 2003. Development of the Arabian-Nubian Shield: perspectives on accretion and deformation in the northern East African Orogen and the assembly of Gondwana. In: Yoshida, M., Windley, B.F., and Dasgupta, S., (Eds.), Proterozoic East Gondwana: supercontinent assembly and breakup. Geological Society, London, special publications 206, pp. 289-325.

Kabete, J.M., McNaughton, N.J., Groves, D.I., and Mruma, A.H., 2012. Reconnaissance SHRIMP U–Pb zircon geochronology of the Tanzania Craton: evidence for Neoarchaean granitoid–greenstone belts in the Central Tanzania Region and the Southern East African Orogen. Precambrian Research 216, 232-266.

Karmakar, S., and Schenk, V., 2015. Neoproterozoic metamorphic events along the eastern margin of the East Sahara Ghost Craton at Sabaloka and Bayuda, Sudan: Petrology and texturally controlled in-situ monazite dating. Precambrian Research 269, 217-241.

Katumwehe, A.B., Abdelsalam, M.G., Atekwana, E.A., and Laó-Dávila, D.A., 2016. Extent, kinematics and tectonic origin of the Precambrian Aswa Shear Zone in eastern Africa. Gondwana Research 34, 241-253.

Kennedy, W.Q. 1964.The structural differentiation of Africa in the Pan-African (± 500 m.y.) Tectonic Episode. 8th Annual Report of the Research Institute of African Geology, University of Leeds, 48-49.

Kinny, P.D. and Maas, R., 2003. Lu–Hf and Sm–Nd isotope systems in zircon. Reviews in mineralogy and geochemistry, 53(1), 327-341.

Koteas, G.C., Williams, M.L., Seaman, S.J., and Dumond, G., 2010. Granite genesis and mafic-felsic magma interaction in the lower crust. Geology 38(12), 1067-1070.

Kröner, A., Jaeckel, P., and Williams, I.S., 1994. Pb-loss patterns in zircons from a high-grade metamorphic terrain as revealed by different dating methods: U-Pb and Pb-Pb ages for igneous and metamorphic zircons from northern Sri Lanka. Precambrian Research 66(1-4), 151-181.

Kröner, A., Willner, A.P., Hegner, E., Jaeckel, P., and Nemchin, A., 2001. Single zircon ages, PT evolution and Nd isotopic systematics of high-grade gneisses in southern Malawi and their bearing on the evolution of the Mozambique belt in southeastern Africa. Precambrian Research 109(3-4), 257-291.

Kröner, A., Muhongo, S., Hegner, E., and Wingate, M.T.D., 2003. Single-zircon geochronology and Nd isotopic systematics of Proterozoic high-grade rocks from the Mozambique Belt of southern Tanzania (Masasi area): implications for Gondwana assembly. Journal of the Geological Society 160(5), 745-757.

Kröner, A., Wan, Y., Liu, X., and Liu, D., 2014. Dating of zircon from high-grade rocks: Which is the most reliable method? Geoscience Frontiers 5(4), 515-523.

Kuiper, Y.D., 2002. The interpretation of inverse isochron diagrams in $^{40}Ar/^{39}Ar$ geochronology. Earth and Planetary Science Letters 203(1), 499-506.

Lalonde, A.E., and Bernard, P., 1993. Composition and color of biotite from granites; two useful properties in characterization of plutonic suites from the Hepburn internal zone of Wopmay Orogen, Northwest Territories. The Canadian Mineralogist 31(1), 203-217.

Lang, X., Liu, D., Deng, Y., Tang, J., Wang, X., Yang, Z., Cui, Z., Feng, Y., Yin, Q., Xie, F., and Huang, Y., 2019. Detrital zircon geochronology and geochemistry of Jurassic sandstones

in the Xiongcun district, southern Lhasa subterrane, Tibet, China. In: Implications for provenance and tectonic setting. Geological Magazine 156(4), 683-701.

Lawley, C., 2012. Geochronology and structure of the Lupa goldfield, Tanzania. Ph.D thesis, Durham University, UK, 220p.

Leggo, J., 1974. A geochronological study of the Basement Complex of Uganda. Journal of the Geological Society, London 130, 263-277.

Link, K., Köhn, D., Barth, M., Tiberindwa, J., Barifaijo, E., Aanyu, K., and Foley, S., 2010. Continuous cratonic crust between the Congo and Tanzania blocks in western Uganda. International Journal of Earth Sciences 99(7), 1559-1573.

Maboko, M.A.H., 2001. Dating post-metamorphic cooling of the Eastern Granulites in the Mozambique Belt of northern Tanzania using the garnet Sm-Nd method. Gondwana Research 4(3), 329-336.

Maboko, M.A.H., and Nakamura, E., 2002. Isotopic dating of Neoproterozoic crustal growth in the Usambara Mountains of Northeastern Tanzania: evidence for coeval crust formation in the Mozambique Belt and the Arabian–Nubian Shield. Precambrian Research 113(3-4), 227-242.

Macdonald, R., 1964. "Charnockites" in the West Nile district of Uganda: A systematic study in the Groves' type area. In: proceedings of the 22nd International Geological Congress 13, New Dehli, 227-249.

Maniar, P.D., and Piccioli, P.M., 1989. Tectonic discrimination of granitoids. Geological Society of America Bulletin 101(5), 635-643.

Mänttäri, I., 2014. Mesoarchaean to Neoproterozoic U-Pb and Sm-Nd ages from Uganda. In: Lehto, T. and Katto, E. (Eds.). GTK Consortium Geological Surveys in Uganda 2008−2012. Geological Survey of Finland, Special Paper 56, pp. 121-164.

Marais, T., 2016. The southeastern 'basement' complex of South Sudan. [Power point presentation]. Abstract, 35th international Geological Congress, Cape Town, South Africa. Available at https://www.americangeosciences.org/igc/16759 [Accessed: 05 July 2017].

Marc, D. 1992. Granites and rhyolites from the northwestern USA: temporal variation in magmatic processes and relations to tectonic setting. Earth Science, Transactions of the Royal Society of Edinburgh 83, 50-65.

Martin, P., and Martin K., 2017. Baseline assessment of small scale and artisanal gold mining in Central and Eastern Equatoria state, South Sudan. South Sudan Mining Report by COIPA INTERNATIONAL. Available at: http://www.coipamining.com/mining_research/pdf/el-technical21.pdf (Accessed: 05 August 2017).

Master, S., Woldai, T., Armstrong, R.A., 2016. The Chaine des Mongos- a newly discovered Precambrian fold belt in Central African Republic and South Sudan. Abstract, 35th international Geological Congress, Cape Town, South Africa. Available at

https://www.americangeosciences.org/sites/default/files/igc/4002.pdf [Accessed: 07 June 2019].

Matteini, M., Dantas, E.L., Pimentel, M.M., and Bühn, B., 2010. Combined U-Pb and Lu-Hf isotope analyses by laser ablation MC-ICP-MS: methodology and applications. Anais da Academia Brasileira de Ciências 82(2), 479-491.

McDonald. C. S., Regis, D., Warren. C. J., Kelley, S. P., and Sherlock. S. C. 2018. Recycling argon through metamorphic reactions: The record in symplectites. Lithos 301, 200-211.

McDougall, I., and Harrison, T.M., 1999. Geochronology and Thermochronology by the $^{40}Ar/^{39}Ar$ Method. Oxford University Press, New York, 212p.

McKenna, A., 2011. Fula rapids, South Sudan. In Encyclopedia Brittanica Online. Available at https://www.britannica.com/place/Bahr-al-Jabal [Accessed: 16 July 2020].

McLennan, S.M., and Taylor, S.R., 1991. Sedimentary rocks and crustal evolution: tectonic setting and secular trends. The Journal of Geology 99(1), 1–21.

Merrihue, C., and Turner, G., 1965. Potassium-Argon dating by activation with fast neutrons. Journal of Geophysical Research 71, 2852-2857.

Mestraud, J.L., Bouvier, P., Dongala, M., and Touveron, G., 1964. Carte géologique de la République Centrafricaine. Bureau de recherches géologiques et minières, Orleans, 186p.

Middlemost, E.A., 1994. Naming materials in the magma/igneous rock system. Earth-Science Reviews 37(3-4), 215-224.

Miettaux, F., 2013. Jebel Kujur-Juba in the making. Available at http://jubainthemaking.com/jebel-kudjur/ [Accessed: 10 July 2020].

Mishra, B.K., Rao, N.S. Rautray, S., and Pattanayak, S., 2014. An Integrated Geoscientific Approach to define zones of gold mineralization. Open Journal of Geology 4, 190-197.

Miyashiro, A., 1974. Volcanic rock series in island arcs and active continental margins. American Journal of Science 274, 321-343.

Muhongo, S., Kröner, A., and Nemchin, A.A., 2001. Single zircon evaporation and SHRIMP ages for granulite-facies rocks in the Mozambique Belt of Tanzania. The Journal of Geology 109(2), 171-189

Muller, D., Rock, N.M.S., and Groves, D.I., 1992. Geochemical discrimination between shoshonitic and potassic volcanic rocks in different tectonic settings. A pilot study: Mineralogy and Petrology 46, 259–289.

Nesbitt, H.W., and Young, G.M., 1982. Early Proterozoic climates and plate motions inferred from major element chemistry of lutites. Nature 299(5885), 715–717.

Nesbitt, H.W., and Young, G.M., 1984. Prediction of some weathering trends of plutonic and volcanic rocks based on thermodynamic and kinetic considerations. Geochimica et Cosmochimica Acta 48(7), 1523-1534.

Nesbitt. H. W., and Young. G. M., 1989. Formation and diagenesis of weathering profiles. The Journal of Geology 97(2), 129–47.

Paine, J.H., Nomade, S., and Renne, P.R., 2006. Quantification of ^{39}Ar recoil ejection from GA1550 biotite during neutron irradiation as a function of grain dimensions. Geochimica et Cosmochimica Acta 70(6), 1507-1517.

Pál-Molnár, E., Lelkes-Felvári, G., Batki, A., and Sassi, R., 2005. Metamorphic petrology and geochemistry of the Sarkadkeresztúr Basement-High with special regard to orthogneiss (Tisza Mega-unit, SE Hungary). Acta Geologica Hungarica 48(4), 395-418.

Passchier, C.W., 1982. Mylonitic deformation in the Saint-Barthélemy Massif, French Pyrenees: with emphasis on the genetic relationship between ultramylonite and pseudotachylyte. GUA Papers of Geology 1, 16-1982.

Passchier, C.W., and Trouw, R.A., 2005. Microtectonics. Springer, Berlin, 366p.

Pearce, J.A. Harris, N.B.W., and Tindle, A.G., 1984. Trace element discrimination diagrams for the tectonic interpretation of granitic rocks. Journal of Petrology 25, 956-983.

Poidevin, J.L., 1994. Boninite-like rocks from the Palaeoproterozoic greenstone belt of Bogoin, Central African Republic: geochemistry and petrogenesis. Precambrian Research 68, 97–113.

Pryer, L.L., 1993. Microstructures in feldspars from a major crustal thrust zone: the Grenville Front, Ontario, Canada. Journal of Structural Geology 15(1), 21-36.

Renne, P.R., Mundil, R., Balco, G., Min, K., R., and Ludwig, K.R., 2010. Joint determination of ^{40}K decay constants and ^{40}Ar/^{40}K for the Fish Canyon sanidine standard, and improved accuracy for ^{40}Ar/^{39}Ar geochronology. Geochimica et Cosmochimica Acta 74, 5349–5367.

Roberts, M.P., and Clemens, J.D., 1993. Origin of high-potassium, I-type, calc-alkaline granitoids. Geology 21, 825–828

Roser, B.P., and Korsch, R.J., 1986. Discrimination of tectonic setting of sandstone-mudstone suites using SiO_2 content and K_2O/Na_2O ratio. The Journal of Geology 94, 635-649.

Roser, B.P., and Korsch, R.J., 1988. Provenance signatures of sandstone-mudstonesuitesdeterminedusingdiscriminant function analysis of major-element data. Chemical Geology 67(1), 119–39.

Rubatto, D., 2017. Zircon: the metamorphic mineral. Reviews in mineralogy and geochemistry, 83(1), 261-295.

Rustad, B.K., 2010. Microstructural and metamorphic study in rocks of the Seiland Igneous Province between Langfjord and Øksfjord, Alta kommune, Northern Norway. Master's thesis, University of Tromsø, Norway, 116p.

Saalmann, K., Mänttäri, I., Nyakecho, C., and Isabirye, E., 2016. Age, tectonic evolution and origin of the Aswa Shear Zone in Uganda: activation of an oblique ramp during convergence in the East African Orogen. Journal of African Earth Sciences 117, 303-330.

Scheibner, E., 1985. Suspect terranes in the Tasman fold belt system, eastern Australia. In: Howell, D.G. (Eds.), Tectonostratigraphic Terranes of the Circum-Pacific Region. Circum-Pacific Council for Energy and Mineral Resources, Houston, 493–514.

Schenk, V., Schumann, A., Jöns, N., Loose, D., Tiberindwa, J.V., Wegner, H., and Wittig, N., 2002. Petrological evidence for crustal thickening, ultra-high temperatures and isobaric cooling in Archaean granulite-facies gneisses from the West Nile area (Uganda). In: Abstracts Volume of the 19th Colloquium of African Geology, El Jadida, Morocco, 165-166.

Schenk, V., Wegner, H., Appel, P., and Schumann, A., 2004. Pan-African granulite-facies reworking of Archaean granulites in the West Nile region (Congo craton; Uganda). In: Abstracts volume of the 20th Colloquium of African Geology. BRGM, Orleans, France, 364p.

Scherer, E.E., Whitehouse, M.J. and Munker, C., 2007. Zircon as a monitor of crustal growth. Elements, 3(1), 19-24.

Schlüter. T., 2006. Geological Atlas of Africa. Springer-Verlag Berlin. Heidelberg Edition 1, 80-87.

Schmitz, M.D., Vervoort, J.D., Bowring, S.A., and Patchett, P.J., 2004. Decoupling of the Lu-Hf and Sm-Nd isotope systems during the evolution of granulitic lower crust beneath southern Africa. Geology 32(5), 405-408.

Shand, S.J., 1943. Eruptive rocks: their genesis, composition, classification, and their relation to ore deposits with a chapter on meteorites. Hafner Publishing Company, New York, 4889p.

Shelley, D., 1993. Igneous and metamorphic rocks under the microscope: classification, textures, microstructures and mineral preferred-orientations. Chapman & Hall, London, 445p.

Smith, M.E., Singer, B.S., Carroll, A.R., and Fournelle, J.H., 2008. Precise dating of biotite in distal volcanic ash: Isolating subtle alteration using $^{40}Ar/^{39}Ar$ laser incremental heating and electron microprobe techniques. American Mineralogist 93(5-6), 784-795.

Snelling, N.J., 1962. Age determination unit. Overseas Geological Survey, Annual Report 61, 27-35.

Snelling, N.J., 1964. A review of age determinations from Northern Rhodesia. Economic Geology 59(6), 961-981.

Stern, R.J., 1994. Arc assembly and continental collision in the Neoproterozoic East African Orogen: implications for the consolidation of Gondwanaland. Annual Review of Earth and Planetary Sciences 22(1), 319-351.

Stern, R.J., 2002. Crustal evolution in the East African Orogen: a neodymium isotopic perspective. Journal of African Earth Sciences 34(3-4), 109-117.

Sun., S. S., and McDonough. W. F., 1989. Chemical and isotopic systematics of oceanic basalts; implications for mantle composition and processes. In: Saunders, A. D., and Norry, M. J. (Eds), Magmatism in the ocean basins. Geological Society of London, Special Publication, pp. 313-345.

Tack, L., Wingate, M.T.D., De Waele, B., Meert, J.G., Belousova, E., Griffin, B., Tahon, A., and Fernandez-Alonso, M., 2009. The Mesoproterozoic "Kibaran Event" in Central Africa: a 1375 Ma intracratonic emplacement of a Large Igneous Province (LIP). Abstract, Geological Society of London Fermor Meeting, Edinburgh, 1p.

Tanner, P.W.G., 1973. Regional metamorphism of low pressure intermediate type in the Ruwenzori fold belt of East Africa. Research Institute for African Geology, University of Leeds, Annual report 17, 20-26.

Tang, L., Pan, M., Tsunogae, T., Takamura, Y., Tsutsumi, Y., and Rakotonandrasana, N.O.T., 2018. Cordierite-bearing granulites from Ihosy, southern Madagascar: Petrology, geochronology and regional correlation of suture zones in Madagascar and India. Geoscience Frontiers. Available at: https://doi.org/10.1016/j.gsf.2018.05.014 (Accessed: 25 May 2019).

Taylor, S.R., and McLennan, S.M., 1985. The Continental Crust: Its Evolution and Composition. Blackwell Science, London, 312p.

Thomas, R.J., Bushi, M., Roberts, N.M.W., and Jacobs, J., 2014. Geochronology of granitic rocks from the Ruangwa region, southern Tanzania-Links with NE Mozambique and beyond. Journal of African Earth Sciences 100, 70-80.

Thompson, R.N., 1983. Continental flood basalts: Arachnids rule OK?. In: Hawkesworth, C.J., and Norry, M.J. (Eds.), Continental Basalts and Mantle Xenoliths, Shiva, Nantwich, 158-185.

Tshwane, I., 2016. Geochronology and origin of quartzofeldspathic biotite paragneisses from Jebel Kujur, Juba, South Sudan. Honours project report, University of the Witwatersrand, South Africa, 55p.

Xiong, Q., Zheng, J., Griffin, W.L., O'Reilly, S.Y., and Pearson, N.J., 2012. Decoupling of U–Pb and Lu–Hf isotopes and trace elements in zircon from the UHP North Qaidam orogen, NE Tibet (China): tracing the deep subduction of continental blocks. Lithos 155, 125-145.

Vail, J. R., 1975. Geological map. The Democratic Republic of Sudan and adjacent areas. DOS 1203A and DOS 1203B. 1:2 000 000. Directorate of Overseas Surveys, British Government Ministry of Overseas Development.

Vail, J.R., 1978. Outline of the geology and mineral deposits of the Democratic Republic of the Sudan and adjacent areas. Overseas Geology and Mineral Resources 49, 66p.

Vail, J.R., 1985. Alkaline ring complexes in Sudan. Journal of African Earth Sciences 3(1-2), 51-59.

Vail, J. R., 1987. Late Proterozoic tectonic terranes in the Arabian-Nubian Shield and their characteristic mineralization. Geological Journal 22, 161-174.

Vail, J. R., 1990. Geochronology of the Sudan. Overseas Geology and mineral resources 66, 58p.

Vavassis, I., De Bono, A., Stampfli, G.M., Giorgis, D., Valloton, A., and Amelin, Y., 2000. U-Pb and Ar-Ar geochronological data from the Pelagonian basement in Evia (Greece): geodynamic implications for the evolution of Paleotethys. Schweizerische Mineralogische und Petrographische Mitteilungen 80, 21-43.

Vervoort, J.D., Patchett, P.J., Blichert-Toft, J., and Albarède, F., 1999. Relationships between Lu-Hf and Sm-Nd isotopicsystems in the global sedimentary system. Earth and Planetary Science Letters 168, 79–99.

Vervoort, J.D., 2015. Lu-Hf Dating: The Lu-Hf Isotope System. In: Rink, W.J., and Thompson, J., (Eds.), Encyclopedia of Scientific Dating Methods, Springer, Netherlands, pp. 379-390.

Vernon, R.H., 2004. A Practical Guide to Rock Microstructure. Cambridge University Press, Cambridge, 594p.

Welay, G.G., 2014. Geology, Geochemistry and geochronology of Neoproterozoic rocks in western Shire, Northern Ethiopia. Masters thesis. University of Oslo, Norway, 88p.

Werner, C.D., 1987. Saxonian Granulites - a contribution to the geochemical diagnosis of original rocks in high-metamorphic complexes. Gerlands Beitrage zur Geophysik 96, 271-290.

Westerhof, A.B., Härmä, P., Isabirye, E., Katto, E., Koistinen, T., Kuosmanen, E., Lehto, T., Lehtonen, M.I., Mäkitie, H., Manninen, T., and Mänttäri, I., 2014. Geology and geodynamic development of Uganda with explanation of the 1: 1,000,000 scale geological map. Geological Survey of Finland, Espoo, Special Paper 55.

Whalen J.B., Currie K.L., and Chappell B.W., 1987. A-type granites: geochemical characteristics, discrimination and petrogenesis. Contributions to Mineralogy and Petrology 95, 407-419.

Whiteman, A.J., 1971. The geology of the Sudan Republic. Clarendon Press, Oxford, 290p.

Winchester, J.A., and Floyd, P.A., 1977. Geochemical discrimination of different magma series and their differentiation products using immobile elements. Chemical Geology 20, 325-343.

Worrall, G.A., 1957. A simple introduction to the geology of the Sudan. Sudan Notes and Records 38, 2-9.

Wu, F.Y., Yang, Y.H., Xie, L.W., Yang. J.H., and Xu, P., 2006. Hf isotopic compositions of the standard zircons and baddeleyites used in U-Pb geochronology. Chemical Geology 234(1-2), 105–126.

Xiao, L., Zhao, B., Duan, P., Shi, Z., Ma, J., and Lin, M., 2016. Geochemical characteristics of trace elements in the No. 6 coal seam from the Chuancaogedan Mine, Jungar Coalfield, Inner Mongolia, China. Minerals 6(2), 28p.

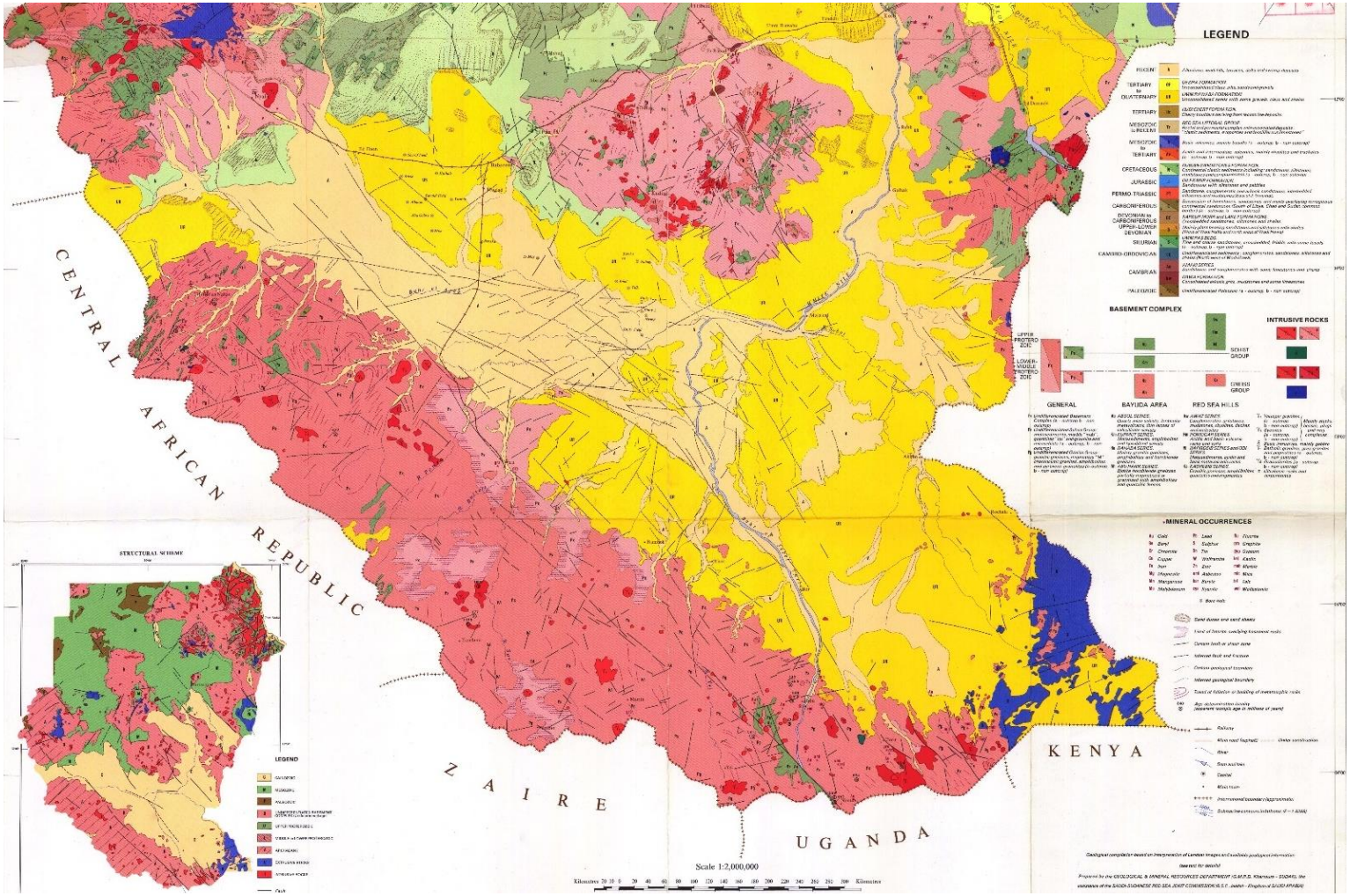
Xiong, Q., Zheng, J., Griffin, W.L., O'Reilly, S.Y., and Pearson, N.J., 2012. Decoupling of U–Pb and Lu–Hf isotopes and trace elements in zircon from the UHP North Qaidam orogen, NE Tibet (China): tracing the deep subduction of continental blocks. Lithos 155, 125-145.

Yassin, Y., Khalil, F.A., and Shafie, G.E., 1984. Explanatory notes to the geological map at the scale 1:2000000 of the Democratic Republic of the Sudan-Bull. Geological and Mineral Resources Department 35, 1-19.

Yoshimura, Y., Motoyoshi, Y., and Miyamoto, T., 2008. Sapphirine + quartz association in garnet: implication for ultrahigh-temperature metamorphism at Rundvågshetta, Lützow-Holm Complex, East Antarctica. Satish-Kumar, M., Motoyoshi, Y., Osanai, Y., Hiroi, Y., and Shiraishi, K., (Eds.), Geodynamic Evolution of East Antarctica: a Key to the East–West Gondwana Connection. Geological Society, London, Special Publication 308, pp. 377-390.

Appendices

Appendix A: Geological map of the Sudan (Vail, 1975)



Appendix B: Geochemical data

Table 1B: Major elements for the granitic gneisses and biotite schists from the Basement Complex, standards highlighted in yellow.

Sample number	(wt%)	SiO2	Al2O3	Fe2O3	FeO	MnO	MgO	CaO	Na2O	K2O	TiO2	P2O5	Cr2O3	NiO	LOI	Total
JK/1		74,84	13,50	0,12	0,97	0,04	0,22	1,27	3,27	5,15	0,13	0,03	0,00	0,00	0,31	99,84
JK/2		75,48	13,44	0,05	0,38	0,01	0,06	1,04	3,39	5,32	0,04	0,02	0,00	0,00	0,25	99,46
JK/3		74,72	14,39	0,12	0,95	0,03	0,19	1,21	4,57	3,79	0,10	0,03	-0,01	0,00	0,24	100,32
JK/4		75,48	13,44	0,05	0,38	0,01	0,06	1,04	3,39	5,32	0,04	0,02	0,00	0,00	0,25	99,46
JK/5		74,72	14,39	0,12	0,95	0,03	0,19	1,21	4,57	3,79	0,10	0,03	-0,01	0,00	0,24	100,32
JK/6		55,63	18,48	0,84	6,82	0,14	4,94	3,14	3,62	4,12	1,13	0,05	0,05	0,02	0,72	99,70
CRMs (Standards)	(wt%)	SiO2	Al2O3	Fe2O3	FeO	MnO	MgO	CaO	Na2O	K2O	TiO2	P2O5	Cr2O3	NiO	LOI	TOTAL
NIM-P		51,79	4,31	1,28	10,38	0,23	25,59	2,64	0,34	0,09	0,19	0,02	3,52	0,08	-0,23	100,46
NIM-D		38,59	0,32	1,71	13,85	0,22	43,81	0,30	0,04	0,01	0,03	0,02	0,48	0,26	-0,51	99,64
W2		52,54	15,39	1,09	8,79	0,16	6,40	10,91	2,21	0,63	1,06	0,13	0,00	0,01	0,19	99,34
NIM-S		64,69	17,54	0,14	1,15	0,01	0,46	0,68	0,36	15,50	0,05	0,12	0,00	0,00	0,42	100,69
GSP2		67,15	15,03	0,50	4,03	0,04	0,98	2,14	2,81	5,49	0,67	0,30	0,00	0,00	0,87	99,12
BCR2		55,04	13,72	1,39	11,27	0,20	3,64	7,20	3,20	1,82	2,29	0,36	0,00	0,00	0,10	100,11
NIM-N		53,24	16,72	0,91	7,34	0,18	7,56	11,52	2,44	0,25	0,20	0,02	0,00	0,02	0,04	100,36
NIM-G		76,14	12,23	0,20	1,62	0,02	0,05	0,79	3,33	5,06	0,10	0,01	0,00	0,00	0,73	99,53
PCC1		44,74	0,73	0,87	7,03	0,13	45,86	0,59	0,04	0,00	0,01	0,01	0,51	0,33	5,09	100,87
BHVO2		50,35	13,71	1,24	10,04	0,17	7,31	11,46	2,22	0,52	2,78	0,27	0,04	0,02	-0,48	100,12
AGV2		60,07	17,18	0,68	5,51	0,10	1,82	5,26	4,29	2,94	1,05	0,48	0,00	0,00	1,80	99,34
G2		69,86	15,48	0,27	2,19	0,04	0,77	1,95	4,07	4,53	0,49	0,14	0,00	0,00	0,64	99,76
DTS1		40,57	0,26	0,86	6,99	0,12	49,88	0,16	0,08	0,00	0,01	0,01	0,71	0,32	-0,02	99,97
SIO2		97,28	0,10	0,00	0,02	0,00	0,04	0,03	-0,03	0,00	0,01	0,01	0,00	0,00	0,00	97,44
BHVO2		50,48	13,70	1,24	10,05	0,16	7,31	11,47	2,23	0,52	2,77	0,28	0,05	0,02	-0,48	100,28
AGV2		60,17	17,15	0,68	5,51	0,10	1,82	5,28	4,32	2,93	1,05	0,48	0,00	0,00	1,80	99,47
G2		69,66	15,45	0,27	2,19	0,03	0,77	1,95	4,09	4,52	0,49	0,14	0,00	0,00	0,64	99,54
DTS1		40,51	0,26	0,87	7,03	0,12	49,87	0,16	0,09	0,00	0,01	0,01	0,70	0,32	-0,02	99,94

Table 2B: Trace and Rare Earth Elements for the granitic gneisses and biotite schists from the basement complex, standards highlighted in yellow.

(ppm)	BCR2	BHVO2	JK/1	JK2	JK3	JK4	JK5	JK/6
Li	10,59	4,69	18,88	5,39	14,89	13,25	137,02	162,61
P	1564,75	1182,72	107,00	29,73	100,96	76,51	101,80	173,55
Sc	32,13	30,88	5,36	0,29	0,56	2,00	8,34	12,33
Ti	13019,76	15603,31	643,33	143,37	516,70	566,23	8055,31	6173,77
V	423,87	321,51	5,80	1,27	5,47	7,62	229,21	178,59
Cr	16,59	292,15	19,67	1,39	3,75	7,66	439,15	321,65
Co	36,64	45,95	2,21	0,18	1,17	1,44	46,88	35,02
Ni	12,67	112,27	52,47	1,46	3,60	6,59	208,94	150,43
Cu	22,26	125,85	7,46	1,00	3,32	3,83	79,15	104,04
Zn	137,17	115,26	25,65	6,39	30,36	25,17	215,57	149,54
Ga	22,32	21,36	16,96	8,43	19,79	20,53	25,58	24,54
Rb	49,27	10,05	121,46	50,34	105,51	114,18	265,03	203,97
Sr	315,90	388,27	121,41	21,03	28,82	25,25	67,67	88,25
Y	30,75	23,19	7,16	2,29	5,57	7,14	8,07	10,24
Zr	186,10	167,09	61,30	24,80	40,32	53,64	112,59	119,41
Nb	11,91	17,73	8,39	1,23	10,23	16,27	8,41	8,96
Ba	666,95	123,88	501,57	22,67	125,22	138,08	357,57	378,55
Sn	2,66	2,37	4,20	0,24	2,11	3,91	2,70	3,19
Cs	1,15	0,11	0,54	0,14	0,22	0,21	3,45	2,99
La	24,47	15,62	23,82	4,06	22,86	9,11	11,14	13,04
Ce	50,83	36,76	50,83	8,42	48,65	22,45	31,41	26,35
Pr	6,21	5,08	4,56	0,97	4,31	1,73	2,31	2,87
Nd	27,29	23,75	16,78	4,03	15,82	6,36	9,40	11,65
Sm	6,33	5,77	3,43	1,03	3,52	1,51	2,03	2,47
Eu	1,95	1,96	0,66	0,16	0,26	0,17	0,71	0,95
Gd	6,44	5,96	3,18	0,93	3,30	1,50	1,97	2,31
Tb	0,96	0,85	0,35	0,10	0,39	0,21	0,25	0,30
Dy	5,90	4,98	1,65	0,51	1,69	1,20	1,46	1,91
Ho	1,19	0,92	0,27	0,09	0,22	0,22	0,29	0,42
Er	3,29	2,30	0,72	0,22	0,46	0,62	0,87	1,34
Tm	0,47	0,30	0,11	0,03	0,05	0,10	0,13	0,23
Yb	3,25	1,99	0,86	0,21	0,36	0,78	1,04	1,71
Lu	0,47	0,26	0,14	0,03	0,06	0,12	0,15	0,26
Hf	4,88	4,21	1,94	1,27	1,43	2,03	2,93	3,13
Ta	0,75	0,98	0,20	0,05	0,81	0,66	0,26	0,31
W	0,56	0,22	0,00	0,01	0,30	0,07	0,05	0,10
Pb	11,11	1,37	31,41	15,97	26,53	25,73	9,06	10,28
Th	5,54	1,17	13,49	6,41	14,48	6,23	4,44	4,07
U	1,742	0,437	0,955	0,394	1,518	1,157	1,055	1,244

Appendix C: Ar-Ar geochronology data

Table 1C: Ar-Ar isotope and age data for sample JK/3 (biotite)

Ar isotope and age data for sample: JK-3_Biotite_32_1__Combi File: Sampl_JK-3_Bt_32_1__Combi.csv

Calculated at 08-05-2016 - 07:45:03

J-value used: 0.001964 +/- 0.000003

Ca/K and Cl/K factors: 2.0153 +/- 0.1137 0.1169 +/- 0.0078 from file: Irrad_ 2016May27_Jvals.csv

Exponential fractionation factor: -0.297999830895521

Common 40Ar/36Ar value used: 298.56 +/- 0.30

number of steps

14

Step name	39Ar-V-Faraday	39/40 Ca+KCorr	Sigma	36/40 Ca+KCorr	sigma	37/39 Ca+KCorr	sigma	38/39 Ca+KCorr	sigma	40/39 rad	Sigma	%39 Ar	Age Ma	+/- 95%	Incl(1/0)	Ca/K	sigma	Cl/K	sigma
7155_JK-3_32_1_10.00A	0.000416	0.011809	4.26E-05	0.001227	1.29E-05	0.009163	0.003818	0.068933	0.001831	53.67	0.493	5.547	180.6	3.252	0	0.018	0.007	0.008	0.000
7156_JK-3_32_1_10.20A	0.000338	0.009949	3.22E-05	0.000489	7.83E-06	0.008631	0.003413	0.071313	0.000538	85.84	0.403	4.510	280.7	2.801	0	0.017	0.006	0.008	0.000
7157_JK-3_32_1_10.40A	0.000509	0.00923	2.21E-05	0.00055	6.08E-06	0.007025	0.001662	0.071553	0.000652	90.55	0.337	6.792	295.0	2.331	0	0.014	0.003	0.008	0.000
7158_JK-3_32_1_10.60A	0.00047	0.009553	3.16E-05	0.000478	6.50E-06	0.000838	0.001933	0.067877	0.001232	89.72	0.403	6.270	292.5	2.694	0	0.001	0.003	0.007	0.000
7160_JK-3_32_1_10.80A	0.000886	0.008697	2.13E-05	0.000312	3.50E-06	0.005232	0.000905	0.064878	0.000726	104.2	0.306	11.81	335.7	2.364	0	0.010	0.001	0.007	0.000
7161_JK-3_32_1_11.00A	0.000629	0.007488	1.60E-05	0.000211	3.60E-06	0.006724	0.001596	0.066267	0.000809	125.1	0.322	8.385	396.0	2.550	0	0.013	0.003	0.007	0.000
7162_JK-3_32_1_11.20A	0.00084	0.006835	1.54E-05	0.000163	3.26E-06	0.006314	0.001566	0.065465	0.001035	139.1	0.335	11.20	435.4	2.611	1	0.012	0.003	0.007	0.000
7163_JK-3_32_1_11.40A	0.001032	0.006559	1.12E-05	0.000145	2.00E-06	0.004057	0.000873	0.065338	0.000776	145.8	0.292	13.76	453.9	2.538	1	0.008	0.001	0.007	0.000
7165_JK-3_32_1_11.60A	0.00055	0.006663	1.60E-05	0.000144	3.10E-06	0	0	0.064442	0.000072	143.6	0.403	7.336	447.8	3.062	1	0	0	0.007	0.000
7166_JK-3_32_1_11.80A	0.000412	0.006671	1.87E-05	0.000141	5.52E-06	0	0	0.065354	0.000974	143.5	0.475	5.494	447.6	3.349	1	0	0	0.007	0.000
7167_JK-3_32_1_12.00A	0.000541	0.006637	1.32E-05	0.00015	3.97E-06	2.59E-05	0.001508	0.064898	0.000732	143.9	0.360	7.220	448.5	2.901	1	5.23E-05	0.003	0.007	0.000
7168_JK-3_32_1_12.20A	0.000228	0.0066	3.05E-05	0.000153	6.72E-06	0	0	0.061431	0.001736	144.6	0.787	3.045	450.5	4.800	1	0	0	0.007	0.000
7170_JK-3_32_1_12.40A	0.000606	0.006759	1.31E-05	0.000168	2.53E-06	0	0	0.063209	0.000679	140.5	0.316	8.080	439.2	2.648	1	0	0	0.007	0.000

7171_JK-3_32_1_12.60A	3.9E-05	0.006581	8.21E-05	0.000468	2.67E-05	0	0	0.061068	0.004699	130.7097	2.423195	0.520121	411.7952	13.13617	0	0	0	0.007139	0.000728

Weighted average of included steps

37/39corr	sigma	38/39corr	Sigma	40/39 rad	sigma	%39Ar sum	Age Ma	+/-95%	Ca/K	Cl/K sigma		sigma
0.003939	7.24E-04	0.064673	3.27E-04	142.9296	0.13715	56.15448	445.887	2.022393	0.007938	0.001526	0.00756	0.000507

Inverse isochron calculation results

40Ar/39Ar(I)	sigma	40Ar/36Ar	Sigma	app. age	+/-95%
222.3139	31.85214	-2887.59	997.4954	652.9153	156.125

End Of Results

Table 2C: Ar-Ar isotope and age data for sample JK/3 (muscovite)

Ar isotope and age data for sample: JK-3_Muscovite_33_1_Combi File: Sampl_JK-3_msc_33_1_Combi.csv

Calculated at 08-05-2016 - 13:48:49

J-value used: 0.001965 +/- 0.000004

Ca/K and Cl/K factors: 2.0153 +/- 0.1137 0.1169 +/- 0.0078 from file: Irrad_ 2016May27_Jvals.csv

Exponential fractionation factor: -0.297999830895521

Common 40Ar/36Ar value used: 298.56 +/- 0.30

number of steps

16

Step name	39Ar-V-Faraday	39/40 Ca+KCorr	Sigma	36/40 Ca+KCorr	sigma	37/39 Ca+KCorr	sigma	38/39 Ca+KCorr	sigma	40/39 rad	Sigma	%39 Ar	Age Ma	+/- 95%	Incl(1/0)	Ca/K	sigma	Cl/K	sigma
7177_JK-3_msc_33_1_10.60A	8.28E-07	0.002043	6.59E-04	0.00362	6.22E-04	4.529296	2.360879	1.65157	0.525585	-39.518	202.2738	0.005456	-145.637	2007.737	0	9.128066	4.785737	0.19306	0.062781
7179_JK-3_msc_33_1_10.80A	3E-06	0.004756	3.11E-04	0.001054	1.53E-03	1.082072	0.324836	0.185179	0.079733	144.116	29.42676	0.019745	449.2615	163.7357	0	2.180741	0.666105	0.021646	0.009432
7180_JK-3_msc_33_1_11.00A	6.9E-05	0.005171	3.87E-05	9.9E-05	2.09E-05	0	0	0.012215	0.004015	187.6686	1.81571	0.454594	565.5928	9.799036	0	0	0	0.001428	0.000479
7181_JK-3_msc_33_1_11.20A	3.33E-05	0.004578	4.00E-05	0.000519	3.22E-05	0	0	0.029912	0.004849	184.5946	3.028124	0.219644	557.6239	15.19533	0	0	0	0.003497	0.000613
7182_JK-3_msc_33_1_11.40A	0.000344	0.00538	1.76E-05	5.21E-05	3.64E-06	0	0	0.013061	0.000853	182.9662	0.634856	2.26338	553.3881	4.006088	1	0	0	0.001527	0.000143
7184_JK-3_msc_33_1_11.60A	0.000994	0.005389	9.09E-06	2.14E-05	2.95E-06	0	0	0.013352	0.000051	184.379	0.349424	6.55201	557.0636	3.07825	1	0	0	0.001561	0.00012
7185_JK-3_msc_33_1_11.80A	0.00032	0.004751	1.43E-05	0.00042	5.01E-06	0	0	0.014108	0.000801	184.1356	0.668931	2.106477	556.4308	4.213304	1	0	0	0.001649	0.000145
7186_JK-3_msc_33_1_12.00A	0.001681	0.005408	6.69E-06	5.68E-05	7.69E-07	0	0	0.01334	0.000393	181.7698	0.246963	11.07555	550.2697	2.683807	1	0	0	0.001559	0.000114
7187_JK-3_msc_33_1_12.20A	0.001878	0.005441	8.78E-06	1.46E-05	5.20E-07	0	0	0.013354	0.000034	182.9925	0.3078	12.37108	553.4565	3.005178	1	0	0	0.001561	0.000112

7189_JK-3_msc_33_1_12.40A	0.003782	0.005418	7.33E-06	7.13E-06	6.29E-07	6.95E-05	0.000496	0.01278	0.000295	184.1655	0.250513	24.92074	556.5085	2.847166	1	0.000014	0.001	0.001494	0.000106
7191_JK-3_msc_33_1_12.60A	0.002631	0.005436	9.58E-06	7.3E-06	9.34E-07	0	0	0.012542	0.000197	183.5654	0.32938	17.3367	554.9479	3.04752	1	0	0	0.001466	0.000101
7192_JK-3_msc_33_1_12.80A	0.002637	0.005417	7.26E-06	1.16E-05	4.44E-07	0.000984	0.000565	0.012802	0.000335	183.9483	0.256292	17.37485	555.9439	2.998067	1	0.001983	0.001145	0.001497	0.000107
7193_JK-3_msc_33_1_13.00A	0.000457	0.005366	1.24E-05	7.23E-05	2.87E-06	0	0	0.010617	0.000944	182.327	0.473058	3.014372	551.7226	3.575244	1	0	0	0.001241	0.000138
7195_JK-3_msc_33_1_13.20A	0.000132	0.00537	3.40E-05	5.84E-05	1.66E-05	0.027636	0.016238	0.008209	0.003782	182.9861	1.476421	0.869358	553.4398	7.621841	1	0.055696	0.032876	0.00096	0.000447
7196_JK-3_msc_33_1_13.40A	0.00011	0.005208	4.28E-05	0.000117	2.49E-05	0.00099	0.016074	0.018881	0.006573	185.3323	2.232003	0.722367	559.5394	11.96674	1	0.001995	0.032395	0.002207	0.000782
7197_JK-3_msc_33_1_13.60A	0.000105	0.005037	4.85E-05	0.000316	1.84E-05	0.006922	0.018011	0.011928	0.002814	179.7829	2.147937	0.693683	545.0789	11.03825	1	0.013949	0.036307	0.001394	0.000342

Weighted average of included steps

37/39corr	sigma	38/39corr	Sigma	40/39rad	sigma	%39Ar sum	Age Ma	+/-95%	Ca/K	sigma	Cl/K	sigma
0.001085	6.41E-04	0.012881	1.39E-04	183.5078	0.112421	99.30056	554.7979	2.561918	0.002187	0.001298	0.001506	0.000102

Inverse isochron calculation results

40Ar/39Ar(I)	sigma	40Ar/36Ar	Sigma	app. age	+/-95%
183.2263	0.221581	296.6044	10.41647	554.0653	2.750295

End Of Results

Table 3C: Ar-Ar isotope and age data for sample JK/6 (biotite)

Ar isotope and age data for sample: JK-6_Biotite_31_3 Combi File: Sampl_JK-6_Bt_31_3_Combi.csv

Calculated at 08-05-2016 - 07:32:55

J-value used: 0.001964 +/- 0.000003

Ca/K and Cl/K factors: 2.0153 +/- 0.1137 0.1169 +/- 0.0078 from file: Irrad_ 2016May27_Jvals.csv

Exponential fractionation factor: -0.297999830895521

Common 40Ar/36Ar value used: 298.56 +/- 0.30

number of steps

14

Step name	39Ar-V-Faraday	39/40 Ca+KCorr	Sigma	36/40 Ca+KCorr	sigma	37/39 Ca+KCorr	sigma	38/39 Ca+KCorr	sigma	40/39 rad	Sigma	%39 Ar	Age Ma	+/- 95%	Incl(1/0)	Ca/K	sigma	Cl/K	sigma
7135_JK-6_31_3_10.20A	1.9E-05	0.005319	1.70E-04	0.00058	1.84E-04	0.28	0.15	0.14	0.03	155.45	10.60	0.09	480.07	57.25	0.00	0.57	0.31	0.02	0.00
7136_JK-6_31_3_10.40A	0.000503	0.005473	1.10E-05	2.97E-05	2.03E-06	0.01	0.00	0.05	0.00	181.08	0.37	2.42	548.25	3.03	1.00	0.02	0.00	0.01	0.00
7137_JK-6_31_3_10.60A	0.001225	0.005526	7.63E-06	1.11E-05	2.01E-06	0.00	0.00	0.04	0.00	180.38	0.27	5.88	546.41	2.72	1.00	0.01	0.00	0.01	0.00
7138_JK-6_31_3_10.80A	0.000809	0.00553	1.77E-05	8.13E-06	3.54E-04	0.01	0.00	0.04	0.00	180.39	0.58	3.89	546.45	3.77	1.00	0.02	0.01	0.01	0.00
7140_JK-6_31_3_11.00A	0.002169	0.005541	1.07E-05	7.08E-06	2.27E-06	0.00	0.00	0.04	0.00	180.08	0.36	10.42	545.64	3.06	1.00	0.00	0.00	0.00	0.00
7141_JK-6_31_3_11.20A	0.005021	0.005498	9.19E-06	4.34E-06	2.45E-06	0.00	0.00	0.04	0.00	181.64	0.32	24.12	549.71	2.95	1.00	0.00	0.00	0.00	0.00
7143_JK-6_31_3_11.40A	0.001611	0.005493	1.86E-05	9.71E-06	2.40E-06	0.00	0.00	0.04	0.00	181.53	0.58	7.74	549.42	3.73	1.00	0.01	0.00	0.00	0.00
7144_JK-6_31_3_11.60A	0.002092	0.005516	1.48E-05	1.17E-05	1.34E-06	0.00	0.00	0.04	0.00	180.65	0.52	10.05	547.13	3.60	1.00	0.00	0.00	0.00	0.00
7146_JK-6_31_3_11.80A	0.001913	0.005521	1.63E-05	3.74E-06	2.27E-06	0.00	0.00	0.04	0.00	180.91	0.56	9.19	547.80	3.87	1.00	0.00	0.00	0.00	0.00
7147_JK-6_31_3_12.00A	0.002352	0.005496	7.73E-06	1.13E-05	8.72E-07	0.00	0.00	0.04	0.00	181.35	0.26	11.30	548.96	2.87	1.00	0.00	0.00	0.00	0.00
7148_JK-6_31_3_12.20A	0.001578	0.005463	8.62E-06	1.57E-05	1.19E-06	0.00	0.00	0.04	0.00	182.19	0.30	7.58	551.14	3.02	1.00	0.01	0.00	0.00	0.00
7149_JK-6_31_3_12.40A	0.001431	0.00542	8.15E-06	1.52E-05	1.40E-06	0.00	0.00	0.04	0.00	183.68	0.30	6.87	555.01	2.92	1.00	0.01	0.00	0.00	0.00
7151_JK-6_31_3_12.60A	6.16E-05	0.005266	5.45E-05	0.000171	2.46E-05	0.01	0.02	0.05	0.01	180.18	2.44	0.30	545.88	13.12	0.00	0.01	0.05	0.01	0.00
7152_JK-6_31_3_12.80A	3.22E-05	0.004615	7.10E-05	0.000593	5.27E-05	0.00	0.00	0.01	0.00	178.28	4.68	0.15	540.93	23.50	0.00	0.00	0.00	0.00	0.00

Weighted average of included steps

37/39corr	sigma	38/39corr	Sigma	40/39 rad	sigma	%39Ar sum	Age Ma	+/-95%	Ca/K	sigma	Cl/K	sigma
0.00277	2.98E-04	0.041249	2.13E-04	181.3147	0.1284	99.4575	548.8566	2.6508	0.0056	0.0007	0.0048	0.0003

Inverse isochron calculation results

40Ar/39Ar(I)	sigma	40Ar/36Ar	Sigma	app. age	+/- 95%
182.6196	38.78903	1452.406	9883.006	552.2587	211.93

End Of Results

Appendix D: U-Pb zircon geochronology data

Table 1D: Operating conditions and data acquisition for U-Pb zircon (Earthlab, University of the Witwatersrand)

ICP-MS	
Instrument	magnetic sector
Manufacturer	Thermo Scientific Instruments
Model	Element XR
RF power [W]	1200-1400
Gas Flows	
Cooling (Ar [l/min]	16
Auxiliary (Ar) [l/min]	0.9-1.0
Sample (Ar) [l/min]	0.3-0.4
Carrier (He) [l/min]	0.9-1.1
N [l/min]	0.02-0.05
Laser	
Instrument	ArF excimer
Manufacturer	Australian Scientific Instruments
Model	Resolution SE155
Wavelength [nm]	193
Spot size [microns]	30
Repetition Rate [Hz]	10-Aug
Laser Fluence [J/cm2]	2.0-2.5

Data Acquisition

Resolution Mode	Low
Protocol	Time-resolved
Scan Mode	E-scan
Scanned Masses	202, 204, 206, 207, 208, 232, 235, 238
Settling Times	0.001
Sample Times	0.0002-0.003
Samples Per Peak	60
Detection Mode	Counting for all isotopes except 238 (analog)
Detector Deadtime [n sec]	25
Background (gas blank) [sec]	two times 15
Ablation Time [sec]	20

Standards

Calibration (primary)	zircon GJ1
Internal	Na
Control (secondary)	Temora-2, Plesovice, 91500

Data Reduction

Software	iolite, in-built into Igor Pro
Data Reduction Scheme(s)	VizualAge

Table 2D: U-Pb zircon geochronology data for sample JK/1

		Ratios							Discordance	Age (Ma)					
Name	Th/U	207Pb/206Pb*	1SE	207Pb/235U*	1SE	206Pb/238U*	1SE	Rho	(%)	207/206	1s	207/235	1s	206/238	1s
JK1_1	10.0	0.049	0.001	0.216	0.025	0.031	0.0032	1.00	89.6	132	30	192	20	196	20
JK1_2	0.26	0.053	0.001	0.361	0.015	0.0497	0.0017	0.95	86.6	312	30	311	11	312	10
JK1_3	0.28	0.063	0.001	0.889	0.024	0.1019	0.0016	0.80	74.18	695	43	643	13	625.3	9.5
JK1_4	0.21	0.070	0.001	1.346	0.039	0.1401	0.0021	0.81	61.14	913	38	861	17	845	12
JK1_5	0.08	0.059	0.001	0.793	0.024	0.0971	0.0019	0.80	70.5	554	40	590	13	597	11
JK1_6	0.16	0.063	0.001	0.909	0.028	0.1037	0.0016	0.76	74.39	691	53	653	15	635.7	9.5
JK1_7	0.58	0.076	0.001	1.887	0.047	0.179	0.0032	1.00	37.8	1103	16	1074	17	1061	18
JK1_8	0.11	0.068	0.001	1.016	0.032	0.1086	0.002	0.84	73.42	870	37	708	16	664	11
JK1_9	0.24	0.073	0.001	1.449	0.039	0.1432	0.0025	0.91	58.5	1010	26	906	16	862	14
JK1_10	0.59	0.058	0.001	0.525	0.025	0.0651	0.0026	0.97	83.22	544	19	424	17	406	16
JK1_11	0.32	0.063	0.000	0.893	0.016	0.1034	0.0013	0.92	66.37	695	15	646.8	8.5	634.3	7.6
JK1_12	0.53	0.064	0.000	1.138	0.039	0.1275	0.0037	0.98	13.5	751	16	766	19	772	21
JK1_13	2.76	0.065	0.000	1.024	0.022	0.1132	0.0019	1.00	68.9	787	11	714	11	691	11
JK1_14	0.54	0.070	0.001	1.41	0.11	0.1402	0.0076	0.98	55.4	908	42	864	44	841	43
JK1_15	0.19	0.070	0.001	1.316	0.045	0.136	0.0029	0.95	48.3	918	30	849	20	821	17
JK1_16	0.33	0.066	0.001	0.94	0.03	0.1034	0.0025	0.96	74.36	809	17	669	16	634	15
JK1_17	0.93	0.065	0.001	1.076	0.039	0.1188	0.0032	1.00	60.47	777	21	736	19	723	19
JK1_18	0.05	0.071	0.001	1.458	0.037	0.1493	0.0026	0.78	39	941	32	910	15	896	15
JK1_19	0.08	0.069	0.001	1.208	0.041	0.1258	0.0026	0.79	69.08	903	44	799	19	763	15
JK1_20	0.25	0.074	0.001	1.519	0.04	0.1501	0.0023	0.92	57.66	1023	25	937	16	901	13
JK1_21	0.82	0.072	0.001	1.611	0.047	0.1603	0.0032	0.98	37.4	988	19	969	19	957	18
JK1_22	0.11	0.076	0.001	1.716	0.03	0.1638	0.0014	0.59	13.3	1081	26	1012	11	977.9	7.8
JK1_23	0.06	0.068	0.002	1.427	0.049	0.1517	0.0025	0.56	53.16	834	61	894	20	910	14
JK1_24	0.91	0.065	0.000	0.962	0.029	0.1073	0.0024	1.00	71.31	763	16	681	15	656	14
JK1_25	0.75	0.061	0.001	0.831	0.039	0.0978	0.0034	0.98	67.4	636	31	607	21	601	20
JK1_26	0.38	0.067	0.000	1.078	0.022	0.1176	0.0018	0.97	68.57	825	11	741	11	717	10

JK1_27	0.21	0.066	0.001	1.089	0.024	0.1202	0.0016	0.80	63.99	799	25	746	12	731.6	9
JK1_28	0.09	0.066	0.002	1.402	0.041	0.1553	0.0021	0.43	50.2	760	58	885	17	930	12
JK1_29	0.22	0.066	0.002	1.224	0.034	0.1343	0.0019	0.63	64.88	795	52	812	16	812	11
JK1_30	0.30	0.070	0.002	1.4	0.048	0.1436	0.0028	0.84	59.72	932	42	883	20	864	16
JK1_31	0.33	0.061	0.000	0.717	0.024	0.086	0.0023	0.98	76.84	634	15	548	15	531	14
JK1_32	0.26	0.065	0.001	1.051	0.027	0.1172	0.0017	0.71	67.74	787	36	729	13	714.1	9.8
JK1_33	0.43	0.069	0.001	1.471	0.039	0.1562	0.003	0.67	43.4	884	37	915	16	935	17
JK1_34	0.54	0.057	0.001	0.616	0.022	0.0774	0.0016	0.88	79.67	483	46	484	14	480.5	9.6
JK1_35	0.25	0.056	0.001	0.53	0.016	0.0689	0.0016	0.88	79.74	429	35	430	11	429.5	9.6
JK1_36	0.47	0.068	0.002	1.615	0.062	0.1709	0.0029	0.72	32.9	832	68	967	25	1017	16
JK1_37	0.03	0.068	0.001	1.301	0.041	0.1413	0.0033	0.83	41.2	853	31	847	20	851	19
JK1_38	0.20	0.065	0.002	1.285	0.039	0.1423	0.0025	0.67	50.3	762	52	837	17	857	14
JK1_39	2.10	0.068	0.000	1.004	0.027	0.1064	0.0022	1.00	74.04	871	14	703	14	651	13
JK1_40	0.16	0.065	0.002	1.219	0.037	0.1353	0.0017	0.76	60.95	751	55	805	18	817.9	9.5
JK1_41	0.33	0.068	0.002	1.488	0.051	0.1595	0.0031	0.55	53.9	820	66	919	21	953	17
JK1_42	0.84	0.075	0.001	1.809	0.045	0.1751	0.003	0.83	41	1064	27	1049	17	1039	17
JK1_43	0.10	0.065	0.001	1.15	0.041	0.1277	0.0028	0.88	60.9	752	46	772	20	774	16
JK1_44	0.22	0.056	0.001	0.531	0.015	0.0683	0.0015	0.92	80.72	453	29	431	10	425.7	8.8
JK1_45	1.40	0.070	0.000	1.231	0.025	0.1262	0.0019	0.98	68.97	940	11	813	11	766	11
JK1_46	0.59	0.062	0.001	0.856	0.068	0.0984	0.0064	0.95	74.4	640	53	608	36	602	37
JK1_47	0.13	0.067	0.001	1.115	0.045	0.1204	0.0036	0.94	41.2	814	33	753	22	732	21
JK1_48	0.14	0.065	0.002	1.257	0.041	0.1403	0.0022	0.74	56	748	55	824	19	846	12
JK1_49	0.14	0.071	0.002	1.723	0.062	0.1756	0.0029	0.68	46.3	923	63	1012	24	1042	16
JK1_50	0.33	0.063	0.001	1.012	0.028	0.1157	0.0021	0.82	62	723	33	709	14	705	12
JK1_51	0.50	0.070	0.002	1.376	0.039	0.1424	0.002	0.71	58.4	944	37	877	17	858	11
JK1_52	0.10	0.066	0.002	1.424	0.051	0.1556	0.0021	0.75	50.4	769	62	892	22	932	12
JK1_53	4.70	0.065	0.001	1.02	0.044	0.1124	0.0038	0.98	68.5	771	28	706	23	686	22
JK1_54	0.21	0.065	0.002	1.318	0.049	0.1474	0.0029	0.71	57.4	730	60	847	21	886	16
JK1_55	0.33	0.061	0.002	1.056	0.036	0.1254	0.0023	0.72	62.71	607	56	727	18	761	13
JK1_56	0.24	0.065	0.001	1.187	0.036	0.1312	0.002	0.75	65.57	764	50	790	17	795	11

JK1_57	0.13	0.067	0.002	1.42	0.04	0.1544	0.0019	0.59	38.8	803	48	893	17	926	10
JK1_58	0.44	0.068	0.002	1.267	0.041	0.1359	0.0025	0.74	64.11	835	52	826	19	821	14
JK1_59	0.88	0.069	0.001	1.177	0.032	0.1243	0.0018	0.83	68.81	903	26	791	14	755	10
JK1_60	0.16	0.066	0.001	1.162	0.03	0.1272	0.0018	0.77	41.5	801	37	782	14	772	10
JK1_61	0.38	0.065	0.002	1.115	0.042	0.1245	0.0027	0.84	66.93	731	55	754	20	756	15
JK1_62	0.53	0.069	0.001	1.292	0.051	0.1345	0.0035	0.88	60.4	902	36	834	23	812	20
JK1_63	0.47	0.068	0.001	1.224	0.04	0.1302	0.0031	0.96	52	860	24	806	18	788	17
JK1_64	0.51	0.068	0.001	0.956	0.029	0.1019	0.0024	0.98	74.93	864	17	682	15	625	14
JK1_65	0.83	0.061	0.002	0.823	0.035	0.097	0.0025	0.86	74.75	612	58	604	20	596	15
JK1_66	0.30	0.066	0.001	0.827	0.025	0.0929	0.002	0.88	76.74	797	19	611	14	572	12
JK1_67	0.06	0.060	0.001	0.882	0.024	0.1073	0.0018	0.74	49.2	569	42	640	13	657	10
JK1_68	0.60	0.065	0.001	0.925	0.026	0.1048	0.0019	0.88	72.55	766	21	662	14	642	11
JK1_69	0.15	0.065	0.001	1.078	0.049	0.1202	0.0043	0.95	50.7	756	34	737	25	730	25
JK1_70	0.64	0.068	0.001	1.1	0.031	0.1191	0.0019	0.83	69.86	863	30	752	15	725	11
JK1_71	0.65	0.067	0.001	1.048	0.03	0.1141	0.0019	0.89	71.71	843	27	724	16	696	11
JK1_72	0.12	0.065	0.001	1.064	0.04	0.1173	0.003	0.91	40.6	775	34	730	19	714	17
JK1_73	7.80	0.064	0.001	0.966	0.043	0.1085	0.0038	1.00	66.7	736	19	679	22	663	22
JK1_74	0.76	0.063	0.000	0.856	0.015	0.099	0.0014	1.00	72.48	696.2	7.7	627.2	8	608.3	7.9
JK1_75	0.18	0.064	0.002	1.088	0.033	0.1235	0.0019	0.72	65.12	714	54	746	17	751	11
JK1_76	0.19	0.063	0.001	0.922	0.03	0.1063	0.0023	0.86	69.56	679	41	660	16	651	13
JK1_77	0.88	0.071	0.000	1.359	0.026	0.1384	0.002	1.00	63.96	959	10	869	11	835	12
JK1_78	0.36	0.066	0.000	1.067	0.03	0.1163	0.0027	0.98	67.95	809	14	734	15	709	15

Table 3D: U-Pb zircon geochronology data for sample JK/2

		Ratios							Discordance	Age (Ma)					
Name	Th/U	207Pb/206Pb*	1SE	207Pb/235U*	1SE	206Pb/238U*	1SE	Rho	(%)	207/206	1s	207/235	1s	206/238	1s
JK2-01	0.57172	0.07219	0.0005	1.58956	0.04176	0.15969	0.0041	0.965	3.95	991	13	966	16	955	22
JK2-02	0.47369	0.07857	0.00083	1.44529	0.06912	0.13342	0.0062	0.975	32.4	1161	20	908	29	807	35

JK2-03	0.45263	0.07207	0.00091	1.44998	0.04305	0.14592	0.0039	0.906	11.9	988	24	910	18	878	22
JK2-04	0.61961	0.09382	0.00087	0.72068	0.02674	0.05571	0.002	0.968	78.81	1504	17	551	16	349	12
JK2_1	0.51026	0.0598	0.0014	0.673	0.082	0.0793	0.0075	0.265	79.7	614	47	511	47	491	44
JK2_2	0.176125	0.05658	0.00072	0.602	0.029	0.0766	0.0032	0.517	71.3	467	30	473	18	475	19
JK2_3	0.999004	0.1205	0.0022	6.37	0.23	0.3816	0.0083	0.324	3.2	1960	29	2014	31	2080	39
JK2_4	0.123264	0.05498	0.00045	0.378	0.018	0.0486	0.0021	0.294	87.34	408	19	323	13	306	13
JK2_5	0.767967	0.0598	0.00091	0.818	0.045	0.0978	0.0039	0.281	54.5	590	37	598	25	601	23
JK2_6	0.192638	0.04778	0.00047	0.223	0.011	0.0336	0.0013	0.546	87.59	84	22	203.1	8.6	212.7	8.4
JK2_7	1.286726	0.0697	0.0018	1.79	0.11	0.1903	0.0081	0.311	-28	899	59	1027	41	1119	43
JK2_8	0.120623	0.0542	0.002	0.442	0.095	0.061	0.013	0.421	81.5	368	82	359	65	376	76
JK2_9	0.198176	0.04663	0.00022	0.0791	0.007	0.0117	0.0011	0.668	96.73	29	11	76.7	6.6	75	6.7
JK2_10	0.057794	0.0556	0.00065	0.571	0.017	0.0749	0.002	0.447	66.2	429	28	457	11	465	12
JK2_11	0.047368	0.0559	0.00068	0.58	0.017	0.0752	0.0017	0.183	64.7	441	30	464	11	469	10
JK2_12	0.135583	0.05917	0.00071	0.735	0.034	0.0897	0.0034	0.275	70.7	567	27	554	20	553	20
JK2_13	3.544444	0.05172	0.00057	0.3324	0.0089	0.04627	0.0008	0.297	85.84	267	27	290.7	6.8	291.5	5
JK2_14	0.467113	0.05715	0.00094	0.655	0.018	0.0831	0.0013	0.264	73.21	483	40	510	11	514.7	7.6
JK2_15	0.252652	0.0511	0.00072	0.374	0.015	0.0528	0.0017	0.39	78.49	236	33	321	11	331	10
JK2_16	0.125917	0.05649	0.00082	0.56	0.039	0.0715	0.0044	0.749	77.5	462	33	446	26	443	26
JK2_17	0.133648	0.05307	0.00096	0.469	0.039	0.062	0.0044	0.829	63.5	316	42	379	27	386	27
JK2_18	0.534783	0.0548	0.0015	0.493	0.065	0.0641	0.007	0.247	78.9	395	65	399	43	400	42

JK2_19	1.940086	0.068	0.0014	1.162	0.069	0.122	0.0056	0.534	68.8	893	33	767	33	740	32
JK2_20	0.27151	0.05329	0.00079	0.44	0.017	0.0594	0.0017	-0.6	79.6	330	35	368	12	371	10

Table 4D: U-Pb zircon geochronology data for samples JK/3 and JK/4

		Ratios							Discordance	Age (Ma)					
Name	Th/U	207Pb/206Pb*	1SE	207Pb/235U*	1SE	206Pb/238U*	1SE	Rho	(%)	207/206	1s	207/235	1s	206/238	1s
JK3-01	0.72868	0.073	0.0011	1.5506	0.052	0.15405	0.0046	0.892	-9.56	1014	29	951	21	924	26
JK4-01	0.76158	0.072	0.00082	1.5549	0.034	0.15663	0.0029	0.851	-5.23	986	22	952	13	938	16
JK4-02	0.01039	0.05846	0.00034	0.8335	0.018	0.10341	0.0022	0.964	16.76	547	12	616	10	634	13
JK4-03	0.01356	0.06377	0.002	0.9056	0.034	0.103	0.0021	0.539	-14.61	734	66	655	18	632	12
JK4-04	0.01563	0.07089	0.00035	1.2193	0.025	0.12476	0.0025	0.972	-21.8	954	10	809	12	758	15
JK4-05	0.70966	0.07393	0.00088	1.5097	0.037	0.14811	0.0032	0.875	-15.35	1039	24	934	15	890	18
JK4-06	0.76807	0.07241	0.00077	1.5327	0.039	0.15352	0.0036	0.909	-8.27	997	21	944	16	921	20
JK4-07	0.85016	0.07254	0.0008	1.5780	0.043	0.15776	0.0039	0.913	-6.11	1001	22	962	17	944	22

Table 5D: U-Pb zircon geochronology data for samples JK/5

		Ratios							Discordance	Age (Ma)					
Name	Th/U	207Pb/206Pb*	1SE	207Pb/235U*	1SE	206Pb/238U*	1SE	Rho	(%)	207/206	1s	207/235	1s	206/238	1s
JK5-01	0.05	0.16178	0.00027	8.7896	0.1426	0.39403	0.00636	0.995	-15.79	2474	3	2316	15	2142	29
JK5-02	0.50	0.17601	0.00046	10.30293	0.16987	0.42454	0.00691	0.987	-15.16	2616	4	2462	15	2281	31
JK5-03	0.23	0.16032	0.00038	8.00136	0.11676	0.36197	0.00521	0.986	-22.06	2459	4	2231	13	1992	25
JK5-04	0.51	0.18171	0.00043	11.77298	0.19249	0.46991	0.0076	0.99	-8.36	2669	4	2587	15	2483	33

JK5-05	0.02	0.16477	0.00051	10.21992	0.15239	0.44985	0.00656	0.978	-5.28	2505	5	2455	14	2395	29
JK5-06	0.12	0.16333	0.00055	9.69736	0.17647	0.43062	0.0077	0.982	-8.68	2490	6	2406	17	2309	35
JK5-07	0.81	0.18789	0.00027	13.33475	0.2321	0.51472	0.00893	0.997	-2.11	2724	2	2704	16	2677	38
JK5-08	0.47	0.07165	0.00032	1.55795	0.02834	0.1577	0.00278	0.97	-3.52	976	9	954	11	944	15
JK5-09	0.23	0.1674	0.00065	10.32884	0.21737	0.44751	0.00926	0.983	-6.97	2532	6	2465	19	2384	41
JK5-10	0.10	0.16369	0.00041	9.70896	0.19776	0.43017	0.0087	0.992	-8.94	2494	4	2408	19	2307	39
JK5-11	0.18	0.16763	0.00063	9.75105	0.18891	0.42189	0.00802	0.981	-12.39	2534	6	2412	18	2269	36
JK5-12	0.65	0.0723	0.00051	1.70301	0.03248	0.17083	0.00302	0.928	2.41	994	14	1010	12	1017	17
JK5-13	0.15	0.07507	0.00071	1.78397	0.03452	0.17235	0.00292	0.874	-4.59	1070	18	1040	13	1025	16
JK5-14	0.99	0.17452	0.00059	9.52143	0.19099	0.3957	0.00782	0.986	-20.4	2601	6	2390	18	2149	36
JK5-15	0.02	0.16439	0.00084	9.76433	0.24031	0.43079	0.01037	0.978	-9.13	2501	9	2413	23	2309	47
JK5-16	0.64	0.20133	0.00063	14.28809	0.32382	0.51472	0.01155	0.99	-6.9	2837	5	2769	22	2677	49
JK5-17	0.02	0.15608	0.00063	8.38145	0.16434	0.38948	0.00747	0.978	-14.24	2414	7	2273	18	2120	35
jk5_1	0.30	0.06558	0.00049	1.057	0.031	0.1164	0.0026	0.998	66.66	791	16	729	15	709	15
jk5_2	0.24	0.094	0.0021	3.07	0.11	0.2353	0.0037	0.905	29.3	1496	41	1418	27	1361	19
jk5_3	0.20	0.1597	0.002	7.84	0.19	0.3586	0.0044	0.863	18.79	2452	21	2223	19	1974	21
jk5_4	0.70	0.1778	0.0037	11.09	0.36	0.4489	0.0093	0.860	9.6	2617	39	2513	36	2386	42
jk5_5	0.09	0.1732	0.001	10.74	0.15	0.4483	0.0048	0.810	7.75	2589	10	2498	13	2387	21
jk5_6	0.61	0.1851	0.0044	10.64	0.36	0.4144	0.0074	0.846	17.3	2678	46	2474	37	2232	34
jk5_7	0.13	0.1392	0.004	6.44	0.29	0.3307	0.0069	0.934	21.5	2187	55	2011	43	1839	33
jk5_8	0.24	0.088	0.0015	2.74	0.11	0.2272	0.0062	0.951	36.5	1386	36	1351	37	1317	32
jk5_9	0.14	0.1471	0.0046	7.09	0.33	0.3443	0.007	0.929	21.4	2278	59	2093	45	1904	34
jk5_10	0.15	0.0994	0.0026	3.26	0.12	0.2359	0.0034	0.894	29.56	1591	47	1459	29	1365	18
jk5_11	0.48	0.17713	0.00085	11.7	0.12	0.4752	0.0047	0.810	4.5	2626.8	8.3	2580.6	9.1	2505	21
jk5_12	0.35	0.1728	0.0015	10.68	0.12	0.4484	0.0036	0.358	7.07	2585	15	2494	10	2387	16
jk5_13	0.31	0.17518	0.00089	11.64	0.11	0.4812	0.0043	0.584	2.85	2607	8.4	2574.5	8.6	2532	19
jk5_14	0.19	0.1698	0.0012	10.136	0.091	0.4331	0.0032	0.430	8.61	2554	11	2446.2	8.2	2319	14
jk5_15	0.04	0.1714	0.0014	10.38	0.11	0.4407	0.0037	0.485	8.24	2569	13	2469.1	9.8	2353	16

jk5_16	0.14	0.1644	0.0027	9.02	0.2	0.3959	0.0056	0.767	13.2	2502	28	2345	18	2152	25
jk5_17	0.28	0.1087	0.0047	4.26	0.32	0.2736	0.0087	0.956	26.8	1721	72	1633	58	1554	44
jk5_18	0.03	0.06018	0.00058	0.76	0.034	0.0915	0.0033	0.971	67.5	614	20	571	20	563	19
jk5_19	0.39	0.17351	0.00062	11.528	0.087	0.4798	0.0039	0.574	2.54	2592.4	6.3	2566.1	7	2526	17
jk5_20	0.43	0.1723	0.002	10.38	0.29	0.4342	0.0084	0.873	9.4	2580	20	2463	25	2321	38
jk5_21	0.17	0.1453	0.0046	7.18	0.35	0.3522	0.0078	0.926	19.1	2257	59	2103	47	1942	37
jk5_22	0.03	0.1716	0.0016	9.89	0.12	0.4187	0.0036	0.543	11.71	2570	15	2422	11	2254	16
jk5_23	0.27	0.1522	0.0041	7.52	0.28	0.3559	0.0054	0.847	19.51	2346	50	2157	36	1961	26
jk5_24	0.30	0.1851	0.0026	10.68	0.18	0.4172	0.0046	0.607	13.97	2698	22	2495	15	2247	21
jk5_25	0.05	0.1459	0.0044	6.93	0.29	0.3404	0.0056	0.927	22.19	2268	56	2079	41	1887	27
jk5_26	0.15	0.1608	0.0051	8.23	0.36	0.3666	0.0055	0.932	21.88	2429	59	2231	43	2012	26
jk5_27	0.05	0.1299	0.0043	5.64	0.26	0.3105	0.0046	0.933	25.73	2060	59	1897	40	1742	22
jk5_28	0.18	0.1503	0.0044	7.46	0.32	0.3554	0.0066	0.887	20.9	2320	54	2144	42	1958	32
jk5_29	0.37	0.1885	0.0025	11.83	0.16	0.4568	0.0039	0.187	9.28	2724	22	2589	12	2425	17
jk5_30	0.21	0.1763	0.0015	10.7	0.11	0.4408	0.0031	0.435	8.84	2616	14	2496.4	9.4	2354	14
jk5_31	0.34	0.1725	0.002	9.94	0.12	0.42	0.0036	0.337	10.65	2578	19	2427	11	2260	17
jk5_32	0.19	0.1631	0.0033	8.66	0.24	0.3839	0.005	0.802	15.93	2496	31	2309	23	2093	24
jk5_33	0.03	0.158	0.0014	7.851	0.095	0.3592	0.0037	0.759	18.38	2432	15	2212	11	1978	18
jk5_34	0.05	0.1637	0.0014	8.59	0.12	0.3778	0.0045	0.825	16.65	2492	14	2293	13	2065	21
jk5_35	0.23	0.1971	0.0074	12.63	0.84	0.452	0.014	0.946	13.23	2763	61	2594	63	2394	64
jk5_36	0.02	0.1583	0.0013	7.917	0.096	0.362	0.0033	0.803	18.67	2436	15	2220	12	1991	16
jk5_37	0.02	0.1135	0.0035	4.34	0.19	0.2741	0.0036	0.941	28.48	1824	55	1682	35	1561	18
jk5_38	0.14	0.06974	0.00074	1.453	0.027	0.1516	0.0017	0.537	2.3	916	22	909	11	909.6	9.7
jk5_39	0.07	0.1269	0.0059	5.47	0.42	0.298	0.011	0.974	29.5	1978	86	1824	70	1677	53
jk5_40	0.10	0.1664	0.0015	8.97	0.11	0.3918	0.0042	0.662	14.97	2520	15	2333	11	2130	19
jk5_41	0.03	0.1608	0.0014	8.46	0.11	0.3819	0.004	0.768	15.48	2462	14	2280	12	2085	19
jk5_42	0.08	0.1666	0.0014	9.42	0.12	0.4133	0.004	0.585	11.49	2522	14	2377	11	2232	18
jk5_43	0.01	0.1493	0.0044	7.83	0.38	0.374	0.01	0.955	16.3	2303	60	2172	54	2041	50
jk5_44	0.23	0.1641	0.0018	9.82	0.15	0.4353	0.0043	0.428	6.32	2497	18	2415	14	2329	19

jk5_45	0.37	0.171	0.0011	11.31	0.12	0.4794	0.0037	0.405	1.45	2567	11	2547.9	9.5	2524	16
jk5_46	0.21	0.1724	0.002	10.53	0.21	0.4429	0.0064	0.801	7.9	2577	19	2477	19	2362	29
jk5_47	0.16	0.164	0.0017	9.13	0.13	0.4036	0.0041	0.713	11.66	2494	17	2349	13	2185	19
jk5_48	0.26	0.2068	0.0028	13.94	0.25	0.4891	0.0072	0.731	10.2	2876	22	2745	18	2579	30
jk5_49	0.13	0.1057	0.0033	3.87	0.18	0.2617	0.0041	0.923	30.9	1697	52	1589	35	1498	21
jk5_50	0.63	0.17452	0.00087	11.53	0.11	0.4788	0.0045	0.574	2.96	2600.8	8.2	2567.3	8.8	2521	20
jk5_51	0.34	0.1579	0.004	8.25	0.33	0.375	0.0074	0.911	15.5	2410	48	2237	40	2050	35
jk5_52	0.14	0.1629	0.0016	8.69	0.1	0.3858	0.0039	0.692	14.65	2483	16	2304	11	2103	18
jk5_53	0.02	0.165	0.0013	9.078	0.087	0.4	0.0031	0.575	13.29	2506	14	2344.8	8.7	2169	14

Table 6D: U-Pb zircon geochronology data for samples JK/6

		Ratios							Discordance	Age (Ma)					
Name	Th/U	207Pb/206Pb*	1SE	207Pb/235U*	1SE	206Pb/238U*	1SE	Rho	(%)	207/206	1s	207/235	1s	206/238	1s
JK6-01	0.05	0.07097	0.0009	1.54	0.032	0.15694	0.0025	0.768	-1.9	957	26	945	13	940	14
JK6-02	0.14	0.15822	0.0026	10.33	0.258	0.47352	0.0090	0.763	3.08	2437	26	2465	23	2499	39
JK6-03	0.05	0.06674	0.0012	1.53	0.086	0.16609	0.0089	0.95	20.92	830	35	942	35	991	49
JK6-04	0.13	0.16081	0.0005	10.01	0.180	0.45145	0.0080	0.985	-3.04	2464	5	2436	17	2402	36
JK6-05	0.30	0.07065	0.0007	1.54	0.024	0.15831	0.0019	0.789	-0.01	947	19	947	10	947	11
JK6-06	0.01	0.15745	0.0003	9.81	0.109	0.45174	0.0049	0.982	-1.26	2428	3	2417	10	2403	22
JK6-07	0.14	0.16093	0.0004	10.02	0.113	0.45137	0.0050	0.98	-3.11	2465	4	2436	10	2401	22
JK6-08	0.14	0.1611	0.0004	10.08	0.150	0.45397	0.0067	0.986	-2.64	2467	4	2442	14	2413	30
JK6-09	0.15	0.14867	0.0005	7.08	0.097	0.34518	0.0046	0.972	-20.75	2331	5	2121	12	1912	22
JK6-10	0.28	0.15104	0.0007	6.98	0.118	0.33521	0.0055	0.96	-24.09	2358	8	2109	15	1864	26
JK6-11	0.43	0.17456	0.0006	11.11	0.200	0.46179	0.0082	0.982	-7.12	2602	5	2533	17	2447	36
JK6-12	0.02	0.15905	0.0004	10.11	0.184	0.46103	0.0083	0.99	-0.07	2446	4	2445	17	2444	37
JK6-13	0.25	0.16888	0.0006	11.02	0.217	0.47326	0.0092	0.986	-2.31	2547	5	2525	18	2498	40
JK6-14	0.18	0.16466	0.0005	10.80	0.160	0.4757	0.0069	0.98	0.21	2504	5	2506	14	2509	30

JK6-15	0.00	0.15091	0.0005	9.21	0.172	0.44264	0.0082	0.987	0.31	2356	5	2359	17	2362	36
JK6-16	0.02	0.15058	0.0007	8.25	0.169	0.39735	0.0080	0.978	-9.78	2353	7	2259	19	2157	37
JK6-17	0.16	0.15759	0.0007	8.29	0.155	0.38139	0.0069	0.972	-16.7	2430	7	2263	17	2083	32
JK6-18	0.07	0.15984	0.0006	9.32	0.157	0.42296	0.0070	0.975	-8.7	2454	6	2370	15	2274	32
JK6-19	0.08	0.15152	0.0007	7.35	0.148	0.35185	0.0069	0.977	-20.54	2363	7	2155	18	1943	33
JK6-20	0.41	0.18491	0.0006	13.06	0.255	0.51224	0.0099	0.985	-1.41	2697	6	2684	18	2666	42
JK6-21	0.02	0.15964	0.0006	9.64	0.196	0.43776	0.0088	0.985	-5.41	2452	6	2401	19	2341	39
JK6-22	0.21	0.12629	0.0009	4.49	0.110	0.25803	0.0061	0.957	-30.96	2047	12	1730	20	1480	31
JK6-23	0.02	0.15208	0.0005	8.11	0.151	0.38677	0.0071	0.985	-12.93	2369	5	2243	17	2108	33
JK6-24	0.11	0.16291	0.0006	9.35	0.222	0.41647	0.0098	0.987	-11.5	2486	6	2373	22	2244	44
JK6-25	0.01	0.15545	0.0005	9.20	0.180	0.42909	0.0083	0.987	-5.19	2407	5	2358	18	2302	37
JK6-26	0.52	0.18047	0.0006	12.68	0.242	0.50968	0.0096	0.987	-0.09	2657	5	2656	18	2655	41
JK6-27	0.09	0.15925	0.0006	8.88	0.202	0.40454	0.0091	0.988	-12.41	2448	6	2326	21	2190	42
JK6-28	0.22	0.16594	0.0006	9.88	0.207	0.43176	0.0089	0.985	-9.61	2517	6	2423	19	2314	40
JK6-29	0.17	0.1582	0.0007	8.78	0.209	0.40243	0.0094	0.985	-12.39	2437	7	2315	22	2180	43
JK6-30	0.09	0.16157	0.0007	9.35	0.205	0.41952	0.0090	0.983	-10.24	2472	7	2373	20	2258	41
jk6_1	0.32	0.16644	0.0010	10.63	0.100	0.4609	0.0038	0.488	3.16	2521.2	9.8	2489.9	8.7	2443	17
jk6_2	0.04	0.11170	0.0037	4.29	0.220	0.274	0.0059	0.936	26.3	1792	58	1665	42	1559	30
jk6_3	1.44	0.17380	0.0014	11.68	0.190	0.4826	0.0046	0.557	2.49	2595	14	2575	15	2538	20
jk6_4	0.04	0.15630	0.0014	8.08	0.093	0.3761	0.0039	0.700	14.57	2414	16	2238	10	2057	18
jk6_5	0.40	0.14230	0.0039	6.51	0.250	0.329	0.0046	0.890	20.81	2229	51	2029	36	1832	22
jk6_6	0.88	0.19159	0.0010	14.35	0.150	0.5419	0.0049	0.668	-1.32	2755.1	8.3	2771.4	9.7	2790	20
jk6_7	1.52	0.19320	0.0043	12.64	0.370	0.4776	0.0068	0.568	8.4	2760	38	2649	29	2515	30
jk6_8	1.17	0.17257	0.0008	11.49	0.098	0.4817	0.0035	0.310	1.79	2582.1	7.8	2563.7	8.2	2536	16
jk6_9	0.49	0.18410	0.0019	10.30	0.220	0.4063	0.0057	0.866	16.73	2687	17	2464	19	2196	26
jk6_10	0.07	0.06162	0.0008	0.81	0.045	0.0949	0.0045	0.972	72.8	660	25	598	27	587	27
jk6_11	0.77	0.18630	0.0015	13.36	0.220	0.5194	0.0055	0.667	0.45	2708	13	2702	15	2695	23
jk6_12	0.08	0.13600	0.0036	6.01	0.210	0.3178	0.0039	0.909	23.39	2152	49	1961	33	1778	19
jk6_13	1.01	0.18170	0.0011	12.24	0.120	0.4874	0.0038	0.432	3.96	2667	10	2622.7	9.7	2559	16
jk6_14	0.06	0.16070	0.0014	8.77	0.110	0.3972	0.0038	0.614	11.98	2461	15	2312	12	2155	17

jk6_15	**0.15**	**0.16150**	**0.0016**	**9.27**	**0.130**	**0.417**	**0.0044**	**0.513**	**8.55**	**2468**	**16**	**2362**	**13**	**2246**	**20**
jk6_16	**0.20**	**0.17130**	**0.0027**	**10.27**	**0.340**	**0.435**	**0.0110**	**0.909**	**9.9**	**2572**	**28**	**2446**	**35**	**2324**	**49**
jk6_17	**0.09**	**0.17110**	**0.0010**	**10.73**	**0.130**	**0.4557**	**0.0042**	**0.745**	**5.6**	**2567**	**10**	**2498**	**12**	**2420**	**19**
jk6_18	**0.02**	**0.12720**	**0.0035**	**5.26**	**0.190**	**0.2973**	**0.0034**	**0.914**	**25.12**	**2034**	**51**	**1846**	**33**	**1677**	**17**
jk6_19	**0.01**	**0.15590**	**0.0041**	**7.96**	**0.330**	**0.3663**	**0.0082**	**0.936**	**19.1**	**2385**	**53**	**2199**	**44**	**2008**	**39**
jk6_20	**0.07**	**0.06281**	**0.0007**	**0.86**	**0.049**	**0.0978**	**0.0046**	**0.988**	**73.3**	**696**	**25**	**618**	**27**	**600**	**27**
jk6_21	**0.09**	**0.07040**	**0.0023**	**1.11**	**0.100**	**0.1108**	**0.0088**	**0.947**	**73.5**	**938**	**70**	**733**	**49**	**671**	**51**
jk6_22	**0.05**	**0.07132**	**0.0005**	**1.59**	**0.019**	**0.162**	**0.0012**	**0.402**	**-1**	**967**	**15**	**966.3**	**7.7**	**967.8**	**6.7**
jk6_23	**0.19**	**0.16410**	**0.0018**	**9.54**	**0.180**	**0.4221**	**0.0056**	**0.628**	**8.6**	**2495**	**18**	**2387**	**17**	**2268**	**25**

Appendix E: Geochronological data for the Basement Complex of South Sudan

Table 1E: K-Ar, Ar-Ar and U-Pb (zircon) geochronology data for the Basement Complex of South Sudan

Sample No.	Locality	Latitude N	Longitude E	Material	Method	Age	Reference
WN 452	170 Km S of Wau	06° 11’	27° 42’	granite	K-Ar	1906 ± 56 Ma	Civetta et al., 1979
WN 452	170 Km S of Wau	06° 11’	27° 42’	granite	K-Ar	1783 ± 51 Ma	Civetta et al., 1979
WN 359	10 Km NE of Yambio	04° 36’	28° 28’	granite	K-Ar	1242 ± 34 Ma	Civetta et al., 1979
WN 441	30 Km N of Tambura	05° 49’	27° 34’	granite	K-Ar	1193 ± 34 Ma	Civetta et al., 1979
WN 443	40 Km N of Tambura	05° 52’	27° 36’	granite	K-Ar	977 ± 28 Ma	Civetta et al., 1979
WN 207b	Near Nimule	03° 38’	32° 00’	gneiss	K-Ar	559 ± 1 8 Ma	Civetta et al., 1979
WN 251	Near Juba	04° 51’	31° 36’	basic dyke	K-Ar	556 ± 18 Ma	Civetta et al., 1979
WN 252	Near Juba	04° 49’	31° 38’	basic dyke	K-Ar	549 ± 18 Ma	Civetta et al., 1979
WN 599	50 Km SE of Torit	04° 02’	32° 49’	granite	K-Ar	654 ± 19 Ma	Civetta et al., 1979
WN 584	60 Km Nimule	04° 06’	32° 15’	granite	K-Ar	594 ± 17 Ma	Civetta et al., 1979
WN 314	80 Km SW of Juba	04° 25’	31° 02’	granite	K-Ar	511 ± 14 Ma	Civetta et al., 1979
WN 207	Aswa Shear NW of Nimule	03°39’	31° 58’	mylonite	K-Ar	443 ± 12 Ma	Civetta et al., 1979
JK/3	West of Juba (J.kujur)	04° 51’	31° 33’	muscovite-biotite gneiss	$^{40}Ar/^{39}Ar$	555 ± 3 Ma	Present work
JK/1	West of Juba (J.kujur)	04° 51’	31° 33’	biotite-hornblende-gneiss	zircon U-Pb	943 ± 47 Ma (emplacement age)	Present work
JK/2	West of Juba (J.kujur)	04° 51’	31° 33’	muscovite-hornblende gneiss	zircon U-Pb	981 ± 12 Ma (emplacement age)	Present work

JK/3	West of Juba (J.kujur)	04° 51’	31° 33’	muscovite-biotite gneiss	zircon U-Pb	924 ± 26 Ma (emplacement age)	Present work
JK/4	West of Juba (J.kujur)	04° 51’	31° 33’	biotite gneiss	zircon U-Pb	933 ± 20 Ma (emplacement age)	Present work
JK/5	West of Juba (J.kujur)	04° 51’	31° 33’	Biotite schist	Detrital zircon U-Pb	920 ± 17 Ma (Max depositional age)	Present work
JK/6	West of Juba (J.kujur)	04° 51’	31° 33’	Biotite-garnet schist	Detrital zircon U-Pb	959 ± 11 Ma (Max depositional age)	Present work